

CERN-LHCC-2012-016

CMS-TDR-011

26 September 2012

CMS TECHNICAL DESIGN REPORT FOR THE PIXEL DETECTOR UPGRADE

The original design goal of the LHC was to operate at $1 \times 10^{34} \text{ cm}^{-2}\text{s}^{-1}$ with 25 ns bunch spacing, where approximately 25 simultaneous inelastic collisions per crossing (“pile-up”) occur. With the upgrade of the accelerators, the luminosity and pile-up will more than double. The current pixel detector is crucial to charged particle tracking, but was not designed to perform effectively in such collision conditions and the physics program of CMS would suffer as a result. We propose to replace the current pixel tracker with a new high efficiency and low mass detector with four barrel layers and three forward/backward disks to provide four-hit pixel coverage out to pseudorapidities of ± 2.5 . This new detector will meet or exceed the original design specifications in these high luminosity environments. In this report, we provide details on the design, construction and installation of the upgraded pixel detector as well as estimates of its expected performance.

Editor

A. Dominguez

Chapter Editors

D. Abbaneo, K. Arndt, N. Bacchetta, A. Ball, E. Bartz, W. Bertl, G.M. Bilei, G. Bolla, H.W.K. Cheung, M. Chertok, S. Costa, N. Demaria, A. Dominguez, K. Ecklund, W. Erdmann, K. Gill, G. Hall, K. Harder, F. Hartmann, R. Horisberger, W. Johns, H.C. Kaestli, K. Klein, D. Kotlinski, S. Kwan, M. Pesaresi, H. Postema, T. Rohe, C. Schäfer, A. Starodumov, S. Streuli, A. Tricomi, P. Tropea, J. Troska, F. Vasey, W. Zeuner.

Acknowledgments

We would like to thank the technical staff from the various institutions for the design, R&D and testing of the many components of this upgrade.

We also wish to thank the LHCC for their oversight and crucial advice during the development of the pixel upgrade project. The important feedback from following CMS internal reviewers greatly helped in the development of this technical design report: D. Contardo, S. Dasu, S.C. Eno, P. Giacomelli, G. Gomez Ceballos, E. Halkiadakis, C. Hill, M. Klute, S. Lowette, M. Mannelli, S. Nahn, I. Shipsey, D. Stuart, S. Tkaczyk and J. Varela.

A special thanks goes to the CMS Secretariat, in particular Anastasia Dolya, for their tireless support during all stages of the project. We also acknowledge the warm support received from the CMS management team and computing project.

Finally, we dedicate this technical design report for the upgrade of the pixel detector to the memory of our two colleagues and friends: Peter Sharp and Manfred Pernicka.

Yerevan Physics Institute, Yerevan, Armenia

S. Chatrchyan, V. Khachatryan, A.M. Sirunyan, A. Tumasyan

Institut für Hochenergiephysik der OeAW, Wien, Austria

W. Adam, E. Aguilo, T. Bergauer, M. Dragicevic, J. Erö, C. Fabjan¹, M. Friedl, R. Frühwirth¹, V.M. Ghete, J. Hammer, N. Hörmann, J. Hrubec, M. Jeitler¹, W. Kiesenhofer, V. Knünz, M. Krammer¹, I. Krätschmer, D. Liko, I. Mikulec, M. Pernicka[†], B. Rahbaran, C. Rohringer, H. Rohringer, R. Schöfbeck, H. Steininger, J. Strauss, A. Taurok, W. Waltenberger, C.-E. Wulz¹

National Centre for Particle and High Energy Physics, Minsk, Belarus

V. Mossolov, N. Shumeiko, J. Suarez Gonzalez

Universiteit Antwerpen, Antwerpen, Belgium

M. Bansal, S. Bansal, T. Cornelis, E.A. De Wolf, X. Janssen, S. Luyckx, L. Mucibello, S. Ochesanu, B. Roland, R. Rougny, M. Selvaggi, H. Van Haevermaet, P. Van Mechelen, N. Van Remortel, A. Van Spilbeeck

Vrije Universiteit Brussel, Brussel, Belgium

F. Blekman, S. Blyweert, J. D'Hondt, R. Gonzalez Suarez, A. Kalogeropoulos, J. Keaveney, M. Maes, A. Olbrechts, W. Van Doninck, P. Van Mulders, G.P. Van Onsem, I. Villella

Université Libre de Bruxelles, Bruxelles, Belgium

B. Clerbaux, G. De Lentdecker, V. Dero, A.P.R. Gay, T. Hreus, A. Léonard, P.E. Marage, A. Mohammadi, T. Reis, L. Thomas, C. Vander Velde, P. Vanlaer, J. Wang

Ghent University, Ghent, Belgium

V. Adler, K. Beernaert, A. Cimmino, S. Costantini, G. Garcia, M. Grunewald, B. Klein, J. Lellouch, A. Marinov, J. McCartin, A.A. Ocampo Rios, D. Ryckbosch, N. Strobbe, F. Thyssen, M. Tytgat, S. Walsh, E. Yazgan, N. Zaganidis

Université Catholique de Louvain, Louvain-la-Neuve, Belgium

S. Basegmez, G. Bruno, R. Castello, L. Ceard, C. Delaere, T. du Pree, D. Favart, L. Forthomme, A. Giammanco², J. Hollar, V. Lemaître, J. Liao, O. Militaru, C. Nuttens, D. Pagano, A. Pin, K. Piotrkowski, J.M. Vizan Garcia

Université de Mons, Mons, Belgium

N. Belyi, T. Caebergs, E. Daubie, G.H. Hammad

Centro Brasileiro de Pesquisas Fisicas, Rio de Janeiro, Brazil

G.A. Alves, M. Correa Martins Junior, T. Martins, M.E. Pol, M.H.G. Souza

Universidade do Estado do Rio de Janeiro, Rio de Janeiro, Brazil

W.L. Aldá Júnior, W. Carvalho, A. Custódio, E.M. Da Costa, D. De Jesus Damiao, C. De Oliveira Martins, S. Fonseca De Souza, H. Malbouisson, M. Malek, D. Matos Figueiredo, L. Mundim, H. Nogima, W.L. Prado Da Silva, A. Santoro, L. Soares Jorge, A. Sznajder, A. Vilela Pereira

Instituto de Fisica Teorica, Universidade Estadual Paulista, Sao Paulo, Brazil

T.S. Anjos³, C.A. Bernardes³, F.A. Dias⁴, T.R. Fernandez Perez Tomei, E.M. Gregores³, C. Lagana, F. Marinho, P.G. Mercadante³, S.F. Novaes, Sandra S. Padula

Institute for Nuclear Research and Nuclear Energy, Sofia, Bulgaria

V. Genchev⁵, P. Iaydjiev⁵, S. Piperov, M. Rodozov, S. Stoykova, G. Sultanov, V. Tcholakov, R. Trayanov, M. Vutova

University of Sofia, Sofia, Bulgaria

A. Dimitrov, R. Hadjiiska, V. Kozhuharov, L. Litov, B. Pavlov, P. Petkov

Institute of High Energy Physics, Beijing, China

J.G. Bian, G.M. Chen, H.S. Chen, C.H. Jiang, D. Liang, S. Liang, X. Meng, J. Tao, J. Wang, X. Wang, Z. Wang, H. Xiao, M. Xu, J. Zang, Z. Zhang

State Key Lab. of Nucl. Phys. and Tech., Peking University, Beijing, China

C. Asawatangkuldee, Y. Ban, Y. Guo, W. Li, S. Liu, Y. Mao, S.J. Qian, H. Teng, D. Wang, L. Zhang, W. Zou

Universidad de Los Andes, Bogota, Colombia

C. Avila, J.P. Gomez, B. Gomez Moreno, A.F. Osorio Oliveros, J.C. Sanabria

Technical University of Split, Split, Croatia

N. Godinovic, D. Lelas, R. Plestina⁶, D. Polic, I. Puljak⁵

University of Split, Split, Croatia

Z. Antunovic, M. Kovac

Institute Rudjer Boskovic, Zagreb, Croatia

V. Brigljevic, S. Duric, K. Kadija, J. Luetic, D. Mekterovic, S. Morovic

University of Cyprus, Nicosia, Cyprus

A. Attikis, M. Galanti, G. Mavromanolakis, J. Mousa, C. Nicolaou, F. Ptochos, P.A. Razis

Charles University, Prague, Czech Republic

M. Finger, M. Finger Jr.

Academy of Scientific Research and Technology of the Arab Republic of Egypt,

Egyptian Network of High Energy Physics, Cairo, Egypt

Y. Assran⁷, S. Elgammal⁸, A. Ellithi Kamel⁹, S. Khalil⁸, M.A. Mahmoud¹⁰, A. Radi^{11,12}

National Institute of Chemical Physics and Biophysics, Tallinn, Estonia

M. Kadastik, M. Müntel, M. Raidal, L. Rebane, A. Tiko

Department of Physics, University of Helsinki, Helsinki, Finland

P. Eerola⁶³, G. Fedi, M. Voutilainen

Helsinki Institute of Physics, Helsinki, Finland

D. Fusi, J. Härkönen, A. Heikkinen, V. Karimäki, R. Kinnunen, M.J. Kortelainen, T. Lampén, K. Lassila-Perini, S. Lehti, T. Lindén, P. Luukka, T. Mäenpää, T. Peltola, E. Tuominen, J. Tuominiemi, E. Tuovinen, D. Ungaro, L. Wendland

Lappeenranta University of Technology, Lappeenranta, Finland

K. Banzuzi, A. Karjalainen, A. Korpela, T. Tuuva

DSM/IRFU, CEA/Saclay, Gif-sur-Yvette, France

M. Besancon, S. Choudhury, M. Dejardin, D. Denegri, B. Fabbro, J.L. Faure, F. Ferri, S. Ganjour, A. Givernaud, P. Gras, G. Hamel de Monchenault, P. Jarry, E. Locci, J. Malcles, L. Millischer, A. Nayak, J. Rander, A. Rosowsky, M. Titov

Laboratoire Leprince-Ringuet, Ecole Polytechnique, IN2P3-CNRS, Palaiseau, France

S. Baffioni, F. Beaudette, L. Benhabib, L. Bianchini, M. Bluj¹³, C. Broutin, P. Busson, C. Charlot, N. Daci, T. Dahms, M. Dalchenko, L. Dobrzynski, A. Florent, R. Granier de Cassagnac, M. Haguenauer, P. Miné, C. Mironov, I.N. Naranjo, M. Nguyen, C. Ochando, P. Paganini, D. Sabes, R. Salerno, Y. Sirois, C. Veelken, A. Zabi

**Institut Pluridisciplinaire Hubert Curien, Université de Strasbourg,
Université de Haute Alsace Mulhouse, CNRS/IN2P3, Strasbourg, France**

J.-L. Agram¹⁴, J. Andrea, R. Baumann, D. Bloch, D. Bodin, C. Bonnin, J.-M. Brom, M. Cardaci,
E.C. Chabert, E. Chambit, L. Charles, C. Collard, E. Conte¹⁴, F. Drouhin¹⁴, J.-C. Fontaine¹⁴,
D. Gelé, U. Goerlach, L. Gross, J. Hosselet, P. Juillot, A.-C. Le Bihan, P. Van Hove

**Centre de Calcul de l'Institut National de Physique Nucleaire et de Physique des Particules,
CNRS/IN2P3, Villeurbanne, France, Villeurbanne, France**

F. Fassi, D. Mercier

**Université de Lyon, Université Claude Bernard Lyon 1, CNRS-IN2P3,
Institut de Physique Nucléaire de Lyon, Villeurbanne, France**

S. Beauceron, N. Beaupere, O. Bondu, G. Boudoul, J. Chasserat, R. Chierici⁵, D. Contardo,
P. Depasse, H. El Mamouni, A. Eynard, J. Fay, S. Gascon, M. Gouzevitch, J.C. Ianigro, B. Ille,
T. Kurca, M. Lethuillier, N. Lumb, L. Mirabito, S. Perries, L. Sgandurra, V. Sordini, Y. Tschudi,
P. Verdier, S. Viret

**Institute of High Energy Physics and Informatization, Tbilisi State University, Tbilisi,
Georgia**

Z. Tsamalaidze¹⁵

RWTH Aachen University, I. Physikalisches Institut, Aachen, Germany

C. Autermann, S. Beranek, B. Calpas, M. Edelhoff, H. Esser, L. Feld, N. Heracleous,
O. Hindrichs, R. Jussen, W. Karpinski, K. Klein, J. Merz, A. Ostapchuk, I. Özen, A. Perieanu,
G. Pierschel, F. Raupach, J. Sammet, S. Schael, S. Schmitz, D. Sprenger, H. Weber, B. Wittmer,
M. Wlochal, V. Zhukov¹⁶

RWTH Aachen University, III. Physikalisches Institut A, Aachen, Germany

M. Ata, J. Caudron, E. Dietz-Laursonn, D. Duchardt, M. Erdmann, R. Fischer, A. Güth,
T. Hebbeker, C. Heidemann, K. Hoepfner, D. Klingebiel, P. Kreuzer, M. Merschmeyer,
A. Meyer, M. Olschewski, P. Papacz, H. Pieta, H. Reithler, S.A. Schmitz, L. Sonnenschein,
J. Steggemann, D. Teyssier, S. Thüer, M. Weber

RWTH Aachen University, III. Physikalisches Institut B, Aachen, Germany

M. Bontenackels, V. Cherepanov, Y. Erdogan, G. Flügge, H. Geenen, M. Geisler,
W. Haj Ahmad, F. Hoehle, B. Kargoll, T. Kress, Y. Kuessel, J. Lingemann⁵, A. Nowack,
L. Perchalla, O. Pooth, P. Sauerland, A. Stahl

Deutsches Elektronen-Synchrotron, Hamburg, Germany

M. Aldaya Martin, J. Behr, W. Behrenhoff, U. Behrens, M. Bergholz¹⁷, A. Bethani, K. Borras,
A. Burgmeier, A. Cakir, L. Calligaris, A. Campbell, E. Castro, F. Costanza, D. Dammann,
C. Diez Pardos, G. Eckerlin, D. Eckstein, T. Eichhorn, G. Flucke, A. Geiser, I. Glushkov,
P. Gunnellini, S. Habib, J. Hampe, J. Hansen, K. Hansen, J. Hauk, G. Hellwig, H. Jung,
M. Kasemann, P. Katsas, C. Kleinwort, H. Kluge, A. Knutsson, M. Krämer, D. Krücker,
E. Kuznetsova, W. Lange, J. Leonard, W. Lohmann¹⁷, B. Lutz, R. Mankel, I. Marfin,
M. Marienfeld, H. Maser, I.-A. Melzer-Pellmann, A.B. Meyer, J. Mnich, C. Muhl, A. Mussgiller,
S. Naumann-Emme, O. Novgorodova, J. Olzem, H. Perrey, A. Petrukhin, D. Pitzl,
A. Raspereza, P.M. Ribeiro Cipriano, C. Riedl, E. Ron, M. Rosin, J. Salfeld-Nebgen,
R. Schmidt¹⁷, T. Schoerner-Sadenius, N. Sen, A. Spiridonov, M. Stein, R. Walsh, C. Wissing,
A. Zuber

University of Hamburg, Hamburg, Germany

L. Berger, V. Blobel, M. Centis Vignali, H. Enderle, J. Erfle, B. Frensch, E. Garutti, U. Gebbert,

M. Görner, M. Gosselink, J. Haller, T. Hermanns, R.S. Höing, K. Kaschube, G. Kaussen, H. Kirschenmann, R. Klanner, J. Lange, T. Lapsien, M. Matysek, F. Nowak, T. Peiffer, N. Pietsch, D. Rathjens, C. Sander, H. Schettler, P. Schleper, E. Schlieckau, A. Schmidt, M. Schröder, T. Schum, S. Schuwalow, M. Seidel, J. Sibille¹⁸, V. Sola, H. Stadie, G. Steinbrück, J. Thomsen, L. Vanelderen

Institut für Experimentelle Kernphysik, Karlsruhe, Germany

C. Barth, T. Barvich, J. Berger, Th. Blank, F. Bögelspacher, C. Böser, M. Caselle, T. Chwalek, W. De Boer, A. Descroix, A. Dierlamm, M. Feindt, M. Guthoff⁵, C. Hackstein, F. Hartmann⁵, T. Hauth⁵, S. Heindl, M. Heinrich, H. Held, K.H. Hoffmann, U. Husemann, I. Katkov¹⁶, J.R. Komaragiri, A. Kornmayer, P. Lobelle Pardo, D. Martschei, S. Mueller, Th. Müller, M. Niegel, A. Nürnberg, O. Oberst, A. Oehler, J. Ott, G. Quast, K. Rabbertz, F. Ratnikov, N. Ratnikova, S. Röcker, F.-P. Schilling, G. Schott, H.J. Simonis, P. Steck, F.M. Stober, D. Troendle, R. Ulrich, J. Wagner-Kuhr, S. Wayand, M. Weber, T. Weiler, M. Zeise

Institute of Nuclear Physics "Demokritos", Aghia Paraskevi, Greece

G. Anagnostou, G. Daskalakis, T. Gerasis, S. Kesisoglou, A. Kyriakis, D. Loukas, I. Manolakos, A. Markou, C. Markou, C. Mavrommatis, E. Ntomari

University of Athens, Athens, Greece

L. Gouskos, T.J. Mertzimekis, A. Panagiotou, N. Saoulidou

University of Ioánnina, Ioánnina, Greece

I. Evangelou, C. Foudas, P. Kokkas, N. Manthos, I. Papadopoulos, V. Patras

KFKI Research Institute for Particle and Nuclear Physics, Budapest, Hungary

G. Bencze, C. Hajdu, P. Hidas, D. Horvath¹⁹, F. Sikler, V. Veszpremi, G. Vesztergombi²⁰

Institute of Nuclear Research ATOMKI, Debrecen, Hungary

N. Beni, S. Czellar, J. Molnar, J. Palinkas, Z. Szillasi

University of Debrecen, Debrecen, Hungary

J. Karancsi, P. Raics, Z.L. Trocsanyi, B. Ujvari

Panjab University, Chandigarh, India

S.B. Beri, V. Bhatnagar, N. Dhingra, R. Gupta, M. Kaur, M.Z. Mehta, N. Nishu, L.K. Saini, A. Sharma, J.B. Singh

University of Delhi, Delhi, India

Ashok Kumar, Arun Kumar, S. Ahuja, A. Bhardwaj, B.C. Choudhary, S. Malhotra, M. Naimuddin, K. Ranjan, V. Sharma, R.K. Shivpuri

Saha Institute of Nuclear Physics, Kolkata, India

S. Banerjee, S. Bhattacharya, S. Dutta, B. Gomber, Sa. Jain, Sh. Jain, R. Khurana, S. Sarkar, M. Sharan

Bhabha Atomic Research Centre, Mumbai, India

A. Abdulsalam, D. Dutta, S. Kailas, V. Kumar, A.K. Mohanty⁵, L.M. Pant, P. Shukla

Tata Institute of Fundamental Research - EHEP, Mumbai, India

T. Aziz, S. Ganguly, M. Guchait²¹, A. Gurtu²², M. Maity²³, G. Majumder, K. Mazumdar, G.B. Mohanty, B. Parida, K. Sudhakar, N. Wickramage

Tata Institute of Fundamental Research - HECR, Mumbai, India

S. Banerjee, S. Dugad

Institute for Research in Fundamental Sciences (IPM), Tehran, Iran

H. Arfaei²⁴, H. Bakhshiansohi, S.M. Etesami²⁵, A. Fahim²⁴, M. Hashemi²⁶, H. Hesari, A. Jafari, M. Khakzad, M. Mohammadi Najafabadi, S. Paktinat Mehdiabadi, B. Safarzadeh²⁷, M. Zeinali

INFN Sezione di Bari ^a, Università di Bari ^b, Politecnico di Bari ^c, Bari, Italy

M. Abbrescia^{a,b}, L. Barbone^{a,b}, C. Calabria^{a,b,5}, P. Cariola^a, S.S. Chhibra^{a,b}, A. Colaleo^a, D. Creanza^{a,c}, R. Ferorelli^a, N. De Filippis^{a,c,5}, M. De Palma^{a,b}, L. Fiore^a, G. Iaselli^{a,c}, G. Maggi^{a,c}, M. Maggi^a, B. Marangelli^{a,b}, C.S. Moon^a, S. My^{a,c}, S. Nuzzo^{a,b}, N. Pacifico^a, A. Pompili^{a,b}, G. Pugliese^{a,c}, G. Sala^a, A. Savoy-Navarro^a, G. Selvaggi^{a,b}, L. Silvestris^a, G. Singh^{a,b}, R. Venditti^{a,b}, P. Verwilligen^a, G. Zito^a

INFN Sezione di Bologna ^a, Università di Bologna ^b, Bologna, Italy

G. Abbiendi^a, A.C. Benvenuti^a, D. Bonacorsi^{a,b}, S. Braibant-Giacomelli^{a,b}, L. Brigliadori^{a,b}, P. Capiluppi^{a,b}, A. Castro^{a,b}, F.R. Cavallo^a, M. Cuffiani^{a,b}, G.M. Dallavalle^a, F. Fabbri^a, A. Fanfani^{a,b}, D. Fasanella^{a,b}, P. Giacomelli^a, C. Grandi^a, L. Guiducci^{a,b}, S. Marcellini^a, M. Mascioveccio, G. Masetti^a, M. Meneghelli^{a,b,5}, A. Montanari^a, F.L. Navarria^{a,b}, F. Odorici^a, A. Perrotta^a, F. Primavera^{a,b}, A.M. Rossi^{a,b}, T. Rovelli^{a,b}, G.P. Siroli^{a,b}, N. Tosi^b, R. Travaglini^{a,b}

INFN Sezione di Catania ^a, Università di Catania ^b, Catania, Italy

S. Albergo^{a,b}, G. Cappello^{a,b}, M. Chiorboli^{a,b}, S. Costa^{a,b}, R. Potenza^{a,b}, N. Giudice^{a,b}, N. Guardone^{a,b}, F. Librizzi^a, A. Tricomi^{a,b}, C. Tuve^{a,b}

INFN Sezione di Firenze ^a, Università di Firenze ^b, Firenze, Italy

G. Barbagli^a, V. Ciulli^{a,b}, C. Civinini^a, R. D'Alessandro^{a,b}, E. Focardi^{a,b}, S. Frosali^{a,b}, E. Gallo^a, S. Gonzi^{a,b}, M. Meschini^a, S. Paoletti^a, G. Sguazzoni^a, A. Tropiano^{a,b}

INFN Laboratori Nazionali di Frascati, Frascati, Italy

L. Benussi, S. Bianco, S. Colafranceschi²⁸, F. Fabbri, D. Piccolo

INFN Sezione di Genova ^a, Università di Genova ^b, Genova, Italy

P. Fabbriatore^a, R. Ferretti, F. Ferro, M. Lo Vetere, S. Minutoli, R. Monge, R. Musenich^a, E. Robutti, S. Tosi^{a,b}

INFN Sezione di Milano-Bicocca ^a, Università di Milano-Bicocca ^b, Milano, Italy

A. Benaglia^a, P. D'Angelo, F. De Guio^{a,b}, L. Di Matteo^{a,b,5}, S. Fiorendi^{a,b}, S. Gennai^{a,5}, A. Ghezzi^{a,b}, S. Malvezzi^a, R.A. Manzoni^{a,b}, A. Martelli^{a,b}, A. Massironi^{a,b}, D. Menasce^a, L. Moroni^a, M. Paganoni^{a,b}, D. Pedrini^a, S. Ragazzi^{a,b}, N. Redaelli^a, S. Sala^a, T. Tabarelli de Fatis^{a,b}

INFN Sezione di Napoli ^a, Università di Napoli "Federico II" ^b, Napoli, Italy

S. Buontempo^a, C.A. Carrillo Montoya^a, N. Cavallo^{a,29}, A. De Cosa^{a,b,5}, O. Dogangun^{a,b}, F. Fabozzi^{a,29}, A.O.M. Iorio^{a,b}, L. Lista^a, S. Meola^{a,30}, M. Merola^a, P. Paolucci^{a,5}

INFN Sezione di Padova ^a, Università di Padova ^b, Università di Trento (Trento) ^c, Padova, Italy

P. Azzi^a, N. Bacchetta^{a,5}, P. Bellan^{a,b}, D. Bisello^{a,b}, A. Branca^{a,5}, R. Carlin^{a,b}, P. Checchia^a, T. Dorigo^a, U. Dosselli^a, F. Gasparini^{a,b}, U. Gasparini^{a,b}, P. Giubilato, A. Gozzelino^a, K. Kanishchev^{a,c}, S. Lacaprara^a, I. Lazzizzera^{a,c}, M. Margoni^{a,b}, A.T. Meneguzzo^{a,b}, M. Nespolo^{a,5}, D. Pantano, J. Pazzini^{a,b}, N. Pozzobon, P. Ronchese^{a,b}, F. Simonetto^{a,b}, E. Torassa^a, M. Tosi^{a,b}, S. Vanini^{a,b}, P. Zotto^{a,b}, A. Zucchetta^{a,b}, G. Zumerle^{a,b}

INFN Sezione di Pavia ^a, Università di Pavia ^b, Pavia, Italy

M. Gabusi^{a,b}, S.P. Ratti^{a,b}, C. Riccardi^{a,b}, P. Torre^{a,b}, P. Vitulo^{a,b}

INFN Sezione di Perugia ^a, Università di Perugia ^b, Perugia, Italy

M. Biasini^{a,b}, G.M. Bilei^a, S. Bizzaglia, M. Bizzarri, B. Checcucci, E. Conti, L. Fanò^{a,b},
G. Farnesini, P. Lariccia^{a,b}, G. Mantovani^{a,b}, M. Menichelli^a, S. Meroli, A. Nappi^{a,b†}, A. Papi,
D. Passeri, P. Placidi, F. Romeo^{a,b}, A. Saha^a, A. Santocchia^{a,b}, G. Scolieri, L. Servoli,
A. Spiezia^{a,b}, S. Taroni^{a,b}

INFN Sezione di Pisa ^a, Università di Pisa ^b, Scuola Normale Superiore di Pisa ^c, Pisa, Italy

P. Azzurri^{a,c}, G. Bagliesi^a, A. Basti, R. Beccherle, J. Bernardini, T. Boccali^a, F. Bosi,
G. Broccolo^{a,c}, D. Caiulo, R. Castaldi^a, M.A. Ciocci, R.T. D’Agnolo^{a,c,5}, R. Dell’Orso^a,
S. Donato, F. Fiori^{a,b,5}, L. Foà^{a,c}, A. Giassi^a, M.T. Grippo, A. Kraan^a, F. Ligabue^{a,c},
T. Lomtadze^a, P. Mammini, L. Martini^{a,31}, A. Messineo^{a,b}, A. Moggi, F. Palla^a, F. Palmonari,
A. Profeti, F. Raffaelli, A. Rizzi^{a,b}, A.T. Serban^{a,32}, P. Spagnolo^a, P. Squillacioti^{a,5}, R. Tenchini^a,
G. Tonelli^{a,b}, A. Venturi^a, P.G. Verdini^a, C. Vernieri

INFN Sezione di Roma ^a, Università di Roma “La Sapienza” ^b, Roma, Italy

L. Barone^{a,b}, F. Cavallari^a, D. Del Re^{a,b}, M. Diemoz^a, C. Fanelli, M. Grassi^{a,b,5}, E. Longo^{a,b},
P. Meridiani^{a,5}, F. Micheli^{a,b}, S. Nourbakhsh^{a,b}, G. Organtini^{a,b}, R. Paramatti^a, S. Rahatlou^{a,b},
M. Sigamani^a, L. Soffi^{a,b}

INFN Sezione di Torino ^a, Università di Torino ^b,

Università del Piemonte Orientale (Novara) ^c, Torino, Italy

N. Amapane^{a,b}, R. Arcidiacono^{a,c}, S. Argiro^{a,b}, M. Arneodo^{a,c}, C. Biino^a, N. Cartiglia^a,
S. Casasso^{a,b}, M. Costa^{a,b}, D. Dattola^a, G. Dellacasa^a, N. Demaria^a, C. Mariotti^{a,5}, S. Maselli^a,
G. Mazza^a, E. Migliore^{a,b}, V. Monaco^{a,b}, M. Musich^{a,5}, M.M. Obertino^{a,c}, L. Pacher^{a,b},
N. Pastrone^a, M. Pelliccioni^a, A. Potenza^{a,b}, A. Rivetti^a, A. Romero^{a,b}, M. Ruspa^{a,c},
R. Sacchi^{a,b}, A. Solano^{a,b}, A. Staiano^a, P. Trapani^{a,b}

INFN Sezione di Trieste ^a, Università di Trieste ^b, Trieste, Italy

S. Belforte^a, V. Candelise^{a,b}, M. Casarsa^a, F. Cossutti^a, G. Della Ricca^{a,b}, B. Gobbo^a,
M. Marone^{a,b,5}, D. Montanino^{a,b,5}, A. Penzo^a, A. Schizzi^{a,b}

Kangwon National University, Chunchon, Korea

T.Y. Kim, S.K. Nam

Kyungpook National University, Daegu, Korea

S. Chang, D.H. Kim, G.N. Kim, D.J. Kong, H. Park, D.C. Son, T. Son

Chonnam National University, Institute for Universe and Elementary Particles, Kwangju, Korea

J.Y. Kim, Zero J. Kim, S. Song

Korea University, Seoul, Korea

S. Choi, D. Gyun, B. Hong, M. Jo, H. Kim, T.J. Kim, K.S. Lee, D.H. Moon, S.K. Park

University of Seoul, Seoul, Korea

M. Choi, J.H. Kim, C. Park, I.C. Park, S. Park, G. Ryu

Sungkyunkwan University, Suwon, Korea

Y. Choi, Y.K. Choi, J. Goh, M.S. Kim, E. Kwon, B. Lee, J. Lee, S. Lee, H. Seo, I. Yu

Vilnius University, Vilnius, Lithuania

M.J. Bilinskas, I. Grigelionis, M. Janulis, A. Juodagalvis

Centro de Investigación y de Estudios Avanzados del IPN, Mexico City, Mexico

H. Castilla-Valdez, E. De La Cruz-Burelo, I. Heredia-de La Cruz, R. Lopez-Fernandez,
J. Martínez-Ortega, A. Sánchez-Hernández, L.M. Villasenor-Cendejas

Universidad Iberoamericana, Mexico City, Mexico

S. Carrillo Moreno, F. Vazquez Valencia

Benemerita Universidad Autonoma de Puebla, Puebla, Mexico

H.A. Salazar Ibarguen

Universidad Autónoma de San Luis Potosí, San Luis Potosí, Mexico

E. Casimiro Linares, A. Morelos Pineda, M.A. Reyes-Santos

University of Auckland, Auckland, New Zealand

D. Krofcheck

University of Canterbury, Christchurch, New Zealand

A.J. Bell, P.H. Butler, R. Doesburg, S. Reucroft, H. Silverwood

National Centre for Physics, Quaid-I-Azam University, Islamabad, Pakistan

M. Ahmad, M.I. Asghar, J. Butt, H.R. Hoorani, S. Khalid, W.A. Khan, T. Khurshid, S. Qazi,
M.A. Shah, M. Shoaib

National Centre for Nuclear Research, Swierk, Poland

H. Bialkowska, B. Boimska, T. Frueboes, M. Górski, M. Kazana, K. Nawrocki,
K. Romanowska-Rybinska, M. Szleper, G. Wrochna, P. Zalewski

Institute of Experimental Physics, Faculty of Physics, University of Warsaw, Warsaw, Poland

G. Brona, K. Bunkowski, M. Cwiok, W. Dominik, K. Doroba, A. Kalinowski, M. Konecki,
J. Krolikowski, M. Misiura

Laboratório de Instrumentação e Física Experimental de Partículas, Lisboa, Portugal

N. Almeida, P. Bargassa, A. David, P. Faccioli, P.G. Ferreira Parracho, M. Gallinaro, J. Seixas,
J. Varela, P. Vischia

Joint Institute for Nuclear Research, Dubna, Russia

I. Belotelov, P. Bunin, M. Gavrilenko, I. Golutvin, I. Gorbunov, A. Kamenev, V. Karjavin,
G. Kozlov, A. Lanev, A. Malakhov, P. Moisenz, V. Palichik, V. Perelygin, S. Shmatov,
V. Smirnov, A. Volodko, A. Zarubin

Petersburg Nuclear Physics Institute, Gatchina (St. Petersburg), Russia

S. Evstyukhin, V. Golovtsov, Y. Ivanov, V. Kim, P. Levchenko, V. Murzin, V. Oreshkin,
I. Smirnov, V. Sulimov, L. Uvarov, S. Vavilov, A. Vorobyev, An. Vorobyev

Institute for Nuclear Research, Moscow, Russia

Yu. Andreev, A. Dermenev, S. Gninenko, N. Golubev, M. Kirsanov, N. Krasnikov, V. Matveev,
A. Pashenkov, D. Tlisov, A. Toropin

Institute for Theoretical and Experimental Physics, Moscow, Russia

V. Epshteyn, M. Erofeeva, V. Gavrillov, M. Kossov, N. Lychkovskaya, V. Popov, G. Safronov,
S. Semenov, I. Shreyber, V. Stolin, E. Vlasov, A. Zhokin

Moscow State University, Moscow, Russia

A. Belyaev, E. Boos, M. Dubinin⁴, L. Dudko, A. Ershov, A. Gribushin, V. Klyukhin, O. Kodolova, I. Lokhtin, A. Markina, S. Obraztsov, M. Perfilov, S. Petrushanko, A. Popov, L. Sarycheva[†], V. Savrin, A. Snigirev

P.N. Lebedev Physical Institute, Moscow, Russia

V. Andreev, M. Azarkin, I. Dremin, M. Kirakosyan, A. Leonidov, G. Mesyats, S.V. Rusakov, A. Vinogradov

State Research Center of Russian Federation, Institute for High Energy Physics, Protvino, Russia

I. Azhgirey, I. Bayshev, S. Bitioukov, V. Grishin⁵, V. Kachanov, D. Konstantinov, V. Krychkine, V. Petrov, R. Ryutin, A. Sobol, L. Tourtchanovitch, S. Troshin, N. Tyurin, A. Uzunian, A. Volkov

University of Belgrade, Faculty of Physics and Vinca Institute of Nuclear Sciences, Belgrade, Serbia

P. Adzic³³, M. Djordjevic, M. Ekmedzic, D. Krpic³³, J. Milosevic

Centro de Investigaciones Energéticas Medioambientales y Tecnológicas (CIEMAT), Madrid, Spain

M. Aguilar-Benitez, J. Alcaraz Maestre, P. Arce, C. Battilana, E. Calvo, M. Cerrada, M. Chamizo Llatas, N. Colino, B. De La Cruz, A. Delgado Peris, D. Domínguez Vázquez, C. Fernandez Bedoya, J.P. Fernández Ramos, A. Ferrando, J. Flix, M.C. Fouz, P. Garcia-Abia, O. Gonzalez Lopez, S. Goy Lopez, J.M. Hernandez, M.I. Josa, G. Merino, J. Puerta Pelayo, A. Quintario Olmeda, I. Redondo, L. Romero, J. Santaolalla, M.S. Soares, C. Willmott

Universidad Autónoma de Madrid, Madrid, Spain

C. Albajar, G. Codispoti, J.F. de Trocóniz

Universidad de Oviedo, Oviedo, Spain

H. Brun, J. Cuevas, J. Fernandez Menendez, S. Folgueras, I. Gonzalez Caballero, L. Lloret Iglesias, J. Piedra Gomez

Instituto de Física de Cantabria (IFCA), CSIC-Universidad de Cantabria, Santander, Spain

J.A. Brochero Cifuentes, I.J. Cabrillo, A. Calderon, S.H. Chuang, J. Duarte Campderros, M. Felcini³⁴, M. Fernandez, G. Gomez, J. Gonzalez Sanchez, A. Graziano, C. Jorda, A. Lopez Virto, J. Marco, R. Marco, C. Martinez Rivero, F. Matorras, F.J. Munoz Sanchez, T. Rodrigo, A.Y. Rodríguez-Marrero, A. Ruiz-Jimeno, L. Scodellaro, I. Vila, R. Vilar Cortabitarte

CERN, European Organization for Nuclear Research, Geneva, Switzerland

D. Abbaneo, I. Ahmed, E. Albert, E. Auffray, G. Auzinger, M. Bachtis, P. Baillon, A.H. Ball, D. Barney, J.F. Benitez, C. Bernet⁶, G. Bianchi, G. Blanchot, P. Bloch, A. Bocci, A. Bonato, C. Botta, H. Breuker, T. Camporesi, G. Cerminara, T. Christiansen, J.A. Coarasa Perez, D. D'Enterria, A. Dabrowski, J. Daguin, A. De Roeck, S. Detraz, D. Deyrail, S. Di Guida, M. Dobson, N. Dupont-Sagorin, A. Elliott-Peisert, F. Faccio, N. Frank, B. Frisch, W. Funk, G. Georgiou, M. Giffels, D. Gigi, K. Gill, D. Giordano, M. Girone, M. Giunta, F. Glege, R. Gomez-Reino Garrido, P. Govoni, S. Gowdy, R. Guida, S. Gundacker, M. Hansen, P. Harris, C. Hartl, J. Harvey, B. Hegner, A. Hinzmann, V. Innocente, P. Janot, K. Kaadze, E. Karavakis, T. Katopodis, A. Kornmayer, L. Kottelat, A. Koukovinis, K. Kousouris, P. Lecoq, Y.-J. Lee, P. Lenzi, C. Lourenço, N. Magini, T. Mäki, M. Malberti, L. Malgeri, M. Mannelli, L. Masetti, F. Meijers, S. Mersi, E. Meschi, S. Michelis, R. Moser, M.U. Mozer, M. Mulders, P. Musella, E. Nesvold, J. Noite, T. Orimoto, L. Orsini, E. Palencia Cortezon, A. Peisert, E. Perez,

J.-F. Pernot, L. Perrozzi, P. Petagna, A. Petrilli, A. Pfeiffer, M. Pierini, M. Pimiä, D. Piparo, G. Polese, H. Postema, L. Quertenmont, A. Racz, W. Reece, J. Rodrigues Antunes, G. Rolandi³⁵, C. Rovelli³⁶, M. Rovere, H. Sakulin, F. Santanastasio, C. Schäfer, C. Schwick, I. Segoni, S. Sekmen, A. Sharma, P. Siegrist, P. Silva, M. Simon, P. Sphicas³⁷, D. Spiga, P. Tropea, J. Troska, A. Tsirou, F. Vasey, G.I. Veres²⁰, B. Verlaet, J.R. Vlimant, H.K. Wöhri, S.D. Worm³⁸, W.D. Zeuner, L. Zwalinski

Paul Scherrer Institut, Villigen, Switzerland

W. Bertl, K. Deiters, W. Erdmann, R. Horisberger, H.C. Kaestli, D. Kotlinski, U. Langenegger, B. Meier, F. Meier, T. Rohe, S. Streuli

Institute for Particle Physics, ETH Zurich, Zurich, Switzerland

F. Bachmair, L. Bäni, R. Becker, P. Bortignon, M.A. Buchmann, B. Casal, N. Chanon, A. Deisher, G. Dissertori, M. Dittmar, M. Donegà, M. Dünser, P. Eller, J. Eugster, K. Freudenreich, C. Grab, D. Hits, U. Horisberger, P. Lecomte, W. Lustermann, A.C. Marini, P. Martinez Ruiz del Arbol, N. Mohr, F. Moortgat, C. Nägeli³⁹, P. Nef, F. Nessi-Tedaldi, F. Pandolfi, L. Pape, F. Pauss, M. Peruzzi, U. Roeser, F.J. Ronga, M. Rossini, L. Sala, A.K. Sanchez, A. Starodumov⁴⁰, B. Stieger, M. Takahashi, L. Tauscher[†], A. Thea, K. Theofilatos, D. Treille, C. Urscheler, H.P. von Gunten, R. Wallny, H.A. Weber, L. Wehrli

Universität Zürich, Zurich, Switzerland

C. AMSLER⁴¹, K. Boesiger, V. Chiochia, S. De Visscher, C. Favaro, M. Ivova Rikova, B. Kilminster, R. Maier, B. Millan Mejias, P. Otiougova, P. Robmann, H. Snoek, S. Tupputi, M. Verzetti

National Central University, Chung-Li, Taiwan

Y.H. Chang, K.H. Chen, C. Ferro, C.M. Kuo, S.W. Li, W. Lin, Y.J. Lu, A.P. Singh, R. Volpe, S.S. Yu

National Taiwan University (NTU), Taipei, Taiwan

P. Bartalini, P. Chang, Y.H. Chang, Y.W. Chang, Y. Chao, K.F. Chen, P.-H. Chen, C. Dietz, U. Grundler, W.-S. Hou, Y. Hsiung, K.Y. Kao, Y.J. Lei, J.-J. Liao, S.-H. Lin, R.-S. Lu, D. Majumder, E. Petrakou, X. Shi, J.G. Shiu, Y.M. Tzeng, X. Wan, M. Wang

Chulalongkorn University, Bangkok, Thailand

B. Asavapibhop, E. Simili, N. Srimanobhas

Cukurova University, Adana, Turkey

A. Adiguzel, M.N. Bakirci⁴², S. Cerci⁴³, C. Dozen, I. Dumanoglu, E. Eskut, S. Girgis, G. Gokbulut, E. Gurpinar, I. Hos, E.E. Kangal, T. Karaman, G. Karapinar⁴⁴, A. Kayis Topaksu, G. Onengut, K. Ozdemir, S. Ozturk⁴⁵, A. Polatoz, K. Sogut⁴⁶, D. Sunar Cerci⁴³, B. Tali⁴³, H. Topakli⁴², L.N. Vergili, M. Vergili

Middle East Technical University, Physics Department, Ankara, Turkey

I.V. Akin, T. Aliev, B. Bilin, S. Bilmis, M. Deniz, H. Gamsizkan, A.M. Guler, K. Ocalan, A. Ozpineci, M. Serin, R. Sever, U.E. Surat, M. Yalvac, E. Yildirim, M. Zeyrek

Bogazici University, Istanbul, Turkey

E. Gülmez, B. Isildak⁴⁷, M. Kaya⁴⁸, O. Kaya⁴⁸, S. Ozkorucuklu⁴⁹, N. Sonmez⁵⁰

Istanbul Technical University, Istanbul, Turkey

K. Cankocak

National Scientific Center, Kharkov Institute of Physics and Technology, Kharkov, Ukraine

L. Levchuk

University of Bristol, Bristol, United Kingdom

J.J. Brooke, E. Clement, D. Cussans, H. Flacher, R. Frazier, J. Goldstein, M. Grimes, G.P. Heath, H.F. Heath, L. Kreczko, S. Metson, D.M. Newbold³⁸, K. Nirunpong, A. Poll, S. Senkin, V.J. Smith, T. Williams

Rutherford Appleton Laboratory, Didcot, United Kingdom

L. Basso⁵¹, K.W. Bell, A. Belyaev⁵¹, C. Brew, R.M. Brown, D.J.A. Cockerill, J.A. Coughlan, K. Harder, S. Harper, J. Jackson, B.W. Kennedy, E. Olaiya, D. Petyt, B.C. Radburn-Smith, C.H. Shepherd-Themistocleous, I.R. Tomalin, W.J. Womersley

Imperial College, London, United Kingdom

R. Bainbridge, G. Ball, R. Beuselinck, O. Buchmuller, D. Colling, N. Cripps, M. Cutajar, P. Dauncey, G. Davies, M. Della Negra, W. Ferguson, J. Fulcher, D. Futyan, A. Gilbert, A. Guneratne Bryer, G. Hall, Z. Hatherell, J. Hays, G. Iles, M. Jarvis, G. Karapostoli, L. Lyons, A.-M. Magnan, J. Marrouche, B. Mathias, R. Nandi, J. Nash, A. Nikitenko⁴⁰, A. Papageorgiou, J. Pela, M. Pesaresi, K. Petridis, M. Pioppi⁵², D.M. Raymond, S. Rogerson, A. Rose, M.J. Ryan, C. Seez, P. Sharp[†], A. Sparrow, M. Stoye, A. Tapper, M. Vazquez Acosta, T. Virdee, S. Wakefield, N. Wardle, T. Whyntie

Brunel University, Uxbridge, United Kingdom

M. Chadwick, J.E. Cole, P.R. Hobson, A. Khan, P. Kyberd, D. Leggat, D. Leslie, W. Martin, I.D. Reid, P. Symonds, L. Teodorescu, M. Turner

Baylor University, Waco, USA

K. Hatakeyama, H. Liu, T. Scarborough

The University of Alabama, Tuscaloosa, USA

O. Charaf, C. Henderson, P. Rumerio

Boston University, Boston, USA

A. Avetisyan, T. Bose, C. Fantasia, A. Heister, J. St. John, P. Lawson, D. Lazic, J. Rohlf, D. Sperka, L. Sulak

Brown University, Providence, USA

J. Alimena, S. Bhattacharya, G. Christopher, D. Cutts, Z. Demiragli, A. Ferapontov, A. Garabedian, U. Heintz, S. Jabeen, G. Kukartsev, E. Laird, G. Landsberg, M. Luk, M. Narain, D. Nguyen, M. Segala, T. Sinthuprasith, T. Speer

University of California, Davis, Davis, USA

R. Breedon, G. Breto, M. Calderon De La Barca Sanchez, S. Chauhan, M. Chertok, J. Conway, R. Conway, P.T. Cox, J. Dolen, R. Erbacher, M. Gardner, R. Houtz, W. Ko, A. Kopecky, R. Lander, O. Mall, T. Miceli, D. Pellett, F. Ricci-Tam, B. Rutherford, M. Searle, J. Smith, M. Squires, M. Tripathi, R. Vasquez Sierra, R. Yohay

University of California, Los Angeles, Los Angeles, USA

V. Andreev, D. Cline, R. Cousins, J. Duris, S. Erhan, P. Everaerts, C. Farrell, J. Hauser, M. Ignatenko, C. Jarvis, G. Rakness, P. Schlein[†], P. Traczyk, V. Valuev, M. Weber

University of California, Riverside, Riverside, USA

J. Babb, K. Burt, R. Clare, M.E. Dinardo, J. Ellison, J.W. Gary, F. Giordano, G. Hanson, G.Y. Jeng⁵³, H. Liu, O.R. Long, A. Luthra, H. Nguyen, S. Paramesvaran, J. Sturdy, S. Sumowidagdo, R. Wilken, S. Wimpenny

University of California, San Diego, La Jolla, USA

W. Andrews, J.G. Branson, G.B. Cerati, S. Cittolin, D. Evans, A. Holzner, R. Kelley, M. Lebourgeois, J. Letts, I. Macneill, B. Mangano, S. Padhi, C. Palmer, G. Petrucciani, M. Pieri, M. Sani, V. Sharma, S. Simon, E. Sudano, M. Tadel, Y. Tu, A. Vartak, S. Wasserbaech⁵⁴, F. Würthwein, A. Yagil, J. Yoo

University of California, Santa Barbara, Santa Barbara, USA

D. Barge, R. Bellan, C. Campagnari, M. D'Alfonso, T. Danielson, K. Flowers, P. Geffert, F. Golf, J. Incandela, C. Justus, P. Kalavase, D. Kovalskyi, V. Krutelyov, S. Lowette, R. Magaña Villalba, N. Mccoll, V. Pavlunin, J. Ribnik, J. Richman, R. Rossin, D. Stuart, W. To, C. West

California Institute of Technology, Pasadena, USA

A. Apresyan, A. Bornheim, Y. Chen, E. Di Marco, J. Duarte, M. Gataullin, Y. Ma, A. Mott, H.B. Newman, C. Rogan, M. Spiropulu, V. Timciuc, J. Veverka, R. Wilkinson, S. Xie, Y. Yang, R.Y. Zhu

Carnegie Mellon University, Pittsburgh, USA

V. Azzolini, A. Calamba, R. Carroll, T. Ferguson, Y. Iiyama, D.W. Jang, Y.F. Liu, M. Paulini, H. Vogel, I. Vorobiev

University of Colorado at Boulder, Boulder, USA

J.P. Cumalat, B.R. Drell, W.T. Ford, A. Gaz, E. Luiggi Lopez, J.G. Smith, K. Stenson, K.A. Ulmer, S.R. Wagner

Cornell University, Ithaca, USA

J. Alexander, A. Chatterjee, N. Eggert, L.K. Gibbons, B. Heltsley, A. Khukhunaishvili, B. Kreis, N. Mirman, G. Nicolas Kaufman, J.R. Patterson, A. Ryd, E. Salvati, W. Sun, W.D. Teo, J. Thom, J. Thompson, J. Tucker, J. Vaughan, Y. Weng, L. Winstrom, P. Wittich

Fairfield University, Fairfield, USA

D. Winn

Fermi National Accelerator Laboratory, Batavia, USA

S. Abdullin, M. Albrow, J. Anderson, J. Andresen, L.A.T. Bauerdick, A. Beretvas, J. Berryhill, P.C. Bhat, K. Burkett, D. Butler, J.N. Butler, V. Chetluru, H.W.K. Cheung, F. Chlebana, J. Chramowicz, D. Christian, G. Deptuch, G. Derylo, V.D. Elvira, I. Fisk, J. Freeman, Y. Gao, H. Gonzalez, D. Green, O. Gutsche, J. Hanlon, R.M. Harris, J. Hirschauer, B. Hooberman, J. Howell, S. Jindariani, M. Johnson, U. Joshi, B. Klima, S. Kunori, S. Kwan, C.M. Lei, C. Leonidopoulos⁵⁵, J. Linacre, D. Lincoln, R. Lipton, J. Lykken, S. Los, K. Maeshima, J.M. Marraffino, S. Maruyama, D. Mason, M. Matulik, P. McBride, K. Mishra, S. Mrenna, Y. Musienko⁵⁶, C. Newman-Holmes, V. O'Dell, O. Prokofyev, A. Prosser, R. Rivera, E. Sexton-Kennedy, S. Sharma, W.J. Spalding, L. Spiegel, P. Tan, L. Taylor, S. Tkaczyk, N.V. Tran, L. Uplegger, E.W. Vaandering, R. Vidal, E. Voirin, J. Whitmore, W. Wu, F. Yang, J.C. Yun

University of Florida, Gainesville, USA

D. Acosta, P. Avery, D. Bourilkov, M. Chen, T. Cheng, S. Das, M. De Gruttola, G.P. Di Giovanni, D. Dobur, A. Drozdetskiy, R.D. Field, M. Fisher, Y. Fu, I.K. Furic, J. Gartner, J. Hugon, B. Kim, J. Konigsberg, A. Korytov, A. Kropivnitskaya, T. Kypreos, J.F. Low, K. Matchev, P. Milenovic⁵⁷, G. Mitselmakher, L. Muniz, M. Park, R. Remington, A. Rinkevicius, P. Sellers, N. Skhirtladze, M. Snowball, J. Yelton, M. Zakaria

Florida International University, Miami, USA

V. Gaultney, S. Hewamanage, L.M. Lebolo, S. Linn, P. Markowitz, G. Martinez, J.L. Rodriguez

Florida State University, Tallahassee, USA

T. Adams, A. Askew, J. Bochenek, J. Chen, B. Diamond, S.V. Gleyzer, J. Haas, S. Hagopian, V. Hagopian, M. Jenkins, K.F. Johnson, H. Prosper, V. Veeraraghavan, M. Weinberg

Florida Institute of Technology, Melbourne, USA

M.M. Baarmand, B. Dorney, M. Hohlmann, H. Kalakhety, I. Vodopiyanov, F. Yumiceva

University of Illinois at Chicago (UIC), Chicago, USA

M.R. Adams, I.M. Anghel, L. Apanasevich, Y. Bai, V.E. Bazterra, R.R. Betts, I. Bucinskaite, J. Callner, R. Cavanaugh, O. Evdokimov, L. Gauthier, C.E. Gerber, D.J. Hofman, B. Kapustka, S. Khalatyan, F. Lacroix, C. O'Brien, C. Silkworth, D. Strom, P. Turner, N. Varelas

The University of Iowa, Iowa City, USA

U. Akgun, E.A. Albayrak, B. Bilki⁵⁸, W. Clarida, F. Duru, J.-P. Merlo, H. Mermerkaya⁵⁹, A. Mestvirishvili, A. Moeller, J. Nachtman, C.R. Newsom, E. Norbeck, Y. Onel, F. Ozok⁶⁰, S. Sen, P. Tan, E. Tiras, J. Wetzel, T. Yetkin, K. Yi

Johns Hopkins University, Baltimore, USA

B.A. Barnett, B. Blumenfeld, S. Bolognesi, A.V. Gritsan, G. Hu, P. Maksimovic, M. Swartz, A. Whitbeck

The University of Kansas, Lawrence, USA

P. Baringer, A. Bean, W. Burg, G. Benelli, M. Everhart, J. Herman, R.P. Kenny Iii, M. Murray, D. Noonan, J. Orcutt, C. Pfannenstiehl, S. Sanders, J. Sibille, R. Stringer, G. Tinti, J.S. Wood, J. Worth, R. Young

Kansas State University, Manhattan, USA

A.F. Barfuss, T. Bolton, I. Chakaberia, A. Ivanov, S. Khalil, M. Makouski, Y. Maravin, S. Shrestha, I. Svintradze, R. Taylor

Lawrence Livermore National Laboratory, Livermore, USA

J. Gronberg, D. Lange, F. Rebassoo, D. Wright

University of Maryland, College Park, USA

A. Baden, B. Calvert, S.C. Eno, J.A. Gomez, N.J. Hadley, R.G. Kellogg, M. Kirn, T. Kolberg, Y. Lu, M. Marionneau, A.C. Mignerey, K. Pedro, A. Skuja, J. Temple, M.B. Tonjes, S.C. Tonwar

Massachusetts Institute of Technology, Cambridge, USA

A. Apyan, G. Bauer, J. Bendavid, W. Busza, E. Butz, I.A. Cali, M. Chan, V. Dutta, G. Gomez Ceballos, M. Goncharov, Y. Kim, M. Klute, K. Krajczar⁶¹, A. Levin, P.D. Luckey, T. Ma, S. Nahn, C. Paus, D. Ralph, C. Roland, G. Roland, M. Rudolph, G.S.F. Stephens, F. Stöckli, K. Sumorok, K. Sung, D. Velicanu, E.A. Wenger, R. Wolf, B. Wyslouch, M. Yang, Y. Yilmaz, A.S. Yoon, M. Zanetti, V. Zhukova

University of Minnesota, Minneapolis, USA

S.I. Cooper, B. Dahmes, A. De Benedetti, G. Franzoni, A. Gude, S.C. Kao, K. Klapoetke, Y. Kubota, J. Mans, N. Pastika, R. Rusack, M. Sasseville, A. Singovsky, N. Tambe, J. Turkewitz

University of Mississippi, Oxford, USA

L.M. Cremaldi, R. Kroeger, L. Perera, R. Rahmat, D.A. Sanders, D. Summers

University of Nebraska-Lincoln, Lincoln, USA

E. Avdeeva, K. Bloom, S. Bose, C. Bravo, D.R. Claes, A. Dominguez, M. Eads, S. Emmel, C. Fangmeier, B. Farleigh, W. Frederick, J. Keller, J. Kelty, D. Knowlton, I. Kravchenko, J. Lazo-Flores, S. Malik, J.A. Monroy, G.R. Snow

State University of New York at Buffalo, Buffalo, USA

A. Godshalk, I. Iashvili, S. Jain, A. Kharchilava, A. Kumar, S. Rappoccio

Northeastern University, Boston, USA

G. Alverson, E. Barberis, D. Baumgartel, M. Chasco, J. Haley, D. Nash, D. Trocino, D. Wood, J. Zhang

Northwestern University, Evanston, USA

A. Anastassov, K.A. Hahn, A. Kubik, L. Lusito, N. Mucia, N. Odell, R.A. Ofierzynski, B. Pollack, A. Pozdnyakov, M. Schmitt, S. Stoynev, M. Velasco, S. Won

University of Notre Dame, Notre Dame, USA

L. Antonelli, D. Berry, A. Brinkerhoff, K.M. Chan, M. Hildreth, C. Jessop, D.J. Karmgard, J. Kolb, K. Lannon, W. Luo, S. Lynch, N. Marinelli, D.M. Morse, T. Pearson, M. Planer, R. Ruchti, J. Slaunwhite, N. Valls, M. Wayne, M. Wolf

The Ohio State University, Columbus, USA

B. Bylsma, L.S. Durkin, C. Hill, R. Hughes, K. Kotov, T.Y. Ling, D. Puigh, M. Rodenburg, C. Vuosalo, G. Williams, B.L. Winer

Princeton University, Princeton, USA

E. Berry, P. Elmer, V. Halyo, B. Harrop, P. Hebda, J. Hegeman, A. Hunt, P. Jindal, S.A. Koay, D. Lopes Pegna, P. Lujan, D. Marlow, T. Medvedeva, M. Mooney, J. Olsen, P. Piroué, X. Quan, A. Raval, H. Saka, D. Stickland, C. Tully, J.S. Werner, A. Zuranski

University of Puerto Rico, Mayaguez, USA

J. Acosta, E. Brownson, J.C. Cuevas, A. Lopez, C. Malca, H. Mendez, S. Oliveros, C. Pollack, J.E. Ramirez Vargas, J. Siado, I. Vergara

Purdue University, West Lafayette, USA

E. Alagoz, K. Arndt, V.E. Barnes, D. Benedetti, G. Bolla, D. Bortoletto, M. Bubna, M. Cervantes, I. Christie, M. De Mattia, Y. Ding, A. Everett, Z. Hu, M. Jones, K. Khan, O. Koybasi, M. Kress, A. Krzywda, A.T. Laasanen, N. Leonardo, G. Lockwood, V. Maroussov, P. Merkel, D.H. Miller, N. Neumeister, V. Noe-Kim, I. Shipsey, D. Silvers, D. Snyder, J. Sun, A. Svyatkovskiy, M. Vidal Marono, H.D. Yoo, J. Zablocki, Y. Zheng

Purdue University Calumet, Hammond, USA

S. Guragain, N. Parashar

Rice University, Houston, USA

A. Adair, B. Akgun, C. Boulahouache, K.M. Ecklund, F.J.M. Geurts, W. Li, B.P. Padley, R. Redjimi, J. Roberts, J. Zabel

University of Rochester, Rochester, USA

B. Betchart, A. Bodek, Y.S. Chung, R. Covarelli, P. de Barbaro, R. Demina, Y. Eshaq, T. Ferbel, A. Garcia-Bellido, P. Goldenzweig, J. Han, A. Harel, D.C. Miner, D. Vishnevskiy, M. Zielinski

The Rockefeller University, New York, USA

A. Bhatti, R. Ciesielski, L. Demortier, K. Goulianos, G. Lungu, S. Malik, C. Mesropian

Rutgers, the State University of New Jersey, Piscataway, USA

S. Arora, A. Barker, E. Bartz, J.P. Chou, C. Contreras-Campana, E. Contreras-Campana, D. Duggan, D. Ferencek, Y. Gershtein, R. Gray, E. Halkiadakis, D. Hidas, A. Lath, S. Panwalkar, M. Park, R. Patel, V. Rekovic, J. Robles, K. Rose, S. Salur, S. Schnetzer, C. Seitz, S. Somalwar, R. Stone, S. Thomas, M. Walker

University of Tennessee, Knoxville, USA

G. Cerizza, M. Hollingsworth, S. Spanier, Z.C. Yang, A. York

Texas A&M University, College Station, USA

R. Eusebi, W. Flanagan, J. Gilmore, T. Kamon⁶², V. Khotilovich, R. Montalvo, I. Osipenkov, Y. Pakhotin, A. Perloff, J. Roe, A. Safonov, T. Sakuma, S. Sengupta, I. Suarez, A. Tatarinov, D. Toback

Texas Tech University, Lubbock, USA

N. Akchurin, J. Damgov, C. Dragoiu, P.R. Duerdo, C. Jeong, K. Kovitanggoon, S.W. Lee, T. Libeiro, Y. Roh, I. Volobouev

Vanderbilt University, Nashville, USA

E. Appelt, A.G. Delannoy, C. Florez, S. Greene, A. Gurrola, W. Johns, P. Kurt, C. Maguire, A. Melo, M. Sharma, P. Sheldon, B. Snook, S. Tuo, J. Velkovska

University of Virginia, Charlottesville, USA

M.W. Arenton, M. Balazs, S. Boutle, B. Cox, B. Francis, J. Goodell, R. Hirosky, A. Ledovskoy, C. Lin, C. Neu, J. Wood

Wayne State University, Detroit, USA

S. Gollapinni, R. Harr, P.E. Karchin, C. Kottachchi Kankanamge Don, P. Lamichhane, A. Sakharov

University of Wisconsin, Madison, USA

M. Anderson, D. Belknap, L. Borrello, D. Carlsmith, M. Cepeda, S. Dasu, E. Friis, L. Gray, K.S. Grogg, M. Grothe, R. Hall-Wilton, M. Herndon, A. Hervé, P. Klabbers, J. Klukas, A. Lanaro, C. Lazaridis, R. Loveless, A. Mohapatra, I. Ojalvo, F. Palmonari, G.A. Pierro, I. Ross, A. Savin, W.H. Smith, J. Swanson

†: Deceased

- 1: Also at Vienna University of Technology, Vienna, Austria
- 2: Also at National Institute of Chemical Physics and Biophysics, Tallinn, Estonia
- 3: Also at Universidade Federal do ABC, Santo Andre, Brazil
- 4: Also at California Institute of Technology, Pasadena, USA
- 5: Also at CERN, European Organization for Nuclear Research, Geneva, Switzerland
- 6: Also at Laboratoire Leprince-Ringuet, Ecole Polytechnique, IN2P3-CNRS, Palaiseau, France
- 7: Also at Suez Canal University, Suez, Egypt
- 8: Also at Zewail City of Science and Technology, Zewail, Egypt
- 9: Also at Cairo University, Cairo, Egypt
- 10: Also at Fayoum University, El-Fayoum, Egypt
- 11: Also at British University, Cairo, Egypt
- 12: Now at Ain Shams University, Cairo, Egypt
- 13: Also at National Centre for Nuclear Research, Swierk, Poland
- 14: Also at Université de Haute-Alsace, Mulhouse, France
- 15: Also at Joint Institute for Nuclear Research, Dubna, Russia
- 16: Also at Moscow State University, Moscow, Russia
- 17: Also at Brandenburg University of Technology, Cottbus, Germany
- 18: Also at The University of Kansas, Lawrence, USA
- 19: Also at Institute of Nuclear Research ATOMKI, Debrecen, Hungary
- 20: Also at Eötvös Loránd University, Budapest, Hungary
- 21: Also at Tata Institute of Fundamental Research - HECR, Mumbai, India
- 22: Now at King Abdulaziz University, Jeddah, Saudi Arabia

- 23: Also at University of Visva-Bharati, Santiniketan, India
- 24: Also at Sharif University of Technology, Tehran, Iran
- 25: Also at Isfahan University of Technology, Isfahan, Iran
- 26: Also at Shiraz University, Shiraz, Iran
- 27: Also at Plasma Physics Research Center, Science and Research Branch, Islamic Azad University, Tehran, Iran
- 28: Also at Facoltà Ingegneria Università di Roma, Roma, Italy
- 29: Also at Università della Basilicata, Potenza, Italy
- 30: Also at Università degli Studi Guglielmo Marconi, Roma, Italy
- 31: Also at Università degli Studi di Siena, Siena, Italy
- 32: Also at University of Bucharest, Faculty of Physics, Bucuresti-Magurele, Romania
- 33: Also at Faculty of Physics of University of Belgrade, Belgrade, Serbia
- 34: Also at University of California, Los Angeles, Los Angeles, USA
- 35: Also at Scuola Normale e Sezione dell' INFN, Pisa, Italy
- 36: Also at INFN Sezione di Roma; Università di Roma "La Sapienza", Roma, Italy
- 37: Also at University of Athens, Athens, Greece
- 38: Also at Rutherford Appleton Laboratory, Didcot, United Kingdom
- 39: Also at Paul Scherrer Institut, Villigen, Switzerland
- 40: Also at Institute for Theoretical and Experimental Physics, Moscow, Russia
- 41: Also at Albert Einstein Center for Fundamental Physics, BERN, SWITZERLAND
- 42: Also at Gaziosmanpasa University, Tokat, Turkey
- 43: Also at Adiyaman University, Adiyaman, Turkey
- 44: Also at Izmir Institute of Technology, Izmir, Turkey
- 45: Also at The University of Iowa, Iowa City, USA
- 46: Also at Mersin University, Mersin, Turkey
- 47: Also at Ozyegin University, Istanbul, Turkey
- 48: Also at Kafkas University, Kars, Turkey
- 49: Also at Suleyman Demirel University, Isparta, Turkey
- 50: Also at Ege University, Izmir, Turkey
- 51: Also at School of Physics and Astronomy, University of Southampton, Southampton, United Kingdom
- 52: Also at INFN Sezione di Perugia; Università di Perugia, Perugia, Italy
- 53: Also at University of Sydney, Sydney, Australia
- 54: Also at Utah Valley University, Orem, USA
- 55: Now at University of Edinburgh, Scotland, Edinburgh, United Kingdom
- 56: Also at Institute for Nuclear Research, Moscow, Russia
- 57: Also at University of Belgrade, Faculty of Physics and Vinca Institute of Nuclear Sciences, Belgrade, Serbia
- 58: Also at Argonne National Laboratory, Argonne, USA
- 59: Also at Erzincan University, Erzincan, Turkey
- 60: Also at Mimar Sinan University, Istanbul, Istanbul, Turkey
- 61: Also at KFKI Research Institute for Particle and Nuclear Physics, Budapest, Hungary
- 62: Also at Kyungpook National University, Daegu, Korea
- 63: Also at Helsinki Institute of Physics, Helsinki, Finland

Contents

1	Introduction	1
1.1	Performance and Schedule of the LHC	1
1.2	Current Performance of the Pixel Detector	3
1.3	Overview of the Planned Pixel Detector Upgrade	5
1.4	Expected Performance of the Upgraded Pixel Detector	8
1.5	Changes since the Technical Proposal	9
1.6	Outline of the Technical Design Report	10
2	Expected Performance & Physics Capabilities	13
2.1	Simulation Setup and Reconstruction	14
2.1.1	Pixel Detector Geometry	16
2.1.2	Pattern Recognition and Track Reconstruction	17
2.1.3	B-tagging Algorithms	18
2.2	Tracking Performance	18
2.2.1	Tracking Efficiency and Fake Rate	19
2.2.2	Track Impact Parameter Studies	23
2.2.3	Vertex Resolution Studies	27
2.2.4	Performance for b-Tagging	29
2.2.5	Robustness to Pixel Inner Layer Inefficiencies	31
2.2.6	Recovery of TIB Inefficiencies	33
2.2.7	Summary of Tracking Performance	35
2.3	Performance for Physics	37
2.3.1	Associated Higgs Production	40
2.3.2	$H \rightarrow ZZ$	44
2.3.3	Supersymmetric Particle Search Using the M_{T2} variable and B-Tagging	51
2.3.4	Two Photons and Missing Energy	56
2.4	Conclusions to Tracking and Physics Studies	58
3	FPIX System	59
3.1	Description of the Upgrade FPIX Detector	59
3.1.1	Geometrical Layout	60
3.1.2	Substrate	60
3.1.3	Carbon Ring with Integrated Cooling Tube	61
3.1.4	Half-disk and its Components	63
3.2	Cooling Design	65
3.3	Thermal Interface Materials (TIM)	66
3.4	Four-blade Thermal Test Sample	68
3.5	Cooling Line Layout	70
3.6	Half Cylinder Design	71
3.7	Material Budget	73
3.8	Assembly and Testing	73
3.9	Testing and Commissioning at TIF	74

4	BPIX System	77
4.1	System Overview	77
4.2	Detector Elements	77
4.2.1	Modules	80
4.2.2	Facets and Layers	80
4.3	Mechanics Design & Prototypes	81
4.3.1	Module Mounting Clamp/Screws	81
4.3.2	Flanges	83
4.3.3	Fabrication, Assembly	83
4.3.4	Prototypes (L1, insertion mock-up)	83
4.4	Supply Tube	84
4.5	The Barrel Pixel Cooling Layout	87
4.6	Material Budget	91
4.7	BPIX Production, Assembly and Functional Testing	91
5	Front End Chips & Readout Chain	93
5.1	ROC development	94
5.1.1	Performance and Limitation of current Pixel ROC	94
5.1.2	Design improvements for upgraded Pixel ROC	95
5.1.3	Simulation results of upgraded Pixel ROCs	97
5.2	TBM development	99
5.3	Opto-link	100
5.4	FED/FEC Development	104
5.4.1	Phase I Pixel Data Acquisition	105
5.4.2	Replacement of the Pixel Front End Control System (FECs)	111
5.4.3	Deliverables, Milestones and Strategy	112
6	Pixel Modules	115
6.1	Silicon sensor requirements	116
6.1.1	Technological choice of sensor	117
6.1.2	Sensor radiation hardness	117
6.2	Silicon sensor acceptance criteria	120
6.3	Module assembly	120
6.3.1	Bare module assembly	121
6.3.2	Assembly of HDI with TBM, power and signal cable	121
6.3.3	Complete module assembly	122
6.4	Module test	122
6.4.1	Module test procedure in a cooling box	123
6.4.2	Pixel defects	123
6.4.3	ROC performance	124
6.4.4	Sensor leakage current requirements	125
6.4.5	Module tests and calibration with X-rays	125
6.5	Construction Database	125
6.5.1	FPIX DB	126

6.5.2	BPIX DB	126
7	The Power System	129
7.1	System Parameters and Conception	129
7.1.1	Power Supplies	131
7.1.2	Power Cables	131
7.1.3	Modularity for BPIX	132
7.1.4	Modularity for FPIX	132
7.1.5	Upgrade of the Power System	132
7.2	DC-DC Converters	133
7.2.1	Working Principle	133
7.2.2	Specification for DC-DC Converters	133
7.2.3	ASIC Development	134
7.2.4	DC-DC Converter Development and Performance	135
7.2.5	Integration of DC-DC Converters	137
7.2.6	Future Developments	139
7.3	Power Supply Modification	139
7.3.1	Further developments	141
7.4	Power System Tests	142
7.4.1	Pixel Module Noise with DC-DC Converters	142
7.4.2	System Tests with LHC Time Structure	143
7.4.3	Remote versus Local Sensing	144
7.4.4	Future Tests	144
8	Beam Pipe & Early Installation Preparations	145
8.1	CMS Beam Pipe System	145
8.2	New Central Beam Pipe Design	147
8.2.1	Design Constraints	147
8.2.2	Choice of Materials	148
8.2.3	Beam Pipe Support Structure	149
8.3	Central Beam Pipe Tolerances and Aperture Calculations	149
8.3.1	Aperture Calculations	151
8.4	Beam Background Simulations	153
8.4.1	Geant4-based Simulations	154
8.4.2	FLUKA-based Simulations	155
8.5	Spare beam pipe and strategies	156
9	CO₂ Cooling	159
9.1	The 2PACL Method	159
9.1.1	Thermodynamic Process Details	159
9.1.2	Implementation in Existing Systems	160
9.2	The CMS Pixel System	161
9.2.1	Requirements and Constraints	161
9.2.2	Cooling Plant Design	162

9.2.3	Prototyping Steps	162
9.2.4	Construction Plans, Schedule, Resources	164
9.3	Design of the Cooling Lines	165
9.3.1	The Cooling Loops on YB0	166
9.3.2	The Region Inside the CMS Cryostat	170
9.3.3	The Barrel Pixel Cooling Layout	171
9.3.4	The Forward Pixel Cooling Layout	173
9.4	Integration of the Cooling Plant in CMS	173
9.4.1	Preliminary Studies on Radiation Protection Issues	174
9.4.2	Cooling Plant Layout and Installation Issues	174
9.5	Qualifications of the Copper Lines on YB0	175
9.6	Cooling Lines from PP1 to Detector	177
9.7	Plan for Cooling Plant Installation and Commissioning	178
9.7.1	Preliminary Installation Scenario & Qualification Tests in Stand-alone . .	178
9.7.2	Connection to the Detector and Qualification Procedure	179
10	Pilot System & Early Integration into CMS DAQ	181
10.1	Description of the Pilot System	182
10.1.1	Parts Needed	183
10.1.2	Development of New Components	183
10.1.3	Assembly and Testing	184
10.2	Installation, Commissioning and Monitoring	185
10.2.1	Integration into DAQ	185
10.2.2	Modification Needed to Existing DAQ and Detector Control System . . .	185
10.2.3	Monitoring	186
10.2.4	Integration into Offline Reconstruction	186
11	Installation, Testing and Commissioning	187
11.1	Considerations on Radiation Protection for Future Pixel Detector Maintenance .	187
11.2	Prerequisites for Pixel Removal and Installation	189
11.3	Extraction of the Present Pixel System and Other Preparatory Work	193
11.4	Phase 1 Pixel Installation	193
11.5	Other Activities Within the Pixel Volume	194
11.6	Other General Considerations	195
11.7	System Calibration, Integration and Commissioning	196
12	Project Organisation, Responsibilities, Planning and Costs	199
12.1	Participating Institutes and Collaborators	199
12.2	Project Organisation	202
12.2.1	Phase 1 Upgrade Management Board (Phase-1 MB)	203
12.2.2	Phase 1 Upgrade Project Leader	204
12.2.3	Phase 1 Upgrade Technical Coordination Team	205
12.2.4	Role of the Resource Manager	205
12.3	Construction Responsibilities	206

12.3.1	FPIX	206
12.3.2	BPIX	206
12.3.3	Common Systems	207
12.3.4	Institutional interests	208
12.4	Construction Schedule	209
12.5	Costs	210
12.5.1	Cost Estimate	210
12.5.2	Expected Funding and Cost Sharing	213
A	Evolution of Pixel Detector	215
A.1	Introduction and Motivations	215
A.2	Sensor Development	216
A.2.1	Thin Planar Sensors	216
A.2.2	3D Pixel Sensors	217
A.2.3	Diamond	218
A.3	Trigger Studies	220
A.4	Readout Chip	220
A.4.1	Readout Chip Technology	220
A.4.2	Analog Front-end	222
A.4.3	Pixel Groups	222
A.4.4	Pixel Trigger	224
A.5	Organization and Development Plan	225
A.5.1	ROC Development	225
A.5.2	Sensor Development	226
A.5.3	System Development	227
B	Glossary	229
	References	235

Chapter 1

Introduction

The proposed upgrade of the CMS pixel detector will support full performance of the CMS experiment at the high instantaneous luminosities and total integrated doses which are now predicted based on the strong performance of the LHC accelerator. It will also address and mitigate many of the weaknesses that have been identified in the current systems.

1.1 Performance and Schedule of the LHC

The physics program at the Large Hadron Collider (LHC) began in 2010 with pp collisions at a center of mass (CM) energy of 7 TeV. By the end of 2011, a data sample with integrated luminosity of 6 fb^{-1} was collected by CMS. The CM energy was increased to 8 TeV and at the time of writing (August 2012) a further 11 fb^{-1} integrated luminosity has been delivered, with instantaneous peak luminosities approaching $7 \times 10^{33} \text{ cm}^{-2} \text{ s}^{-1}$. The excellent performance of LHC through this period of operation is summarized in Figure 1.1. Throughout this period, the LHC has operated with bunch trains with 50 ns bunch spacing.

Current planning for the LHC and injector chain foresees a series of three long shutdowns, designated LS1, LS2, and LS3. In LS1 (in the period 2013-2014), the CM energy will be increased to 14 TeV (or slightly lower). In the period through LS2 (2018), the injector chain will be improved and upgraded to deliver very bright bunches (high intensity and low emittance) into the LHC. In LS3 (2022), the LHC itself will be upgraded with new low- β triplets and crab-cavities to optimize the bunch overlap at the interaction region. The original performance goal for the LHC, to operate at an instantaneous luminosity of $1 \times 10^{34} \text{ cm}^{-2} \text{ s}^{-1}$ with 25 ns bunch spacing, is likely to be achieved soon after LS1. Under these conditions, CMS will experience an average of about 25 inelastic interactions per bunch crossing (referred to as event pile-up). This is the operating scenario for which the CMS experiment was designed. Based on the excellent LHC performance to date, and the upgrade plans for the accelerators, it is anticipated that the peak luminosity will be close to $2 \times 10^{34} \text{ cm}^{-2} \text{ s}^{-1}$ before LS2, and perhaps significantly higher after LS2. Delivering high bunch brightness will be more challenging with 25 ns bunch spacing than with 50 ns. While the plan is to operate at 25 ns after LS1, further 50 ns operation cannot be ruled out at this time.

As a result, CMS must be prepared to operate for the rest of this decade with average event pile-up ($\overline{\text{PU}}$) of 50 as a baseline, with the possibility that it may be significantly higher at the beginning of LHC fills. Higher PU causes increased fake rates in tracking, reduced resolution in calorimetry with contamination due to overlapping signals. The total integrated luminosity prior to LS2 will reach of order 200 fb^{-1} , with 500 fb^{-1} achieved by LS3. The goal for the High Luminosity LHC program (HL-LHC) is to deliver a further 2500 fb^{-1} beyond LS3. In this period $\overline{\text{PU}}$ will be well over 100 for the entire fill, with luminosity leveling employed. With

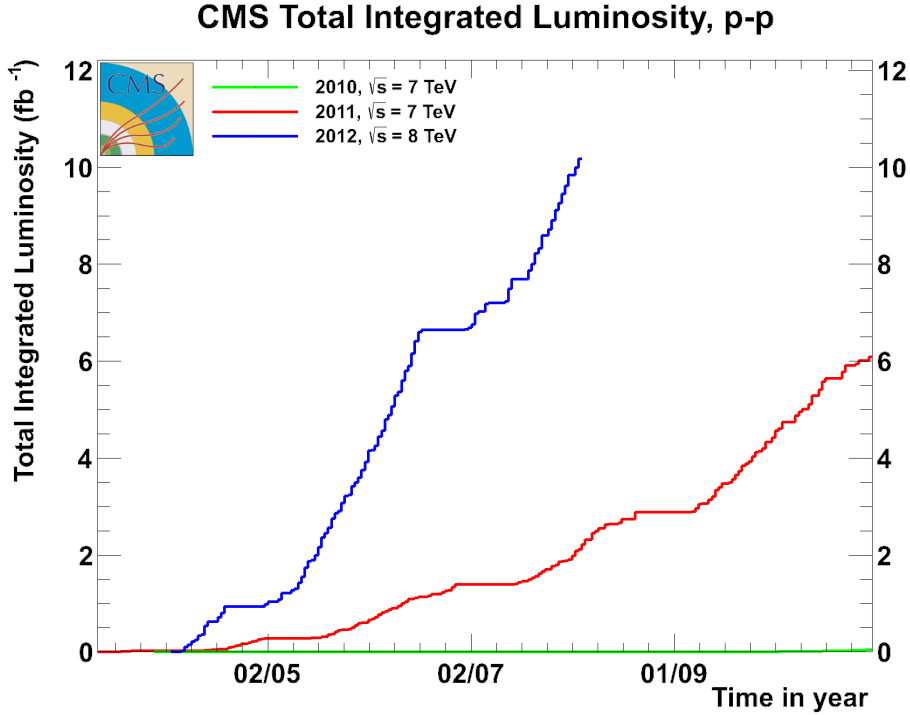


Figure 1.1: Luminosity performance of LHC over the period 2010-2012.

the higher CM energy and very high luminosities beyond LS1, and with the recent discovery of a boson at a mass of 125 GeV [1], the CMS physics program will include both searches for new physics and at the same time measuring the couplings of the new boson in many decay modes. The detector performance, with good reconstruction efficiency at relatively low transverse energy, must be maintained even at a PU several times higher than the original design specification. This is the goal of the CMS upgrade program. Through LS2, three major upgrades are planned: a replacement of the pixel detector with a four-layer high-data-rate design, improvement to the L1-Trigger system with higher granularity and additional processing capabilities, and an upgrade to the photo-detectors and electronics for the hadron calorimeters (HCAL) to reduce background signals and improve measurement of jets and missing-energy at high PU. The pixel detector upgrade is the subject of this report.

The pixel detector is a crucial component of the all-silicon CMS tracker [2, 3]. The present detector was designed to record efficiently and with high precision the first three space-points near the interaction region, out to pseudorapidities of ± 2.5 , in operating conditions up to the nominal instantaneous luminosity of $1 \times 10^{34} \text{ cm}^{-2} \text{ s}^{-1}$ and 25 ns colliding bunch spacing. Under these conditions, an average of about 25 simultaneous overlapping events, or pile-up, are expected per bunch crossing.

In this technical design report, we are proposing to replace the present system with a four-layers/three-disks, low mass silicon pixel tracker capable of delivering high performance tracking in the high luminosity environment of the LHC through LS3 (referred as phase 1). CMS has been designed to allow relatively easy access to the central detectors and the pixel system is likewise designed to be serviceable during a year-end technical stop, capable of being quickly removed and reinstalled in CMS. We are preparing to replace the present detector if necessary before LS2, targeting the year-end technical stop of 2016/17. This strategy of decoupling from the long-shutdown puts CMS in a strong position, with the potential to profit fully from en-

hancements of the LHC performance and the large amount of integrated luminosity expected to be delivered before LS2. As described above, a sizable fraction of the integrated luminosity will be delivered between LS1 and LS2. If LS2 is delayed to 2019 or later, this fraction would be even larger. Installation of a higher performance pixel detector as soon as it is ready would maximize the physics potential by taking advantage of as large a fraction of this integrated luminosity as possible.

1.2 Current Performance of the Pixel Detector

Before describing the proposed upgrade of the pixel detector and its expected performance, it is instructive to review the excellent performance of the current pixel detector in operation since 2009. During collisions, more than 95% of the pixel channels have been active during data taking. Due to its high segmentation, the pixel detector not only forms high quality seeds for the track reconstruction algorithm offline, but is also used to do fast tracking online in the high level trigger (HLT) for primary vertex reconstruction, electron/photon identification, muon reconstruction, tau identification and b-tagging.

A schematic view of the current CMS tracker, including the pixel detector, is shown in Figure 1.2. The current pixel detector consists of three barrel layers (BPIX) at radii of 4.4 cm, 7.3 cm and 10.2 cm, and two forward/backward disks (FPIX) at longitudinal positions of ± 34.5 cm and ± 46.5 cm and extending in radius from about 6 cm to 15 cm. The BPIX contains 48 million pixels covering a total area of 0.78 m^2 and the FPIX has 18 million channels covering an area of 0.28 m^2 . These pixelated detectors produce 3-D measurements along the paths of the charged particles with single hit resolutions between $10 - 20 \mu\text{m}$.

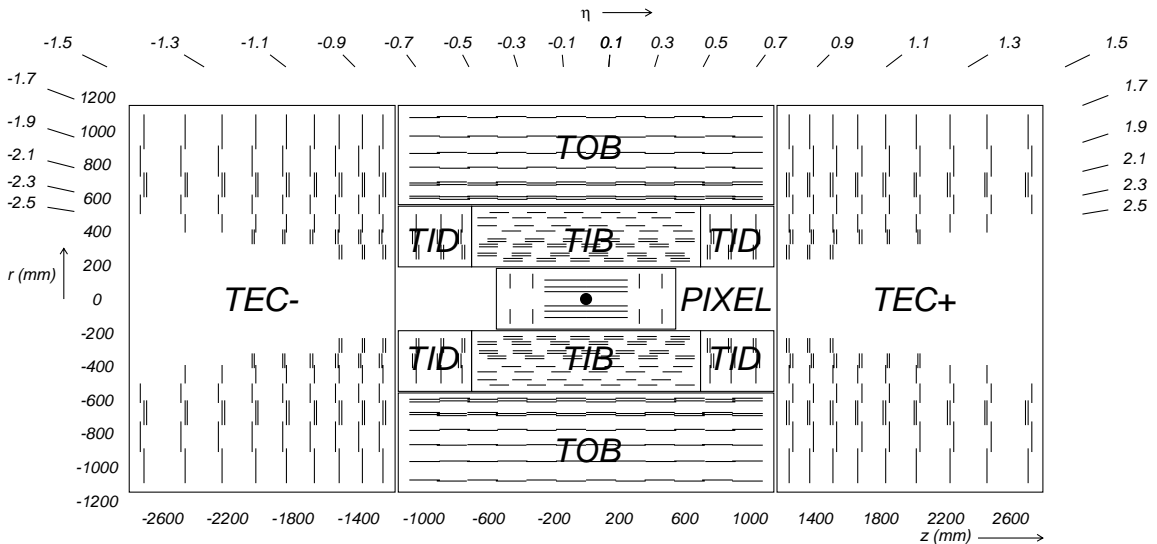


Figure 1.2: Cross section of the current CMS tracker, showing the nomenclature used to identify different sections. Each line represents a detector module. Double lines indicate back-to-back modules which deliver stereo hits in the strip tracker.

Figure 1.3 shows the average single hit efficiency for the various layers of the pixel detector in collisions during 2010 and 2011 [4]. This hit efficiency depends on several factors. The leading effect is a dynamic inefficiency which increases with instantaneous luminosity and

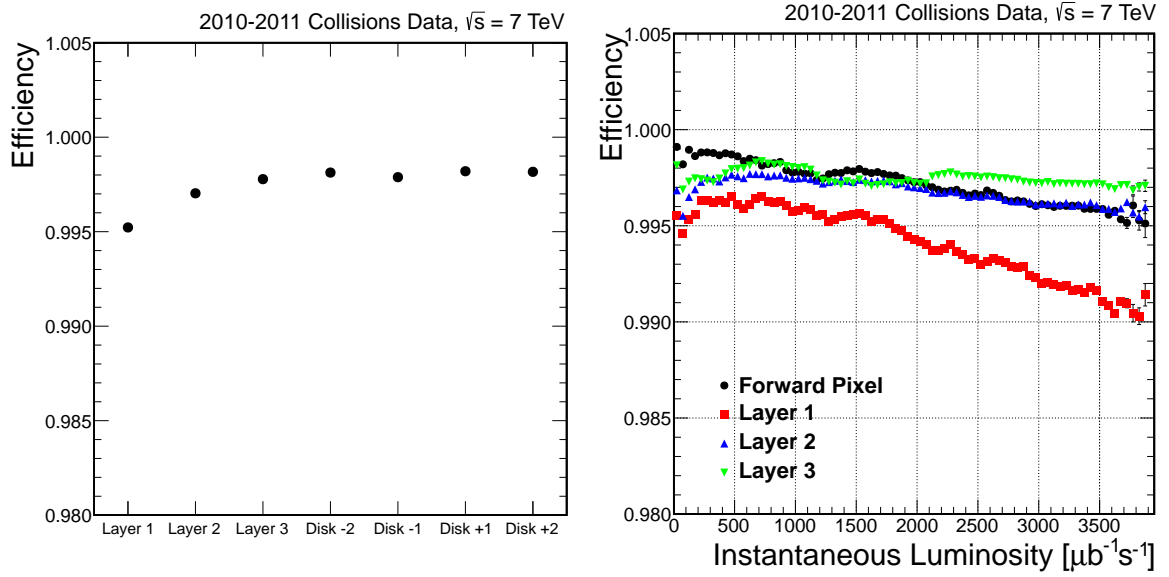


Figure 1.3: Pixel tracking performance measurements from 2010 and 2011 data. Left: Average module hit efficiency per layer/disk in the pixel detector once modules excluded from the readout are excluded from the measurement. Right: Average module hit efficiency as a function of the instantaneous luminosity.

trigger rate due to limits in the internal readout chip buffers. The next main effect comes from single event upsets which cause the temporary loss of a module. These dynamic inefficiencies become significant for the inner layers when $\overline{\text{PU}}$ reaches 50 or more.

The track reconstruction efficiency has also been measured in 2011 data where a Z boson decays into a pair of muons. A “tag-and-probe” method is employed to measure this efficiency as a function of the number of primary vertices and pseudorapidity of the probe muon [4], which is illustrated in Figure 1.4. The tracking efficiency is high and well described in the simulation, but slowly degrades as the number of pile-up events increases until it reaches about 40 when it begins to rapidly degrade due to filling buffers on the readout chip. There is also a noticeable dip in the efficiency in the pseudorapidity region near $\eta = \pm 1.5$ where the bulkhead with services from BPIX meets the FPIX.

Passive material in the tracking region is dominated by mass outside the pixel volume, but a significant portion of it is found in the overlap region between the BPIX and FPIX near $|\eta| \sim 1.5$, as can be seen in Figure 1.5. The BPIX bulkhead has services in this region, which in the upgrade will be moved further out in the longitudinal direction outside the active tracking volume.

The passive material in the tracking volume plays a visible role for tracks with intermediate momenta, as illustrated in Figures 1.6 and 1.7, which show the impact parameter resolutions as measured in 2010 collision data, compared to simulation, versus track η and ϕ [5]. At low momenta the transverse impact parameter resolution worsens at higher η due to the material traversed by the track. The impact of the 18 cooling pipes in the BPIX is clearly visible for lower momentum tracks versus ϕ .

The current pixel readout electronics were designed and optimized for the data rates and pixel occupancies expected up to the LHC design luminosity of $1 \times 10^{34} \text{ cm}^{-2}\text{s}^{-1}$ with 25 ns bunch spacing. There will be a dynamic inefficiency of about 4% from the current readout chip,

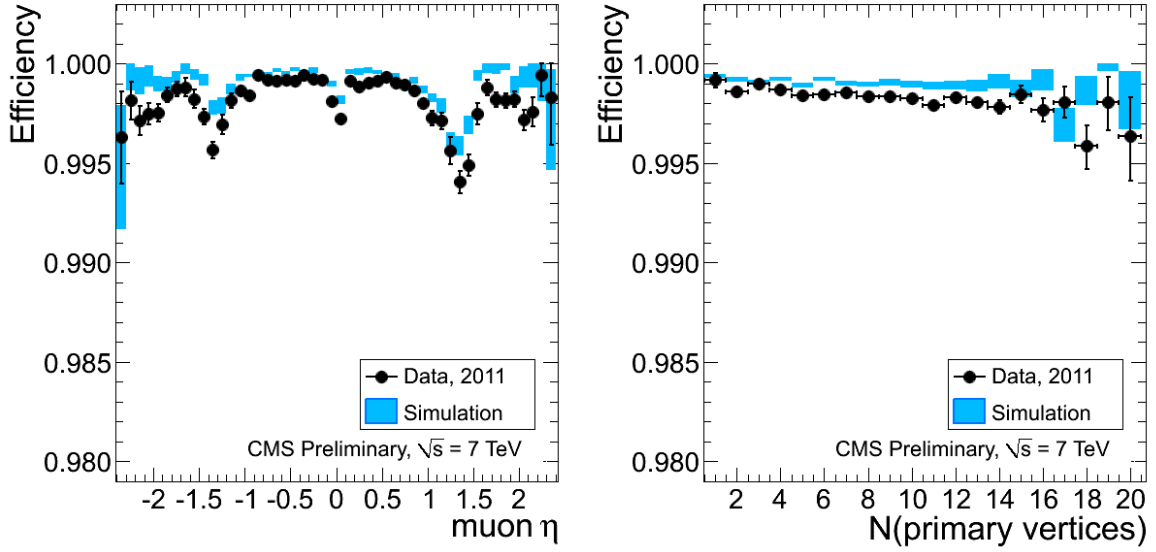


Figure 1.4: Results of the tag-and-probe fit for the tracking efficiency as a function of the muon η and the number of reconstructed primary vertices in the event for 2011 data (black) and simulation (blue).

PSI46v2, at this luminosity in the innermost layer. These losses are shown in Figure 1.8 as a function of the level-1 trigger accept (L1A) rate as measured in test beam runs with particle fluxes as expected for LHC design luminosity [6]. At the nominal L1A accept rate of 100 kHz, the data loss will increase to 16% in the innermost layer as the luminosity goes up by a factor of two (for 25 ns bunch crossing) to $2 \times 10^{34} \text{ cm}^{-2}\text{s}^{-1}$. These losses are understood by simulations and characterizations of the PSI46v2 readout chip to be coming from two sources: the column drain dead time (0.8%) and readout-related losses (3.0%). Hit pixels are transferred using column drain readout to the chip periphery where the hits are stored in buffers during the L1 trigger latency (3.9 μs). If instead the LHC runs with 50 ns bunch spacing at $2 \times 10^{34} \text{ cm}^{-2}\text{s}^{-1}$, then the data losses continue to increase almost exponentially, with losses on the order of 50% for the innermost layer for example.

Figure 1.9 illustrates the impact on the performance of charged particle tracking from these data losses. In these simulated $t\bar{t}$ events at instantaneous luminosities up to $2 \times 10^{34} \text{ cm}^{-2}\text{s}^{-1}$ with 25 ns and 50 ns bunch spacing, we see substantial decreases in the tracking efficiency and increases in the fake rate. The degradation with 50 ns bunch spacing would be catastrophic. The conclusion is that the current readout chip is not able to cope with these rates in the innermost layers of the pixel detector.

1.3 Overview of the Planned Pixel Detector Upgrade

The goal of the Phase 1 upgrade is to replace the present pixel detector with one that can maintain a high tracking performance at luminosities up to $2 \times 10^{34} \text{ cm}^{-2}\text{s}^{-1}$ and $\overline{\text{PU}}$ up to and exceeding 50. As mentioned previously, due to data losses in the read out chip (ROC), the present system will not sustain the extreme operating conditions expected in Phase 1. The replacement is therefore planned in the year-end technical stop of 2016/2017. A view of the upgraded four-layer pixel detector can be seen in Figure 1.10 and Figure 2.1. The modularity allows a fast installation and is a key design feature. The figure should help understanding descriptions in the following chapters.

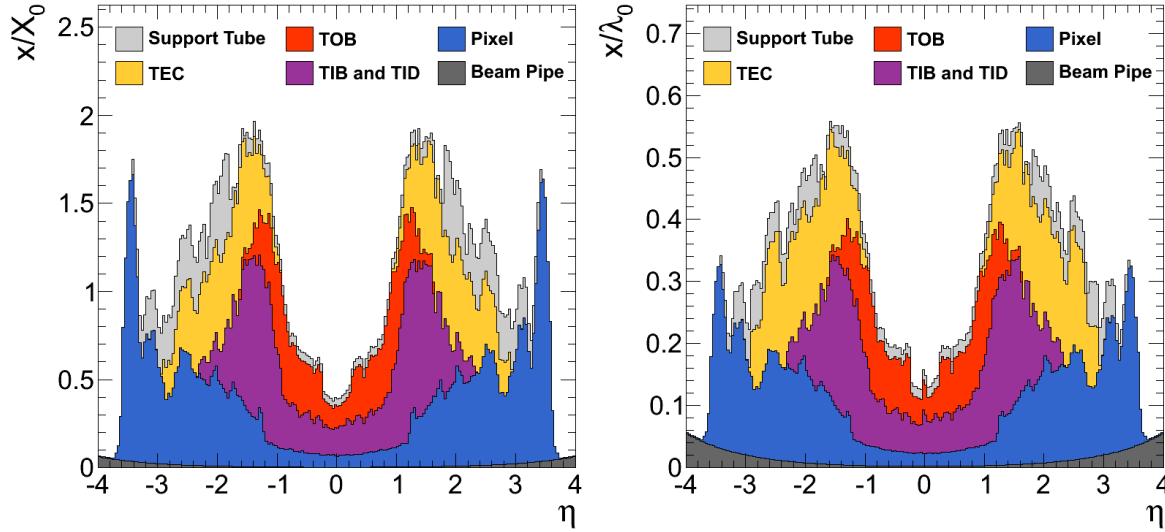


Figure 1.5: Material budget in units of radiation length (left) and hadronic interaction lengths (right) as a function of pseudo-rapidity η , for the various sub-detectors that make up the CMS tracker [4].

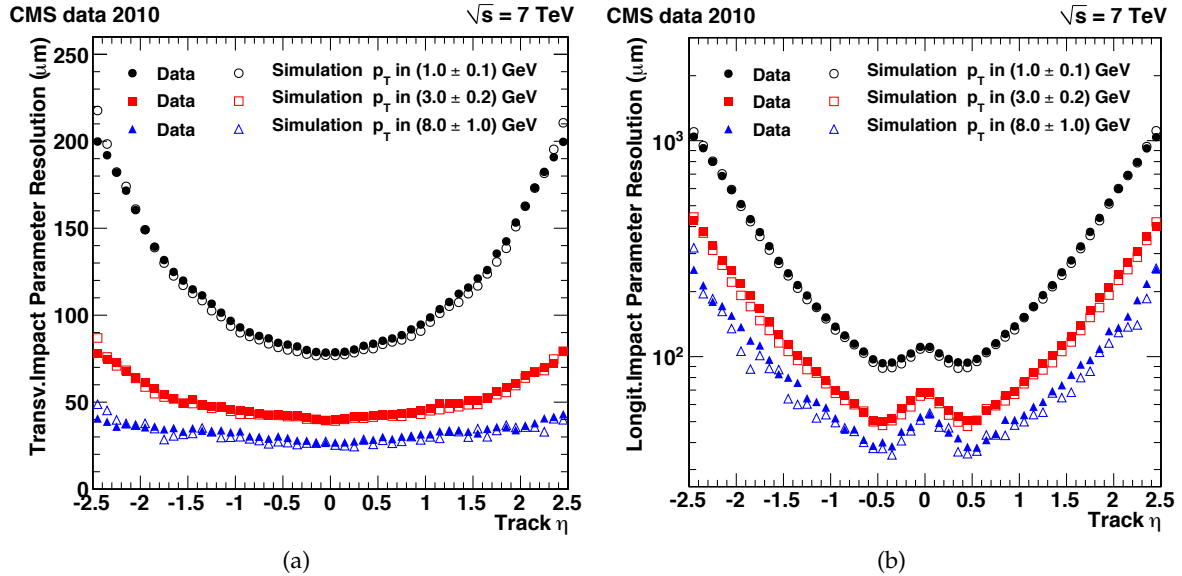


Figure 1.6: Measured resolution of the track transverse (a) and longitudinal (b) impact parameter as a function of the track η for transverse momenta in 1.0 ± 0.1 GeV (circles), in 3.0 ± 0.2 GeV (squares) and in 8.0 ± 1.0 GeV (triangles). Filled and open symbols correspond to results from data and simulation, respectively [5].

The overriding design specification of the new pixel detector is that it should function at high luminosities ($2 \times 10^{34} \text{ cm}^{-2} \text{ s}^{-1}$) with the same or better performance as the current pixel detector does at low luminosities. This general specification leads to the following design choices, requirements and constraints:

- In running with 50 or more pile-up, maintain the high efficiencies and low fake rates of the current pixel detector which is operating in relatively low pile-up;
- New pixel readout chip (ROC) to minimize data loss due to latencies and limited

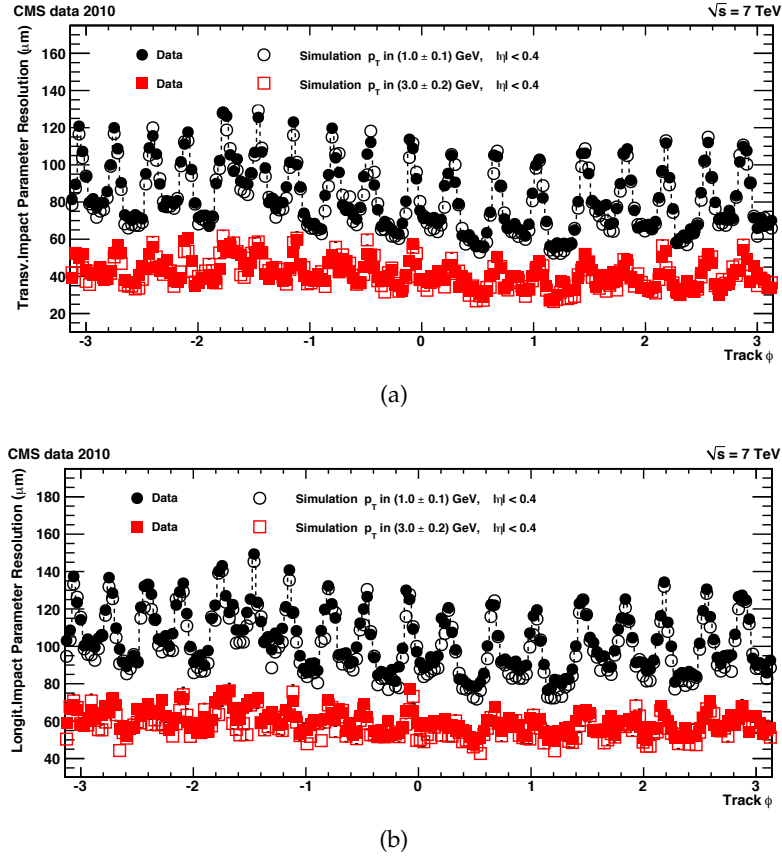


Figure 1.7: Measured resolution of the track transverse (a) and longitudinal (b) impact parameter as a function of the track ϕ for transverse momenta in 1.0 ± 0.1 GeV (circles) and in 3.0 ± 0.2 GeV (squares). Filled and open symbols correspond to results from data and simulation, respectively [5]. The 18 peaks correspond to the 18 cooling structures in the BPIX as described in the text.

buffering in high luminosity running;

- Minimize degradation due to radiation damage;
- Optimized detector layout for 4-pixel-hit coverage over the η range with minimal innermost layer radius improving pattern recognition and track reconstruction;
- To reduce material, adopt two-phase CO₂ cooling and light-weight mechanical support, moving the electronic boards and connections out of the tracking volume;
- To reuse the current patch panel and off-detector services, cooling pipes, cables and fibers, adopt DC-DC power converters and higher bandwidth electronics;
- Reduce number of module types and interfaces simplifying production and maintenance;
- New smaller diameter beam pipe to accommodate the placement of the inner pixel layer closer to the interaction region.

If the new detector is to be installed in the relatively short period of time during a slightly extended year-end technical stop, then both the new beam pipe and the new CO₂ cooling plant need to be ready in advance of such a shutdown. Because of this constraint, the new beam pipe is planned to be installed during LS1 beginning in 2013. The CO₂ cooling system will also be

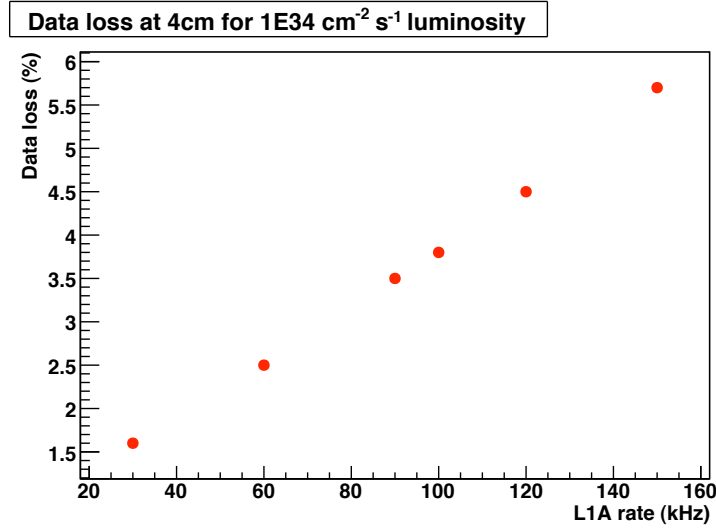


Figure 1.8: Data losses as a function of the L1 accept rate of the innermost layer of the current pixel detector [6]. The instantaneous luminosity is $1 \times 10^{34} \text{ cm}^{-2} \text{ s}^{-1}$ and the bunch spacing is 25 ns. CMS has been designed for maximum average L1 trigger rates of 100 kHz. The data points beyond this rate in the plot simply illustrate the linear nature of this data loss at this particular instantaneous luminosity with the PSI46v2 readout chip.

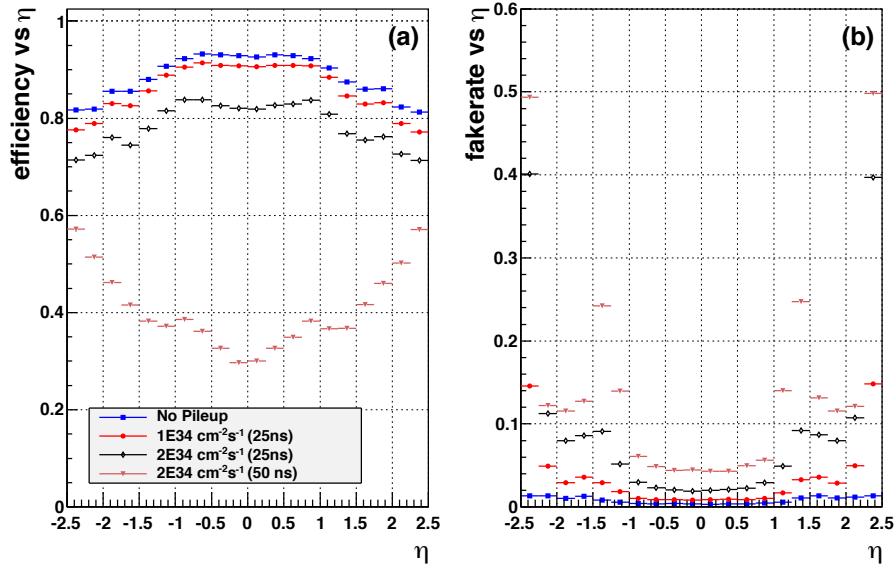


Figure 1.9: Performance of the current pixel detector in simulated $t\bar{t}$ events: a) efficiency; b) fake rate. Results are shown for the current pixel detector with zero pileup (blue squares), an average pileup of 25 (red dots), an average pileup of 50 (black diamonds), and an average pileup of 100 (magenta triangles).

installed and commissioned in advance of the installation of the new pixel detector.

1.4 Expected Performance of the Upgraded Pixel Detector

Improvements from the new detector cannot be summed up by one number, but are characterized by higher efficiencies, lower fake rates, lower dead-time/data-loss, and an extended lifetime of the detector. This leads to better muon ID, b-tagging, photon/electron ID, and tau

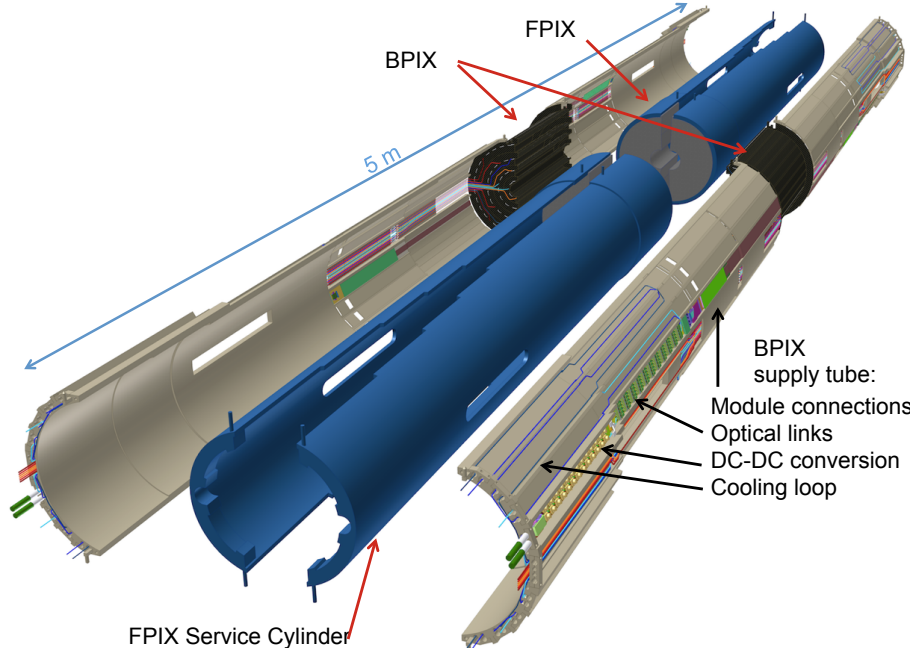


Figure 1.10: Exploded view of the upgraded pixel detector. The figure shows the positions of the different partitions FPIX and BPIX and their respective service cylinders. The necessary services, namely connections, optical links and DC-DC converters are located at high η regions outside the tracking volume.

reconstruction, both offline and in the HLT. Missing energy reconstruction in the offline could also improved since “particle flow” has become an important tool in CMS. Good track reconstruction forms the foundation for the vast majority of our physics analyses, whatever they may be in the future.

In Figure 1.11, we see the expected tracking efficiency and fake rate of the upgraded pixel detector in various pile-up scenarios ($\overline{PU} = 0, 50$ and 100) in simulated $t\bar{t}$ events. The very large losses in efficiency with the current detector at high luminosities as seen in Figure 1.8 have largely been recovered. This leads to improvements in higher-level reconstructed objects like b-tagged jets, which can be seen in Figure 1.12. For example, the 15% absolute gain in efficiency for a fake rate of 1% translates into large gains in physics analyses that require more than one b-tag, such as the $ZH \rightarrow \mu^+ \mu^- b\bar{b}$ analysis discussed later. In addition to the gains in offline reconstruction, improvements in single track reconstruction play a beneficial role in the high-level trigger, when Level-1 objects are reconfirmed by tracks made from pixel hits alone. A gain in Higgs signal efficiency corresponds to greater sensitivity with the same amount of integrated luminosity.

Finally, besides improving pattern recognition, increasing efficiencies and lowering fake rates, the addition of the fourth outer layer of the new pixel detector plays another role. In the case that the inner layers of the TIB are compromised, the fourth layer largely offsets such losses, especially at high pile-up.

1.5 Changes since the Technical Proposal

Substantial progress has been made in specifying designs of the various components of the upgrade. The first version of the new ROC has been received from the fab, the CO₂ cooling system has been designed with prototypes in operation, the DC-DC power converters have

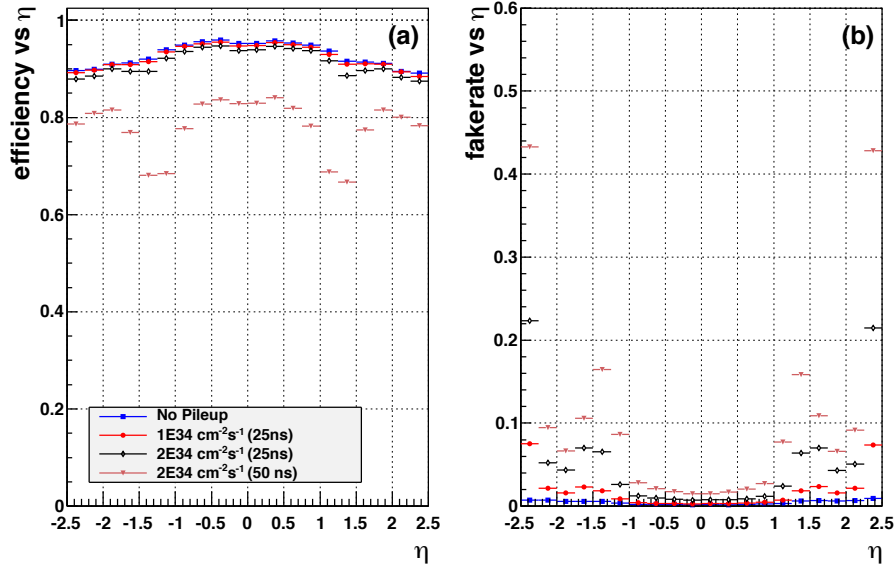


Figure 1.11: Performance of the upgraded pixel detector in simulated $t\bar{t}$ events: a) efficiency; b) fake rate. Results are shown for the upgraded pixel detector with zero pileup (blue squares), an average pileup of 25 (red dots), an average pileup of 50 (black diamonds), and an average pileup of 100 (magenta triangles).

been designed with prototypes currently being characterized, the optical readout system has also advanced, components have been chosen and prototypes are in operation. Progress has also been made in breaking down the costs and clearly specifying the contributions from each institution and country collaborating on the project.

We continue to improve the track reconstruction algorithms of both the current detector and the upgrade. This has led to a better understanding of how to best reconstruct tracks and higher level objects like b-tagged jets in high luminosities. The CMS management structure has been substantially changed in such a way that physics studies for the Phase-1 (and Phase-2) upgrades are integrated in each of the physics analysis and physics object groups. This important change has allowed us to estimate the relative gains in physics from an upgraded detector and are key to preparing us to be ready on the first day of operation of the new detectors. In this report, we have estimated the improvements from an upgraded pixel detector in a representative set of physics analyses that depend on the pixel detector.

1.6 Outline of the Technical Design Report

An overview of the timeline and milestones of the upgrade construction project is shown in Figure 1.13. Estimates of the gains in tracking and physics performance are made immediately in the following chapter. Subsequent chapters deal in-depth with the construction, testing and installation activities outlined in Figure 1.13. The organization of the project, costs and institutional responsibilities are spelled out in Chapter 12. Future research and development related to the next steps of the pixel upgrade project are discussed in Appendix A. Finally, a glossary of acronyms used in this report is given in Appendix B.

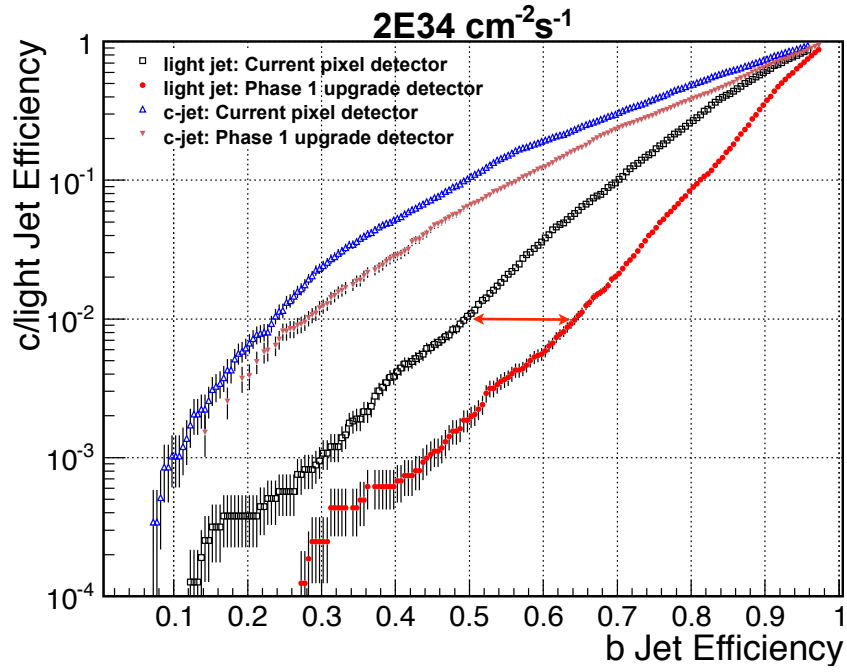


Figure 1.12: Performance of the Combined Secondary Vertex b-tagging algorithm for jets with $p_T > 30$ in a $t\bar{t}$ sample with $\overline{\text{PU}} = 50$. The performance for the standard geometry is shown by the open points while the solid points are for the Phase 1 geometry. The triangular points are for c-jets while the circle and square points are for uds jets.

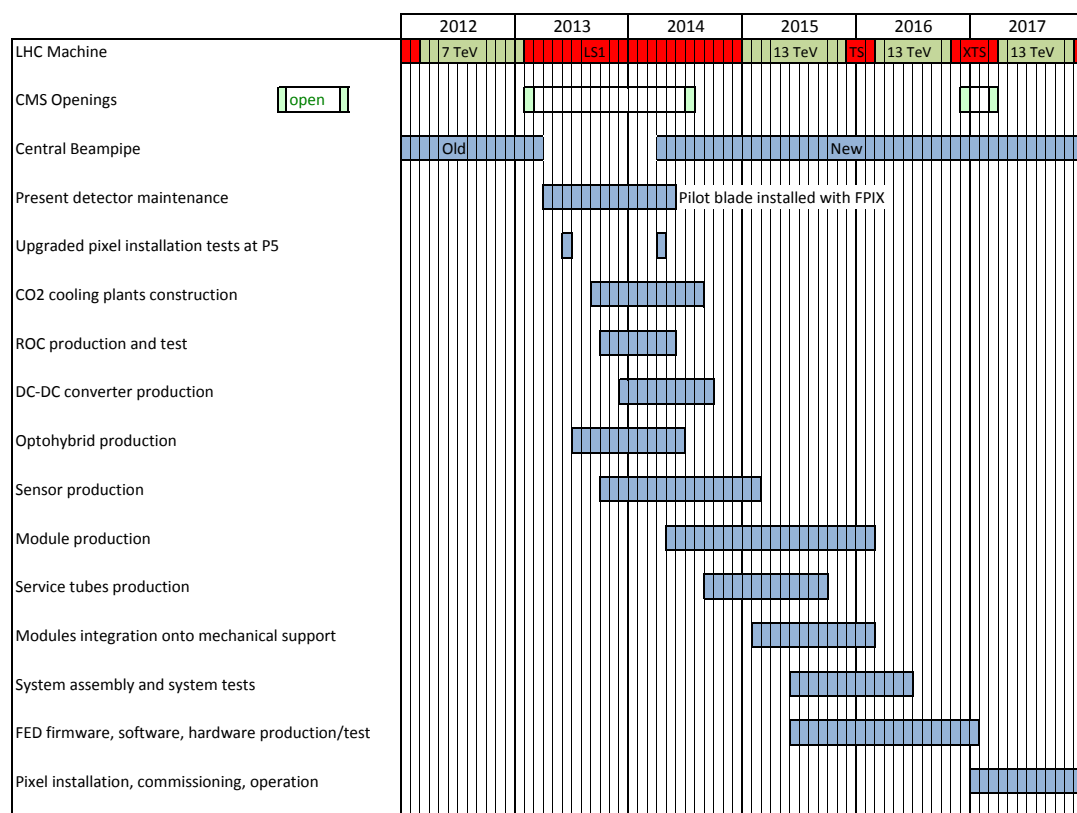


Figure 1.13: Overview of the construction schedule for the Pixel Phase 1 Upgrade project.

Chapter 2

Expected Performance & Physics Capabilities

We report on simulation studies of the proposed Phase 1 upgrade pixel detector operating at a luminosity of $2 \times 10^{34} \text{ cm}^{-2}\text{s}^{-1}$. We compare the upgrade tracking and b-tagging performance with those for the present pixel detector, and show the gain for important physics channels.

The key limitations of the current pixel detector that should be addressed by the upgrade are summarized below:

- *Data loss at high occupancy and trigger rate.* The current pixel detector was designed for a peak luminosity of $1 \times 10^{34} \text{ cm}^{-2}\text{s}^{-1}$ with a crossing time of 25 ns. Beyond this the pixel readout chip (ROC) suffers from significant dynamic data loss. This loss of data depends on both the occupancy and trigger rates and comes primarily from two sources, buffer size and readout speed. Between L1 triggers pixel hits are stored in a finite sized buffer before being readout at the next L1 trigger, if this buffer is full the ROC cannot record any more hits and subsequent hits are lost. When a L1 triggers the readout, double columns that are being read out are blocked from having hits recorded and the buffer is cleared after the readout; thus, data can be lost if the readout is slow or the L1 trigger rate is high. Using a simulation of pp collisions and an emulation of the pixel readout, for the current pixel detector running at $1 \times 10^{34} \text{ cm}^{-2}\text{s}^{-1}$ with a crossing time of 25 ns (50 ns) we expected a hit inefficiency of 4% (16%) for the inner pixel barrel layer. At $2 \times 10^{34} \text{ cm}^{-2}\text{s}^{-1}$ and a crossing time of 25 ns (50 ns) the expected dynamic inefficiency raises to 15% (50%) for ROCs in the inner region. A new ROC for the upgrade pixel detector will largely eliminate this dynamic data loss.
- *Lower tracking efficiency or higher fake rates at high pileup.* With more interactions per crossing giving rise to addition hits in the tracking detectors, the pattern recognition becomes more difficult. At high pileup the processing of the tracking algorithms is one of the dominant contributions to the CPU time in both the High Level Trigger (HLT) and the offline processing. The offline processing time is one of the main limits to our data-taking rate in 2012 so the CPU time for tracking must be kept under control as the pileup increases. Additionally to keep the same level of tracking efficiency we would suffer from a higher level of fake tracks; alternatively, we can tune the tracking for lower fake rate at the expense of reduced efficiency. At $2 \times 10^{34} \text{ cm}^{-2}\text{s}^{-1}$ to keep both the CPU time and fake rate under control we expect to have to tune the tracking to have generally lower efficiency than at lower luminosities. Requiring hits in all 3 pixel layers leads to lower tracking efficiencies [7].
With an extra pixel layer negative effects of pileup can be partly mitigated with the upgrade pixel detector.
- *Degradation in performance due to radiation damage.* Due to reduced charge collection,

hit detection efficiency and resolution for the pixel detector is expected to deteriorate with irradiation. Although the degradation can initially be mitigated mostly with increase in voltage, and modification of the pixel cluster hit templates, eventually the reduced collected charge cannot be compensated. The hit efficiency is expected to be less affected but the reduced charge sharing and eventual breaking up of clusters will degrade the hit resolution. A radiation fluence of $1.2 \times 10^{15} \text{ n}_{eq}/\text{cm}^2$ is expected to be exceeded during the Phase 1 run of the LHC. After this exposure, according to simulations, the detector's hit resolution deteriorates by roughly a factor of two in the transverse plane. Although the upgrade pixel sensor will suffer similar radiation damage, the new ROC will have a much lower charge threshold for pixel hits, which largely mitigates the effects of reduced collected charge, so degradation in hit resolution should be much reduced comparing to the same radiation fluence.

- *Degradation in performance due to material.* Particularly in the higher η part of the tracking region the pixel detector contains a sizable amount of material. Photons and pions can be lost in this material due to conversion and nuclear interactions respectively, electrons will lose energy through bremsstrahlung, and charged particles will suffer scattering effects close to the main pp interaction point which can affect vertexing. These effects may contribute to additional confusion for track pattern recognition in a high pileup environment. The upgrade pixel detector, even with an extra layer has less material in the tracking volume, due to a new lightweight construction, cooling, and relocation of passive material out of the tracking region.

The limitations of the current pixel detector were studied using a detailed simulation of the detector and the results are presented in this chapter. The mitigation of the degradation in tracking performance by the proposed upgrade detector replacement is illustrated with detailed simulation studies. The tracking algorithm is not optimized for the new geometry to allow a direct comparison.

Although the limitations of the current pixel detector mentioned above are not expected to cause a catastrophic failure of the tracking when running at $2 \times 10^{34} \text{ cm}^{-2}\text{s}^{-1}$, the loss of pixel hits and the worsening of hit resolutions coupled with the higher occupancies at high pileup leads to degradations in a number of tracking performance metrics. It is the combination of all the degradations that lead to unacceptable loss in sensitivity or physics reach. The proposed upgrade pixel detector not only suffers less from dynamic data loss and high pileup but will provide improvement even at moderate pileup, and in addition will improve the robustness of the tracking when the outer tracking starts degrading due to radiation damage.

2.1 Simulation Setup and Reconstruction

The performance studies were done using a slightly modified version of the CMS simulation software Geant 4 [8, 9]. Besides implementing a Geant 4 description of the Phase 1 upgrade detector, other modifications of the simulation code, the standard Monte Carlo production configuration, and the reconstruction code were made for a more representative comparison with the current pixel geometry. The modifications made to the 2012 CMS simulation are listed below.

1. *Geometry.* Beam pipe radius; Pixel detector geometry and material, including descriptions for the support and services.

2. *Beam conditions.* 14 TeV center-of-mass energy; Gaussian beam spot; four pileup scenarios: zero pileup $\overline{PU} = 0$, an average pileup of $\overline{PU} = 25$ (for $1 \times 10^{34} \text{ cm}^{-2}\text{s}^{-1}$ with 25 ns crossing time), an average pileup of $\overline{PU} = 50$ (for $2 \times 10^{34} \text{ cm}^{-2}\text{s}^{-1}$ with 25 ns crossing time)), and an average pileup of $\overline{PU} = 100$ (for $2 \times 10^{34} \text{ cm}^{-2}\text{s}^{-1}$ with 50 ns crossing time).
3. *Detector conditions.* Ideal conditions, with no dead detector elements in the pixel detector. Pixel dynamic data loss simulation (see below).
4. *Local reconstruction.* The CPE (cluster position error) pixel templates are not used for the final pixel rechit positions and errors, instead the “generic” algorithm is used leading to slightly worse hit resolutions.
5. *Track reconstruction.* Reduced and modified the iterative tracking steps (see below).

Modification 1 is obviously needed to simulate the Phase 1 upgrade pixel detector, and 2 is to simulate the expected conditions during the latter part of the Phase 1 period, where a Gaussian beam spot of $15 \mu\text{m}$ in the transverse plane and 5.3 cm in the longitudinal direction is assumed.

Table 2.1: Values of dynamic data loss used in the simulations of the current and upgrade pixel detector operating at $1 \times 10^{34} \text{ cm}^{-2}\text{s}^{-1}$ (25 ns crossing time) and $2 \times 10^{34} \text{ cm}^{-2}\text{s}^{-1}$ (25 ns and 50 ns crossing time) for each barrel layer and forward disk and for particular bunch crossing intervals.

Detector	Radius (cm)	% Data loss for (cm ⁻² s ⁻¹ @ ns)		
		1 × 10 ³⁴ @ 25	2 × 10 ³⁴ @ 25	2 × 10 ³⁴ @ 50
Current detector				
BPIX1	4.4	4.0	16.0	50.0
BPIX2	7.3	1.5	5.8	18.2
BPIX3	10.2	0.7	3.0	9.3
FPIX1 and 2		0.7	3.0	9.3
Upgrade detector				
BPIX1	3.0	1.19	2.38	4.76
BPIX2	6.8	0.23	0.46	0.93
BPIX3	10.2	0.09	0.18	0.36
BPIX4	16.0	0.04	0.08	0.17
FPIX1–3		0.09	0.18	0.36

To compare the performance of the upgrade pixel detector with the current one we implemented the configurations 3 and 4. Simulation of the expected data loss in the pixel detector due to the ROC and readout is implemented with the data loss values given in Table 2.1. Since we do not yet have the pixel CPE templates implemented for the upgrade pixel detector we

used non-template pixel positions and errors for the simulation studies of both detectors. Note that this causes the pixel hit position resolutions in this simulation study to be slightly worse for the current detector than what is currently achievable with the 2011/2012 data. Details for the configuration of the track reconstruction used is given in Section 2.1.2.

2.1.1 Pixel Detector Geometry

Figure 2.1 shows a conceptual layout for the Phase 1 upgrade pixel detector. The current 3-layer barrel (BPIX), 2-disk endcap (FPIX) system is replaced with a 4-layer barrel, 3-disk endcap system for four hit coverage. Moreover the addition of the fourth barrel layer at a radius of 16 cm provides a safety margin in case the first silicon strip layer of the Tracker Inner Barrel (TIB) degrades more rapidly than expected, but its main role is in providing redundancy in pattern recognition and reducing fake rates with high pile-up.

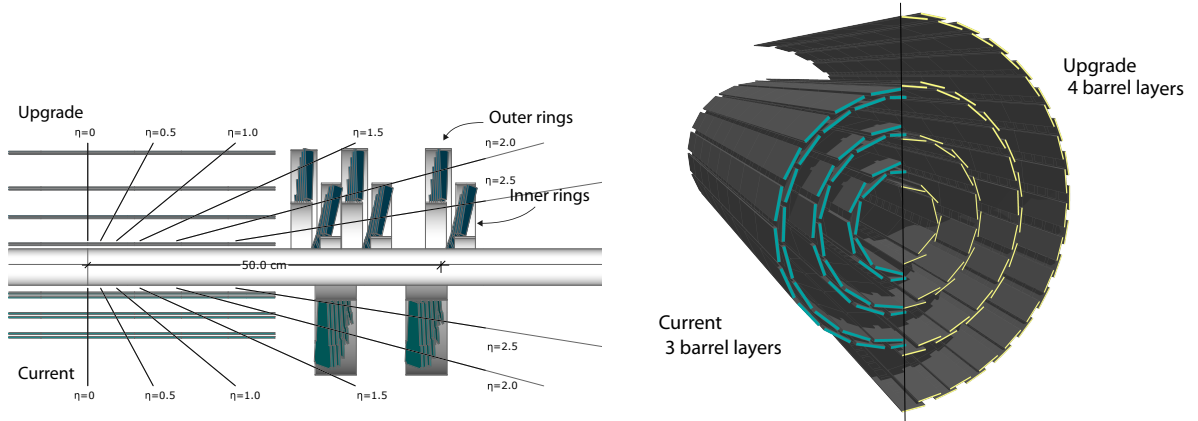


Figure 2.1: Left: Conceptual layout comparing the different layers and disks in the current and upgrade pixel detectors. Right: Transverse-oblique view comparing the pixel barrel layers in the two detectors.

Since the extra pixel layer could easily increase the material of the pixel detector, the upgrade detector, support, and services are redesigned to be lighter than the present system, using an ultra-lightweight support with CO₂ cooling, and by relocating much of the passive material, like the electronic boards and connections, out of the tracking volume.

Table 2.2 shows a comparison of the total material mass in the simulation of the present pixel detector and of the Phase 1 upgrade pixel detector. Since significant mass reduction was achieved by moving material further out in z from the interaction point, the masses are given for a limited range in η that covers most of the tracking region.

Also shown in Table 2.2 is the mass of the carbon fiber tube that sits outside of the pixel detector and is needed by the Tracker Inner Barrel (TIB) and for bakeout of the beampipe. By convention, the material for this tube is usually included as part of the pixel system “material budget”; this tube is expected to remain unchanged for the Phase 1 upgrade.

Another comparison of the “material budget” for the current and Phase 1 pixel detectors was done using the standard CMS procedure of simulating neutrinos in the detector and summing the radiation length and nuclear interaction length along a straight line at fixed values of η originating from the origin. Figure 2.2 shows a comparison of the radiation length and nuclear interaction length of the present and upgrade pixel detectors as a function of η . The green histogram are for the current pixel detector while the Phase 1 upgrade detector is given by the

Table 2.2: Total material weight for the pixel barrel and forward pixel detectors, and for the carbon fiber tube outside of the pixel barrel that is needed for the TIB and for beam pipe bakeout.

Volume	Mass (g)	
	Present Detector	Phase 1 Upgrade Detector
BPIX $ \eta < 2.16$	16801	6686
FPIX $ \eta < 2.50$	8582	7040
Barrel Outer Tube $ \eta < 2.16$	9474	9474

black points. Note that the “barrel outer tube” mentioned above and in Table 2.2 is included in the material budget for both present and upgrade pixel detectors for the comparisons shown in Figure 2.2.

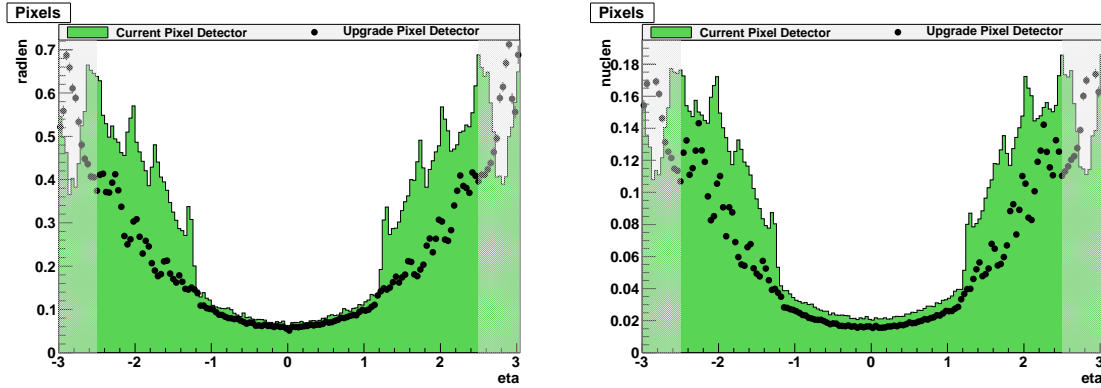


Figure 2.2: The amount of material in the pixel detector shown in units of radiation length (left), and in units of nuclear interaction length (right) as a function of η ; this is given for the current pixel detector (green histogram), and the Phase 1 upgrade detector (black points). The shaded region at high $|\eta|$ is outside the region for track reconstruction.

2.1.2 Pattern Recognition and Track Reconstruction

The normal pattern recognition and track reconstruction use an iterative procedure [10] consisting of a number of steps where the idea is that better tracks are reconstructed first and their hits removed before other tracks are reconstructed from the remaining hits. The “best” tracks are those that are less likely to be fake tracks. Each of the tracking steps starts with a collection of “seeds” formed from 2 (a pair seed) or 3 (a triplet seed) pixel hits consistent with some minimum track p_T , and coming from some region of the beam spot. The first step uses triplet seeds and higher minimum track p_T , these are followed by steps using pair seeds and/or lower p_T . The later steps use seeds that contain or only consists of hits from the silicon strip detector to find detached tracks, *e.g.* from decay products of K_s^0 mesons or Λ^0 baryons. For the studies presented in this chapter the later steps used to reconstruct detached tracks have been omitted to speed up the reconstruction and reduce memory usage that can be an issue for the largest pileup scenario studied.

With the additional barrel layer and end cap disks, the upgraded pixel detector will have excellent four-hit coverage over its whole η range. This allows for the creation of four-hit (“quadru-

plet”) track seeds with an intrinsically lower fake rate than that of three-hit (“triplet”) seeds. For the upgrade detector the first tracking step uses quadruplet seeds, before triplet seeds are used. Other than that the tracking step procedure for the upgrade detector proceeds in the same fashion as for the current detector.

2.1.3 B-tagging Algorithms

A number of b-jet tagging algorithms are used in the analyses of 2010 and 2011 CMS data [11]. For the studies presented in this chapter the algorithms have not yet been tuned for the maximal pileup conditions expected when running at a luminosity of $2 \times 10^{34} \text{ cm}^{-2}\text{s}^{-1}$ (25 ns crossing time) but have been used “as-is”. In addition no tuning of the b-tagging algorithms was performed for use with the upgrade pixel detector, so the b-tagging performance could in the future be improved for the upgrade detector compared to those presented in this chapter. One of the algorithms found to perform well in MC studies “as-is” for these pileup conditions for both the current and upgrade detectors is the “Combined Secondary Vertex” (CSV) method [12], this is the tagging algorithm used for the associated Higgs and $M_T 2b$ analyses described in this chapter.

The Combined Secondary Vertex b-tagging algorithm makes use of secondary vertices, together with other lifetime information, like the impact parameter (IP) significance and decay lengths. The use of a combination of information increases the likelihood that a useful tag can be made even in the highest pileup scenario. If a secondary vertex cannot be reconstructed, tracks with higher IP significances (> 2) can be used to form a “pseudo vertex” for which a subset of vertex based quantities can be computed even without an actual vertex. When there are not enough tracks reconstructed with high enough IP significances, selected tracks in the jet are used to compute the probability for the jet to be compatible with the primary vertex.

The b-tagging performance plots shown in this chapter were obtained in a MC study of jets reconstructed in a $t\bar{t}$ sample with $p_T > 30 \text{ GeV}$ and $|\eta| < 2.4$. Charged and neutral hadrons, photons, and leptons are reconstructed using the CMS particle-flow algorithm [13] before they are clustered to form jets using the anti- k_T jet algorithm [14] with a cone size $\Delta R = 0.5$. The jet clustering software used is FASTJET version 2.4.2 [15, 16]. Relative and absolute jet energy corrections [17] are applied to the raw jet momenta to establish a uniform jet response in p_T and η . An offset correction, determined using from simulation and using a charge hadron subtraction method, is made to correct for the effects of event pileup. In the Monte Carlo study the reconstructed jets are matched to the truth partons to categorize if a jet is truly a b-jet, a c-jet or a light quark (dusg) jet. The tagging algorithm is then applied to the jet to evaluate the efficiency for tagging or mis-tagging the jet as a b-jet.

2.2 Tracking Performance

The track collections used for most analyses in CMS involve fairly tight selections. The standard collection used for the studies presented here are “high purity” tracks which are filtered using the hit pattern, track p_T , normalized χ^2 of the track, and compatibility of originating from a pixel vertex. The selection criteria tuned for lower pileup conditions of 2012 data were kept as-is for these studies. This collection is used to evaluate the tracking performance in a $t\bar{t}$ sample. To illustrate the performance for muons, a muon sample is used and an additional requirement that the number of tracking layers with hits is at least eight is made to significantly reduce the fake rate which is more typical of analyses involving high p_T muons. Descriptions of the generation of the $t\bar{t}$ and muon samples are given below.

The tracking performance quantities presented in this chapter are the efficiency to reconstruct a charged particle track (track efficiency) and the probability that a reconstructed track is a fake track (track fake rate). Track parameters like the impact parameter resolution, and vertex resolutions were also studied and as well as the performance for tagging (mis-tagging) a b-jet (non-b-jet) as a b-jet.

2.2.1 Tracking Efficiency and Fake Rate

The track efficiency and fake rate were studied using two different signal samples, a muon sample and a $t\bar{t}$ sample. The muon “signal” consists of four muons coming from a common primary vertex, with p_T values taken randomly from a flat spectrum from 0.9 to 200 GeV and with track η also taken randomly from a flat distribution from -2.5 to 2.5 . For the $t\bar{t}$ sample Pythia 6.4 [18] was used for the signal generation of pp collisions at 14 TeV and the top quarks and all daughters allowed to decay inclusively.

The four pileup scenarios as given in Section (2.1) were studied: $\overline{PU} = 0, 25, 50, 100$. The $\overline{PU} = 0$ scenario does not represent a realistic running condition of the LHC, but rather is used to factorize improvements from the geometric changes in the upgrade separately from the improvements to the readout chip efficiencies. The $\overline{PU} = 25, 50, 100$ scenarios correspond to the original nominal LHC beam conditions and to upgraded LHC conditions with 25 ns and 50 ns bunch spacing.

The track reconstruction efficiency and fake rate presented are defined as follows:

$$\text{Tracking efficiency} = \frac{\text{Number of truth tracks matched to reconstructed tracks}}{\text{Number of truth tracks}} \quad (2.1)$$

$$\text{Track fake rate} = \frac{\text{Number of reconstructed tracks not matched to truth tracks}}{\text{Number of reconstructed tracks}} \quad (2.2)$$

where for (2.1) the only truth tracks considered are those from the signal interaction with (truth) $p_T > 0.9$ GeV. For the track fake rate given in (2.2) all reconstructed tracks with reconstructed $p_T > 0.9$ GeV are considered.

Figure 2.3 shows the tracking efficiency and track fake rate for “high purity” tracks with $p_T > 0.9$ GeV from the $t\bar{t}$ sample, for various luminosity scenarios for the current and upgrade pixel detector, with the expected dynamic pixel ROC data loss appropriate for the luminosity scenario as detailed in Table 2.1. It can be seen that with the current pixel detector the performance is only slightly degraded at $1 \times 10^{34} \text{ cm}^{-2}\text{s}^{-1}$ (25 ns crossing time), but rapidly deteriorates with higher pileup losing efficiency as well as suffering from more fake tracks. The situation is significantly improved for the upgrade pixel detector where very little efficiency is lost even at $2 \times 10^{34} \text{ cm}^{-2}\text{s}^{-1}$ (25 ns crossing time), though degradation starts to become significant if running at a crossing time of 50 ns.

When the highest track reconstruction efficiency is de-emphasized in favor of minimizing the fake rate, we can require additional cuts like a minimum number of tracking layers with hits as is done for the results shown in Figure 2.4. This figure shows the tracking efficiency and track fake rate for tracks in the muon sample for the different luminosity scenarios. The same trend is evident with the current pixel detector degrading much faster with increased luminosity (or pileup) than the proposed upgrade detector. This is illustrated by comparing the performance of the two detectors for $2 \times 10^{34} \text{ cm}^{-2}\text{s}^{-1}$ (25 ns crossing time) in Figure 2.5.

To try to disentangle the effects of the dynamic ROC data loss from those due to the high

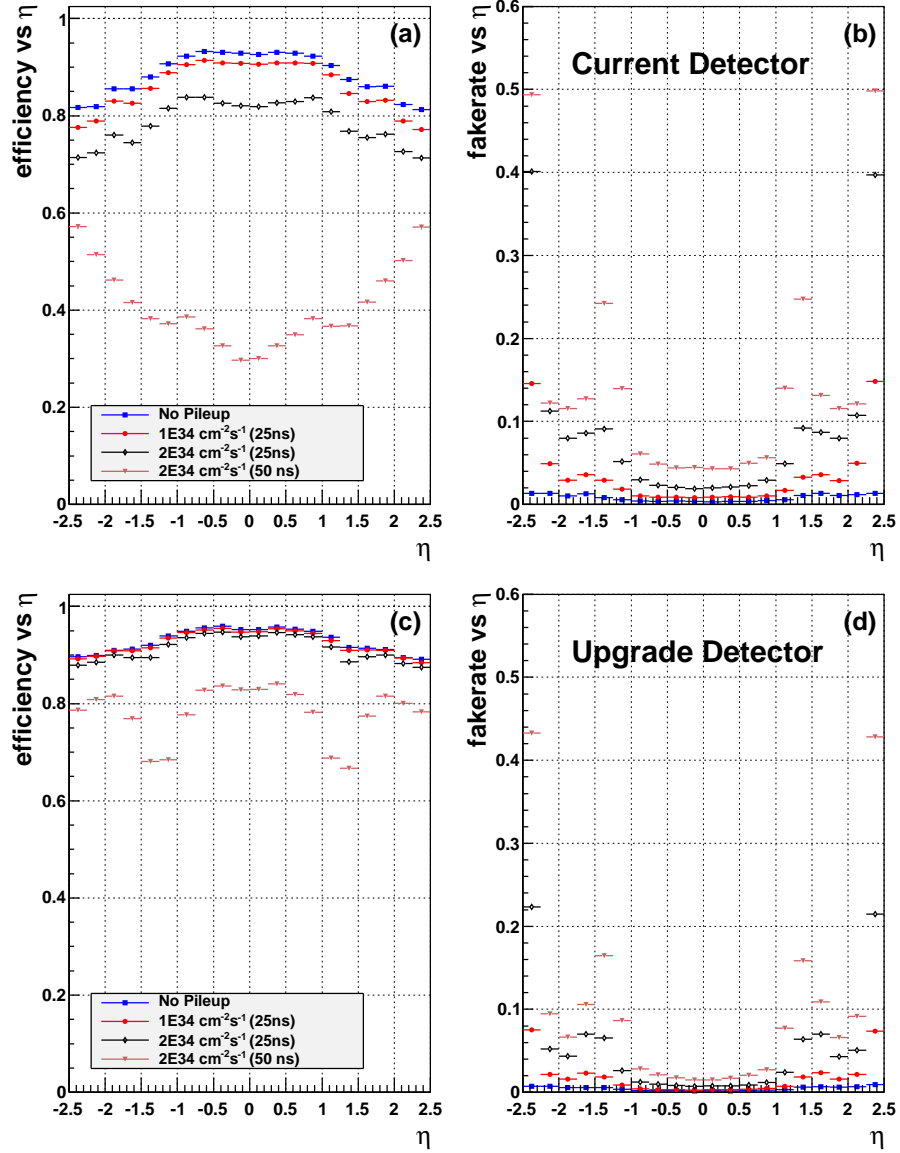


Figure 2.3: Tracking efficiency (a,c) and fake rate (b,d) for the $t\bar{t}$ sample as a function of track η , for the current detector (a,b) and the upgrade pixel detector (c,d). Results are shown for zero pileup (blue squares), an average pileup of 25 (red dots), an average pileup of 50 (black diamonds), and an average pileup of 100 (brown triangles) with ROC data loss simulation expected at the given luminosities as detailed in the text.

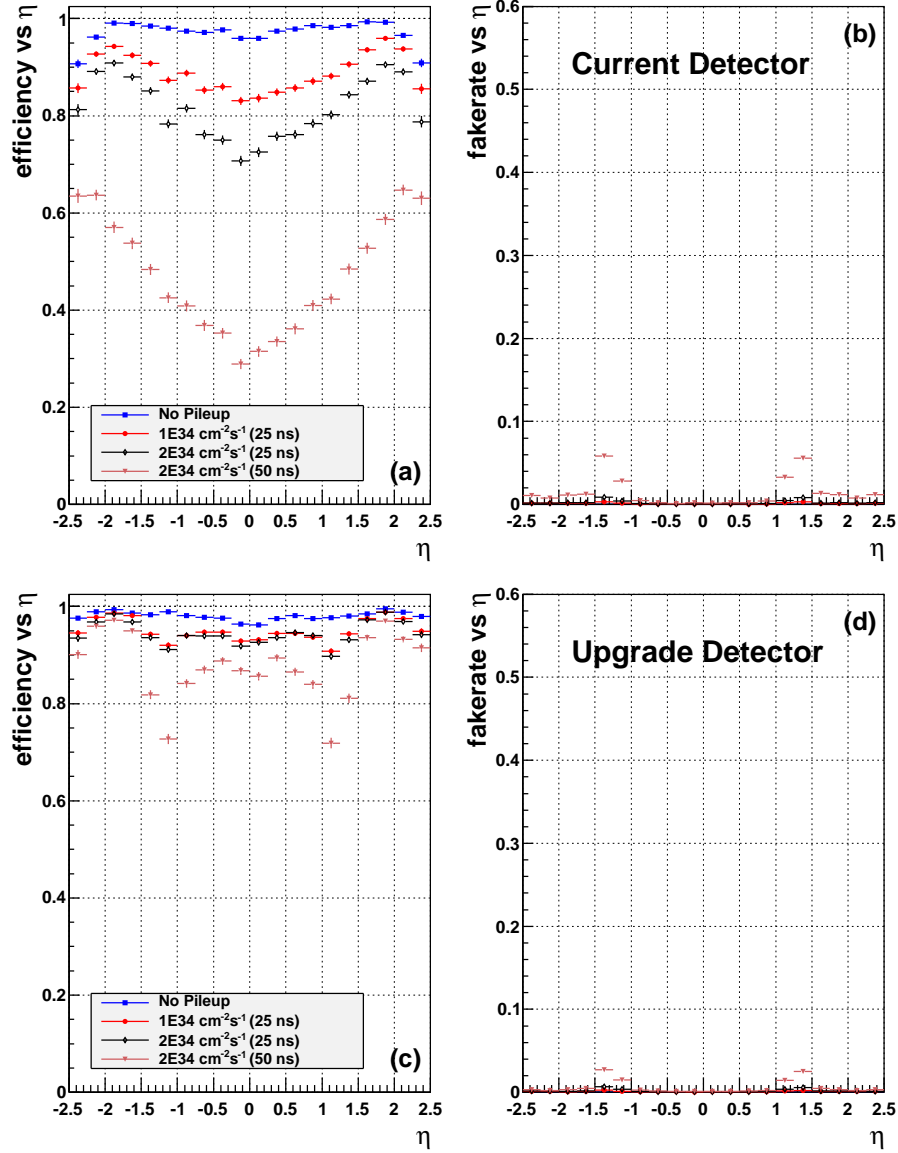


Figure 2.4: Tracking efficiency (a,c) and fake rate (b,d) for the muon sample as a function of track η , for the current detector (a,b) and the upgrade pixel detector (c,d). Results are shown for zero pileup (blue squares), an average pileup of 25 (red dots), an average pileup of 50 (black diamonds), and an average pileup of 100 (brown triangles) with ROC data loss simulation expected at the given luminosities as detailed in the text.

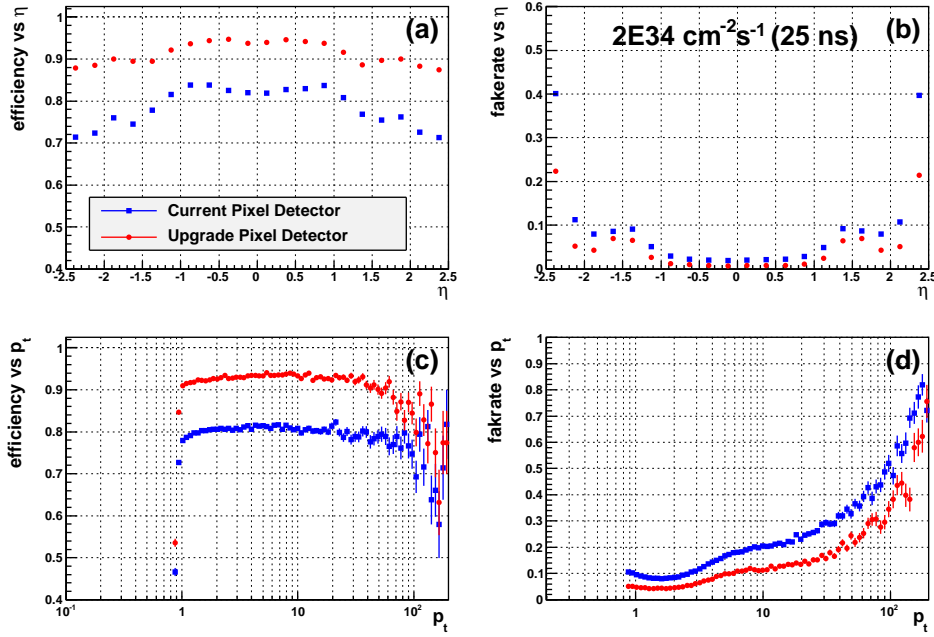


Figure 2.5: Tracking efficiency (a,c) and fake rate (b,d) for the $t\bar{t}$ sample as a function of track η (a,b) and track p_T (c,d). Results are shown for an average pileup of 50 with ROC data loss simulation expected for the current pixel detector (blue squares) and for the upgrade pixel detector (red dots).

Table 2.3: Average tracking efficiencies and track fake rates for muons with the additional cleanup cut and for a $t\bar{t}$ sample with default cuts for the current and upgrade pixel detector operating at zero pileup and at $2 \times 10^{34} \text{ cm}^{-2}\text{s}^{-1}$ (25 ns crossing time, *i.e.* 50 average pileup) without and with dynamic data loss (DL) simulated. The dynamic data loss simulated for the results below are fixed to the expected values for $2 \times 10^{34} \text{ cm}^{-2}\text{s}^{-1}$ (25 ns crossing time, *i.e.* 50 average pileup). The statistical uncertainties on the efficiencies are about 0.1% and on the fake rates about 0.01%.

Sample and Conditions		Tracking Efficiency (%)		Track Fake Rate (%)	
Sample	PU/DL/Cuts	Current	Upgrade	Current	Upgrade
Muon	0/No/Cleanup	97.4	98.1	0.0	0.0
Muon	0/Yes/Cleanup	93.9	97.9	0.0	0.0
Muon	50/No/Cleanup	90.1	94.9	0.22	0.17
Muon	50/Yes/Cleanup	81.5	94.4	0.23	0.17
$t\bar{t}$	0/No/Default	89.6	93.5	0.71	0.40
$t\bar{t}$	0/Yes/Default	85.6	93.2	0.68	0.41
$t\bar{t}$	50/No/Default	84.9	92.2	8.72	5.09
$t\bar{t}$	50/Yes/Default	79.7	92.0	9.49	5.13

pileup, the average tracking efficiencies were determined for a number of scenarios and shown in Table 2.3. Comparing the efficiencies at zero pileup with and without the dynamic ROC data loss expected for $2 \times 10^{34} \text{ cm}^{-2}\text{s}^{-1}$ (25 ns crossing time), the dynamic data losses cause a only 3.5% (4.0%) loss of tracking efficiency for muons ($t\bar{t}$) with the current pixel detector. However at the pileup conditions for $2 \times 10^{34} \text{ cm}^{-2}\text{s}^{-1}$ (25 ns crossing time) simulations show that the expected loss in efficiency due to the dynamic data loss increases to 8.6% (5.2%) for muons ($t\bar{t}$). With much lower dynamic data loss for the upgrade pixel detector, the resultant loss in tracking efficiency is less than 0.5% in both pileup conditions. The track fake rate is hardly affected by the dynamic data loss.

To isolate the effects of high pileup, we can compare the performance at zero pileup with those at high pileup without any ROC dynamic data loss simulated. The results in Table 2.3 for which the ROC data loss was not implemented show that the pileup conditions for $2 \times 10^{34} \text{ cm}^{-2}\text{s}^{-1}$ (25 ns crossing time) by itself would cause a 7.3% (4.7%) loss of tracking efficiency for muons ($t\bar{t}$) in the current pixel detector. The extra pixel layer in the upgrade detector adds information that reduces this loss in efficiency by more than half to 3.2% (1.3%) for muons ($t\bar{t}$), and decreases the fake rate by about a factor of two.

With both the effects of dynamic data loss and the high pileup expected for $2 \times 10^{34} \text{ cm}^{-2}\text{s}^{-1}$ (25 ns crossing time), the loss in tracking efficiency for the current detector is 15.9% (9.9%) for muons ($t\bar{t}$), while for the upgraded detector it is reduced by more than a factor of 4 (6) to 3.7% (1.5%) for muons ($t\bar{t}$). Although this is not catastrophic, the degradation is worse than linear and is expected to become unacceptable at moderately higher pileup as illustrated in Figure 2.6. The track fake rate also rapidly increases with pileup but is about a factor of two lower for the upgrade pixel detector.

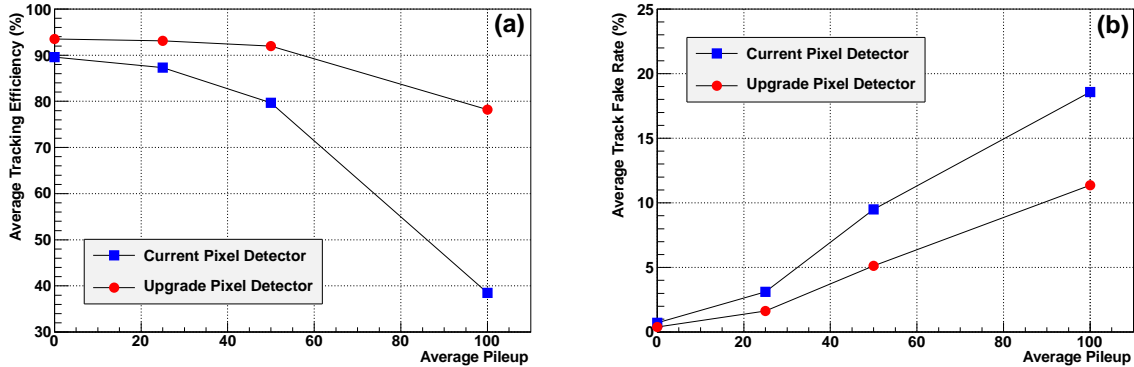


Figure 2.6: Average tracking efficiency (a) and average track fake rate (b) for the $t\bar{t}$ sample as a function of the average pileup. Results were determined using the expected ROC data loss expected for each given average pileup, and for the current pixel detector (blue squares) and for the upgrade pixel detector (red dots).

2.2.2 Track Impact Parameter Studies

The track impact parameter resolution was studied in the Phase 1 upgrade detector and compared to the current detector. The track sample used for the impact parameter resolution measurements were from a muon Monte Carlo generated flat in energy (instead of flat in p_T). Figures 2.7 and 2.8 show respectively the transverse and longitudinal impact parameter resolutions for the current and upgrade pixel detectors as a function of the track (total) momentum for zero pileup. The ratio of the impact parameter resolutions show that the impact parameter

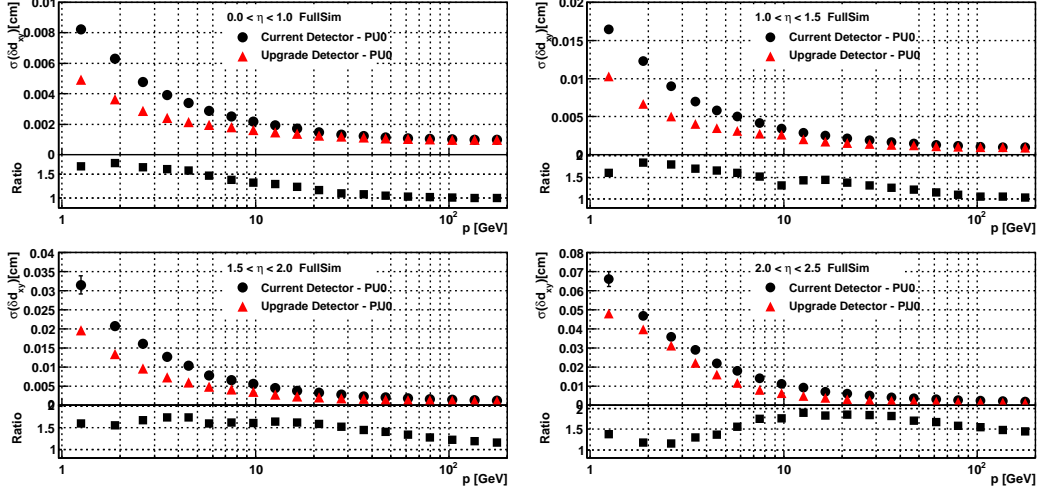


Figure 2.7: Transverse impact parameter resolution for muon tracks as a function of the track momentum for different η regions for the current pixel detector (black circles) and the Phase 1 upgrade detector (red triangles) in zero pileup. The lower part of each plot shows the ratio of the current detector resolution to the upgrade resolution. (top-left) $0 < \eta < 1$; (top-right) $1 < \eta < 1.5$; (bottom-left) $1.5 < \eta < 2$; (bottom-right) $2 < \eta < 2.5$.

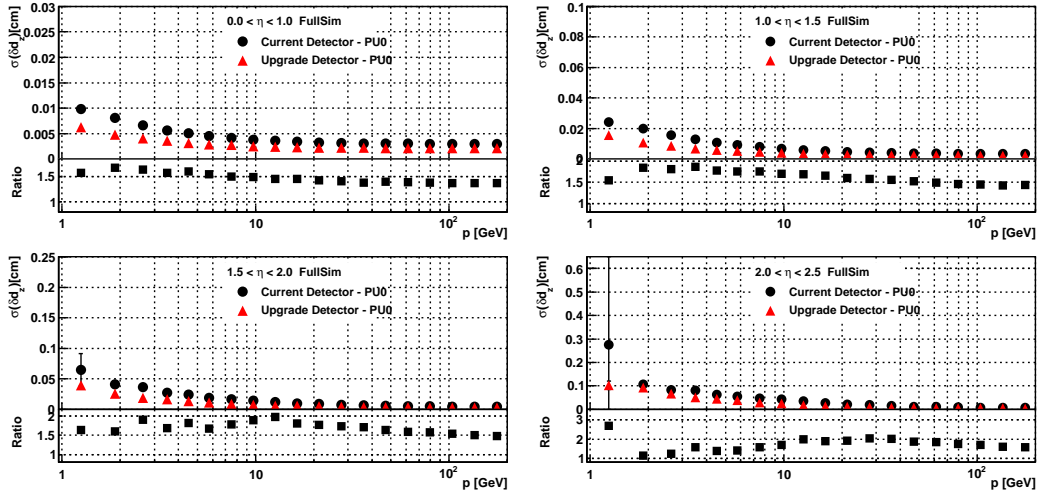


Figure 2.8: Longitudinal impact parameter resolution for muon tracks as a function of the track momentum for different η regions for the current pixel detector (black circles) and the Phase 1 upgrade detector (red triangles) in zero pileup. The lower part of each plot shows the ratio of the current detector resolution to the upgrade resolution. (top-left) $0 < \eta < 1$; (top-right) $1 < \eta < 1.5$; (bottom-left) $1.5 < \eta < 2$; (bottom-right) $2 < \eta < 2.5$.

resolution is expected to be greatly improved for the upgrade detector compared to the current pixel detector, more so for the longitudinal resolution. The improvement at lower absolute momentum is expected due to the reduction of material in the upgrade detector and where the resolution is dominated by multiple Coulomb scattering. For the transverse resolution the improvement falls off with momentum in the central region while the longitudinal impact parameter resolution is improved over the whole momentum range in all four η regions.

We also studied the impact parameter resolution at an average pileup of 50 interactions per crossing, corresponding to $2 \times 10^{34} \text{ cm}^{-2}\text{s}^{-1}$ luminosity (25 ns crossing time). The results are shown in Figures 2.9 and 2.10.

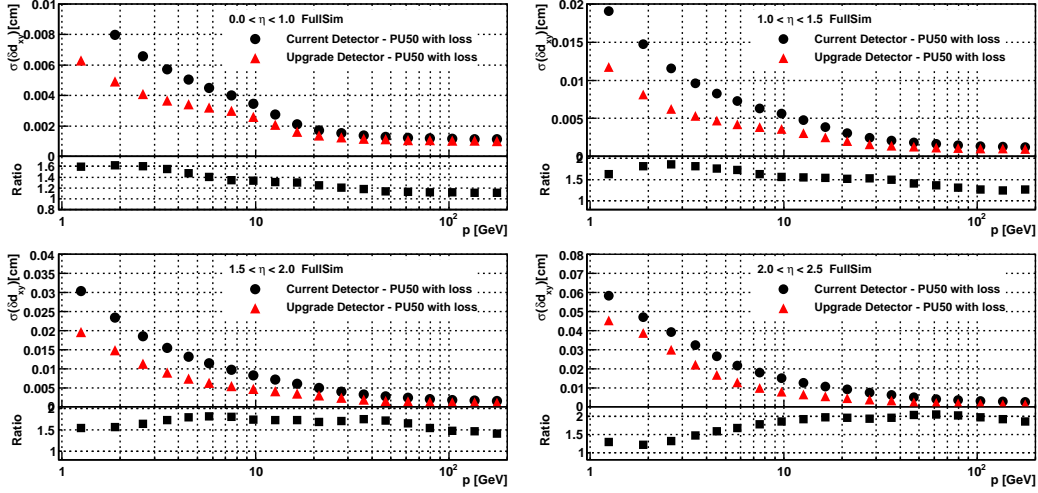


Figure 2.9: Transverse impact parameter resolution for muon tracks as a function of the track momentum for different η regions for the current pixel detector (black circles) and the Phase 1 upgrade detector (red triangles) for an average pileup of 50. The lower part of each plot shows the ratio of the current detector resolution to the upgrade resolution. (top-left) $0 < \eta < 1$; (top-right) $1 < \eta < 1.5$; (bottom-left) $1.5 < \eta < 2$; (bottom-right) $2 < \eta < 2.5$.

The effect of the higher pileup and the dynamic data loss is to increase the impact parameter resolutions, much more so for the current detector than with the upgrade pixel detector, so that the upgrade detector shows an even larger improvement than at zero pileup. This larger improvement in the resolutions is most evident in the higher momentum regions in all η ranges. To study the effect of the dynamic data loss alone on the impact parameter resolutions we compared with the current detector the resolutions at zero pileup without and with the dynamic data loss expected for $2 \times 10^{34} \text{ cm}^{-2}\text{s}^{-1}$ luminosity (25 ns crossing time). As shown in Figures 2.11 and 2.12 for the transverse and longitudinal resolutions respectively, the main effect of the dynamic data loss is to degrade the resolution substantially in the high momentum regions.

We conclude that the upgrade pixel detector with an extra layer and the innermost layer closer to the interaction point will improve the impact parameter resolution by as much as a factor of 1.5 in the zero pileup scenario compared to the current detector. The improvement is mainly at the lower momentum ranges for the transverse resolution but extends to high momentum for the longitudinal resolution. At $2 \times 10^{34} \text{ cm}^{-2}\text{s}^{-1}$ luminosity (25 ns crossing time) both the effects of pileup and dynamic data loss degrades the resolutions so that the upgrade pixel detector provides an even greater improvement compared to the current detector in all η and momentum regions and for both transverse and longitudinal resolutions. The dynamic data loss accounts for a substantial part of the degradation of the resolution in the high momentum

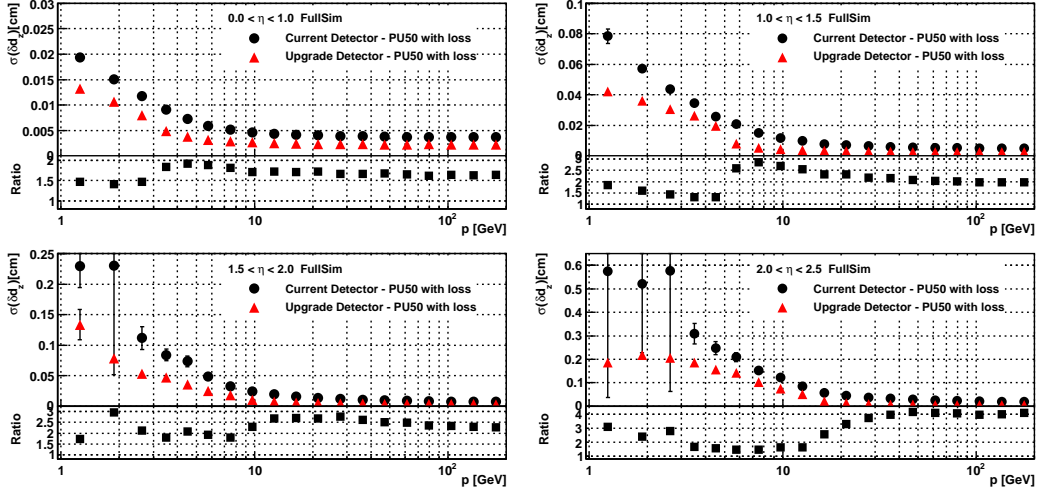


Figure 2.10: Longitudinal impact parameter resolution for muon tracks as a function of the track momentum for different η regions for the current pixel detector (black circles) and the Phase 1 upgrade detector (red triangles) for an average pileup of 50. The lower part of each plot shows the ratio of the current detector resolution to the upgrade resolution. (top-left) $0 < \eta < 1$; (top-right) $1 < \eta < 1.5$; (bottom-left) $1.5 < \eta < 2$; (bottom-right) $2 < \eta < 2.5$

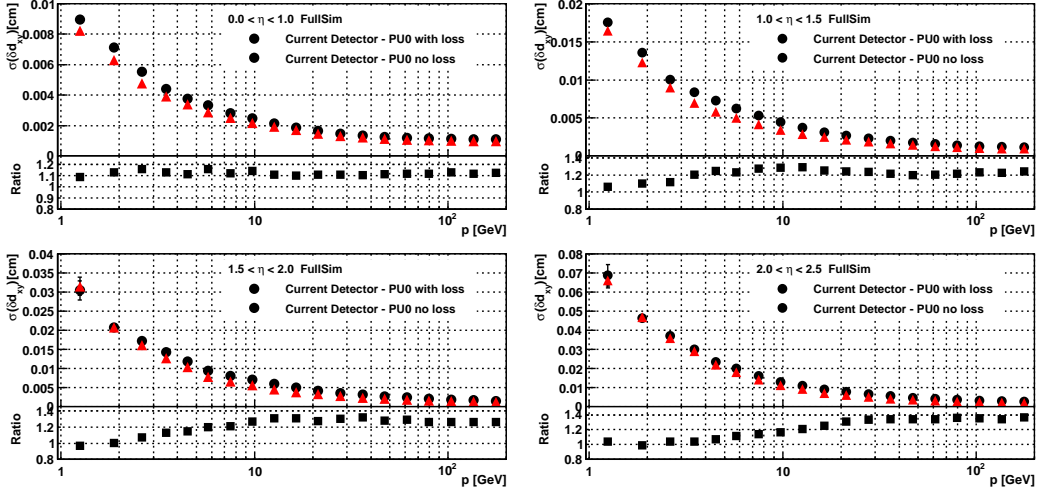


Figure 2.11: Transverse impact parameter resolution for muon tracks with zero pileup as a function of the track momentum for different η regions for the current pixel detector with (black circles) and without (red triangles) the dynamic data loss expected at $2 \times 10^{34} \text{ cm}^{-2} \text{ s}^{-1}$ luminosity. The lower part of each plot shows the ratio of the resolution with dynamic data loss to the resolution without. (top-left) $0 < \eta < 1$; (top-right) $1 < \eta < 1.5$; (bottom-left) $1.5 < \eta < 2$; (bottom-right) $2 < \eta < 2.5$.

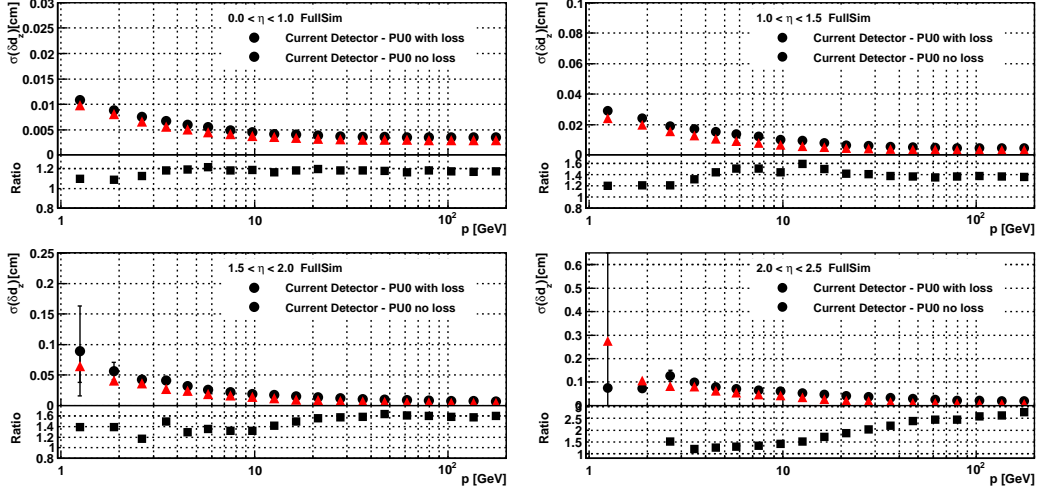


Figure 2.12: Longitudinal impact parameter resolution for muon tracks with zero pileup as a function of the track momentum for different η regions for the current pixel detector with (black circles) and without (red triangles) the dynamic data loss expected at $2 \times 10^{34} \text{ cm}^{-2} \text{s}^{-1}$ luminosity. The lower part of each plot shows the ratio of the resolution with dynamic data loss to the resolution without. (top-left) $0 < \eta < 1$; (top-right) $1 < \eta < 1.5$; (bottom-left) $1.5 < \eta < 2$; (bottom-right) $2 < \eta < 2.5$

range.

2.2.3 Vertex Resolution Studies

The primary vertex resolution was measured using a Monte Carlo $t\bar{t}$ sample. Figure 2.13 shows the transverse and longitudinal primary vertex resolutions as a function of the number of tracks in the vertex for a $t\bar{t}$ sample. Comparisons are shown for the current and upgrade pixel detectors for both the $\overline{\text{PU}} = 0$ and $\overline{\text{PU}} = 50$ scenarios. The ratios of the resolutions show a significant improvement for the upgrade pixel detector, with about a 50% improvement in a zero pileup environment and an even better improvement of almost 100% in the high pileup conditions for $2 \times 10^{34} \text{ cm}^{-2} \text{s}^{-1}$ luminosity (25 ns crossing time).

The primary vertex resolutions degrade at high pileup, and this effect is much worse for the current pixel detector. To study the cause we determined for the current pixel detector the resolutions with and without the dynamic data loss (expected for $2 \times 10^{34} \text{ cm}^{-2} \text{s}^{-1}$ (25 ns crossing time)), at both zero pileup and an average pileup of 50. These results are shown in Figure 2.14. The same $t\bar{t}$ sample is used for the four configurations: zero pileup, zero pileup with dynamic data loss, and average pileup of 50 with and without dynamic data loss. The primary vertex resolution for an event for all four cases are plotted against the number of tracks found in the primary vertex for the zero pileup case. So for a given number-of-tracks-bin the resolution is shown in all four configurations for the same set of $t\bar{t}$ events, any difference in resolution is due to either pileup or dynamic data loss, or both. These results show that the dynamic data loss is the dominant cause of the worsening of the primary vertex resolution, particularly for the transverse resolution. For the longitudinal resolution the pileup also plays a significant part. Both the data loss and pileup together worsens the primary vertex resolution by about 20–40%.

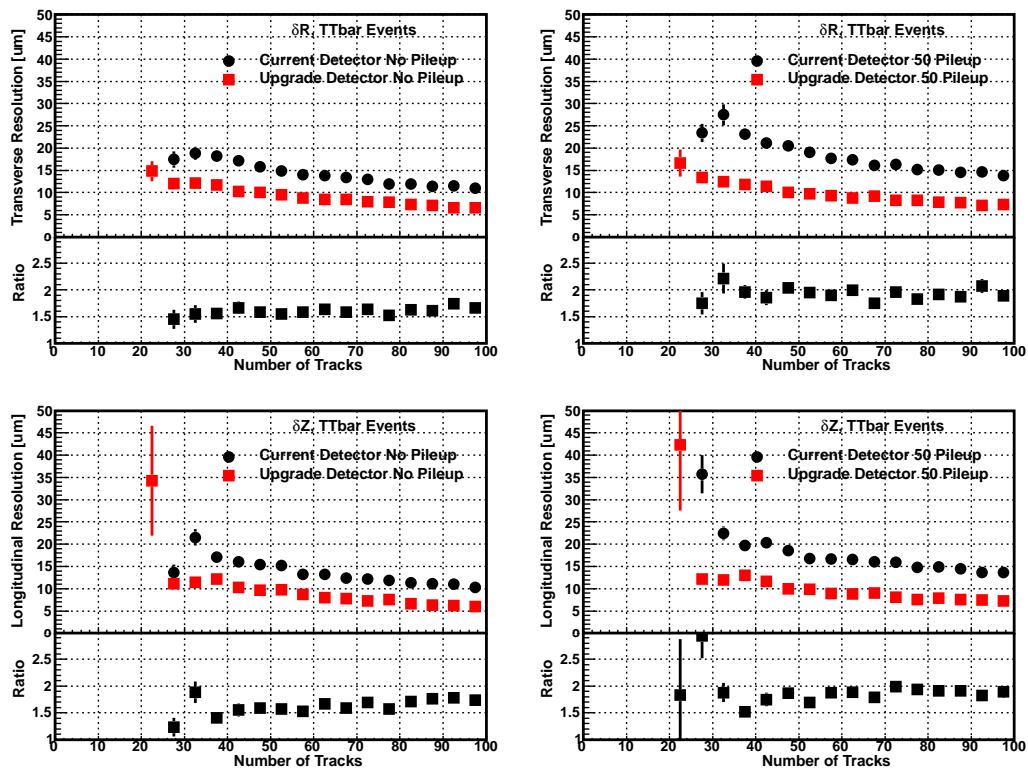


Figure 2.13: Transverse (top) and longitudinal (bottom) primary vertex resolutions as a function of the the number of tracks in the vertex for a $t\bar{t}$ sample with (left) zero pileup, and (right) with an average pileup of 50. The resolutions are shown for the current pixel detector (black circles) and the Phase 1 upgrade detector (red squares). The lower part of each plot shows the ratio of the current detector resolution to the upgrade resolution.

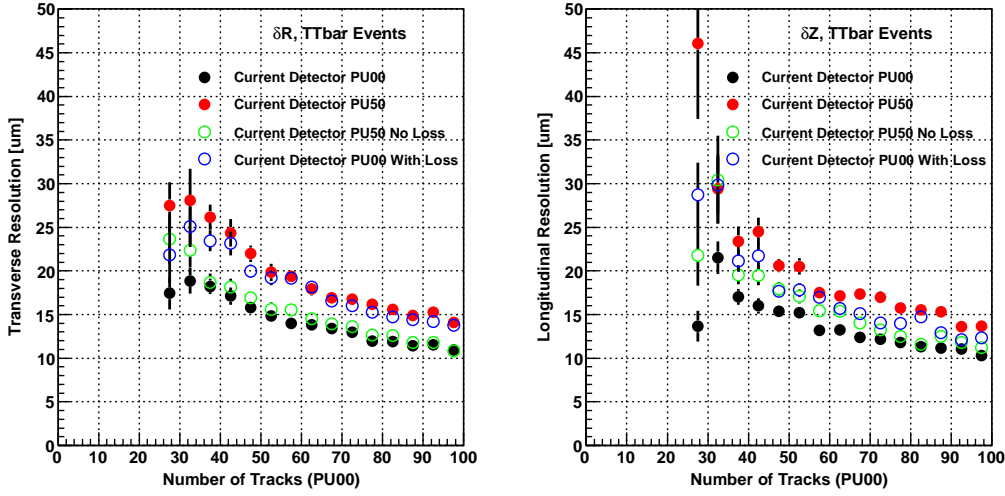


Figure 2.14: Transverse (left) and longitudinal (right) primary vertex resolutions for a $t\bar{t}$ sample. These are plotted as a function of the the number of tracks in the vertex for the zero pileup case as described in the text. The resolutions are shown for zero pileup (black points), zero pileup with data loss (blue open circles), 50 pileup with data loss (red points), and 50 pileup without data loss (green open circles).

2.2.4 Performance for b-Tagging

With the expected improvements in the tracking efficiency, track impact parameter resolution, and primary vertex resolutions shown in the previous sections we expect the b-tagging performance for the Phase 1 upgrade pixel detector to be significantly better than the current detector at high pileup.

The b-tagging performance of the CMS b-tagging algorithms were studied using a $t\bar{t}$ simulation sample. Results for the “Combined Secondary Vertex” algorithm as described in Section 2.1.3 are presented. No tuning was done for high pileup or for the upgrade detector on the selection criteria for the track collections used in the algorithms, nor was any tuning done of the b-tagging algorithms themselves.

Figure 2.15 shows the b-tagging performance of the “Combined Secondary Vertex” algorithm with no pileup and with an average pileup of 50 interactions per crossing. The plot shows the fraction of c-jets and (light) dusg-jets that are misidentified as a b-jet as a function of the efficiency for identifying a b-jet correctly as a b-jet. The results show that the b-tagging performance is significantly better for the upgrade pixel detector even at zero pileup when the performance of the current pixel detector is neither degraded by dynamic data loss nor by high pileup. This illustrates the power of both having the extra pixel layer in the upgrade detector and having the innermost layer closer to the interaction point.

At $2 \times 10^{34} \text{ cm}^{-2}\text{s}^{-1}$ luminosity (25 ns crossing time) when the current pixel detector suffers more dynamic data loss and from the effects of high pileup the difference in b-tagging performance is further amplified for the upgrade pixel detector. At a light quark jet b-mistag rate of 1% the b-tagging efficiency for b-jets in the upgrade detector is better by a relative 28% than for the current detector, while at a light quark jet b-mistag rate of 0.1% the performance for the upgrade detector is higher by a relative 46%.

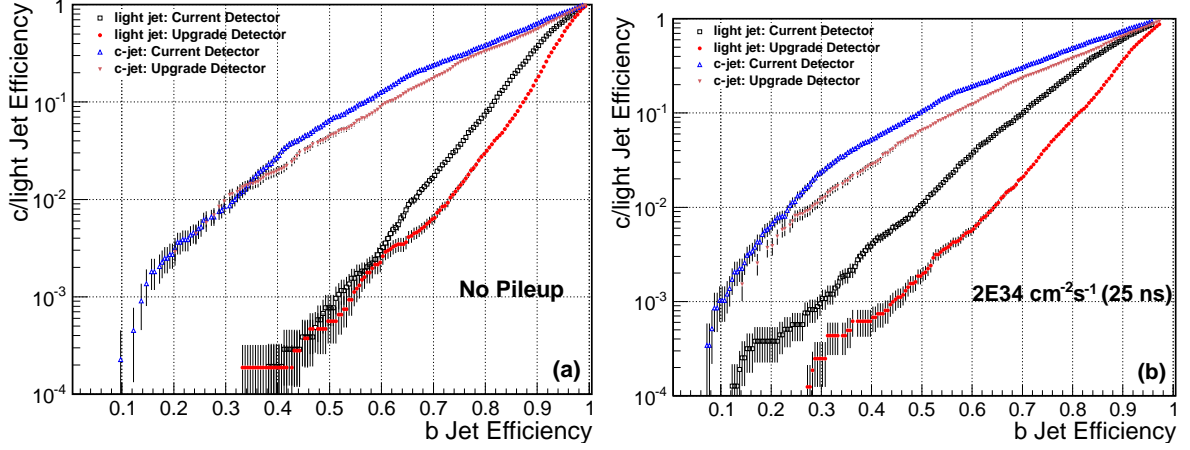


Figure 2.15: Performance of the Combined Secondary Vertex b-tagging algorithm for jets with $p_T > 30$ GeV in a $t\bar{t}$ sample with (a) zero pileup, and (b) an average pileup of 50. The performance for the current detector are shown by the open points while the solid points are for the upgrade detector. The triangular points are for c-jets while the circle and square points are for light quark jets.

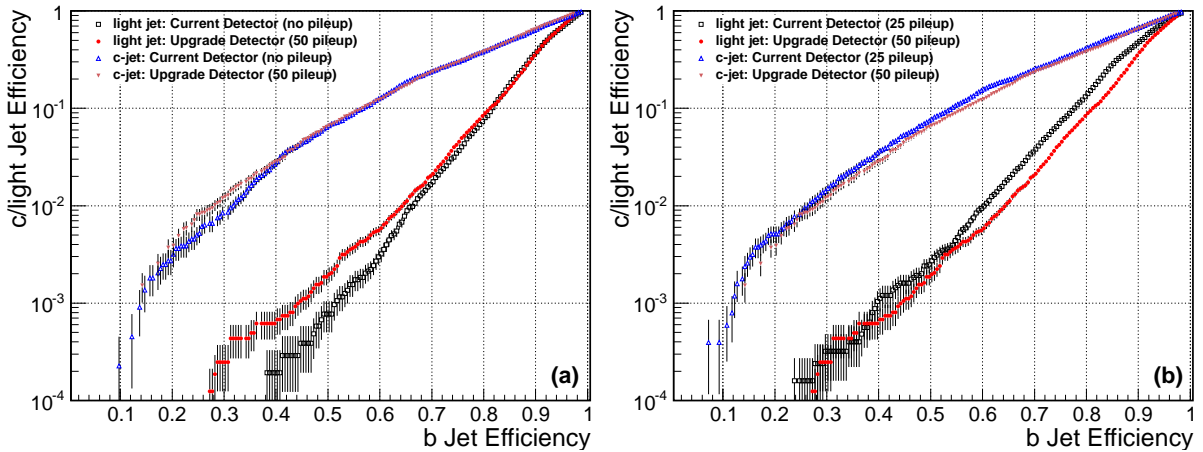


Figure 2.16: Comparison of the performance of the Combined Secondary Vertex b-tagging algorithm for jets with $p_T > 30$ GeV in a $t\bar{t}$ sample for the Phase 1 upgrade detector with an average pileup of 50, and for (a) the current pixel detector with zero pileup, (b) the current pixel detector with an average pileup of 25. The performance for the current detector are shown by the open points while the solid points are for the upgrade detector. The triangular points are for c-jets while the circle and square points are for light quark jets.

It can be seen in Figure 2.16 that the b-tagging performance for the upgrade pixel detector at $2 \times 10^{34} \text{ cm}^{-2}\text{s}^{-1}$ is almost as good as that for the current detector with no pileup, and superior to the current detector running in pileup conditions similar to 2012 data (average pileup of 25).

With the uncertainty in the LHC luminosity upgrade path, we also studied the b-tagging performance in the $\overline{\text{PU}} = 100$ scenario. Figure 2.17 shows the b-tagging performance of the Combined Secondary Vertex b-tagging algorithm. As expected the performance is significantly impacted by this higher pileup and dynamic data loss. The difference in performance of the Phase 1 upgrade pixel detector is even greater compared to the current detector under these conditions.

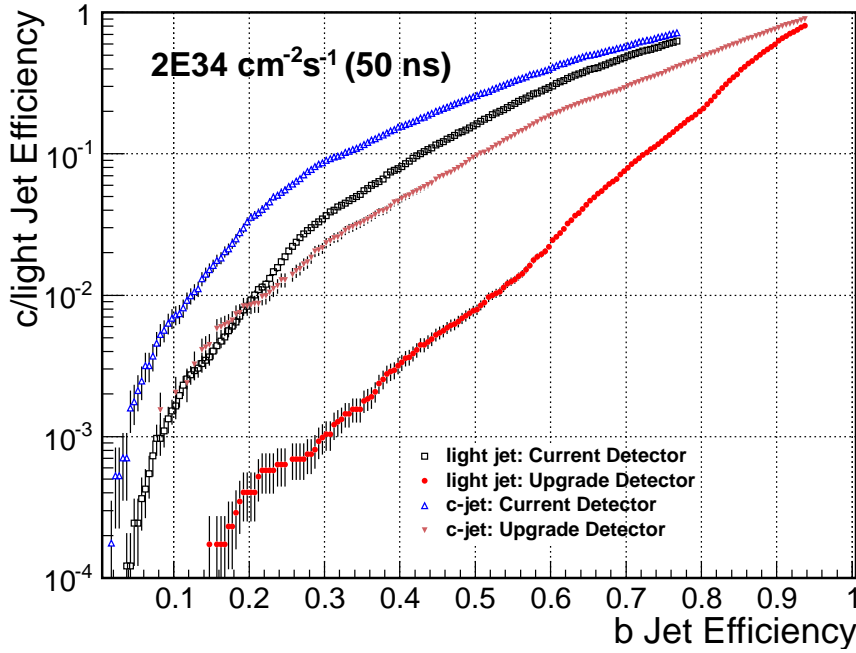


Figure 2.17: Performance of the Combined Secondary Vertex b-tagging algorithm for jets with $p_T > 30 \text{ GeV}$ in a $t\bar{t}$ sample with an average pileup of 100. The performance for the current detector are shown by the open points while the solid points are for the upgrade detector. The triangular points are for c-jets while the circle and square points are for light quark jets.

As an indication of the relative b-tagging performance between the current pixel detector and the upgrade, the b-tagging efficiencies for b-jets are shown in Figure 2.18 for two specific light quark and charm quark jet mis-tag rates. It can be seen that the b-tagging efficiency rapidly degrades with pileup (and dynamic data loss) and this degradation is much worse for the current pixel detector, with degradations of factors of 1.5 to 2 depending the operating point and scenario.

2.2.5 Robustness to Pixel Inner Layer Inefficiencies

It was shown in the previous sections that the upgrade detector is less degraded by the effects of higher luminosities. This is both because the upgrade detector suffers less from dynamic data loss due to a new pixel ROC, and also because an extra hit in the additional pixel layer helps to mitigate the negative effects of high pileup.

The additional pixel layer in the upgrade detector also adds redundancy in the case when the inner pixel layer degrades, *e.g.* due to radiation damage. To illustrate the additional robustness,

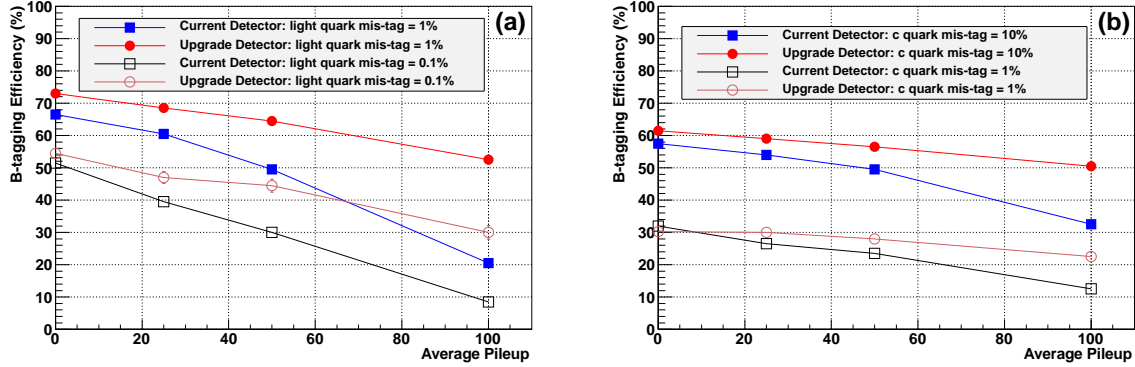


Figure 2.18: The b-tagging efficiencies for b-jets with $p_T > 30$ GeV in a $t\bar{t}$ sample plotted against average pileup for (a) light quark jet mis-tag rates of 1% (solid points) and 10% (open points), and for (b) charm quark jet mis-tag rates of 10% (solid points) and 1% (open points). Values for the current pixel detector are shown in circular points while those for the Phase 1 upgrade detector are shown with squares.

both the tracking performance and the b-tagging performance was determined for various inefficiencies in the inner pixel barrel layer (BPIX1). A $t\bar{t}$ sample was used with an average pileup of 50, and no (dynamic) data loss was simulated in any layer other than BPIX1.

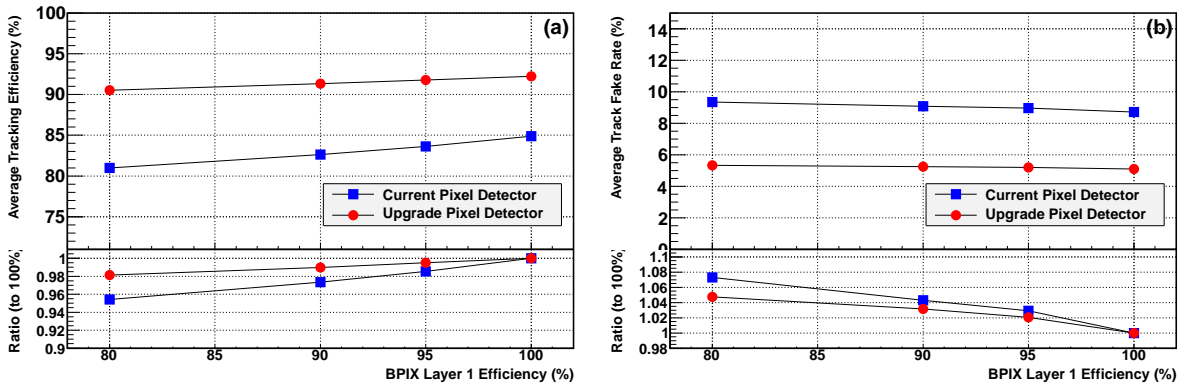


Figure 2.19: Average tracking efficiency (a) and average track fake rate (b) for the $t\bar{t}$ sample as a function of the efficiency of the first layer of the barrel pixel detector. Results were determined for the current pixel detector (blue squares) and for the upgrade pixel detector (red dots). The ratios given in the lower part of the plot are to the efficiency (a) or fake rate (b) when the first barrel pixel layer is 100% efficient.

The results of the tracking performance study is given in Figure 2.19. It can be seen that as expected the average tracking efficiency drops with the inefficiency in the first pixel barrel layer for both the current and upgrade pixel detectors but the drop is less sharp for the upgrade detector, reducing the relative tracking efficiency loss by about a factor 2–3. The average track fake rate is also seen to increase less with the upgrade pixel detector.

For the b-tagging study, the b-tagging performance are shown in Figure 2.20. To illustrate the improvement with the upgrade pixel detector for a particular operating point, the b-tagging efficiencies for a light quark mis-tag rate of 1% are plotted against the BPIX1 efficiency in Figure 2.21(a). The relative loss of b-tagging efficiency due to inefficiencies in BPIX1 compared to

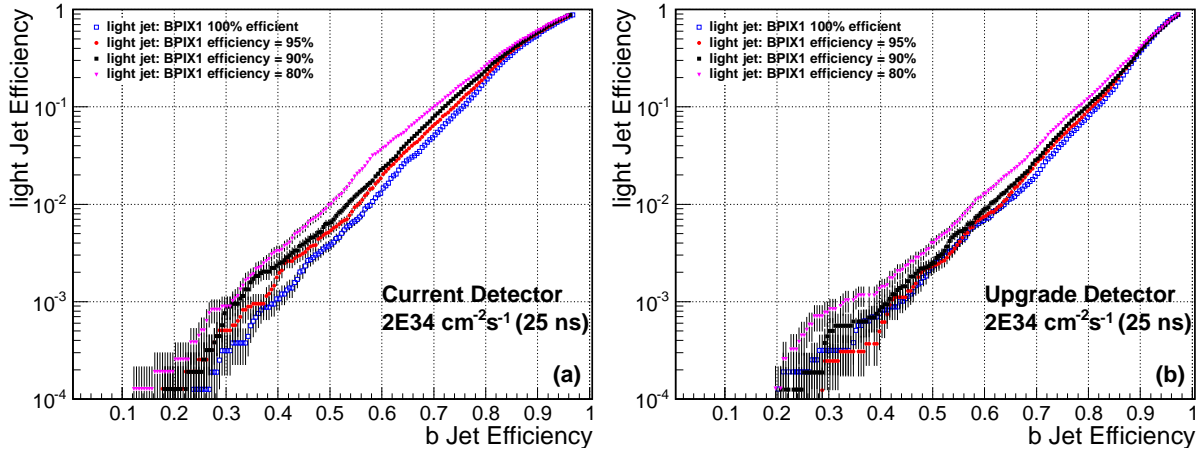


Figure 2.20: The b-tagging performance for jets with $p_T > 30$ GeV in a $t\bar{t}$ sample for (a) current pixel detector and (b) upgrade pixel detector. Performance is shown for various efficiencies of the first layer of the barrel pixel detector.

when BPIX1 is 100% efficient is shown in Figure 2.21(b). Again it can be seen that the upgrade detector helps to mitigate the loss in performance due to inefficiency in the barrel pixel inner layer.

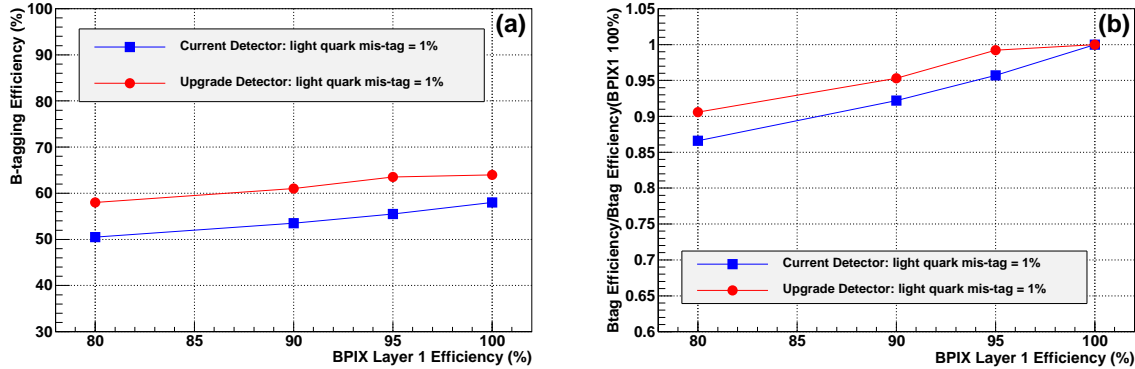


Figure 2.21: (a) The b-tagging efficiencies for b-jets with $p_T > 30$ GeV in a $t\bar{t}$ sample plotted against the BPIX1 efficiency for a light quark jet mis-tag rate of 1% for the current and upgrade pixel detectors. (b) The same data is also presented as ratios to the b-tagging efficiency where the first layer of the current barrel pixel detector is fully efficient.

2.2.6 Recovery of TIB Inefficiencies

A study of the tracking efficiencies when the outer tracker layer efficiencies are reduced is used to illustrate the efficiency recovery with a fourth pixel layer. The outer pixel barrel layer in the upgrade pixel detector is much closer to the Tracker Inner Barrel (TIB) - the innermost part of the outer tracker. To study the effect on the tracking performance due to a degraded TIB efficiency we simulated a 20% uniform inefficiency in the first two TIB layers. The tracking efficiency for this scenario is shown in Figs. 2.22(a) and (b). The modifications to the normal simulation and track reconstruction procedures as described in Sections 2.1 and 2.1.2 were used for this simulation study. Also the tracking performance was done using the $t\bar{t}$ sample with no pileup and with an average pileup of 50.

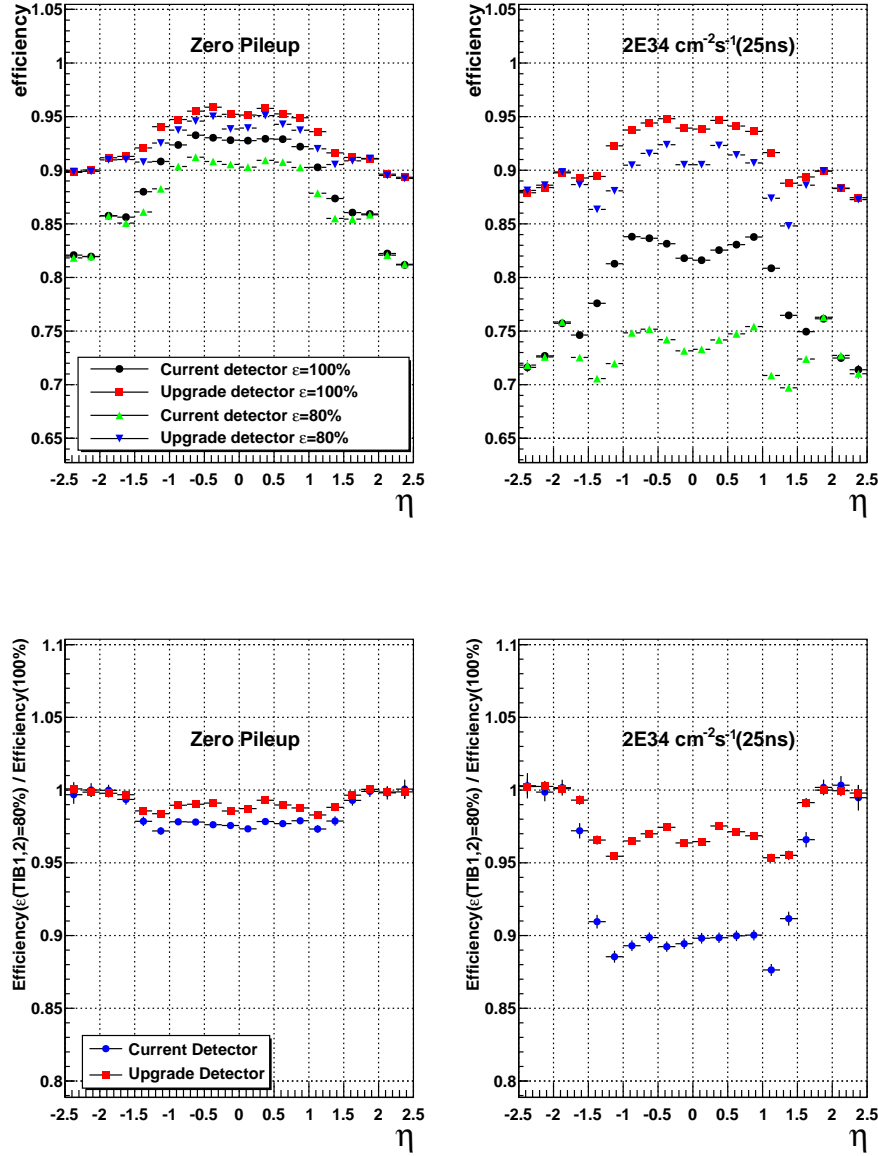


Figure 2.22: Tracking efficiency as a function of η for default tracks in a $t\bar{t}$ sample with (left) zero pileup, and (middle-left) an average pileup of 50. Results are shown for the current detector (black circles, green triangles), and the upgrade detector (red squares, blue inverted triangles); with TIB1 and TIB2 at 100% efficiency (black circles, red squares), and with TIB1 and TIB2 at 80% efficiency (green triangles, blue inverted triangles). Ratio of the tracking efficiencies with TIB1 and TIB2 at 80% efficiency to the tracking efficiency with TIB1 and TIB2 at 100% efficiency as a function of η for default tracks in a $t\bar{t}$ sample with (middle-right) zero pileup, and (right) an average pileup of 50. Results are shown for the current detector (blue circles), and the upgrade detector (red squares).

It can be seen that a uniform 20% inefficiency in the first two TIB layers reduces the tracking efficiency for both the current pixel detector and with the upgrade pixel detector; the loss in tracking efficiency is worse at high pileup. The simulation results show that the loss in tracking efficiency due to degradation in the TIB is reduced in the upgrade detector compared to the current detector. This is illustrated in Figure 2.22 which shows the relative loss of tracking efficiency due to the TIB degradation. With no pileup the relative tracking efficiency loss is small, about 1–2% for the current and upgrade pixel detectors. With an average pileup of 50 the relative efficiency loss with the current pixel detector is dramatically worse at about 10%, it is much lower for the upgrade detector at about 4%. The upgrade pixel detector can thus significantly mitigate the loss in tracking efficiency due to a degradation in the TIB.

Figure 2.23 shows the track fake rates for this scenario of a uniform 20% inefficiency in the first two TIB layers. The track fake rates are negligible at zero pileup. At an average pileup of 50 the inefficiency in the TIB causes an increase in the track fake rate for the current detector by as much as 40%, while almost no effect is seen with the upgrade pixel detector.

The robustness of the upgrade pixel detector to degradation in the outer tracker layers was studied in a more realistic scenario. A number of modules in the outer tracker are currently operating at higher than design temperatures due to insufficient cooling, and are either degraded or expected to degrade in the future. These modules are illustrated in the black regions of the CMS “Tracker Map” shown in Figure 2.24.

The above study was repeated but switching the modules indicated in Figure 2.24 off instead of a 20% inefficiency in the first two TIB layers. The results are shown in Figs. 2.25 and 2.26. In this scenario it can be seen that again the upgrade detector is much more robust than the current pixel detector to the dead tracker modules, both at zero pileup, and even more so at an average pileup of 50.

We conclude that the upgrade pixel detector is much more robust to outer tracker inefficiencies, and for the two scenarios studied, the loss in tracking efficiency due to inefficiencies in the outer tracker is typically about half of that compared to the current detector. In addition the track fake rate with the upgrade pixel detector is hardly affected by outer tracker inefficiencies while it will increase substantially for the current detector.

2.2.7 Summary of Tracking Performance

The expected dynamic data loss due to the pixel ROC and readout causes a significant number of degradations: lower track reconstruction efficiency, worse impact parameter resolutions, and worse primary vertex resolution. The level of data loss expected for the current pixel detector at $2 \times 10^{34} \text{ cm}^{-2}\text{s}^{-1}$ (25 ns crossing time) would cause a 3.5% (4.0%) loss of tracking efficiency for muons ($t\bar{t}$) in a low pileup environment, but in the pileup conditions for $2 \times 10^{34} \text{ cm}^{-2}\text{s}^{-1}$ (25 ns crossing time) simulations show that the expected loss in efficiency is more than quadrupled (doubled) to 15.9% (9.9%) for muons ($t\bar{t}$). The difference is because the exact loss depends on the track distributions in p_T and η as well as on the track selection criteria. The dynamic data loss causes the transverse impact parameter (IP) resolution to degrade by 10% in the central region raising to almost 40% worse in the forward regions at high momentum. This degradation is doubled for the longitudinal impact parameter resolution. The primary vertex (PV) resolution is similarly worsened by about 20%. The much smaller dynamic data loss expected in the upgrade pixel detector because of the new ROC and readout means that we do not have similar degradations of the tracking efficiency and IP and PV resolutions from this source.

The effects of higher pileup are harder to quantify since they depend on the exact analysis and

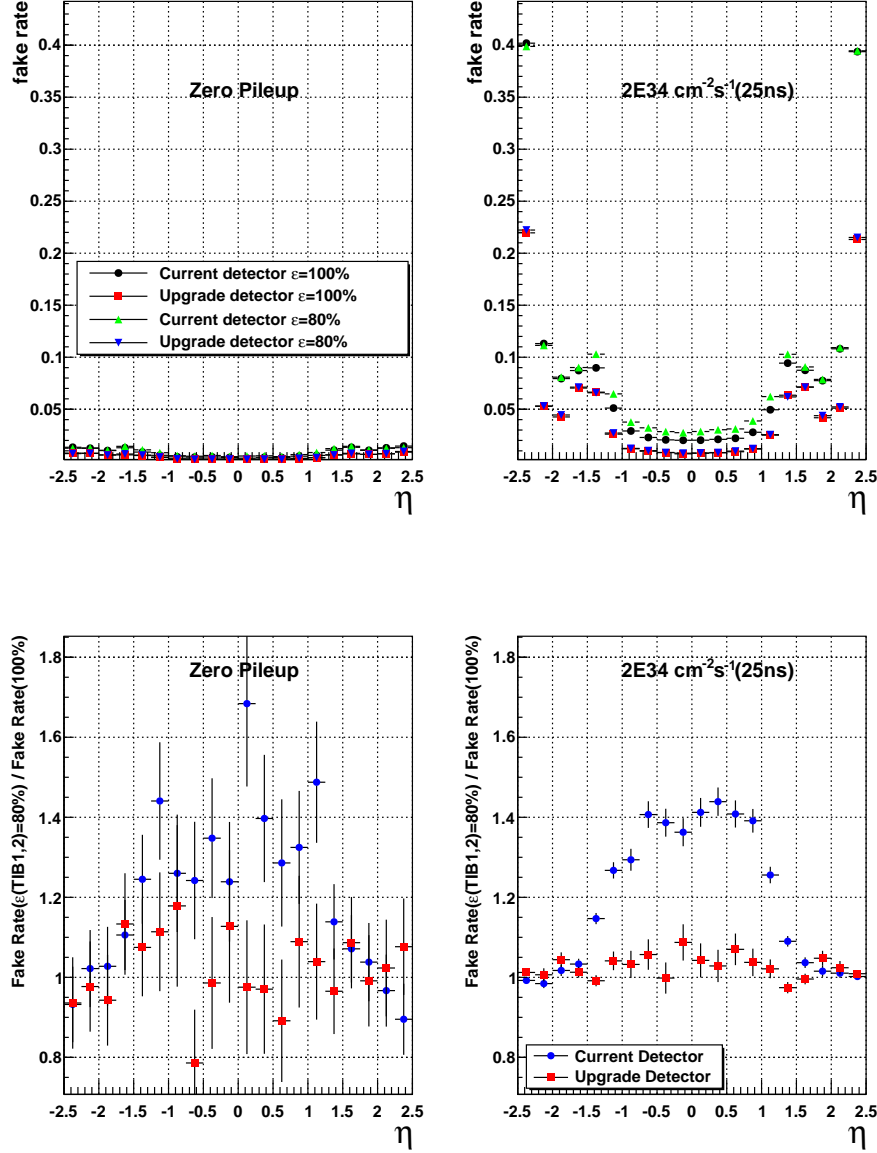


Figure 2.23: Track fake rates as a function of η for default tracks in a $t\bar{t}$ sample with (left) zero pileup, and (middle-left) an average pileup of 50. Results are shown for the current detector (black circles, green triangles), and the upgrade detector (red squares, blue inverted triangles); with TIB1 and TIB2 at 100% efficiency (black circles, red squares), and with TIB1 and TIB2 at 80% efficiency (green triangles, blue inverted triangles). Ratio of the track fake rates with TIB1 and TIB2 at 80% efficiency to the track fake rates with TIB1 and TIB2 at 100% efficiency as a function of η for default tracks in a $t\bar{t}$ sample with (middle-right) zero pileup, and (right) an average pileup of 50. Results are shown for the current detector (blue circles), and the upgrade detector (red squares).

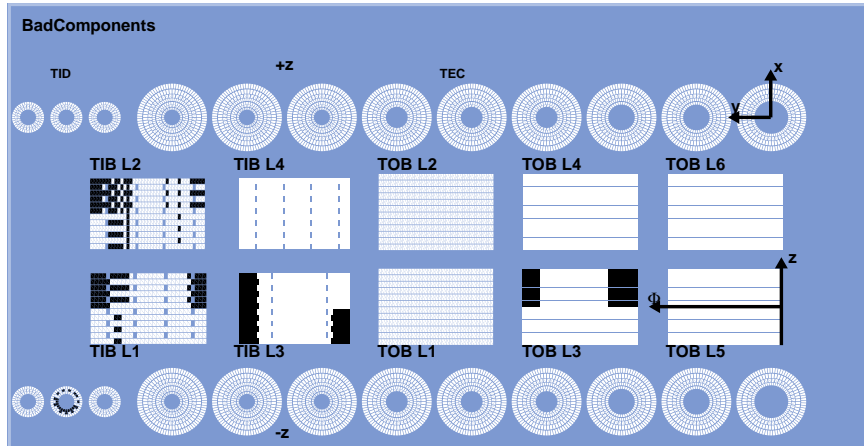


Figure 2.24: A CMS “Tracker Map” showing modules in black that are expected to degrade in performance in the future.

tuning of the tracking. What is clear for the tracking is that in general higher pileup leads to longer CPU processing times and a higher rate of fake tracks. Some tuning of the algorithms can be done to mitigate both of these but usually at the expense of lower track reconstruction efficiency. With the track tuning that is able to handle 2012 data, simulation studies for which the ROC data loss was not implemented show that the pileup conditions for $2 \times 10^{34} \text{ cm}^{-2}\text{s}^{-1}$ (25 ns crossing time) by itself would cause a 7.3% (4.7%) loss of tracking efficiency for muons ($t\bar{t}$) in the current pixel detector. The extra pixel layer in the upgrade detector adds information that reduces this loss in efficiency by more than half to 3.2% (1.3%) for muons ($t\bar{t}$). The extra pixel layer also decreases the track fake with the upgrade detector by a factor of two compared to the current detector, and makes the upgrade detector much more robust to degradations in the outer tracker strip detector or in the inner pixel barrel layer. The high pileup worsens somewhat the IP and PV resolutions but the effect is much smaller than that caused by the dynamic data loss in the pixel detector. Again the extra pixel layer in the upgrade pixel detector, coupled with the inner layer 1.4 cm closer to the interaction point, improves both the IP and PV resolution compared to the current pixel detector. The lower material of the upgrade detector means that the IP resolution is vastly improved for low momentum tracks.

The b-tagging performance is used to illustrate the degradation in tracking performance due to both the effect of dynamic data loss at $2 \times 10^{34} \text{ cm}^{-2}\text{s}^{-1}$ and the large pileup in the current detector. Compared to low pileup and at a light quark jet b-mistag rate of 1% the b-tagging efficiency for b-jets is worse by a relative 28% at $2 \times 10^{34} \text{ cm}^{-2}\text{s}^{-1}$ (25 ns crossing time). At a light quark jet b-mistag rate of 0.1% the b-tagging efficiency for b-jets is degraded even more by a relative 46%. The b-tagging performance of the upgrade detector is already better compared to the current detector at low pileup and at high pileup the degradation is much smaller so that the b-tagging performance for the upgrade pixel detector at $2 \times 10^{34} \text{ cm}^{-2}\text{s}^{-1}$ (25 ns crossing time) is comparable to the current detector at low pileup, and better than the current detector operating at current 2012 conditions. The upgrade detector therefore recovers the low pileup b-tagging performance at the high pileup conditions of $2 \times 10^{34} \text{ cm}^{-2}\text{s}^{-1}$ (25 ns crossing time).

2.3 Performance for Physics

The basic improvements to tracking, vertexing and b-tagging have been shown to be substantial. In an effort to quantify potential gains from such improvements on our physics program,

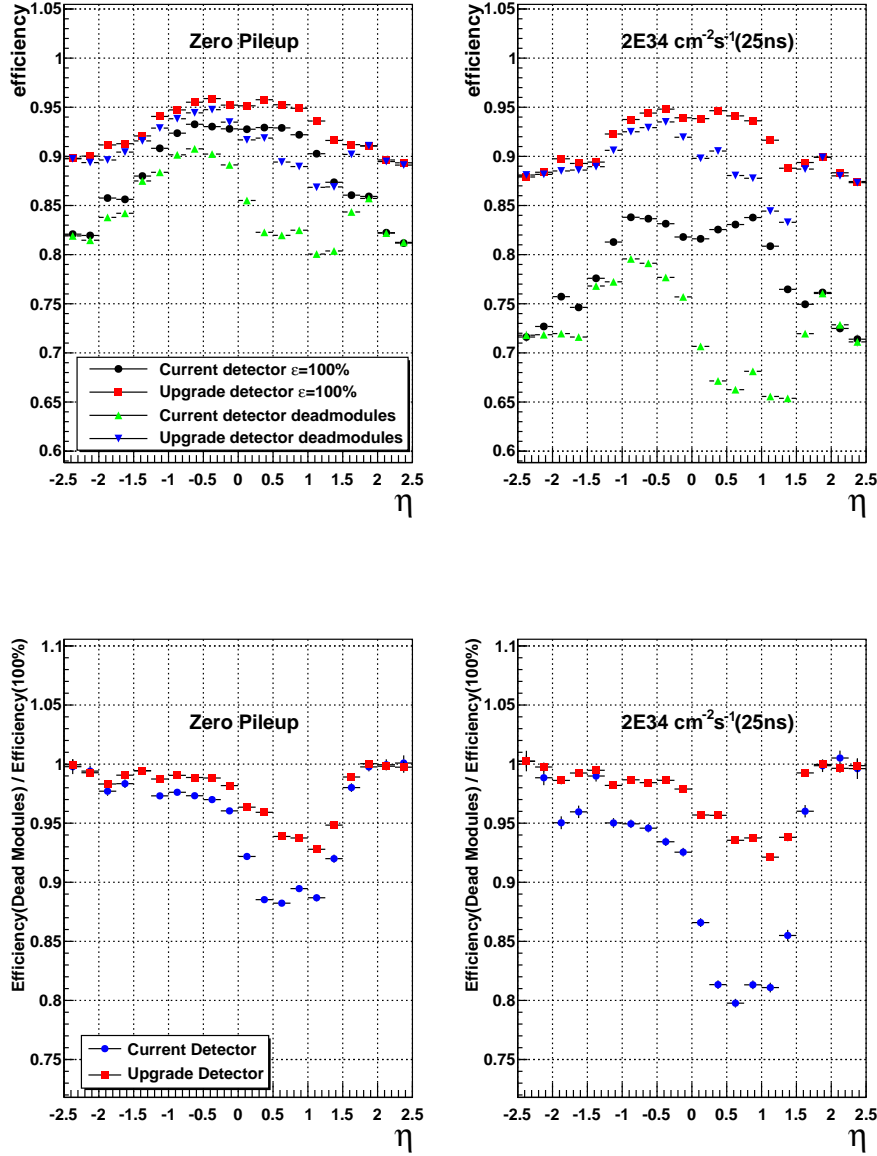


Figure 2.25: Tracking efficiency as a function of η for default tracks in a $t\bar{t}$ sample with (left) zero pileup, and (middle-left) an average pileup of 50. Results are shown for the current detector (black circles, green triangles), and the upgrade detector (red squares, blue inverted triangles); with Tracker modules at 100% efficiency (black circles, red squares), and with dead Tracker modules as explained in the text (green triangles, blue inverted triangles). Ratio of the tracking efficiencies with dead Tracker modules to the tracking efficiency with Tracker modules at 100% efficiency as a function of η for default tracks in a $t\bar{t}$ sample with (middle-right) zero pileup, and (right) an average pileup of 50. Results are shown for the current detector (blue circles), and the upgrade detector (red squares).

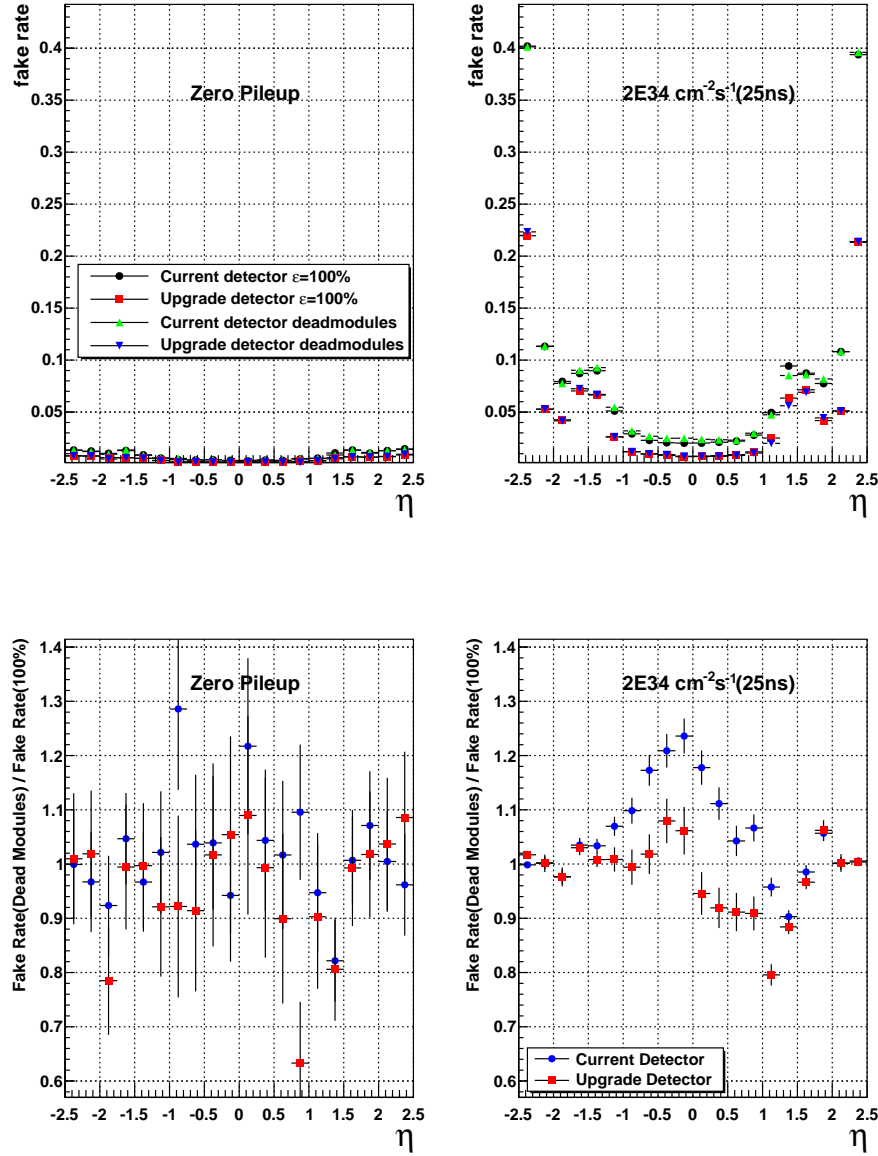


Figure 2.26: Track fake rate as a function of η for default tracks in a $t\bar{t}$ sample with (left) zero pileup, and (middle-left) an average pileup of 50. Results are shown for the current detector (black circles, green triangles), and the upgrade detector (red squares, blue inverted triangles); with Tracker modules at 100% efficiency (black circles, red squares), and with dead Tracker modules as explained in the text (green triangles, blue inverted triangles). Ratio of the track fake rates with dead Tracker modules to the track fake rate with Tracker modules at 100% efficiency as a function of η for default tracks in a $t\bar{t}$ sample with (middle-right) zero pileup, and (right) an average pileup of 50. Results are shown for the current detector (blue circles), and the upgrade detector (red squares).

we have studied the relative performance of the current pixel detector and the upgrade in the high luminosities expected in later 14 TeV running with 50 pile-up events per crossing. The upgrade and the current pixel detectors are simulated with the previous data losses¹ for the 50 pileup event scenario. We produced samples of signal events and some backgrounds for a representative set of physics analyses: associated Higgs production $ZH \rightarrow \ell^+ \ell^- b \bar{b}$; the $H \rightarrow ZZ$ channel for $Z \rightarrow \mu^+ \mu^-, e^+ e^-$; searches for fully hadronic events with large missing energy and b-jets which are sensitive to SUSY scenarios with heavy squarks and light gluinos; and SUSY searches for events with large missing energy and two high p_T photons.

These are important components of the current CMS physics program at 7 TeV and 8 TeV running. To properly prepare these analyses for running conditions at 14 TeV with 50 pile-up events will take reoptimization of the both the analyses themselves and the reconstructed physics objects used by them. Such improvements will take place, but are beyond the scope of these studies for this report. Instead, we evaluate the improvements from the upgraded pixel detector by using today's analyses optimized for 7-8 TeV running and apply them to the two scenarios of using the current detector versus using the upgrade. In this way, we learn what kind of improvements we should expect in the future and roughly to what level they would benefit us.

2.3.1 Associated Higgs Production

The study of ZH with the Z decaying to muons and the Higgs boson to $b \bar{b}$ will benefit significantly from the increased muon tracking efficiency and b tagging. A similar analysis with the Z decaying to electrons will in addition benefit from the decreased material in the tracking volume. Second order effects such as improved particle flow and charged hadron subtraction will also undoubtedly benefit, although these are harder to quantify.

To demonstrate the improvement expected in the $ZH \rightarrow \ell^+ \ell^- b \bar{b}$ ($\ell = \mu, e$) channel, a study was conducted using full Monte Carlo simulation. Samples were produced using the $\overline{\text{PU}} = 50$ events scenario and the expected ROC inefficiencies shown in table 2.1.

Although studies of a Higgs-like boson will have moved from discovery to measurement by the time the upgraded pixel detector will be running, this would require a completely reworked analysis. As such the analysis currently used on data, with some minor changes, was applied to the new samples to get an estimate of the signal yield for both the current detector and the upgraded detector. These limitations, and the fact that an actual analysis for either scenario considered would be much more highly tuned, mean that this study cannot be taken as an indication of the absolute sensitivity, but can only be used to quantify the relative difference between each detector.

Finally, we estimate the expected gain in sensitivity for the dimuon channel assuming the efficiency gain we have measured.

2.3.1.1 Analysis

The current 4.7 fb^{-1} $ZH \rightarrow \ell^+ \ell^- b \bar{b}$ analysis[19] uses boosted decision trees to get the highest possible sensitivity, but also has a simpler cut based approach as a cross check. It is this cut based approach that is being applied for the upgrade study. Note that the more recent ICHEP 2012 analysis[20] drops the cut based cross check and so was not referred to during this study. The approach starts with the normal CMS particle flow reconstruction sequence[21], but with lepton isolation relaxed. Lepton isolation had not been tuned for the simulated beam condi-

¹No other losses, such as TIB modules or further degradations in the BPix, are considered for these studies

tions, and since it was not central to the aims of the study it was simply relaxed to allow study of the rest of the analysis.

Leptons and jets are required to have $p_T > 20$ GeV, and candidate events with at least two jets and two leptons are extracted. A Higgs boson candidate is created using the di-jet combination with the highest vectorially combined p_T , and Z boson candidate created using the two oppositely charged leptons with highest p_T . In the electron channel and muon channel both leptons are required to be of the respective flavor. The Z boson candidate is required to have an invariant mass between 75 GeV and 105 GeV.

Requiring highly boosted events improves background reduction and so both the boson candidates are required to have $p_T > 100$ GeV. Since the Z and Higgs bosons should also be produced back to back, a cut of 2.9 is applied on the difference in the ϕ angle between the two candidates.

The jets from the Higgs candidate are tagged using the Combined Secondary Vertex (CSV) algorithm (described in Section 2.1.3). The results from the studies in Section 2.2.4 were used to choose CSV discriminators that result in a fixed light jet mistag efficiency for each of the detectors. The highest tagged Higgs candidate jet is required to pass a 0.1% light mistag discriminator, and the other jet is required to pass a 1% light mistag discriminator.

The published analysis also applies cuts on the Higgs candidate mass and the number of jets other than those in the Higgs candidate. However, jet energy corrections have not been tuned for running at 14 TeV with high pile-up. Both variables were found to be much higher than expected and need further study. Since these quantities are unrelated to the items under study, performance was assessed without these cuts.

The reconstructed Z boson mass was also found to be slightly high (approximately 2 GeV) in the electron channel. This is a known effect from pile-up that has corrections based on measurements in data. Since the shift is small, no correction was applied rather than an arbitrary untuned correction.

2.3.1.2 Estimate of the HLT impact

Any increased efficiency from the High Level Trigger (HLT) will of course benefit the analysis. Whilst not the direct responsibility of this study, since it is a detailed study in itself, an estimate of the improvement from the HLT is possible. The HLT runs pixel only tracking, because anything more complex is too processor intensive to run in the required trigger decision time. Pixel only tracking requires at least 3 pixel hits to form a track, and hence a muon with fewer than 3 pixel hits would not be triggered on in the HLT. Requiring that both muons from the Z have at least 3 pixel hits can give an indication of the double muon trigger efficiency; requiring this for one muon can give an indication of the single muon trigger efficiency.

2.3.1.3 Comparative Results

The starting point for the analysis is the identification of two leptons - unless both leptons from the Z boson are found, the event is rejected. Figure 2.27 shows the number of electrons or muons found in the respective $ZH \rightarrow e^+e^-b\bar{b}$ or $ZH \rightarrow \mu^+\mu^-b\bar{b}$ sample for the two detectors.

In both samples the upgraded detector reconstructs more events with both leptons, with the muon channel being more efficient. Note that no tuning of the complex electron reconstruction was performed for the more challenging beam conditions, so with further study the electron efficiency would be expected to improve.

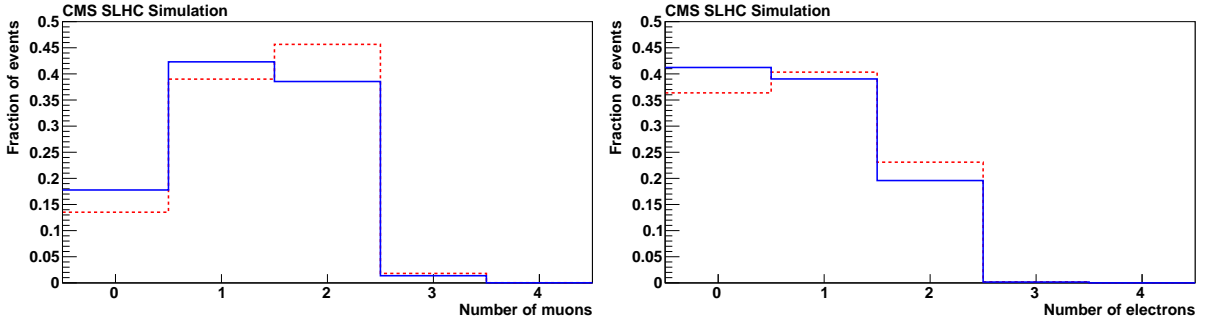


Figure 2.27: The fraction of events with a given number of muons in the $ZH \rightarrow \mu^+\mu^-b\bar{b}$ sample (left); and electrons in the $ZH \rightarrow e^+e^-b\bar{b}$ sample (right). Current detector is in solid blue and the Phase-1 upgrade is in dashed red. All quality cuts have been applied but the isolation has been loosened as described in the text.

The ratio of the number of events left after each cut in the muon channel is shown in Figure 2.28, as the number of upgrade events divided by the number of current detector events. For the electron channel, this ratio is shown in Figure 2.29.

The improvement from the upgraded detector is roughly similar between the two channels, with both showing approximately 65% more signal events with the upgraded detector than the current detector. The big improvement gains are from the number of candidate events of the correct type (i.e. where the leptons have been correctly reconstructed) and in the b-tagging as expected. There are also noticeable improvements from the di-jet p_T cut and the $\Delta\phi$ cut which were not foreseen. After initial study it was found that the analysis with the upgraded detector assigns the correct jets to the Higgs candidate more often. Although this explains the increased performance of the di-jet p_T and $\Delta\Phi$ cuts, exactly why this happens is currently the subject of further investigation.

When looking at the improvement including the single HLT muon trigger estimate, the upgraded detector was found to have approximately 75% more signal. With the double muon trigger estimate there were approximately 175% more signal events. In both cases the trigger estimate appears uncorrelated with the other cuts. This dramatic increase is because the upgraded detector is barely affected by the three pixel hit requirement, so the numerator in the ratio is almost unchanged.

2.3.1.4 Conclusions

The upgraded detector produces significantly increased signal yield in both electron and muon channels, although further work is required to check whether backgrounds remain under control. In addition, variables such as the additional jet activity and di-jet mass need to be understood.

The double muon trigger estimate appears to be quite dramatic, although this should be tempered with the fact that there are other possible ways to improve trigger efficiency and this test plays to the strengths of the upgrade. In any case, the current analysis does not use a double muon trigger. This should be seen as a windfall, rather than a justification in itself.

The increased signal efficiencies will lead to increased sensitivities. For example, if we pessimistically assume that the backgrounds scale at the same rate as the increase in signal efficiency, then for 300 fb^{-1} at 14 TeV the $ZH \rightarrow \mu^+\mu^-b\bar{b}$ measurement will go from a significance of 3.6σ to 4.9σ . In other words, with the same amount of integrated luminosity, this subchannel

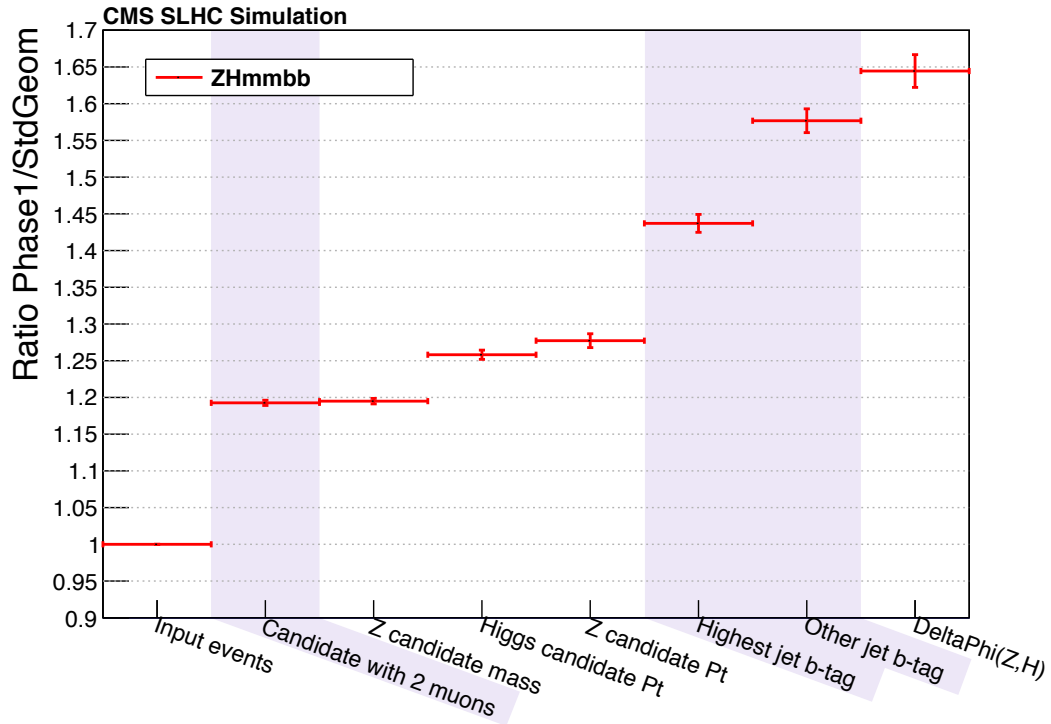


Figure 2.28: The ratio Phase-1 /current of the number of events left after each cut. Values greater than 1 show increased efficiency for the Phase-1 upgrade and vice versa. The cuts where the upgraded detector is expected to excel are highlighted.

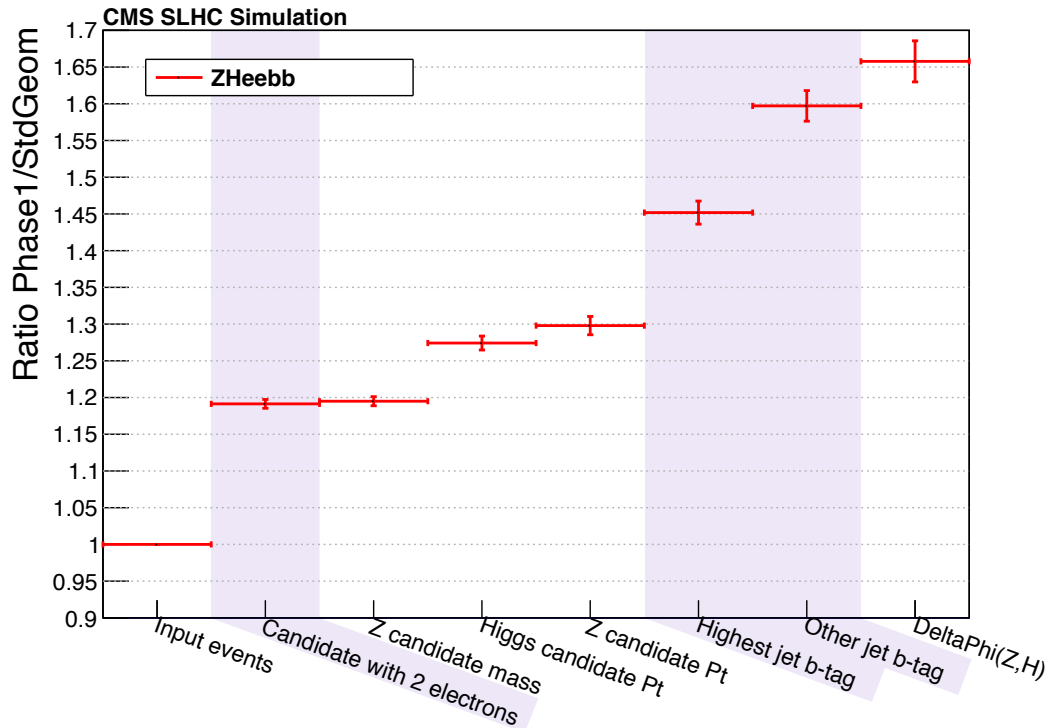


Figure 2.29: The ratio Phase-1 /current of the number of events left after each cut in the electron channel. The cuts where the upgraded detector is expected to excel are highlighted.

would become an observation with the upgraded detector.

Although limited in complexity, this study shows that the proposed pixel detector upgrade would bring dramatic benefits to the measurement capabilities of CMS in the $ZH \rightarrow \ell^+ \ell^- b\bar{b}$ analysis.

2.3.2 $H \rightarrow ZZ$

This study aims to evaluate the change in performances of the analysis used for the Higgs boson search in the $H \rightarrow ZZ \rightarrow 4l$ ($l = e, \mu$) channel. The analysis is optimized for the search of a Higgs boson in the mass range $110 \text{ GeV} < m_H < 160 \text{ GeV}$ for center-of-mass energies of 7-8 TeV. The analysis has not been optimized to the different beam conditions under which the pixel upgrade will be operated, namely a higher center-of-mass energy of 14 TeV and larger pile-up. As a benchmark, we have used a Higgs boson MC sample with $m_H = 125 \text{ GeV}$. The search essentially relies on the reconstruction and identification of leptons well isolated from other particles in the event. One or both Z bosons can be off-shell.

2.3.2.1 Analysis

Two dedicated simulated Higgs boson samples (both with $m_H = 125 \text{ GeV}$) have been used for this study: $gg \rightarrow H \rightarrow ZZ$ with $Z \rightarrow \ell^+ \ell^-$ for the current pixel detector and for the upgrade at $\overline{\text{PU}} = 50$.

The 2012 reference analysis [22, 23] has been used, but a few simple modifications were necessary due to the different beam conditions. In an attempt to quantify the benefit arising from a fourth layer of pixels to the triggering of events, we have required some additional trigger conditions. Normally, in order to trigger an event, at least two leptons are required to have respectively $p_T^l > 17 \text{ GeV}$ and $p_T^l > 8 \text{ GeV}$. In this study, we have additionally required that these leptons must have a minimum number of hits in the Pixel detector: $N_{\text{PixelHits}} > 2$. In the 2012 reference analysis, a complete reconstruction of the individual particles is obtained via the particle flow (PF) technique. This technique uses the information from all CMS sub-detectors to identify and reconstruct the particles emerging from each collision. Electrons are reconstructed within the geometrical acceptance $|\eta^e| < 2.5$ and for $p_T^e > 7 \text{ GeV}$. The reconstruction combines the information from the clusters of energy deposits in the ECAL and the trajectory in the inner tracker. In particular, the trajectories are fitted with a Gaussian sum filter. Their identification relies on a multivariate technique which combines observables sensitive to the amount of bremsstrahlung along the electron trajectory, the geometric and momentum matching between the electron trajectory and the associated clusters, as well as shower-shape observables is used. Muons are reconstructed within $|\eta^\mu| < 2.4$ and for $p_T^\mu > 5 \text{ GeV}$. The reconstruction combines the information from the silicon tracker and the muon spectrometer. The PF muons are selected among the reconstructed muon track candidates by applying minimal requirements on the track components in the muon system and taking into account a matching with small energy deposits in the calorimeters.

One key distinction between signal and background leptons is the amount of energy in the nearby vicinity – signal leptons tend to be isolated, while leptons from hadron decay are immersed in jets leaving substantial energy depositions nearby. The isolation depends on the pile-up scenario, thus the isolation criteria used in the published reference selection was modified to study higher pile-up scenarios. Figure 2.30 contrasts the isolation distributions for the reference analysis and the scenario considered in the upgrade study for $H \rightarrow ZZ \rightarrow 4\mu$, justifying moving the cut from 0.4 in the reference analysis to 5.0 in the current study.

The electron and muon pairs from Z decays should originate from the primary vertex. This is

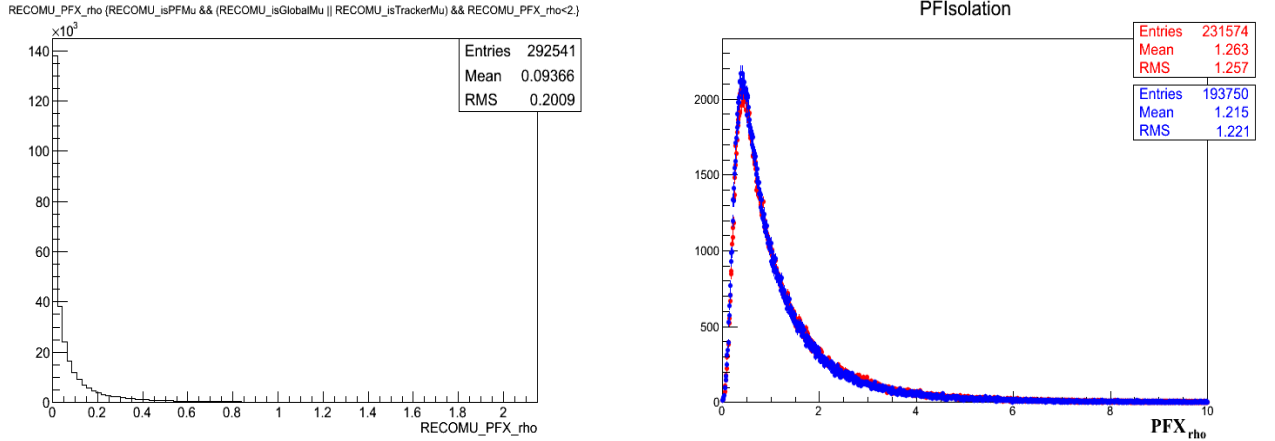


Figure 2.30: Isolation variable distribution, for muons (in the $H \rightarrow 4\mu$ channel analysis). Left: Higgs boson Monte Carlo sample, with $m_H = 120$ GeV, at $\sqrt{s} = 7$ TeV. Right: Higgs boson MC sample, with $m_H = 125$ GeV, at $\sqrt{s} = 14$ TeV; in blue, for the current detector; in red, the Phase 1 Pixel detector scenario. Plots are normalized to the number of entries in the Phase 1 Pixel detector scenario.

ensured by requiring that the significance of the impact parameter to the event vertex, $SIP_{3D} = \frac{IP}{\sigma_{IP}}$ satisfies $|SIP_{3D}| < 4$, for each lepton. The IP is the lepton impact parameter in three dimensions at the point of closest approach with respect to the primary interaction vertex and σ_{IP} is the associated uncertainty.

Using well identified and isolated leptons, a 4ℓ candidate is then selected. The lepton isolation requirements suppress the Z +jet, $Zb\bar{b}$ and $t\bar{t}$ backgrounds. The requirement on the significance of the impact parameter to the event vertex further suppresses the $Zb\bar{b}$ and $t\bar{t}$ backgrounds. When building the Z candidates, a Z candidate is formed by a pair of leptons with the same flavor and opposite charge (l^+l^-). The lepton pair with the invariant mass closest to the nominal Z mass is denoted Z_1 and it is required to have $40 \text{ GeV} < m_{Z_1} < 120 \text{ GeV}$. Then, considering all remaining leptons, a second l^+l^- pair, with mass denoted m_{Z_2} , is required to satisfy $12 \text{ GeV} < m_{Z_2} < 120 \text{ GeV}$. The 12 GeV cut provides an optimal sensitivity for a Higgs boson mass hypothesis in the range $110 \text{ GeV} < m_H < 160 \text{ GeV}$. If more than one Z_2 candidate satisfies all the criteria, the ambiguity is resolved by choosing the lepton pair with highest p_T . Among the four selected leptons forming the two Z candidates, at least one should have $p_T > 20 \text{ GeV}$ and another one should have $p_T > 10 \text{ GeV}$. To reduce the background from leptons originating from hadronic decays in jet fragmentation, or from the decay of low mass hadronic resonances, it is required that any opposite charge lepton pair chosen among the four selected leptons (irrespective of flavour) satisfies $m_{l^+l^-} > 4 \text{ GeV}$. The phase space for the search for the SM Higgs boson is finally defined by restricting the mass range to $m_{4\ell} > 100 \text{ GeV}$.

2.3.2.2 Comparative Results

The Phase-1 pixel detector consists of four successive layers of sensors, one more than the current detector. This implies that the average number of hits for each track in the upgrade detector is expected to change from three (as it is in the current detector scenario) to four. This is clearly visible in Figure 2.31.

The Phase-1 pixel detector significantly improves the impact parameter (IP) measurement of the individual leptons, with respect to the current detector. This improves the vertex assignment, as well as the vertex reconstruction itself. In particular, the vertex assignment is crucial

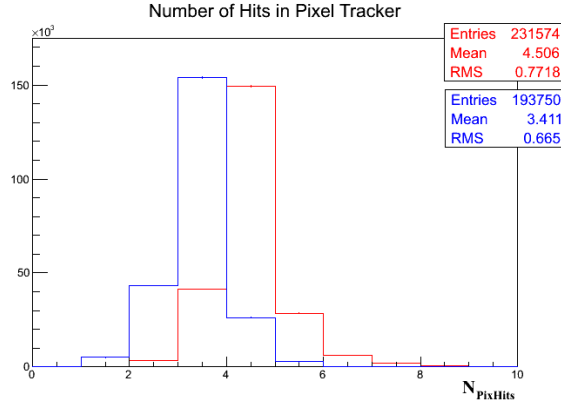


Figure 2.31: Number of hits in the pixel detector, for individual muon tracks (in the $H \rightarrow 4\mu$ channel analysis). In blue, the current detector scenario; in red, the Phase 1 Pixel detector scenario. Plots are normalized to the number of entries in the Phase 1 Pixel detector scenario.

for this analysis, since individual leptons are required to originate from the primary vertex and they are required to satisfy $|SIP_{3D}| = \frac{IP}{\sigma_{IP}} < 4$. The improvement is significant, as is visible in Figure 2.32, with reductions of 50% in the RMS.

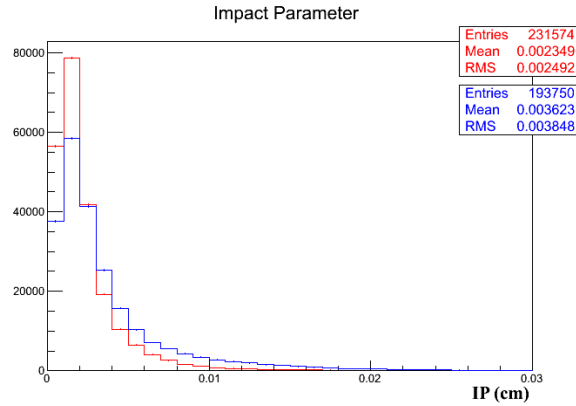


Figure 2.32: Reconstructed IP of single muons (in the $H \rightarrow 4\mu$ channel analysis). In blue, the current detector scenario; in red, the Phase 1 Pixel detector scenario. Plots are normalized to the number of entries in the Phase 1 Pixel detector scenario.

The distributions of the perpendicular and the longitudinal distances (D_{xy} and D_z respectively) of the individual tracks from the primary vertex (PV), for each collision event (Figure 2.33), also greatly benefit from the Phase 1 Pixel detector.

The tracking improvements due to the introduction of the Phase 1 Pixel detector provide a significant increase in the number of leptons passing all the selection requirements. This is shown in Figure 2.34. In a large fraction of the events, the number of selected leptons increases to four. Since we are looking for a $4l$ candidate, this improvement determines a significant efficiency gain, with respect to the current detector. This is visible in the m_{Z_1} distribution, shown in Figure 2.35. In the 2012 reference analysis, m_{Z_1} is required to be in the range $40 \text{ GeV} < m_{Z_1} < 120 \text{ GeV}$. Since in the Phase 1 Pixel detector scenario, a larger fraction of events pass this requirement, this improvement provides an efficiency gain, with respect to the current detector.

All the improvements described above, due to the introduction of the Phase 1 Pixel detector, with respect to the current detector scenario, lead to an important gain in signal efficiency, at the end of the analysis selection chain. The efficiency ratios, for every step of the analysis, are

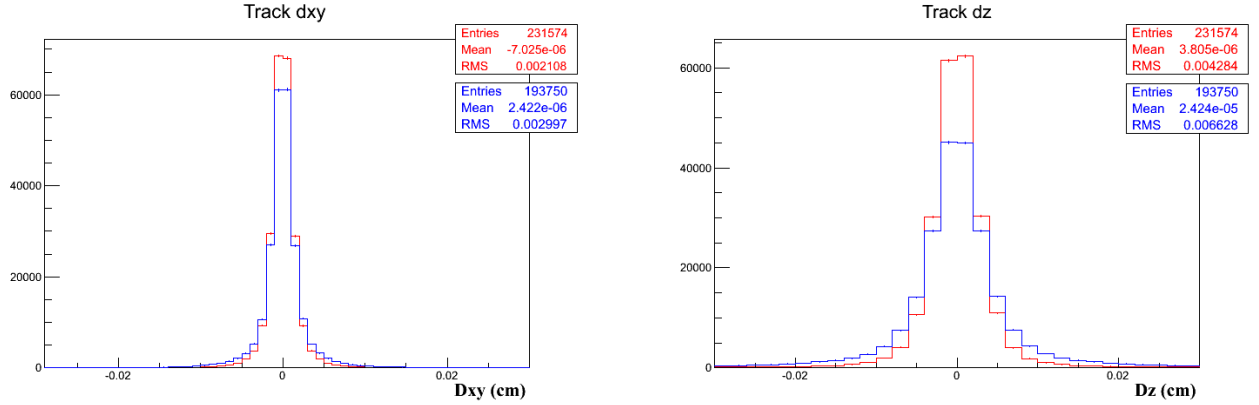


Figure 2.33: Left: distribution of the 2D perpendicular distances of the muon tracks (in the $H \rightarrow 4\mu$ channel analysis). Right: distribution of the longitudinal distances of the same muon tracks. In blue, the current detector scenario; in red, the Phase 1 Pixel detector scenario. Plots are normalized to the number of entries in the Phase 1 Pixel detector scenario.

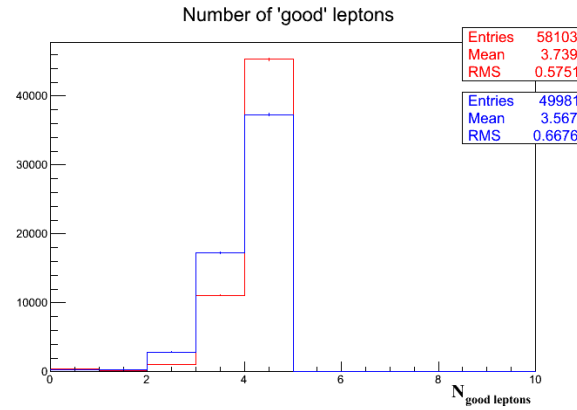


Figure 2.34: Number of muons passing all selection requirements, (in the $H \rightarrow 4\mu$ channel analysis). In blue, the current detector scenario; in red, the Phase 1 Pixel detector scenario. Plots are normalized to the number of entries in the Phase 1 Pixel detector scenario.

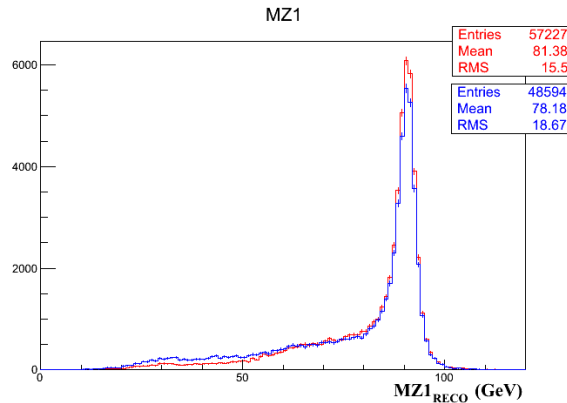


Figure 2.35: Distribution of m_{Z_1} (in the $H \rightarrow 4\mu$ channel analysis). In blue, the current detector scenario; in red, the Phase 1 Pixel detector scenario. Plots are normalized to the number of entries in the Phase 1 Pixel detector scenario.

shown by the cut flow charts in Figure 2.36 for the $H \rightarrow 4\mu$ channel, in Figure 2.37 for the $H \rightarrow 4e$ channel and in Figure 2.38 for the $H \rightarrow 2e2\mu$ channel.

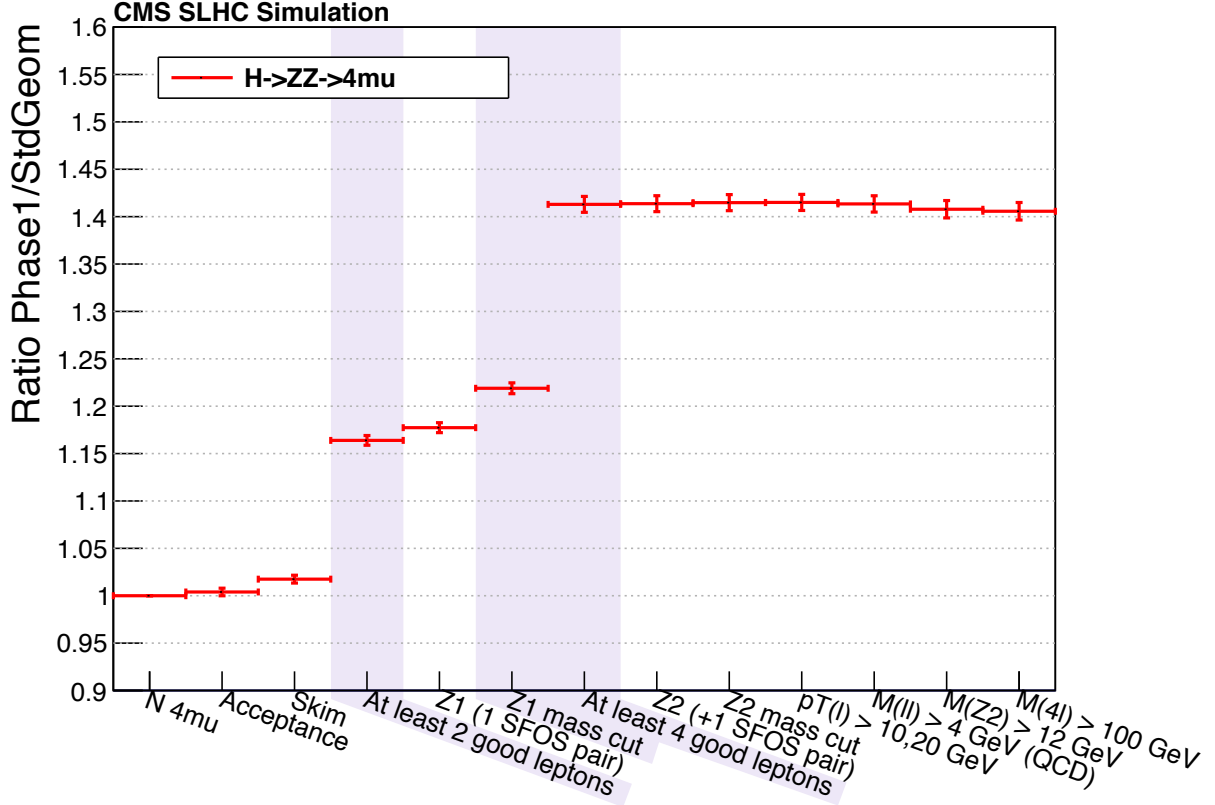


Figure 2.36: Cut flow chart for the $H \rightarrow 4\mu$ channel. The ratio of the numbers of events selected with the Phase-1 upgrade detector and the ones selected with the current detector is plotted with $\overline{\text{PU}} = 50$.

A gain in selection efficiency of $\sim 41\%$ is obtained in the $H \rightarrow 4\mu$ channel, of $\sim 51\%$ in the $H \rightarrow 4e$ channel and of $\sim 48\%$ in the $H \rightarrow 2e2\mu$ channel. A summary of efficiencies obtained in both scenarios (upgrade detector versus current detector) is reported in Table 2.4.

Table 2.4: Efficiencies for the $H \rightarrow ZZ \rightarrow 4l$ analysis, with the upgrade detector and with the current detector in the $\overline{\text{PU}} = 50$ scenario. The efficiency gain is given by the ratio of the two efficiencies.

Channel	Overall Efficiency		Efficiency gain
	Phase 1 Pixels	Current Pixels	
$H \rightarrow 4\mu$	$(36.0 \pm 0.2)\%$	$(25.6 \pm 0.2)\%$	1.41
$H \rightarrow 4e$	$(18.7 \pm 0.2)\%$	$(12.4 \pm 0.1)\%$	1.51
$H \rightarrow 2e2\mu$	$(25.9 \pm 0.1)\%$	$(17.5 \pm 0.1)\%$	1.48

The larger number of selected candidates might negatively affect the m_{4l} distribution. This distribution, in both scenarios (with and without upgrade), is shown in Figure 2.39. However, the distribution look very much the same in the two cases, despite the much larger number of candidates selected in the upgrade scenario.

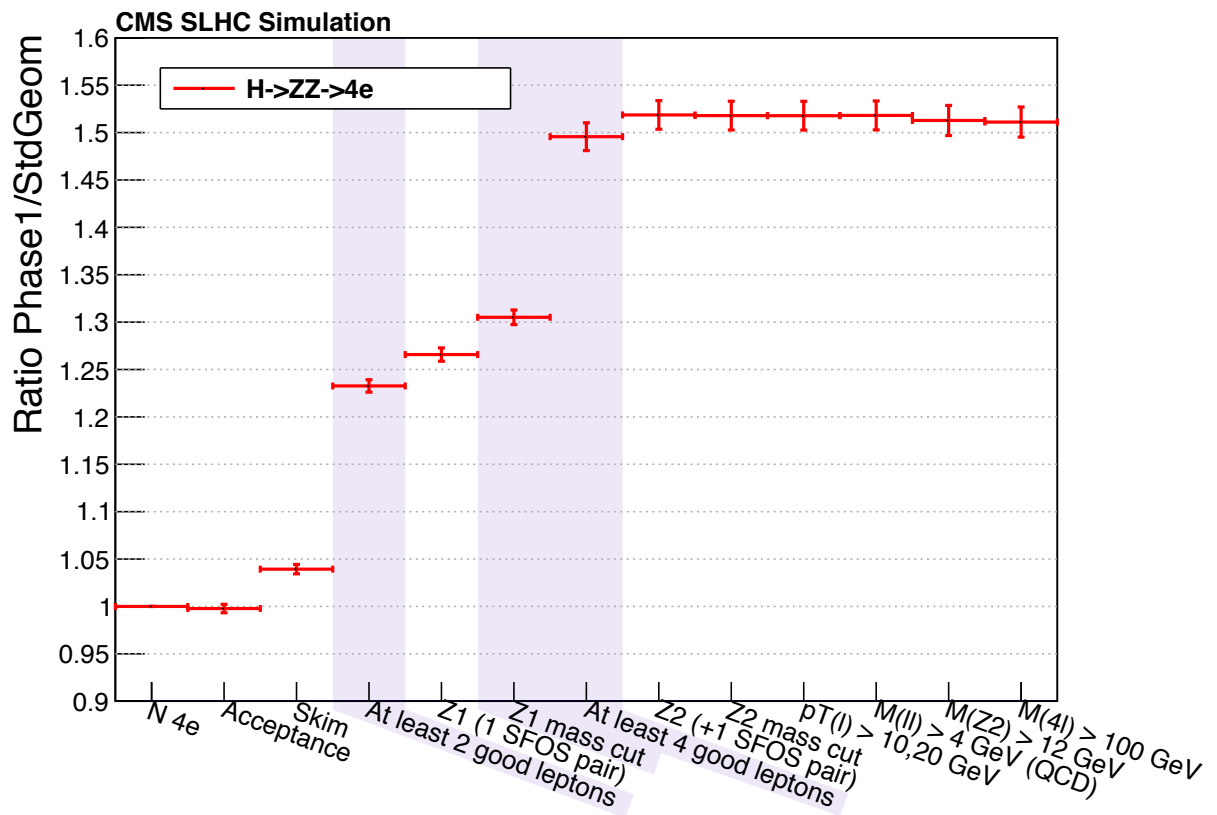


Figure 2.37: Cut flow chart for the $H \rightarrow 4e$ channel. The ratio of the numbers of events selected with the Phase-1 upgrade detector and the ones selected with the current detector is plotted with $\overline{\text{PU}} = 50$.

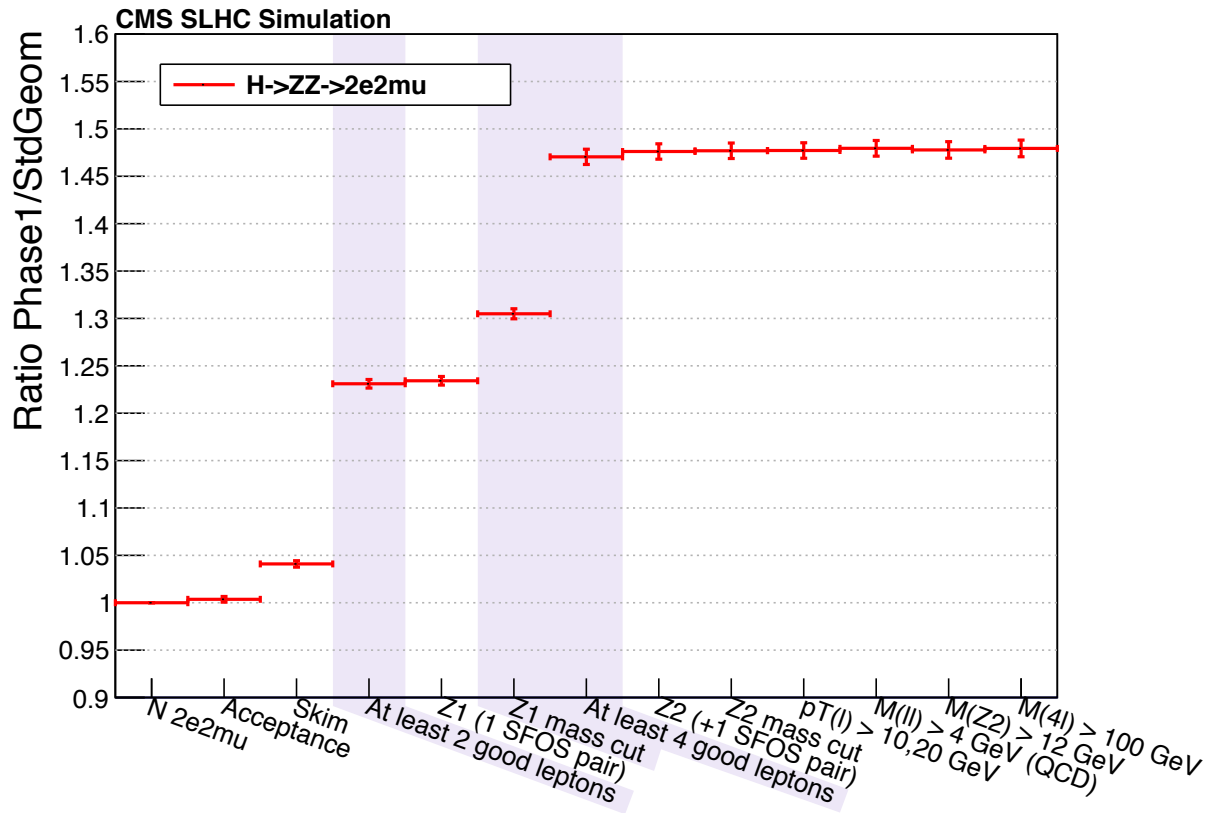
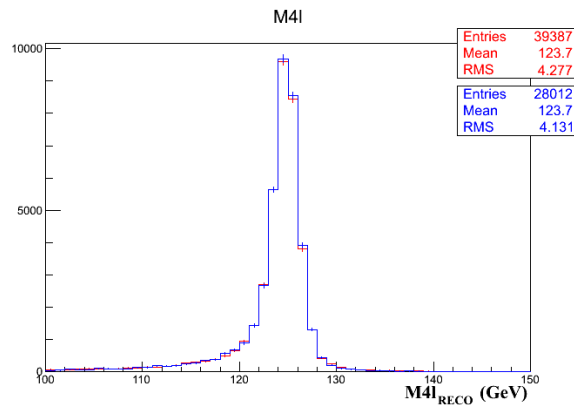


Figure 2.38: Cut flow chart for the $H \rightarrow 2e2\mu$ channel. The ratio of the numbers of events selected with the Phase-1 upgrade detector and the ones selected with the current detector is plotted with $\overline{\text{PU}} = 50$.

Figure 2.39: Distribution of m_{4l} (in the $H \rightarrow 4\mu$ channel analysis), in a Higgs boson Monte Carlo sample, with $m_H = 125$ GeV, at $\sqrt{s} = 14$ TeV. In blue, the current detector scenario; in red, the Phase 1 Pixel detector scenario; plots are normalized to the number of entries in the Phase 1 Pixel detector scenario. The distribution looks identical in the two cases, despite the much higher number of candidates collected in the upgrade scenario.



2.3.2.3 Conclusions

The upgrade detector is expected to significantly improve the reconstruction of the impact parameter of the individual leptons. This improvement is therefore expected to benefit the $H \rightarrow ZZ \rightarrow 4l$ ($l = e, \mu$) analysis, in all the lepton channels. In particular, the number of selected leptons in each event is seen to significantly increase, resulting in a better reconstruction of the Z candidates and finally in an absolute gain of selection efficiency varying from $\sim 41\%$ to $\sim 51\%$, with respect to the current pixels scenario. Moreover, the distribution of the Higgs candidates mass (m_{4l}) does not change, despite the larger number of collected candidates. Therefore, in the upgrade scenario, one is expected to reach the same results as in the current one, but with a significantly lower (from $\sim 41\%$ to $\sim 51\%$) integrated luminosity.

2.3.3 Supersymmetric Particle Search Using the M_{T2} variable and B-Tagging

In this study, the supersymmetric transverse mass distribution, M_{T2} , is studied using a signal sample as well as a $t\bar{t}$ sample which is the dominant background of the $M_{T2}b$ analysis for a center-of-mass energy of 14 TeV. The yields resulting from the current geometry are compared to those of the new geometry with the pixel detector replaced as proposed. It is shown that the signal selection efficiency would increase if the new pixel detector was implemented due to the much improved b-tagging, which is central to this analysis of supersymmetric particles. The same $\overline{\text{PU}} = 50$ scenario as used by the other analyses is considered here.

2.3.3.1 Analysis

The M_{T2} analysis is a search for new physics such as supersymmetry (SUSY) [24] with R-parity conservation, that manifests itself in a fully hadronic final state accompanied by a large missing transverse momentum (E_T^{miss}). The search uses the supersymmetric transverse mass (stransverse) variable M_{T2} . M_{T2} is the natural extension of the classical transverse mass M_T to the case of supersymmetry where two colored sparticles are pair-produced and both decay through a cascade of jets and possibly leptons to the Lightest Supersymmetric Particle (LSP). The LSP is not visible in the detector and leads to a missing transverse momentum signature. M_{T2} is used here purely as discovery variable which is found to be very sensitive to the presence of new SUSY-like physics. Indeed, the distribution of M_{T2} reflects the produced particle masses and these are much lighter for the standard model background processes than for the SUSY processes we are looking for. Hence, new physics is expected to show up as an excess in the tail of M_{T2} .

The target of this search is the observation of supersymmetric events dominated by gluino-gluino production where the gluinos giving rise to 3-body decays with relatively small E_T^{miss} . The events could be rich in b quarks since the stop and sbottom squarks, whose virtual exchange mediate the gluino decay, are expected to be lighter than the first and second generation squarks. The requirement of at least one b-tagged jet thus keeps a high signal efficiency.

The variable M_{T2} , called stransverse mass, was introduced [25, 26] to measure the mass of primary pair-produced particles in a situation where both ultimately decay into undetected particles (e.g. neutralino LSPs) leaving the event kinematics underconstrained. It assumes that the two produced sparticles give rise to identical types of decay chains with two visible systems defined by their transverse momenta, $\vec{p}_T^{\text{vis}(i)}$, energies $E_T^{\text{vis}(i)}$, and masses $m^{\text{vis}(i)}$. They are accompanied by the unknown LSP transverse momenta, $\vec{p}_T^{\chi(i)}$. In analogy with the transverse mass used for the W mass determination, we can define two transverse masses ($i = 1, 2$)

$$(m_T^{(i)})^2 = (m^{\text{vis}(i)})^2 + m_\chi^2 + 2 \left(E_T^{\text{vis}(i)} E_T^{\chi(i)} - \vec{p}_T^{\text{vis}(i)} \cdot \vec{p}_T^{\chi(i)} \right) \quad (2.3)$$

These have the property (like for W decays) that for the true LSP mass their distribution cannot exceed the mass of the parent particle of the decay and they present an endpoint at the value of the parent mass. The momenta $p_T^{\chi(i)}$ of the unseen particles are not experimentally accessible individually and only their sum, the missing transverse momentum p_T^{miss} , is known. Therefore, in the context of SUSY, a generalization of the transverse mass is needed and the proposed variable is M_{T2} . It is defined as

$$M_{T2}(m_\chi) = \min_{p_T^{\chi(1)} + p_T^{\chi(2)} = p_T^{\text{miss}}} \left[\max \left(m_T^{(1)}, m_T^{(2)} \right) \right], \quad (2.4)$$

where the LSP mass m_χ remains as a free parameter. This formula can be understood as follows: as neither of $m_T^{(1)}$ nor $m_T^{(2)}$ can exceed the parent mass if the true momenta are used, the larger of the two can be chosen. To make sure that M_{T2} also does not exceed the parent mass, a minimization is performed on trial LSP momenta fulfilling the E_T^{miss} constraint.

We attempt to use M_{T2} as a variable to distinguish SUSY production events from backgrounds. The use of M_{T2} as a discovery variable was first proposed in [27], but in this note we propose a different approach. Several choices for the so-called “visible system”, which is used as input to the M_{T2} calculation can be considered; in this analysis we choose to group jets together to form two systems or “pseudojets” and use those as visible systems.

For this comparison between the current degraded detector at 50 pile-up and the performance of the upgrade, we study the effect of b-tagging to the acceptance of SUSY signals.

2.3.3.2 Samples and Event Selection

Table 2.5 lists all Monte Carlo samples and cross sections that have been used in this study. All MC samples were produced using the Pythia [18] generator. The properties of the LM9 signal sample are summarized in Table 2.6.

Table 2.5: List of MC samples used in this study, and their cross sections. The both samples have been generated twice, once in the current detector design, once with the proposed pixel upgrade. The cross-sections used are taken from [28] for $t\bar{t}$ and [29] for LM9.

Process	$t\bar{t}$	LM9
σ (pb)	8.74e+02	3.98e+01

Table 2.6: Definition of the benchmark point, from [29].

Benchmark point	m_0	$m_{1/2}$	$\tan \beta$	A_0	μ	$m_{\tilde{g}}$	$m_{\tilde{\chi}}$	$m_{\tilde{t}}$	$m_{\tilde{u}, \tilde{d}}$
LM9	1450	175	10	0	+	1295	207	1290	3000

The event and object selections are very close to the one of the 2011 reference analysis [30]. The objects are reconstructed using the particle-flow (PF) algorithm [31], which identifies and reconstructs individually the particles produced in the collision, namely charged hadrons, photons, neutral hadrons, electrons, and muons.

Electrons and muons with $p_T \geq 10$ GeV and $|\eta| \leq 2.4$ are considered isolated if the transverse momentum sum of charged and neutral hadrons, and photons, surrounding the lepton within a cone of radius $\sqrt{(\Delta\eta)^2 + (\Delta\phi)^2} = 0.4$ is less than 2.0 times the lepton’s transverse momentum.

All particles, apart from the isolated electrons and muons, are clustered into jets using the anti- k_T jet clustering algorithm [32] with distance parameter 0.5. Energies are calibrated by applying correction factors as a function of the transverse momentum and the pseudorapidity of the jet. The effect of pile-up is reduced by using the FastJet pile-up subtraction procedure [15, 16] for data and simulated events. Jets are required to pass loose identification criteria [33] and to satisfy $p_T > 20$ GeV and $|\eta| \leq 2.4$. The b-jet tagging is based on the combined secondary vertex algorithm (CSV).

Events are required to contain at least one good primary vertex. The H_T value, computed from PF jets with $p_T > 50$ GeV, must satisfy $H_T \geq 750$ GeV. At least four jets are required, where a p_T threshold of 40 GeV is used for jet counting. The two leading jets are required to have $p_T > 100$ GeV. The value of E_T^{miss} is required to exceed 30 GeV. To reject events where a significant fraction of the momentum imbalance arises from forward or soft jets, a maximum difference of 70 GeV is imposed on the modulus of the difference between the \vec{E}_T^{miss} and \vec{H}_T^{miss} vectors, where \vec{H}_T^{miss} is the negative vector sum of all selected jets. Events containing jet candidates with $p_T > 50$ GeV that fail the jet identification criteria are also rejected. The last two rejection criteria remove a large majority of events arising from detector noise.

To reduce the background from QCD multijet events with large E_T^{miss} , arising from mismeasurements or leptonic heavy flavor decays, a minimum azimuthal difference $\Delta\phi_{\min}([j_1 - j_4], \vec{E}_T^{\text{miss}}) > 0.3$ is required between the directions of \vec{E}_T^{miss} and four leading jets. As a potential SUSY signal comes often with many jets, this variable is calculated using only the four hardest jets to avoid a major loss in signal efficiency. The background due to QCD multijet events is not studied here, but it has been shown in the reference analysis that its contribution after the requirement $\Delta\phi_{\min}([j_1 - j_4], \vec{E}_T^{\text{miss}}) > 0.3$ is negligible for high M_{T2} values. Finally, events are rejected if they contain an isolated electron or muon, to suppress the contributions from W+jets, Z+jets and top-quark backgrounds.

2.3.3.3 Comparative Results

To compare the performance of the two detectors in this high pile-up regime, we set the CSV mistag rate for light quarks to 0.1% as a working point. The working point was calculated from the mistag rate in $t\bar{t}$ simulation and confirmed in the LM9 signal sample. In Figure 2.40, the M_{T2} distribution is shown with the selection as described above, before any b-tag requirement.

It can be seen in the ratio plot of selected events in the upgraded geometry over the selected events in the current geometry there is no difference observable (i.e. the ratio is around 1) for both the $t\bar{t}$ background and the LM9 benchmark point. The ratio of yields with the upgraded detector to the standard detector demonstrates that no perturbation to the M_{T2} distribution is introduced by the upgraded detector.

The gain in the upgrade detector comes through enhanced btagging capabilities. To evaluate the performance of b-tagging in the SUSY benchmark point, we apply the previous event selection and then calculate the efficiencies to correctly identify b-jets versus light and charm jets. This is illustrated in Figure 2.41, where it can clearly be seen that the upgrade detector allows us to correctly identify b-jets in these SUSY samples at higher efficiencies and lower relative fake rates. This confirms that the improvements seen in Figure 2.18 in $t\bar{t}$ samples are also present after making the $M_{T2}b$ event selection in the LM9 SUSY benchmark point.

We choose, as mentioned above, to illustrate the upgrade b-tagging improvement using a working point where the CSV mistag rate for light quarks is set to 0.1%. In Figure 2.42, the tagging efficiency for this working point is shown as a function of jet p_T for b-jets, c-jets and light jets.

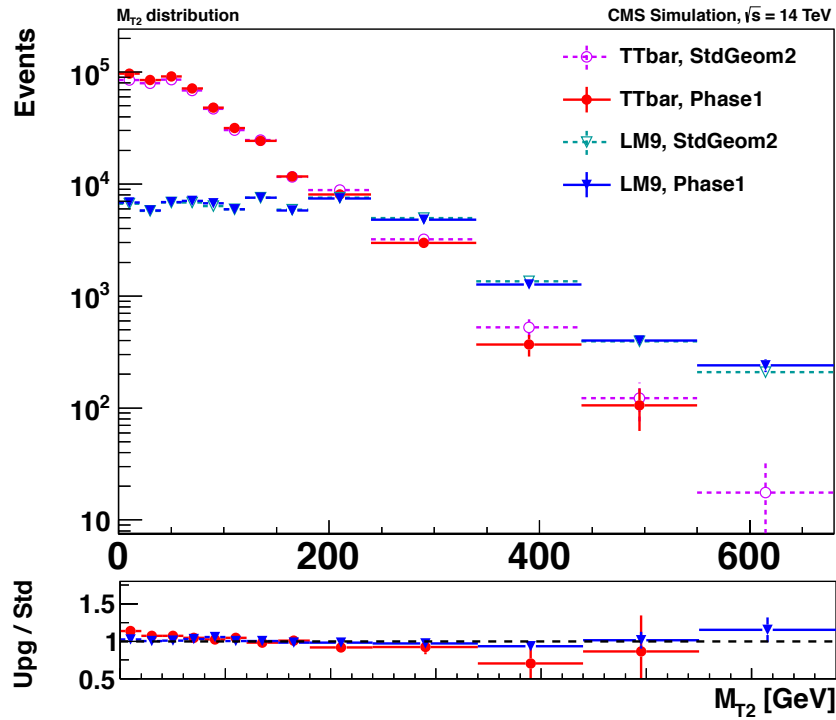


Figure 2.40: The M_{T2} distribution for the $M_{T2}b$ selection before any b-tag requirement

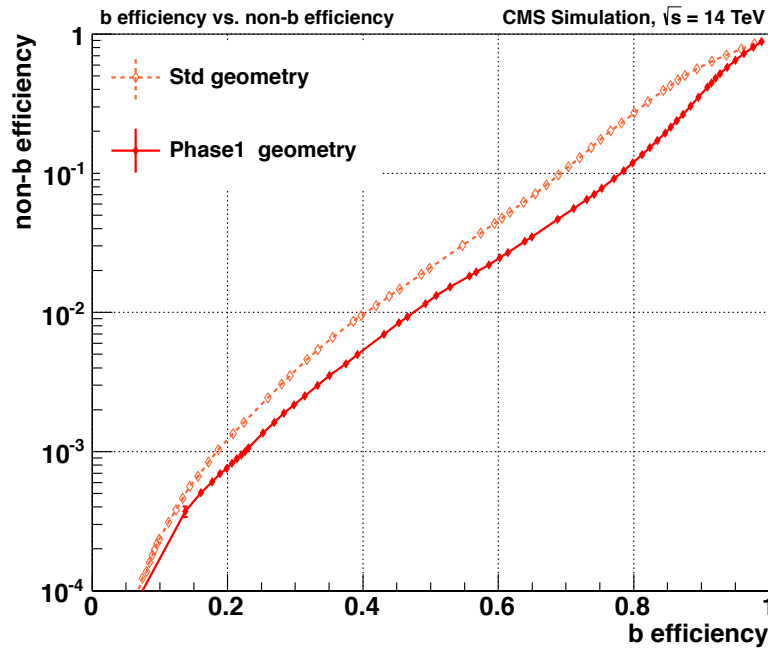


Figure 2.41: B-tagging efficiency versus overall mistag efficiency using the CSV tagger.

For the same light mistag rate the overall b-jet efficiency is increased from 40.5% in the current detector geometry to 47.5% in the upgraded geometry.

Adding the requirement of at least one b-tag ($p_T > 30$ GeV), where the working point was chosen such that the CSV mistag rate for light quarks is 0.1%, there is no change in shape observed

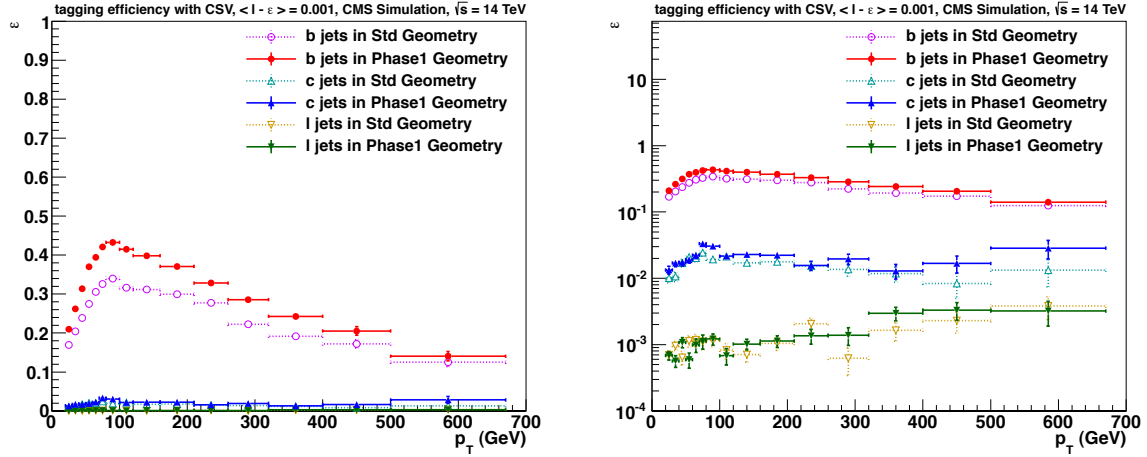


Figure 2.42: Tagging efficiency as function of jet p_T for b-jets, c-jets and light jets for the chosen working point of 0.1% mistag rate for light quarks. Left: plot in linear scale, Right: plot in log scale

(within statistical fluctuations) as shown in Figure 2.43, but the overall yield is increased by 20% (30%) for the LM9 signal ($t\bar{t}$ background) in an signal region of $M_{T2} > 200$ GeV. The cut was placed at the value where the signal becomes larger than the $t\bar{t}$ background. It should be noted that the strong increase in $t\bar{t}$ is expected as these events contain at least two b-jets. The LM9 signal yields usually in either zero, two, or four b-jets per event.

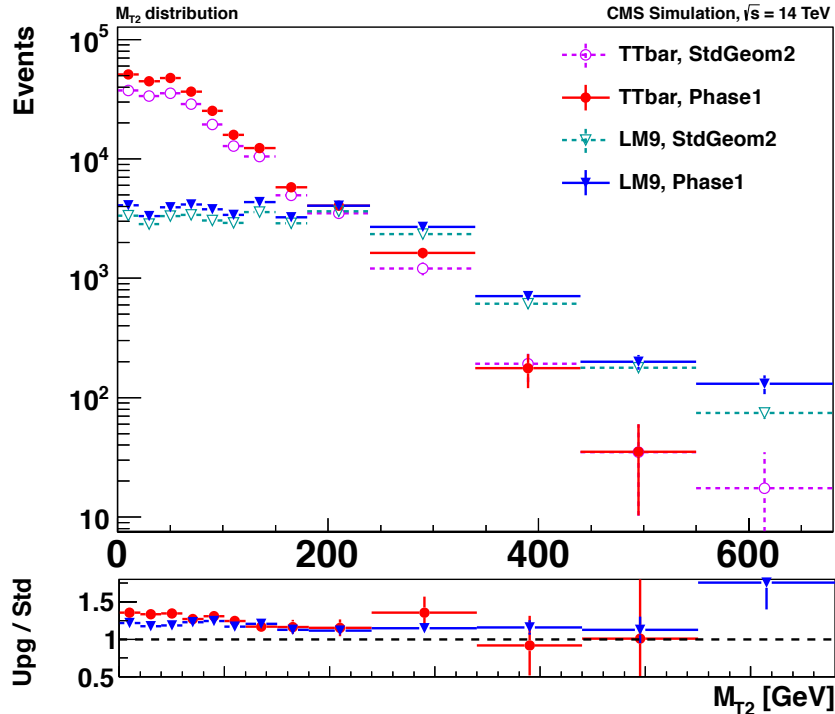


Figure 2.43: The M_{T2} distribution for the $M_{T2}b$ selection requiring at least one b-tag. The upper plot is with fixed bin width, the lower plot with variable bin width.

Table 2.7: Photon identification cuts for diphoton plus missing energy analysis.

	Photons	Electrons	Fakes
p_T	$> 40/25 \text{ GeV}$	$> 40/25 \text{ GeV}$	$> 40/25 \text{ GeV}$
$ \eta $	< 1.379	< 1.379	< 1.379
Combined Isolation ($dR < 0.3$)	$< 6 \text{ GeV}$	$< 6 \text{ GeV}$	$> 6 \text{ GeV}$
H/E	< 0.05	< 0.05	< 0.05
$\sigma_{i\eta i\eta}$	< 0.011	< 0.011	< 0.011
Pixel Seed	No	Yes	No

2.3.3.4 Conclusions

For a supersymmetric analysis requiring at least one b-tag, the most important improvement resulting from the pixel upgrade comes from a higher b-tag efficiency at a fixed fake rate. In summary, a 20% higher signal selection efficiency can be obtained without substantial efforts to optimize the analysis for the new detector and high pile-up.

2.3.4 Two Photons and Missing Energy

The upgrade can provide several benefits to SUSY analyses with photons compared with the current pixel detector at high luminosities. This study examines the improvement to photon identification under $\overline{\text{PU}} = 50$ scenario at the nominal LHC energy of 14 TeV.

2.3.4.1 Analysis

The SUSY search in the $\gamma\gamma + E_T^{\text{miss}}$ channel looks for diphoton events with large E_T^{miss} as a signature of new physics. As the SM does not predict many processes to have two photons and large true E_T^{miss} , the majority of the events in the E_T^{miss} distribution comes from the mismeasurement of events without true E_T^{miss} . The only irreducible background, SM processes with two photons and true E_T^{miss} , comes from $W\gamma\gamma$ and $Z\gamma\gamma$ which have very small cross-sections.

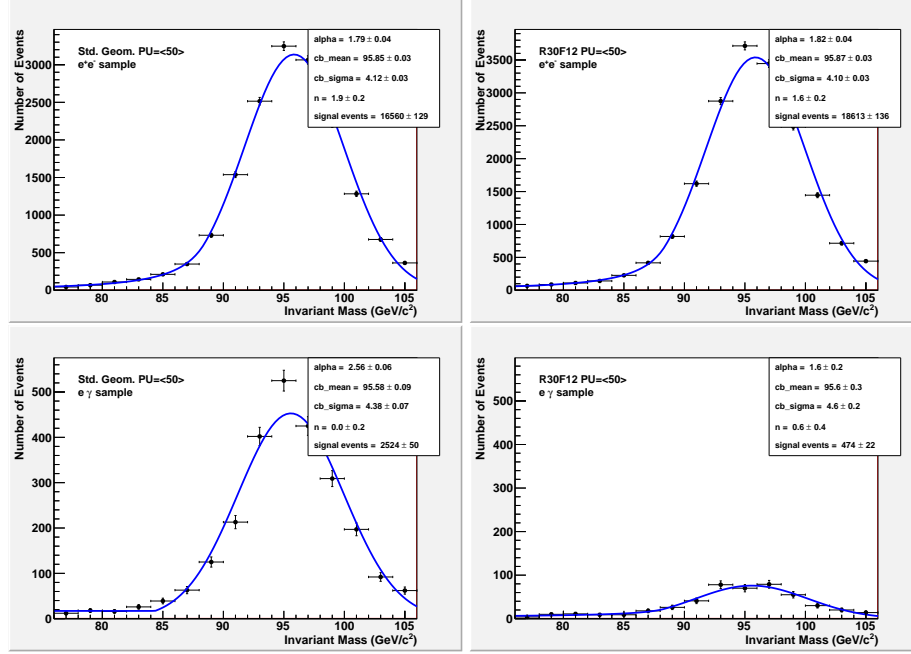
2.3.4.2 Event Selection

Events passing the trigger are then classified into four types of events based on the photon candidates they contain: diphoton ($\gamma\gamma$), dielectron (ee), electron-photon ($e\gamma$), and fake-fake (ff). The selection criteria to identify the photon candidates is listed in Table 2.7.

QCD can contribute diphoton events, either through direct diphoton or multijet production where one or more jets are misidentified as photons. To model the QCD background, a template is created using either dielectron or fake-fake events, both of which have no true E_T^{miss} and represent the shape of the E_T^{miss} distribution due to mismeasurement. As the mismeasurement of the energy is due primarily to the difference in energy resolution between the ECAL and HCAL, the size of the fake E_T^{miss} is correlated with the total p_T of the two photon candidates. To more accurately model the shape of the E_T^{miss} distribution, each bin is reweighted based on the ratio of the di-EM p_T between the diphoton and dielectron or fake-fake events. The template E_T^{miss} distribution is then normalized to the signal events based on the region with $E_T^{\text{miss}} < 70 \text{ GeV}$. Due to the limited amount of MC available for the Pixel Upgrade, only the dielectron template method was used in this analysis.

Electroweak processes can contribute to diphoton signal through W or Z decays to electrons, where electrons are misidentified as photons. To determine the amount of this contribution a study was performed to determine the fake rate for photons due to electron misidentification.

Figure 2.44: The Z-mass peak is shown for the current and Phase-1 pixel detectors at $\overline{\text{PU}} = 50$. The calculated fake rates are 7.0% and 1.25% for the current and Phase-1 pixel detectors, respectively.



The photon fake rate was determined by measuring the amount of misidentified electrons in the $e\gamma$ events. This is done by fitting the Z peak in the ee and $e\gamma$ samples. The ratio of Z events in the two samples can then be used to determine the fake rate.

To examine the overall effect on the background for the upgrade with respect to the current detector, the fake rates were studied using the dielectron events in the Drell-Yan sample.

2.3.4.3 Comparative Results

As the photon fake rate directly influences the amount of electroweak background, the Phase-1 Pixel detector can improve sensitivity of the diphoton analysis by reducing the fake rate. Since the photon and electron identification criteria only differ by the presence of a pixel seed, the fake rate is almost completely dependent on the performance of the Pixel detector. The additional barrel layer in the Phase-1 Pixel Detector provides an extra opportunity for a hit, and thus a Pixel Seed, in the detector. Additionally, due to insufficient buffer sizes in the readout chips, the current Pixel detector suffers from a significant inefficiency at high pileup. The Phase-1 Pixel detector uses new chips that eliminate this inefficiency. Using the fits to the Z-peak shown in Figure 2.44, the fake rate was determined to be 7.0% and 1.25% for the Standard and Upgrade geometries, respectively.

2.3.4.4 Conclusions

The current design of the CMS Pixel Detector has several weaknesses that are clearly evident in high pile-up conditions like that which is expected in the LHC. The resulting increase in fake rate due to the inefficiency of the pixel detector to provide pixel seeds and thus correctly differentiate electrons from photons will add a significant additional background in the diphoton + MET analysis. By comparison the Phase-1 upgrade does not show much degradation due to the expected conditions in the LHC due to the four-layer geometry, lower mass and reduced data loss. The projected fake rate of 1.25% at high luminosities with the upgrade is comparable

to the measured fake rate in the current pixel detector during the lower pile-up runs of 2011-12.

2.4 Conclusions to Tracking and Physics Studies

We have designed an upgraded pixel detector that should perform as well or better than the current detector does at low luminosity running, but at high luminosity running. We have taken the designs detailed in subsequent chapters of this report and implemented them in our simulation program to study the performance of this new detector with respect to what we would expect if we left the current detector in CMS during the high luminosity running of the LHC expected before and after long shutdown 2. Improvements from a four-layer barrel, three forward disk, low mass high performance pixel detector are broad and substantial and will have a significant impact on our physics program. We expect gains in physics signal efficiencies between 20% to 70% which, for example, translate into an increase in Higgs sensitivity of 40% in the ZH channels.

Chapter 3

FPIX System

The Phase 1 upgrade of the Forward Pixel system will have three disks in each endcap. The three disks are located at each end of the central barrel detector, with a radial coverage ranging from 4.5 to 16.1 cm. The location of the first disk along the beam line is 29.1 cm from the interaction point and the second and third disks are located at 39.6 cm and 51.6 cm from the interaction point. Together with the four Barrel pixel layers, this provides a four-hit coverage for all tracks over the pseudorapidity range up to ± 2.5 . A common design goal for both BPIX and FPIX upgrades is to reduce material by using superlight mechanical support, CO₂ cooling, and locating the readout electronics away from the active region. The guiding principles in designing the upgrade Forward Pixel System are:

- Fits within the Phase 1 FPIX envelope definition
- Requires only one type of modules: 2x8 ROC modules
- Modules oriented radially to improve resolution in $r - \phi$ (previous detector has $100 \times 150 \mu\text{m}$ pixels oriented at 90° to this proposed detector)
- Locates all outer radius sensors as far forward and out in radius as possible (to minimize the gap in 4-hit coverage between the end of the 4th-barrel layer and the forward-most disk)
- All three identical disks on each side of the I.P.
- Individual modules are removable and replaceable without disassembling disks
- Maximize 4-hit coverage between the ends of the 4th barrel layer up to η of ± 2.5 using a minimum number of (2x8) modules
- Minimizes the amount of material required for cooling and module support, where module location is repeatable and stable to $< 10 \mu\text{m}$ with thermal cycling and vibrations
- Readout requiring no more than 500 available optical fibers
- Uses identical geometries of HDI/pigtail cables.
- Separate inner from outer assemblies to allow replacement of modules on the inner ring (with earlier radiation damaged).

3.1 Description of the Upgrade FPIX Detector

Before describing in detail the upgraded detector, it is good to review the current FPIX. The current FPIX detector consists of two completely separate sections, one on each side of the interaction region. They are located inside the BPIX supply tube but are mounted on separate insertion rails. Each section is split vertically into symmetrical halves so the detector can be

installed around the beam-pipe and removed for servicing during major maintenance periods. Each of these four halves is called a half-cylinder. Each half-cylinder consists of a carbon fiber shell with two half-disks located at its front end, one at 34.5 cm from the IP and the other at 46.5 cm. The half-disks support the pixel modules that extend from 59.7 mm to 144.6 mm in radius from the beam. The panels that support the pixel are rotated by 20 degrees to form a turbine-like geometry to enhance charge sharing induced by the $E \times B$ drift.

The present FPIX disks are populated with 672 pixel modules called plaquettes. Due to geometrical constraints, five types of plaquettes with different dimensions (with two to ten ROCs) are needed. The assembly of FPIX was significantly complicated by the different modules required. There is a large amount of material in the current FPIX detector. Most of the material between $1.2 < \eta < 2.4$ is in the half-disks and between $2.4 < \eta < 3.6$ in cables and cooling.

3.1.1 Geometrical Layout

The upgraded FPIX detector consists of two sections which are vertically separated with a left and a right set of half-disks on each side. The pixel modules are assembled on half-disk support structures which are mounted on a service half cylinder (HC). The pixel module radial coverage ranges from 4.5 to 16.1 cm. Cooling tubes and the readout electronics are placed on the half cylinders most of which will be located away from the region of coverage.

The upgrade layout uses only one module type, with 16 readout chips in a 2×8 ROC arrangement, the same as for the barrel. The modules are arranged radially on a light-weight substrate called a blade. There are a total of 56 modules (896 ROCs) per half-disk. Half-disks are divided into an outer assembly with 34 modules and an inner ring with 22 modules. The outer and inner assemblies are supported directly from the half cylinder so that the two assemblies could be easily separated. The pixel modules are attached to the substrate by a pair of module holders and are removable and replaceable without disassembling the half-disks. Modules which suffer failure or degradation can be easily replaced during an annual technical stop.

All the modules on the outer assembly are located to minimize the gap in 4-hit coverage between the end of the fourth barrel pixel layer and the forward innermost disk. The design maximizes the 4-hit coverage up to pseudorapidities of 2.5, for particles originating at the interaction point ± 5 cm, using a minimum number of modules.

Each blade on the outer assembly is rotated by 20° in a turbine geometry similar to the current FPIX. However, to obtain excellent resolution in both the azimuthal and radial directions throughout the FPIX acceptance angle for the inner assembly, the blades are arranged in an inverted cone array with the blades tilted by 12° with respect to the interaction point, combined with the 20° rotation. Figure 3.1 shows a cross-sectional view of the new pixel system and its arrangement.

3.1.2 Substrate

Thermal pyrolytic graphite (TPG) will be used for the blade substrate. TPG is a material with excellent in-plane thermal conductivity (>1500 W/mK), and is easily machinable. On the other hand, it is brittle and may contain some carbon dust on its surface. For these reasons, we will encapsulate the 0.68 mm thick TPG substrate with one ply of carbon-fiber reinforced plastic (CFRP) on both sides. Extra plies of CFRP are added at the ends of the TPG substrates for structural reinforcement. The ends of the blade are trimmed with a 45° chamfer to increase the end-surface area for better bonding of the TPG blade to the half rings. The conceptual design of the blade with its components is as shown in Figure 3.2. Each blade has two modules, one on each side of the same substrate, shifted in ϕ by 11° . The orientation of the modules on the

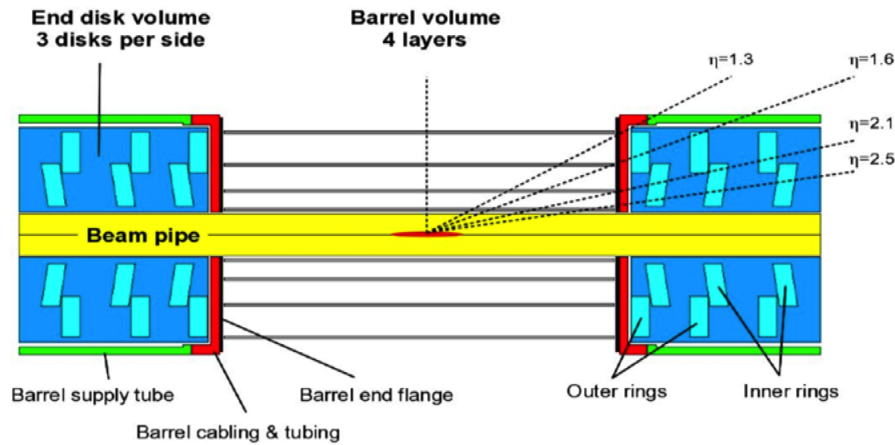


Figure 3.1: Schematic view of the upgrade pixel detector layout. There are three end cap disks on each side, with each disk separated into an inner and outer ring. The inner ring is tilted at 12 degree towards the interaction point. The disks are positioned to maximize the 4 hit eta coverage.

rotated turbine blades aligns the 150 micron dimension of each pixel in the radial direction and the 100 micron dimension of each pixel in the phi direction, with more overlap between neighboring sensors than in the current design and no gaps in the coverage. This will also ease the spatial alignment for track reconstruction. The reduced number of interfaces in the modules and blades simplifies assembly and reduces material.

Each module has a pair of module holders made of PEEK, one glued at each end of the module for attachment to the threaded inserts on the TPG substrate. All pixel module are fastened to the blades with #00-90 screws through the module holders. The PEEK holder at the outer end of each module has an extra function in strain-relieving the Aluminum flex-cable which is used to readout the pixel modules. A tiny plug, made out of PEEK, is jammed tight against the flex-cable when it is engaged within the wedged wings of the module holder.

3.1.3 Carbon Ring with Integrated Cooling Tube

The pixel modules will be mounted on ultra-light-weight support structures integrated with the cooling distribution system. Two-phase CO₂ cooling will replace the current single phase C₆F₁₄ resulting in significant material reduction. Thin-wall stainless steel tubing (with an outer diameter of ~ 1.6 mm and wall thickness of 0.1 mm) in a continuous loop provides sufficient cooling power for each pixel sub-assembly. The stainless steel tubes for CO₂ cooling are embedded in the outer and inner assembly rings made of light-weight carbon fiber reinforced carbon material (C-C) as shown in Figure 3.3. Cooling is provided through the ends of the TPG substrates which are made to be in good thermal contact with the actively cooled rings. To improve the thermal contact, we plan to use metallic bonding as it has excellent thermal conductivity (see Section 3.3). The TPG substrates will be bonded to the C-C rings by indium alloy solder bonding. The entire ring with embedded cooling tubes and TPG substrates could be constructed as a complete turbine-like mechanical support and cooling structure and tested before the pixel modules are placed on the blades. Further material reduction will be achieved by using long light-weight aluminum flex-cables and by locating the Optical Hybrid Boards, Port Cards and cooling manifold out of the tracking region.

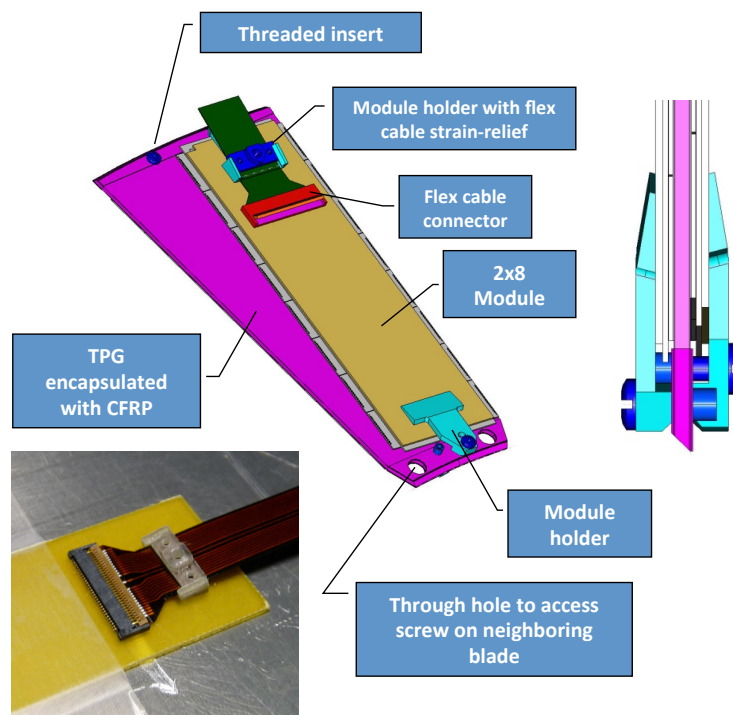


Figure 3.2: The conceptual design of the Forward Pixel blade with its components.

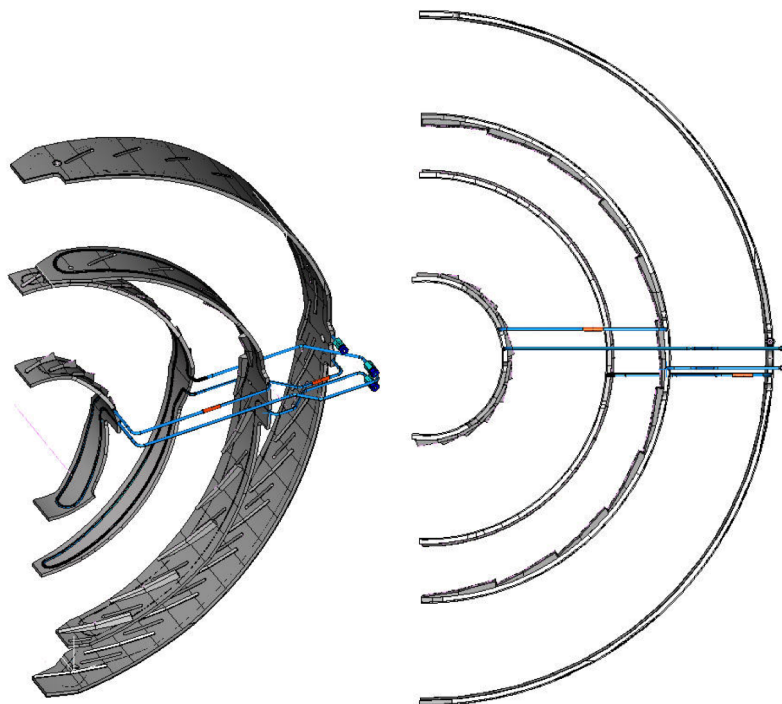


Figure 3.3: The tubing layout within each half-disk.

3.1.4 Half-disk and its Components

The upgraded half-disk consists of two turbine like mechanical support structures with the inner assembly providing a sensor coverage from radius = 45 mm to 110 mm with 11 blades while the outer assembly covers from radius = 96 mm to 161 mm with 17 blades. Both outer and inner blade assemblies are secured to the half cylinder separately so that the modules on the inner assemblies can be removed only for early sensor damage repair without disturbing the outer assemblies. Both assemblies have mounts employing a spherical washer concept such that minor angular mis-alignment is allowed without inducing stress into the half-disks when they are fastened with the M2 screws. The design of the half-disk and mounts are as shown in Figure 3.4.

The C-C rings have a series of 45° tabs on the curved surfaces for bonding to the blade. These half rings function as support structures and as heat sinks. They are machined with a groove cut into the side opposite of the curved surface with tabs for blade bonding. The 1.6 mm outer diameter stainless steel tubing for CO₂ cooling is embedded in the groove. Tin alloy solder bonding will be used to reduce the thermal resistance between the tubing and the groove wall in the bottom half of the groove while thermal fillers will be used to fill up the upper half. The groove with the embedded tubing will be covered with 0.5 mm thick CFRP to serve as a structural reinforcement facing. The tubing within the four half rings of each half-disk is connected in series. All the grooves within the rings have an “omega” shaped loop so that all the tubing inlets/outlets are located at the same 3 o’clock position. As a result, tubing length and material in the half-disks is minimized while providing sufficient contact area between coolant and support structure for effective heat transfer. To connect the tubing in the 4 half-disk rings in series, 5 joints are required, in which 2 joints connecting outer and inner rings within each assembly can be made permanent while the last 3 joints are removable and reworkable so that the inner assembly can be removed easily. The tubing layout within each half-disk is shown in Figure 3.3 (with the blades and CF facing not visible for better illustration) and the permanent joints are shown in orange.

A full prototype of the outer assembly tubing is being made to confirm the manufacturing feasibility. Although an initial prototype has shown that the tubing can be bent into this complex shape, a full prototype will be needed to demonstrate that the tube ends can be aligned in situ and the joint coupler can be inserted and brazed properly. A rapid prototype of the outer assembly was made with all tubing grooves exposed for checking the tube fitting, as shown in Figure 3.5.

The design of the removable coupling is shown in Figure 3.6.

The design combines features from several different commercial products. The coupling consists of a male nut, a female nut, a gland, and a gasket. Removability is enabled by M3.5x0.6 threads machined in 4 mm hexagonal 303 stainless steel alloy material to form the nuts. To prevent leaks, the male nut and gland are separately laser-welded to the tubing and create permanent seals. The only reworkable seal is made by the knife-edge faces of the male nut and gland cutting into the replaceable soft aluminum gasket when the coupling is fastened. This will be an extremely leak-tight, metal-to-metal seal and is commonly used in ultra-vacuum holding technology as demonstrated by Conflat flanges. A new aluminium gasket will be used whenever the couplings are re-fastened.

A couple of prototypes have been machined and laser-welded. Vacuum leak checks of these two prototypes confirmed the seal made by the replaceable aluminum gasket. However, leaks were found in the welded joints between the male nut and the tubing where extra welding

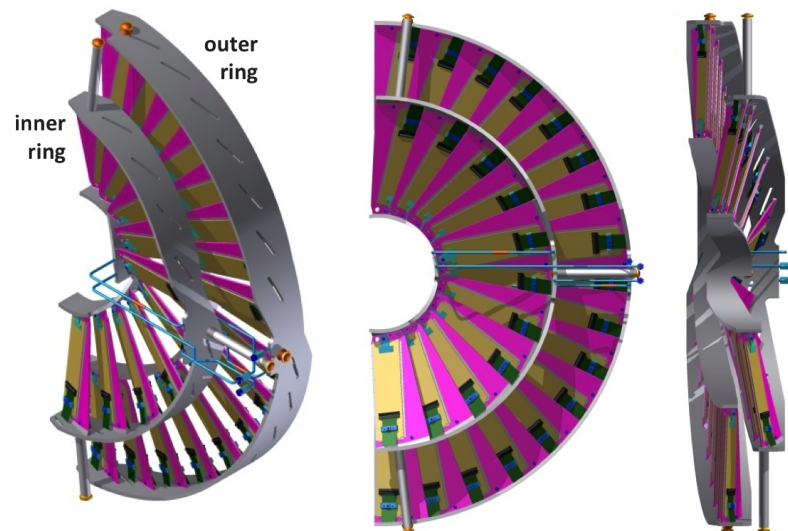


Figure 3.4: The conceptual design of the half-disk.

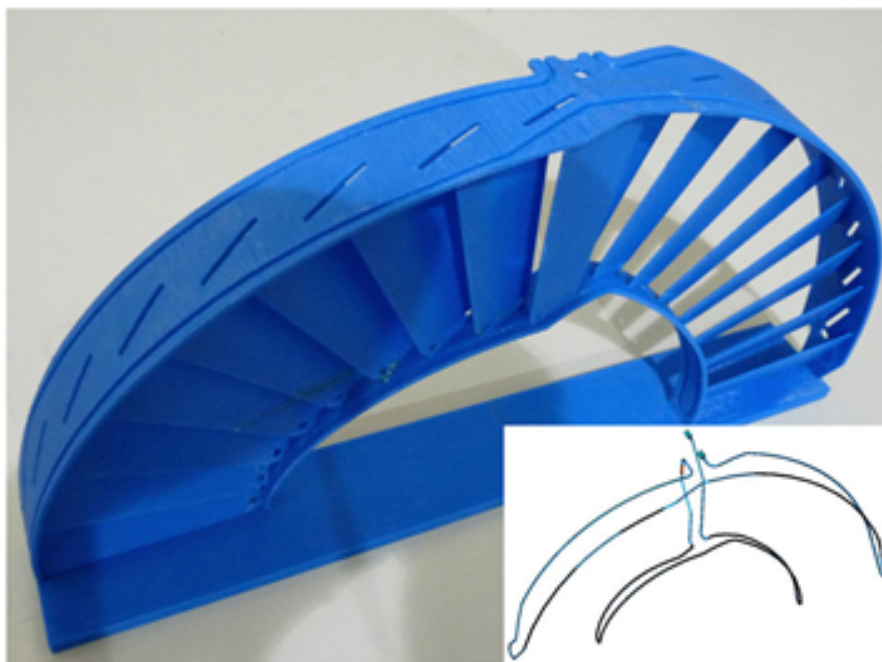


Figure 3.5: The rapid-prototype of the outer assembly.

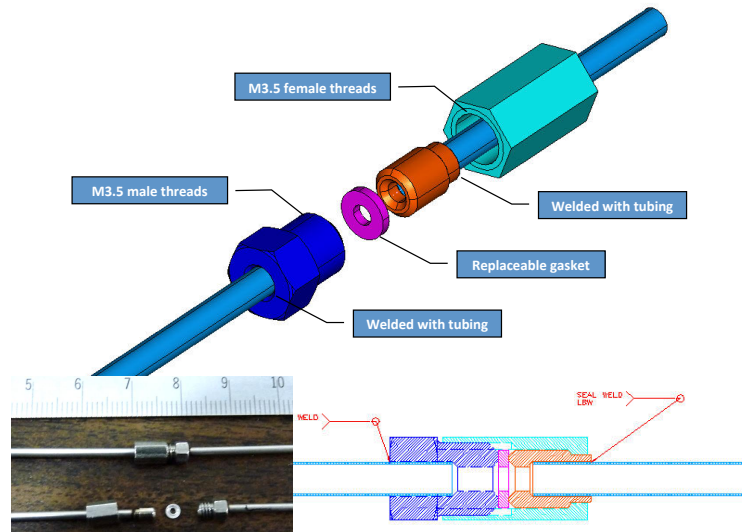


Figure 3.6: The conceptual design of the removable coupling.

rod was used to complete the welding because of the undesirable large clearance (0.005"). The other welded joints between the gland and the tubing with a fitting clearance of 0.002" was found to be sealed. New coupling parts are being fabricated and will be welded and pressure tested to confirm the leak-tightness of the design.

The basic assembly sequence for the half-disk is as follows:

- Laser-weld removable fittings on tubing and bend the tubing into shape for the half-rings
- Glue threaded inserts on the TPG blade
- Bond C-C segments to form C-C half ring
- Indium-bond stainless steel tubing in the C-C half ring
- Glue CFRP facing with the C-C half ring after the groove is filled up with thermal fillers.
- Indium-bond the blades to the half rings with the aid of a Coordinate Measuring Machine (CMM)
- Glue half-disk mounting fittings onto the half rings with the aid of a CMM
- Soft-solder couplers connecting tubing from outer and inner half rings
- Mount modules on the blades with thermal interface material in between and then with screw.

3.2 Cooling Design

An important consideration for our design which makes use of edge cooling is the temperature difference between the CO₂ in the cooling tube and the edge of the substrate. There are a few thermal interfaces and we have to make sure that this temperature drop remains low. Our design target is that the overall temperature drop from the CO₂ coolant to the pixel module should be within 10 °C with a heat load of 3W per module. This heat load includes a 50% safety margin. To meet this requirement, an efficient cooling scheme is designed with light-weight and highly thermally conductive materials including interface materials. The heat generated

from the module will be transferred to the TPG heat spreader underneath and towards the ends where the half rings are set. These half rings, which are used to support all the module substrates as well, basically consist of 3 parts namely as follows. The first part is the carbon-carbon ring in which contact tabs for the TPG heat spreaders on one side but with a groove provision on the other side are made. The second part is the embedded stainless steel cooling tube inside the groove, and the final part is a sheet of carbon-fiber facing that covers the tubing completely. This is a very simple cooling design and the heat path will go through the following 3 interface layers.

1. An interface layer between module and the TPG heat spreader where thermally conductive grease or equivalent is needed as modules are needed to be removable.
2. Bonding layer between TPG heat spreader end and carbon-carbon half ring >> structural and thermally conductive material is needed.
3. The gap between the stainless-steel tubing and the groove wall within the half ring >> thermally conductive material is needed.

While the heat spreader and heat sink could use materials with very high thermal conductivity (k), these interface layers basically have the highest thermal resistance and hence temperature drop through this heat path. In order to meet the overall temperature drop requirement to be within 10 °C, improved thermal interface materials (TIM) with much higher k are needed for these interface layers. An extensive search on the market for these enhanced TIMs was thus conducted and studied.

3.3 Thermal Interface Materials (TIM)

There are a few thermal interfaces between the coolant and the edge of the substrate. TIMs play a key role in the thermal management of electronic systems by providing a path of low thermal resistance between the heat generating devices and the heat spreader/heat sink. Typical TIM solutions could include those polymer TIMs like adhesives, greases, gels, phase change materials, pads, and metal TIMs like solder alloys. In order to improve the thermal conductivity of the polymer matrix of the TIM, filler particles like silver, boron nitride, alumina, aluminum, zinc oxide and diamond can be added. Besides polymeric TIMs, an interesting option is to use the metallic solder bond which usually has a much higher thermal conductivity. An excellent candidate for this kind of solder TIM is indium and its alloys because of their high thermal conductivity (indium at 86 W/mK), low melting point (indium at 157 °C), ease of compression and application. The key to achieving the advantages of the metallic TIM is making intimate contact with the working surfaces as the interfacial barriers are broken down by fusing the molten metal to make liquid contact. The thermal impedance is thus greatly enhanced and it is the lowest among all kinds of TIMs.

An extensive search and study on the existing TIMs available in the market was performed, as shown in Table 3.1.

The thermal properties of Dow Corning's TC-5600 and Laird's tpcm583 were found to be the same as specified by the vendor. Also, the bond line thickness of these two TIMs could be made quite thin at 0.093 mm and 0.070 mm respectively. These two TIMs are the best candidates for using in the module placement on the TPG heat spreader. One surprisingly good result came from the thermal conductivity result of the C-C. The measured value was 319 W/mK and was

		thickness @ 25°C (mm)	bulk density p @ 25°C (g/cm ³)	temperature (°C)	specific heat C _p (J/g-K)	diffusivity α (mm ² /s)
	EG7659	0.714	2.21	25	0.731	0.838
✓	C-C substrate (A1)	1.76	1.82	25	0.733	238
	CGL7019-LB	0.030	2.0	25	1.0	0.167
✓	TPCM583	0.070	2.5	25	0.8	2.04
	Duralco 135	0.067	2.7	25	0.8	0.525
	Duralco 135 (repeat)	0.057	2.7	25	0.8	0.533
✓	Dow TC-5600	0.093	2.7	25	0.8	2.91

		tested conductivity λ (W/m-K)	tested resistance R (mm ² - K/W)	claimed conductivity λ (W/m-K)	claimed resistance R (mm ² -K/W)
	EG7659	1.35	-	11.40	-
✓	C-C substrate (A1)	319	5.33	200	-
	CGL7019-LB	0.334	89.8	20.000	3.0
✓	TPCM583	4.08	17.1	4.00	1.2
	Duralco 135	1.13	59.0	5.80	-
	Duralco 135 (repeat)	1.15	49.5	5.80	-
✓	Dow TC-5600	6.28	14.8	7.10	4.0

Table 3.1: Results thermal testing of selected TIMs.



Figure 3.7: Joint samples of TPG and CC using Indium 52In48Sn.

much higher than that estimated by the vendor. It was learned in this study that a metallic TIM was feasible even for the carbon materials. As the thermal conductivity of metal was so attractive, further R&D was pursued to explore more. Indium alloy 52In48Sn with a tensile strength 1720 psi and a thermal conductivity of 34 W/mK was selected. However, since indium bonding only works for metal-to-metal surface but not carbon, a silver metal coating with good wettability was selected. In addition, it was confirmed that extra diffusion barrier coating(s) like nickel, which is quite inert with respect to its adjacent metals, was needed also. Two recipes of this coating were thus attempted. The first one was nickel and silver only and the second one was with additional aluminum and titanium on top of the first recipe. Coatings were then sputtered on carbon parts within a vacuum chamber. Indium alloy 52In48Sn was then used to make some joint samples that consisted of the straight edge of TPG and a flat surface of the C-C block. It turned out both recipes worked and they wetted nicely. The joint strength was found to be also good even though the bonding surface was actually a narrow strip about 0.68 mm wide. These joint samples are shown in Figure 3.7. More joint samples were made, one that also included the stainless steel tubing. A section was cut and it revealed that indium was deposited well between the parts as shown in Figure 3.8. As indium bonding has been proven applicable, this bonding approach will be used also for the stainless steel tubing within the C-C groove. Heat fluxes going through the lower portion were verified with FEA as shown in Figure 3.9. It is planned that only the lower portion will be bonded with indium and the rest of the groove will be covered with regular polymeric TIMs in order to reducing the mass being used (about 7.4 g saving for each half-disk).

3.4 Four-blade Thermal Test Sample

A small sector of the outer ring assembly has been made to conduct a thermal test. Four pieces of TPG were bonded between two pieces of C-C ring segments with different kinds of TIMs. Two blades were bonded with indium while the other two were glued with thermally conductive adhesives. Blank pieces of silicon served as dummy modules were used in this test sample. Plastic module holders and polyimide thermofoil heater were then glued on top of this dummy module which was then mounted on the TPG. Thermal test of the four-blade assembly is still ongoing.

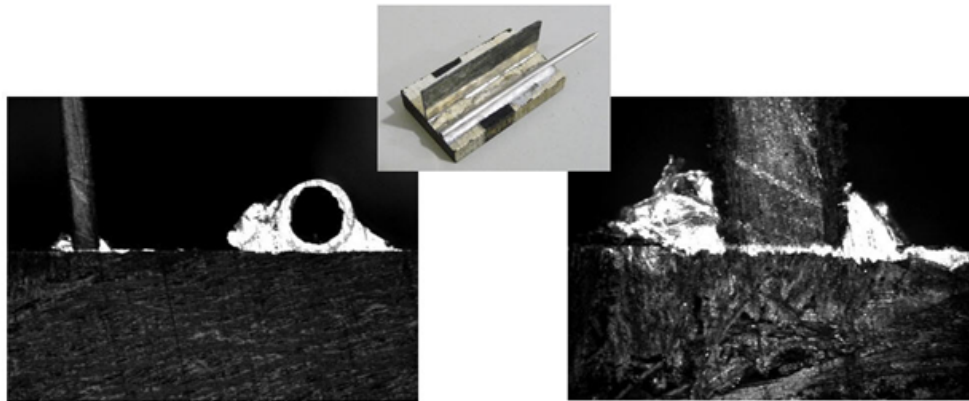


Figure 3.8: X ray image of joint sample of TPG and C-C showing indium deposition.

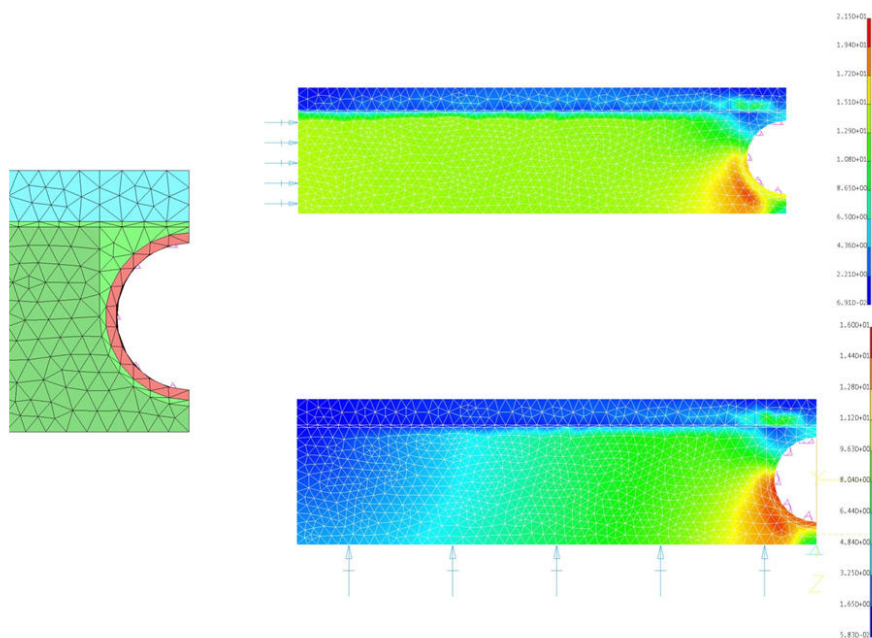


Figure 3.9: FEA studies of heat fluxes from stainless steel tubing to C-C ring.

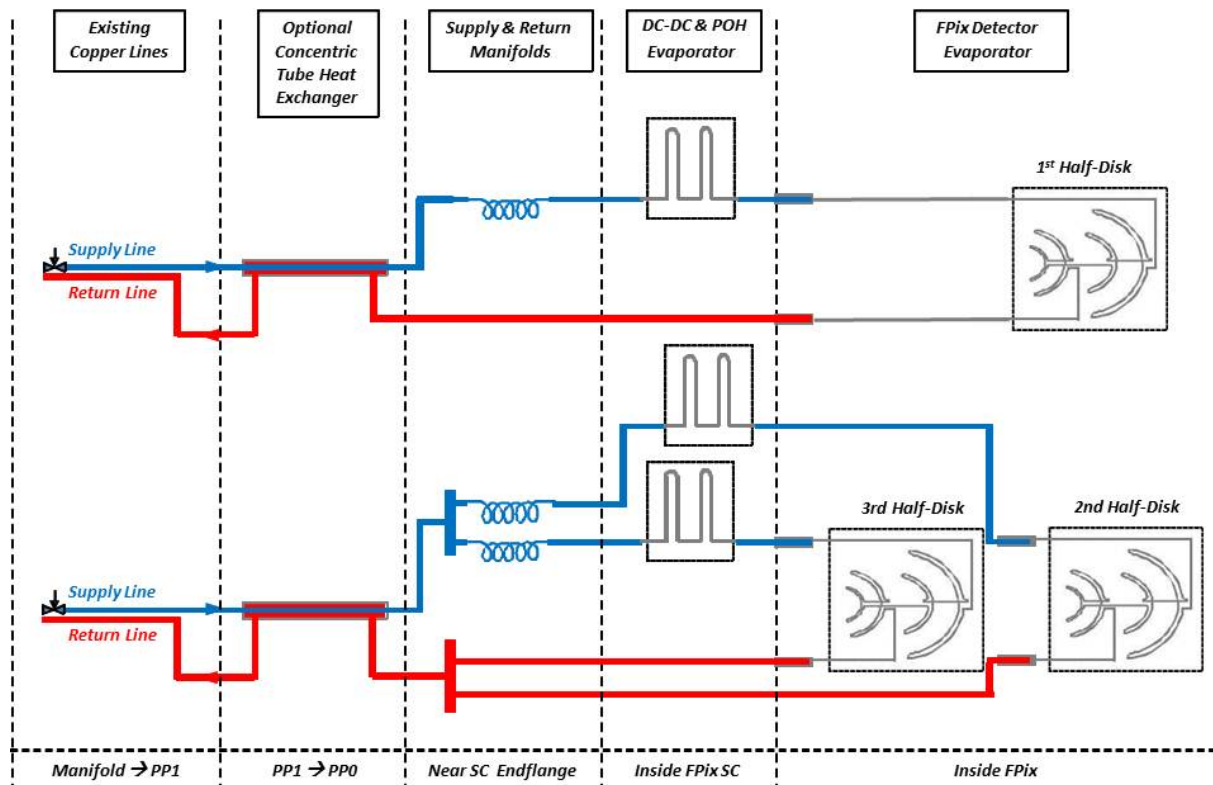


Figure 3.10: Schematic showing the cooling tube layout within the FPIX half-cylinder

3.5 Cooling Line Layout

There are four main supply/return lines from the cooling plant available for FPIX at each side of the interaction point. The three half-disks in each half cylinder will be cooled by two main cooling loops as shown in Figure 3.10. For each service cylinder, one main cooling line will be manifolded at PP0 to cool the second and third half-disks, and one main line will be used to cool the first half disk. Each half-disk cooling tube is routed in series through the four C-C ring structures supporting the detector blades.

A schematic of the tube layout for each half-disk in a half-cylinder is given in Figure 3.10. As the cooling tube for a half-disk enters the half-cylinder, it is routed below the DC-DC converter bus-boards and then the electronic port cards that are associated with the same half-disk. In this region, the CO₂ is heated by the ancillary electronics to the saturation point and evaporation begins before the CO₂ flows through the half-disks.

Cooling calculations have been performed to evaluate the temperature and pressure drop along the cooling lines. Results of the calculations of the baseline FPIX configuration are shown in Figure 3.11. The calculation shows that an inlet coolant temperature of -20 °C and a flow rate of about 2 g/s results in a maximum ΔT between coolant minimum temperature and external tube surface temperatures of about 5 °C. This satisfies the requirement for a pixel sensor temperature below 0 °C (with a margin of about 5 °C), when combined with an efficient thermal contact between the tubes and sensors and a ΔT between tubes and sensors of less than 10 °C. Calculations of BPIX cooling line performance have shown good agreement with experimental data. A full cooling loop mock-up will be made to similarly evaluate the cooling performance of the FPIX layout experimentally.

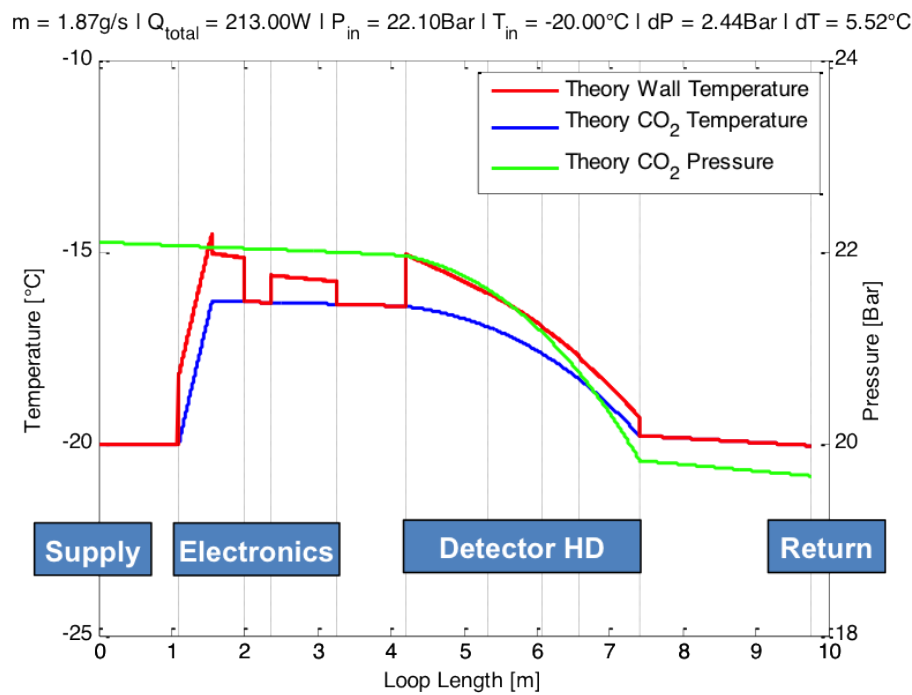


Figure 3.11: Calculated temperature and pressure drop along the FPIX cooling tubes on the half-cylinder.

3.6 Half Cylinder Design

A light and stiff half cylinder (HC) made of CFRP is being designed. To allow removing the inner assemblies from the pixel detector for module maintainance in the future, the flex cables and cooling tube of the inner assemblies should be located outside of the HC so that they can be accessed easily. A corrugated profile in the detector front section is thus designed in which the outer troughs will house the inner assembly cables while the inner troughs will take the outer assembly cables. This front section will be a single-wall CFRP structure and mixing of carbon fiber prepregs is planned to be used, i.e. super stiff CFRP will be laid up in the longitudinal direction while regular CFRP will be laid up in the angular directions so that carbon fibers will not get broken at the trough fillet corners. Careful CFRP layup design will thus be needed in order to get quasi-isotropic properties as close as possible. This is needed because the support legs at front will not be at the very front end but somewhere beyond the detectors section and the corresponding deflection due to bending and shear loads in this loading case is non-trivial. The double-wall CFRP structure of the existing HC design will be kept for the rear section for the upgraded HC so that most of the existing mandrels for making the CFRP parts can be reused. The front and rear sections will be overlapped and glued together in a transition region. The conceptual design of this upgraded HC is shown in Figure 3.12.

A preliminary finite element analysis (FEA) as an aid for designing the front and transition regions was initiated. This was a simplified model with 3 beam spokes simulating the half-disk. In addition, the rear section, whose results would be disregarded in this FEA, was modeled and meshed like the single wall structure at front. A load of 3.9 N, representing a half-disk, was applied at the 3 half-disk locations. A series of wall thickness was input to check out the sensitivity of the front section resultant displacements. The deflection results are as shown and summarized in Figure 3.13.

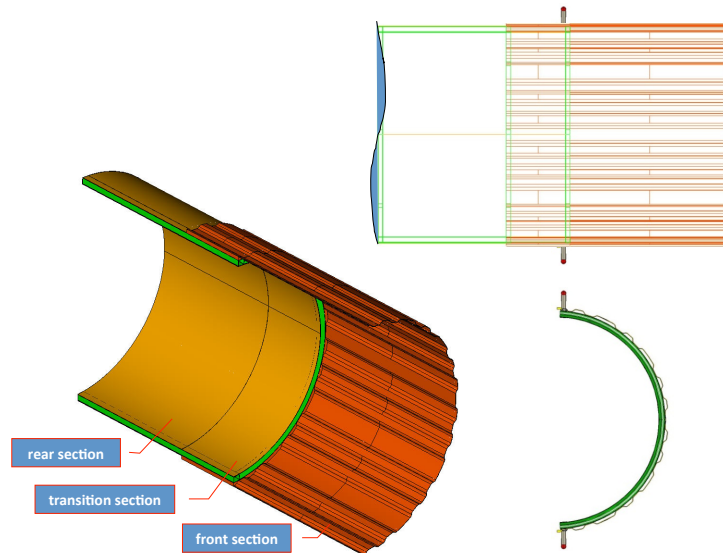


Figure 3.12: Conceptual design of the upgraded half cylinder.

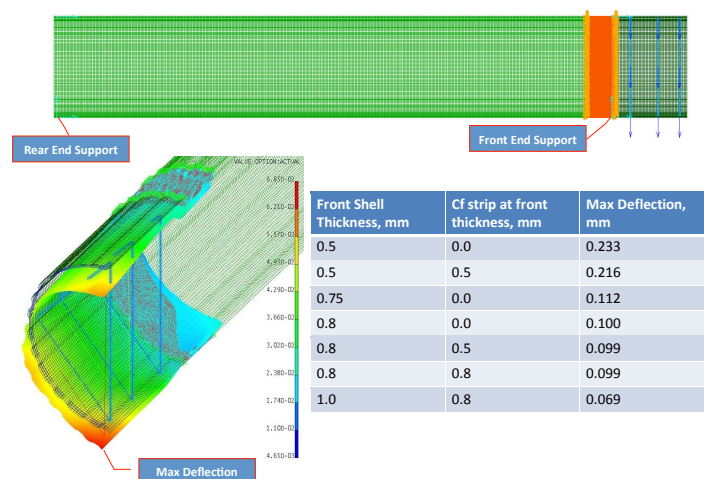


Figure 3.13: The preliminary FEA model and results of the upgraded half cylinder.

3.7 Material Budget

We estimate the overall mass of the FPIX detector can be reduced by $\sim 40\%$, with a $\sim 50\%$ reduction in radiation length in the half-disks (which is most of the FPIX material budget in the $1.5 < \eta < 2.5$ FPIX acceptance). The goal is accomplished primarily by removing the VHDI and by using CO₂ cooling for a huge reduction in the mass of the cooling channels and coolant. The weight of the half-disk is estimated to be 400 g, to be compared with 610 g of the current half-disk. The radiation length of the new half-disk is estimated to be 2.00% to be compared with 4.95% of the current FPIX half-disk. Within the η coverage, the total weight of the half cylinder including cooling tubes, CO₂ coolant, flex-cables, and connectors is calculated to be 480 g. This gives the total weight of the half-cylinder including the three half-disks to be 1.68 kg.

3.8 Assembly and Testing

The modules for the current FPIX were built manually at Purdue while the integration into panels and blades was done at FNAL. For the new detector we will have automated module construction sites at Purdue and Nebraska and continue having an integration facility at FNAL. Our plan is to build the half-disk support with the TPG blades and the integrated cooling lines on the C-C ring at Fermilab. The module assembly and testing schedule will depend on the throughput of the pixel modules delivered from the bump-bonding vendors to the module assembly sites.

Robotic pick-and-place machines, with integrated optics, pattern recognition, and glue dispensing, will be used to join High Density Interconnect flex circuits (HDI) to 2 x 8 Bump-Bonded Modules (BBM), improving the uniformity of the production technique. The module assembly sequence begins by manually placing pre-tested, known good 2 x 8 BBMs and HDI on vacuum chucks on the baseplate of the pick-and-place machine. The machine program successively moves the camera (fixed to the machine motion head) to view the fiducial on the BBM sensors and HDI components and acquires the fiducial location using pattern recognition, picks up a dispensing tool from a the tool rack and dispenses epoxy on the sensors, returns the dispensing tool to the tool rack, picks up a vacuum tool from the tool rack to pick-and-place individual HDI onto sensors (making adjustments based on the actual part locations in the machine to accurately align and join the components), and returns the vacuum tool to the tool rack. Module end holders are also aligned and glued to the modules using custom tooling and the pick-and-place machine.

Following mechanical assembly, HDI are wirebonded to the ROCs using semi-automated ultrasonic wirebonding machines. Routine pull tests of sample wirebonds will be performed for quality control. The wirebonds will be encapsulated with an elastomeric compound using semi-automated dispensing equipment. The module assembly sites will also be responsible for the testing and characterization of the assembled pixel modules. Modules will be thermally cycled within the operating temperature range (-20 °C to 20 °C) while monitoring ROC digital and analog currents. Modules which pass the acceptance criteria will then be assembled onto the half-disk blades.

The half-disk mechanical support structure (with TPG blades and integrated cooling lines in C-C rings) will be assembled and tested at Fermilab. The complete half-disk mechanical and cooling structures can be assembled and tested independent of the module assembly and testing. All cooling tubes will be helium-leak checked and hydrostatically-pressure tested up to 120 bars. A variety of thermal performance tests, including thermal cycling the CO₂ coolant

(+15 °C to -20 °C) with dummy module heaters, will be conducted to validate half-disk mechanics prior to module installation.

Custom tooling will be used to pick-and-place the modules with readout cables onto the blade assemblies. The modules are fastened to threaded inserts in the blades using screws through the module holders, with a thin layer of reworkable thermal interface material between the modules and blades to improve heat transfer. The light-weight aluminum flex cables are routed through slots in the outer rings of the blade assemblies.

In-detector supply and return cooling tubes will be assembled on a dedicated jig and anchored to the inside of the service cylinders, with space between anchor points to allow for thermal contraction of the tubes. Metal blocks will be clamped to the cooling supply tubes for mounting/cooling DC-DC converters on bus boards and Pixel Optical Hybrids (POH). All DC-DC converters and electronic boards will be tested before integration in the HC. The fully assembled HCs, with electronics and cooling lines, will be tested (including thermal cycling) before the modules are installed.

The blade assemblies are independently fastened to 3 mounts previously installed in the HC using M2 screws. Cooling tube coupling fittings are joined and pressure and leak tested following the installation of each blade assembly, before the next blade assembly is installed. Readout flex cables are routed along the forward section of the HC (outer blade flex cables routed inside the HC, and inner blade flex cables passed through slots and routed outside the forward section of the HC, then passed back through slots to the inside of the HC) and connected to flat flex connectors on both sides at the forward ends of the port cards. Modules on each blade assembly are tested for basic functionality before the next blade assembly is installed.

All alignments are set during gluing/bonding processes with the aid of precision tooling and Coordinate Measuring Machine (CMM). Module holder mounting holes are aligned to sensor fiducials when gluing the holders at each end of the pixel modules, and threaded inserts are precisely aligned and glued into the bare blade substrates. Carbon-carbon ring segments are glued together to form a completed carbon-carbon half-ring. With the aid of CMM, survey balls on the ring segments will be used to verify the precision half-ring formation. The module mounting holes in the blades are aligned to the carbon-carbon rings when the blades are bonded with indium-tin alloy solder to the rings using low-CTE tooling. Inserts for mounting the blade assemblies to the service cylinder and survey balls that provide a half-disk reference are aligned and glued to the blade assemblies. Modules are then installed on the blade assemblies and a CMM survey performed to transfer the alignment of all modules to the half-disk reference system. Survey balls will also be aligned and glued to the service cylinder. A final survey of the locations of the blade assemblies will be made with reference to another set of survey balls glued on the service cylinder.

3.9 Testing and Commissioning at TIF

After the half-disks are inserted into the half cylinder, we will begin commissioning tests. This can be done at both Fermilab and at the Tracker Integration Facility at CERN. Commissioning tests include cooling with CO₂ at -20 °C inlet temperature, with the service cylinders in insulated boxes with chilled, dry purge air.

The fully assembled modules would be transported from the assembly sites to Fermilab or CERN for final integration and extensive system tests prior to installation in CMS. After arriving at CERN, we will re-mount the half-disks to the half cylinder. Then we will carry out

a commissioning of each half cylinder. After that, we plan to perform a system test of each FPIX cylinder for a few weeks at TIF. To prepare for this, we will need to equip TIF with all the needed electronics, power supply modules, as well as a CO₂ cooling system. We will also have a full DCS/DSS installed and tested during this system test.

Chapter 4

BPIX System

4.1 System Overview

The barrel part of the pixel detector is designed with four concentric, cylindrical layers with a length of 548.8 mm and radii between 30 mm and 160 mm. Compared to the present CMS pixel barrel, there is one new layer at high radius. The radius of the innermost layer is reduced by 10 mm while layers 2 and 3 are almost unchanged. Each layer consists of a varying number of 22 mm wide facets populated with a total of 1184 rectangular modules, which are nearly identical to the FPIX. The total number of pixels increases by a factor 1.6 from 48 M to 79 M.

A low mass support structure with integrated cooling tubes provides mounting points for the modules. The cooling tube diameter is significantly reduced with respect to the present detector, because the CO₂ cooling requires a much smaller mass flow than C₆F₁₄. This reduces substantially the amount of material in the tracking region. A further, significant reduction is achieved by moving the module connector area from the detector bulkheads to higher z , outside of the tracker acceptance, by using longer module cables.

The overall layout of the system is unchanged. The detector barrel is complemented with supply tubes on the $+z$ and $-z$ sides. The supply tubes carry electrical connections and cooling lines from the patch panels to the barrel bulkheads and house auxiliary on-detector electronics. Detector barrel and supply tubes are divided vertically, allowing insertion in the presence of the beam pipe. This is necessary for the installation of the upgraded detector in an extended technical stop. It is also crucial for the ability to replace the inner detector layer with fresh modules when the performance degrades after radiation damage. The degradation is gradual and one replacement during a period corresponding to an integrated luminosity of 500 fb⁻¹ is foreseen.

The ladder arrangement provides between 0.5 mm and 1 mm of overlap in the r - ϕ direction. The division into half-barrels is made in such a way that all facets and modules have the same geometry and no special modules are needed for the boundary region (Figure 4.3). The modules do not overlap along the z -direction. The size of this insensitive region between modules, including sensor guard rings, is 2.2 mm, corresponding to 3.3% of the active area.

4.2 Detector Elements

The barrel detector mechanically consists of two half-barrels (Figure 4.4), each divided into four layers. The layers are separate mechanical structures which are only joined after all modules are mounted. The mechanical structure and all connections are arranged in a way that permits replacement of the inner layer without disconnecting the other layers.

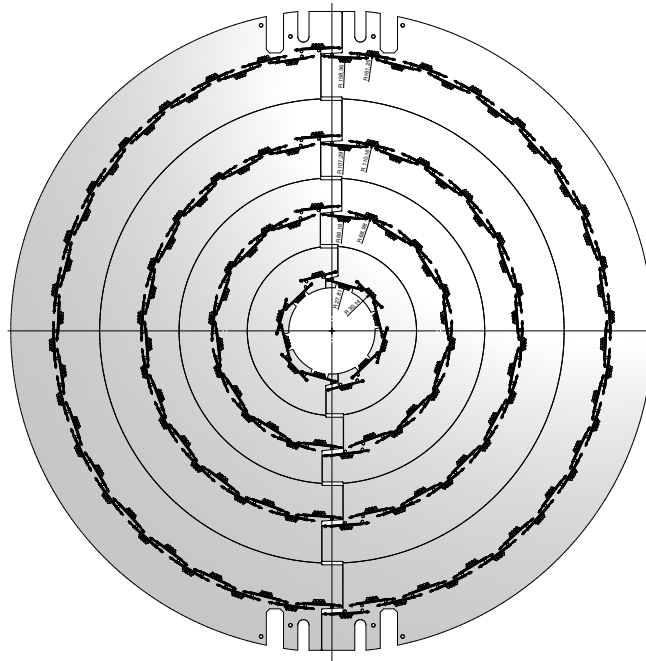


Figure 4.1: Pixel Barrel cross section showing the facet arrangement in the four detector layers. The inner layer (L1) is the 12 facet design for the 45 mm diameter beam-pipe. Details of the end-flange and wheels are not shown.

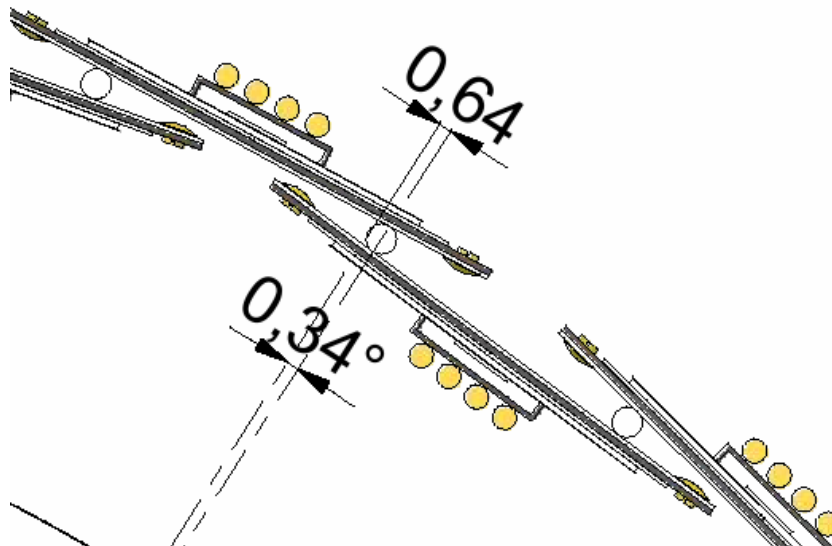


Figure 4.2: Detail of the barrel cross section showing the module positions on the cooling tubes (white circles). The overlap between modules varies, in this case the active regions overlap by the nominal beam position. The yellow circles illustrate the cables of modules positioned closer to the center of CMS (in z) which lie on top of other modules.



Figure 4.3: Boundary region of the barrel half-shells. After closing the half-shells with the adjustable wheel, full ϕ coverage is achieved. All modules, including those on the barrel edges, have the same geometry. The available width for facets in layer 1 is smaller than in L2-L4. Modules in L1 are therefore mounted without base-strips.

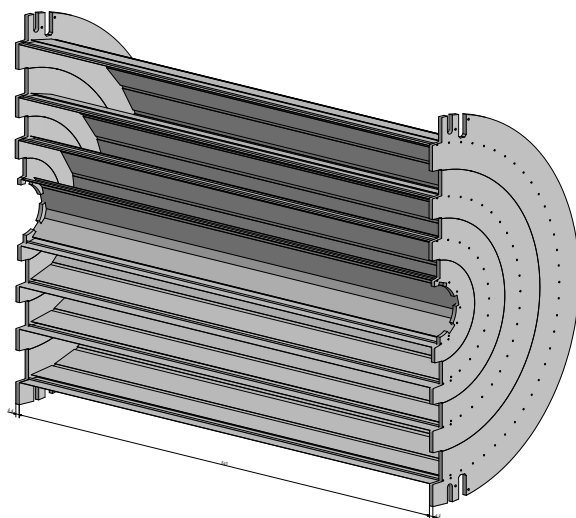


Figure 4.4: Drawing of one half-shell of the pixel barrel detector. Each of the four layers has a separate mechanical structure including cooling tubes and end-flange.

layer	radius	facets	modules
4	160 mm	64	512
3	109 mm	44	352
2	68 mm	28	224
1	30 mm	12	96
(1*)	(39 mm)	(16)	(128)
			1184

Table 4.1: Barrel layer summary. The last row (1*) shows the alternative layout using the old beam pipe with 59.6 mm outer diameter. The 12 facet design requires the smaller beam pipe with 45 mm outer diameter.

4.2.1 Modules

All layers are equipped with 2×8 -ROC modules of the same size (22 mm \times 66 mm). The module is slightly wider than those installed in 2008 because of the increased periphery of the readout chip. The length (z-coordinate) is unchanged. A detailed description of the module is found in Chapter 6.

4.2.2 Facets and Layers

A row of 8 modules forms a 22 mm wide facet with a length of 560 mm. The facets approximate the cylindrical shape of the barrel. Their surfaces are perpendicular to the radial direction without tilt (Figure 4.1). The radial positions of adjacent facets alternate by ~ 3 mm, allowing an overlap in the $r - \phi$ direction. Furthermore, the orientation of the facets alternates between pointing inside and pointing outside in adjacent layers in order to be able to cool two neighbouring facets through the same cooling tube (Figure 4.2). A summary of the layers is given in Table 4.1.

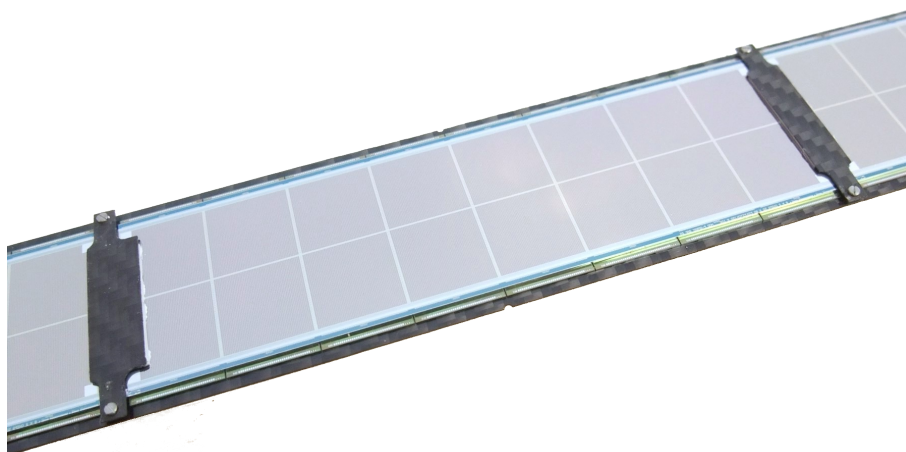


Figure 4.5: Carbon fiber blades with Layer 1 module (without HDI). The modules have no base strips and are held by carbon fiber pieces.

4.3 Mechanics Design & Prototypes

Cooling tubes running parallel to the beam pipe along the length of the pixel barrel form the skeleton of the mechanical structure. The tubes are held in position by end-flanges at $z = \pm 270$ mm. Modules are mounted onto Carbon fiber blades with a thickness of $200\ \mu\text{m}$ which are glued onto two cooling tubes. The carbon fiber sheets of the blades are connected at the edges by glue joints to improve the stiffness of the structure. Unnecessary material under the modules is cut away from the sheets.

4.3.1 Module Mounting Clamp/Screws

The modules of layer 2, 3 and 4 have base strips with $0.7\ \text{mm}$ mounting holes in parts of the base strips that extend $6\ \text{mm}$ beyond the ROC periphery (Figure 6.1). Two $0.5\ \text{mm}$ screws per module and corresponding nuts glued to the CF blades hold the modules. This mounting scheme has been used successfully for the first CMS pixel detector. The geometry of the innermost layer can not accommodate the additional module width needed for the basestrips and screws. Instead, screws will be placed in the area between (in z) two modules. The inactive part of the sensor extends $0.8\ \text{mm}$ beyond the edge of the outermost ROC, such that between the last ROCs of one module and the first ROC of the next module an area of $1.1 \times 1.6\ \text{mm}$ is available for screws. Carbon fiber pieces mounted across the facet are attached by those screws and hold the modules (Figure 4.5). Handling and mounting of modules without base-strips are delicate. This procedure will be restricted to the first layer.

4.3.1.1 Installation Design Issues

The barrel detector half-shells are going to be installed when the beam-pipe and its support structure are in place. The diameter of the beam-pipe increases from $45\ \text{mm}$ in the central region to $95\ \text{mm}$ at the patch panel, from where the detector is installed ($130\ \text{mm}$ including the flange at $|z| = 3120\ \text{mm}$). For insertion the detector half-shells move on wheels guided in grooves that have a separation of $185\ \text{mm}$ at the patch-panel and converge to a parallel section with a distance of $66\ \text{mm}$ in the central region. These grooves have already been used for the first pixel installation. In order to accommodate the reduced clearances and tolerances, the wheels of the upgraded detector are adjustable, both horizontally and vertically. While the vertical adjustability is only needed to allow for offsets of the beampipe position relative to



Figure 4.6: Bottom part of the transition between the end of the supply tube (left) and the pixel barrel (right) in the installation test setup-up. The remote operation tool (left) with miniature camera and light source is engaged in the horizontal adjustment. The wheel is shown in the insertion position, 6 mm away from the nominal position. The wheel for the supply tube (not shown) is not adjustable.

the CMS experiment, the horizontal adjustment is also used to maximize the clearance during insertion.

When the half-shells have reached the center of CMS, they are moved inwards horizontally to their final positions. A remote operation tool has been developed for this purpose (Figure 4.6). It engages in Allen screws attached to operate a lever/wedge system that can move the detector horizontally between +6 mm (away from the beam) and -4 mm (towards the beam), or vertically by ± 3 mm. Larger vertical offsets (up to ± 6 mm) can be accommodated by inserting (or removing) spacers before insertion. Only the bottom set of wheels has the vertical adjustment mechanism, while the top wheels are pushed towards the grooves by springs. The length of the remote operation tools is given by the distance between the insertion point (the PP0 patch panel) and the barrel endflange in its final position, about 2.3 m. A camera and light source attached near the tooltip allow precise operation without direct view. For operating the top wheels, the tool will be supported to avoid any risk for the beam-pipe during this procedure.

The supply tubes and the detector barrel are inserted together as no connections can be made when the detector is in its final position. The supply tube has its own wheels that can move independently from the detector barrel wheels. During insertion, the distance between barrel and supply tube is constant at the (horizontally) outer edge of the barrel where the cooling tubes come in. It varies in the center where the wheels are when detector barrel and supply tube are not both parallel to the beam-pipe. The wheels for the supply tube are not adjustable. Cables and cooling pipes connecting detector barrel and supply tube are flexible enough to follow the adjustments made to the barrel (Figure 4.11).

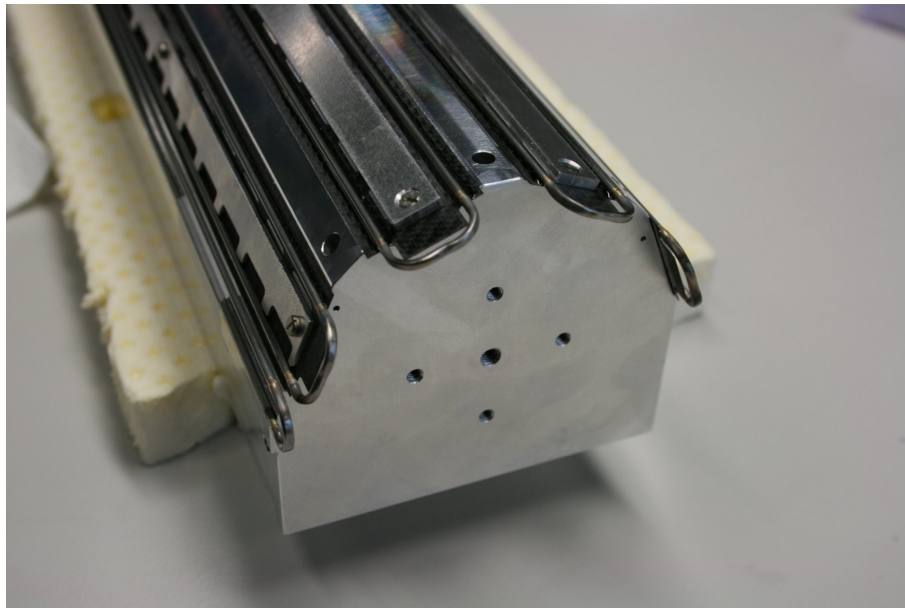


Figure 4.7: Layer 1 assembly jig. The inward-facing carbon fiber blades are mounted on jig and temporarily held by metal bars. The pre-assembled cooling loop structure is glued onto the carbon fiber. Later, the outward-facing carbon fiber facets are added. The picture shows a prototype for the 16 facet design.

4.3.2 Flanges

Flanges at both ends of the barrel detector stabilize the mechanical structure. A low mass sandwich structure consisting of 4 mm thick Airex foam covered by 200 μm carbon fiber sheets is foreseen. Each of the four half-flanges consists of four separate rings for the four layers of the detector. The adjustable wheels are attached to the top and bottom of each of the four half-flanges. Carbon fiber rods running outside of layer 4 between the +z and the -z flange absorb forces that arise during insertion or extraction when the barrel system is pushed into the CMS detector. Additional carbon fiber pieces re-inforce the flanges at those points.

4.3.3 Fabrication, Assembly

The mechanical structure of each layer is assembled on CNC machined jigs defining precisely the positions of carbon fiber blades, cooling tubes and flanges. Carbon fiber parts are cut out of flat sheets with a water-jet cutter to a precision better than 10 μm . Holes for module-mounting screws are drilled on a separate jig. Cooling loops are assembled and brazed on a dedicated jig and glued onto the inner set of carbon fiber facets as one piece. Finally the outer set of facets is added. The assembly of the layer 1 prototype mechanics is shown in figure 4.7 before adding the outer facets.

The carbon fiber and foam pieces of the flanges are also made with water-jet cutting. The flanges have slits for the cooling tubes and carbon fiber facets and are mounted onto the fully assembled structure.

4.3.4 Prototypes (L1, insertion mock-up)

Key elements of the detector structure have been fabricated as prototypes: A layer 1 support including flanges and cooling tubes (Figure 4.8), adjustable wheels and one 1/4 supply tube.



Figure 4.8: Layer 1 support structure prototype (16 facet design). All layers form independent mechanical structures that are joined when fully populated with modules. The first layer can be removed and replaced without separating the remaining layers.

The L1 mechanics prototype was built in production quality and demonstrated the feasibility of the assembly procedure. The vertical deflection caused by the gravitational force on a load corresponding to the detector modules was found to be $40\text{ }\mu\text{m}$ in the weakest direction. No change of the mechanical properties or delamination was found after thermocycling 48 times between $-10\text{ }^{\circ}\text{C}$ and room temperature.

To verify clearances and the insertion, a full size model of the pixel volume including the groove system was built (Figure 4.9). The insertion test structures are less detailed but model accurately the envelopes of the pixel volume inside CMS, the beam-pipe with supports, the supply tube and the barrel detector. A groove system made after the original CAD drawings of the CMS detector is included and the insertion of the complete system with adjustable wheels and remote operation tools has been exercised and optimized.

4.4 Supply Tube

The supply tubes on both (z) sides of the barrel detector carry power, control and cooling connections from the patch panel area to the barrel detector. Additional on-detector electronics, such as electrical-to-optical converters and DC-DC converters are also mounted there. The supply tubes occupy the radial region between 175 mm and 190 mm radius (215 mm at $|z| > 1970\text{ mm}$). Like the detector itself they are divided vertically for installation, hence four 1/4-cylinders are needed. In the z -direction, the supply tube can be thought of as organized into four regions (Figure 4.10). The end of the supply tubes that is near the detector (segment D) lies inside of the core tracking region of CMS. The first 50 cm ($|z| < 800\text{ mm}/\eta < 2.2$) contain as little material as possible beyond what is needed for the service connections. Connectors for the module cables are placed in the next segment (C). Spreading connectors properly along the z -direction according to the position of the corresponding module on the barrel permits using a single cable length for all modules. Cables from layers 1+2 will be routed to the inner surface and connected there while cables from layers 3+4 are connected on the outer surface.

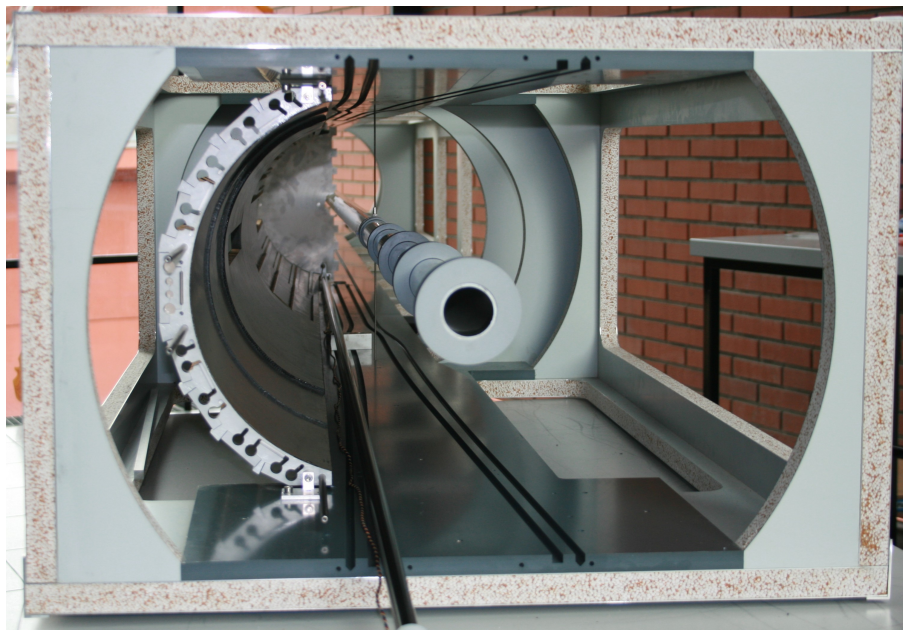


Figure 4.9: CMS pixel volume mock-up with installation groove system. The conical part of the beam-pipe is represented by PVC pieces around the cylindrical tube. One quarter supply tube prototype with barrel mock-up has been inserted.

Close to the connectors in the third segment (B) are the electrical-to-optical converters (POH) for transmitting the detector data and the on-detector part of the detector control system. The last segment (A) which is closest to the flange at the patch-panel contains DC-DC converters. Optical transmitter/receivers and DC-DC converter in segments A and B are outside of the tracking acceptance at $|z| > 130$ cm ($|\eta| > 2.7$). The PP0-side flange is a 15 mm thick Al ring. It stabilizes the supply tube and provides strain relief for the stiff power cables that are clamped firmly to the flange.

In the transverse view the 1/4-supply tube is organized into 9 phi-sectors. Eight sectors are equipped with electronics providing services for the barrel. The ninth (central) sector is not fully useable because it contains an opening for the horizontal beam-pipe support that is pulled into position after insertion of the pixel detector in segment (B). The (A) segment of this central sector contains the optical converters for the CCU system that is used to provide configuration data and monitoring for the auxiliary electronics in the other eight sectors. The other eight sectors are electrically identical and contain the components for electrical-optical conversion, fast control, readout and DC-DC converters.

The fast control system provides clocks, triggers and ROC configuration data. It is almost unchanged with respect to the first pixel detector. In each sector it contains two independent optical control links (DOH). A PLL separates trigger and clock signals. An adjustable delay chip aligns the signal phase with the LHC clock and the fast control data with the clock. The five address bits of the TBM permit a maximum of 32 modules connected to each control group. Each sector of L4 has 16 modules. The number of modules in layers 1,2,3 varies. The pixel modules with ROCs and TBM receive their configuration data through fast control links from the FECs. The electronics on the supply tubes is configured by the CCU system. It has a ring architecture with one CCU per sector plus one additional CCU in the central sector which is needed for redundancy. Either one of two optical links can be used to operate a CCU ring. The optical hybrid for the CCU system is also located in the central sector. In contrast to the previous de-

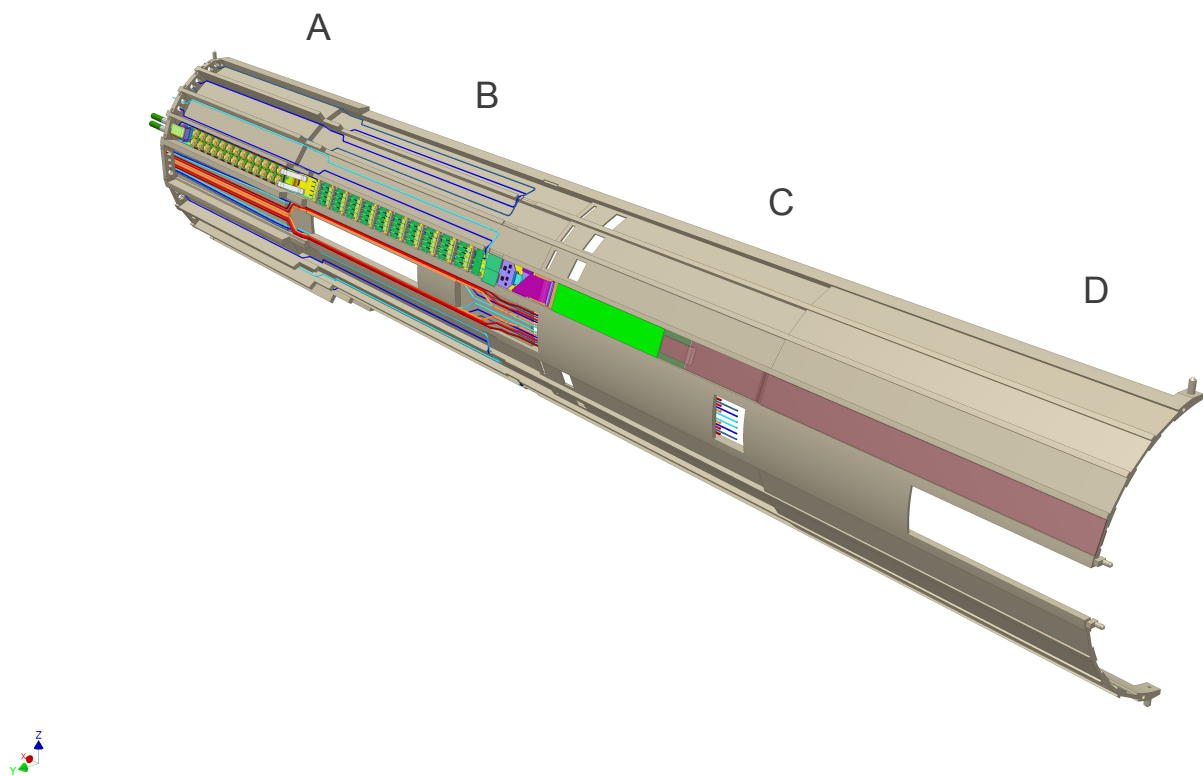


Figure 4.10: Pixel barrel supply tube. The (D) segment is the one closest to the detector with the lowest mass. Module cables are connected in segment (C), both, inside and outside. The outer segments contain auxiliary electronics (B) and the DC-DC converters (A). Only one sector is shown with electronics. Cooling loops for the auxiliary electronics and DC-DC converters are visible in the other sectors of segments (A,B). The central sector with the opening for the beam-pipe support contains cooling loops. The CCU-electronics is not shown.

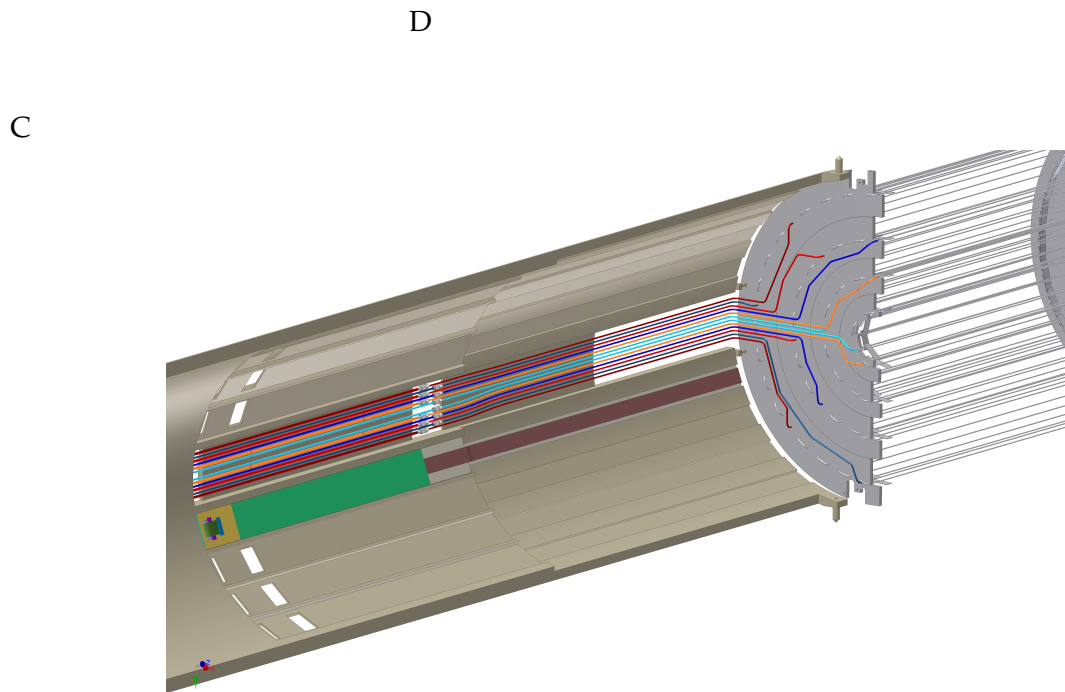


Figure 4.11: Transition between supply tube (left) and pixel barrel (right). The cooling lines are in the central sector. Cooling tubes can move freely between the connection point in segment C and the barrel to allow sufficient flexibility during insertion. The other sectors contain connection boards receiving the module cables. Only one such board is shown.

tector, each CCU is now physically located in the sector that it operates. This was necessitated by the large number of connections required for the control of the DC-DC converter system.

4.5 The Barrel Pixel Cooling Layout

In the Barrel Pixel detector, each one of the four layers will be connected to two separate cooling loops from the cooling plant, one arriving to the detector on the $+z$ end of CMS and the other on the $-z$. Before entering the Pixel support tube each main cooling loop will need to be manifolded into the numerous detector-cooling loops, following the segmentation described in Table 4.2. Each detector loop will cool the full barrel length over a given azimuthal range, and its inlet and outlet pipes will be located on the same z -side (Figure 4.12). All inlet detector-cooling tubes, mounted on the supply tube shells, will be used to cool the electronic devices there. In this way, the subcooled CO_2 that is fed by the cooling plant will be able to reach saturation and start boiling before reaching the detector section of the cooling loop. Detector loops connected to a single main loop (also called "parallel loops") will be designed such that they exhibit very similar operation parameters even under changing thermal load conditions. Calculated typical operation parameters are shown in Table 4.3. In addition, the unavoidable small differences in thermodynamic behavior between the different loops will be mitigated by the presence of capillaries after the manifolding. The expected performance of this cooling system is shown for the most demanding detector-cooling loop 2 of layer 2 in Figure 4.13, where CO_2 and tube wall temperatures are plotted along the full length of the loop. In order to visualize the correspondance between thermal load and temperature behaviour the distribution of the thermal load is also indicated. It is calculated that the tube's surface temperature will not exceed -14°C when the CO_2 inlet temperature is -20°C even under the most stringent

z-axis	Transfer Lines inlet & outlet	Support Tube half cyl. shell name	x-axis	slot# on ST shell (#1 on top)	Detector Layer	Loop name	Loop length [cm]
+z	ML1P	BpI	+x	3,4	LYR1	L1D1PN	948
		BpO	-x	6,5		L1D2PF	948
	ML2P	BpO	-x	3,4	LYR2	L2D1PF	1174
		BpI	+x	6,5		L2D2PN	1174
	ML3P	BpO	-x	1,2,3,4	LYR3	L3D1PF	1291
		BpI	+x	8,7,6,5		L3D4PN	1291
		BpI	+x	1,2,3,4		L3D2PN	1277
		BpO	-x	8,7,6,5		L3D3PF	1277
	ML4P	BpI	+x	1,2	LYR4	L4D1PN	1299
		BpO	-x	8,7		L4D4PF	1299
		BpO	-x	1,2		L4D2PF	1164
		BpI	+x	8,7		L4D3PN	1164
	ML1M	BmO	-x	3,4	LYR1	L1D1MF	949
		BmI	+x	6,5		L1D2MN	949
	ML2M	BmI	+x	3,4	LYR2	L2D1MN	1172
		BmO	-x	6,5		L2D2MF	1172
	ML3M	BmI	+x	1,2,3,4	LYR3	L3D1MN	1291
		BmO	-x	8,7,6,5		L3D4MF	1291
		BmO	-x	1,2,3,4		L3D2MF	1274
		BmI	+x	8,7,6,5		L3D3MN	1274
	ML4M	BmO	-x	1,2	LYR4	L4D1MF	1188
		BmI	+x	8,7		L4D4MN	1188
		BmI	+x	1,2		L4D2MN	1164
		BmO	-x	8,7		L4D3MF	1164

Table 4.2: The table details the connection of the detector cooling loops to the transfer lines and defines the orientation of the loops within the CMS co-ordinate system. The loop names are constructed by the layer number, a loop number counting the loops on a single shell and the z- and x-polarity (P/M and N/F respectively). In addition the total loop length starting and ending at PP0 is given.

beam conditions. The difference between those $-14\text{ }^{\circ}\text{C}$ and the proposed $-4\text{ }^{\circ}\text{C}$ sensor temperature corresponds roughly to the observed temperature rise in the currently CMS-operated Bpix detector which, however, operates under a much smaller power dissipation (about a factor 2 less than the most exposed layer 1 of the upgraded detector). While the principal design of the detector structure does not differ much between the existing and the proposed detector, the necessary improvement in the heat conduction between cooling tubes and sensors can be achieved using thermal grease between the detector modules and the carbon fiber structure. In addition, the choice of a better conductive CFK material (K1100 carbon-carbon filling) and a conductively enhanced glue (e.g. OMEGABOND(R) 200) is investigated to keep the sensors temperature below $-4\text{ }^{\circ}\text{C}$ under all conceivable loads.

z side	Detector loop	Low thermal load [W]	Lumi = 0 Fluence = 0				High thermal load [W]	Lumi = 2.5×10^{34} Fluence = 250 fb^{-1}			
			P input [bar]	ΔP [bar]	vapour quality	TCO_2 max [°C]		P input [bar]	ΔP [bar]	vapour quality	TCO_2 max [°C]
+z	L1D1PN	80	20.7	1.04	0.12	-18.4	171	21.4	1.74	0.24	-17.4
	L1D2PF	80	20.7	1.05	0.12	-18.4	171	21.4	1.75	0.24	-17.4
	L2D1PF	158	21.9	2.20	0.22	-16.7	188	22.1	2.43	0.26	-16.3
	L2D2PN	158	21.9	2.21	0.22	-16.6	222	22.7	2.97	0.30	-15.5
	L3D1PF	161	22.0	2.30	0.22	-16.8	197	22.5	2.84	0.27	-15.8
	L3D4PN	161	22.0	2.32	0.22	-16.6	197	22.5	2.86	0.27	-15.7
	L3D2PN	169	22.0	2.39	0.23	-16.5	206	22.65	2.88	0.28	-15.6
	L3D3PF	169	22.1	2.35	0.23	-16.4	206	22.6	2.90	0.28	-15.6
	L4D1PN	174	22.2	2.50	0.24	-16.3	199	22.5	2.86	0.27	-15.7
	L4D4PF	174	22.2	2.51	0.24	-16.3	199	22.5	2.87	0.27	-15.7
	L4D2PF	166	21.9	2.20	0.23	-16.7	190	22.2	2.54	0.26	-16.2
	L4D3PN	166	21.9	2.22	0.23	-16.7	190	22.2	2.56	0.26	-16.1
-z	L1D1MF	96	20.8	1.14	0.14	-18.2	220	21.8	2.08	0.31	-16.9
	L1D2MN	96	20.9	1.15	0.14	-18.2	220	21.8	2.10	0.31	-16.9
	L2D1MN	142	21.8	2.11	0.20	-16.8	199	22.5	2.81	0.27	-15.8
	L2D2MF	142	21.8	2.12	0.20	-16.8	199	22.5	2.82	0.27	-15.8
	L3D1MN	145	21.9	2.13	0.20	-16.7	178	22.3	2.61	0.24	-16.0
	L3D4MF	145	21.9	2.14	0.20	-16.7	178	22.3	2.62	0.24	-16.0
	L3D2MF	169	22.1	2.34	0.23	-16.4	206	22.6	2.89	0.28	-15.6
	L3D3MN	169	22.1	2.36	0.23	-16.4	206	22.6	2.91	0.28	-15.6
	L4D1MF	158	21.8	2.12	0.22	-16.8	182	22.1	2.41	0.25	-16.4
	L4D4MN	158	21.8	2.13	0.22	-16.8	182	22.1	2.42	0.25	-16.3
	L4D2MN	166	21.8	2.20	0.23	-16.7	290	22.2	2.54	0.26	-16.2
	L4D3MF	166	21.9	2.22	0.23	-16.7	290	22.2	2.55	0.26	-16.1

Table 4.3: Calculated operational parameters for all detector-cooling loops under two extreme load conditions for a typical flow of 2.5 g/s. Listed are the starting pressure, the pressure drop over the loop, the accumulated vapor fraction (called vapor quality) and the maximum CO_2 temperature obtained. For the transfer of liquid CO_2 a temperature of -20°C has been chosen.

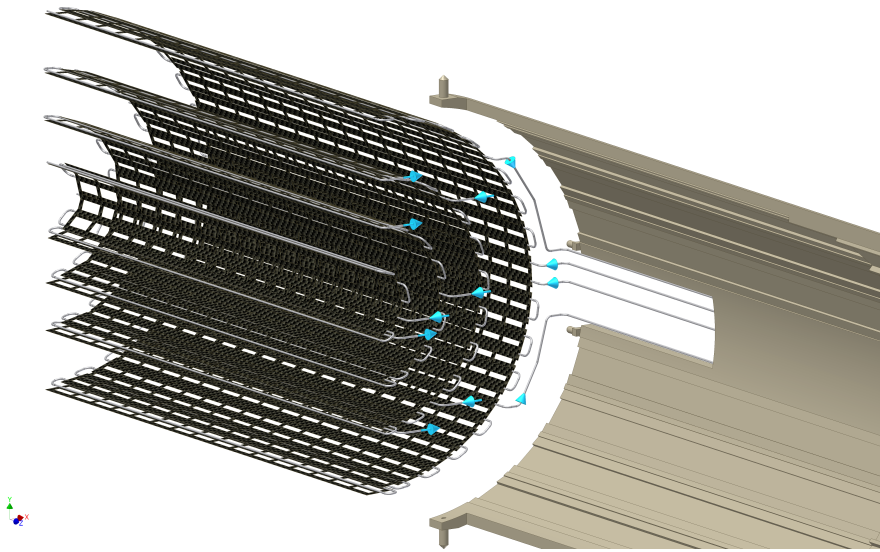


Figure 4.12: The CAD picture shows a 3-dimensional view of half of the BPIX detector and some of its cooling connections to the supply tube. Connections on the other end have been omitted to enhance clarity. The gap between detector and supply tube is not to scale.

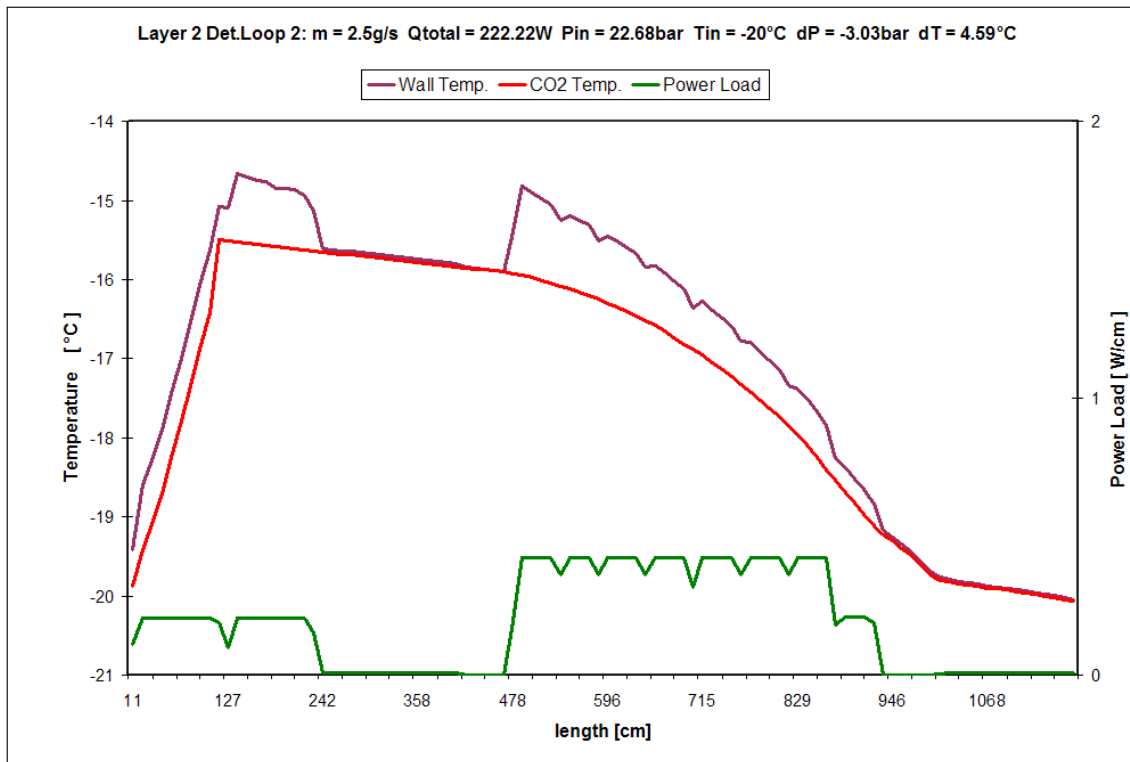


Figure 4.13: Expected heat load and CO₂ temperature along a cooling loop in BPIX layer 2. The temperature of the pipe illustrates the changes of heat transfer coefficient of the coolant. The rise at the left side is caused by cooling the DC-DC-converters using pure liquid. After about 120cm the subcooled liquid reaches saturation and starts boiling. From this point on the temperature of the 2-phase mixture decreases in correspondance with the pressure loss mainly caused by friction. The thermal load (in green) shown in the left as well as in the right section of the loop is emitted from electronic devices on the supply tube. The detector modules are the origin for the high load in the central part. In addition, the temperature of the tube's wall is shown indicating that heat transfer within the coolant improves with increasing vapor quality resulting in a smaller difference between coolant and wall temperature.

4.6 Material Budget

The amount of material in the tracking volume is reduced with respect to the existing pixel barrel mainly by relocating the module connectors and by using the low mass CO₂ cooling. The material budget in the innermost layer is further improved by thinning the ROCs and by the omission of the SiN base-strips. The mass of a L1 module (excluding the cable) is 1.6 g, half of which is contributed by the sensor. An outer layer module with base-strips and 175 μm thick ROCs has a mass of 2.4 g. Including overlaps, the modules represent a thickness corresponding to 1.1% of a radiation length for normal incidence in the outer layers and 0.74% in layer 1. Cooling tubes, CO₂ and CF support correspond to an average 0.2% of a radiation length and the contribution of the module cables varies between 0 and 0.3% depending on z . The prototype Layer 1 mechanics (Figure 4.8) has a mass of 55 g per half-shell. The full mass of the detector barrel (without supply tubes) is estimated to be 5 kg, significantly less than the existing 3 layer detector. The material budget as a function of pseudo-rapidity is shown in Figure 2.2.

4.7 BPIX Production, Assembly and Functional Testing

The production of the barrel modules happens in production centers in Switzerland, Italy, Germany and at CERN. Assembled and fully tested modules are mounted on the respective mechanical structure which is transported to the integration site when fully populated.

The modules for layers 2-4 are mechanically almost identical to the present pixel detector and the same mounting procedure will be followed. A tool exists to pick up a module and place it on the carbon fiber facet. It includes holes to guide the screw driver for fixing the module without risk of damaging the module. A rotating fixture permits mounting each module in a vertical direction. In contrast to the previous detector, cable connections are not made on the barrel itself and the long module cables need to be fixed to auxiliary cylinders similar to the first segment of the supply tubes. At this point individual modules can still be tested with air cooling alone. This will verify that modules were not damaged during mounting or transportation to the integration site.

The final assembly steps are the mechanical connections of the barrel layer half-shells to complete half-barrels and the connection to the supply tubes at the integration site.

Twelve cooling tubes on each ($\pm z$) side of a half-barrel are connected to the supply tube lines with miniature fittings in segment C of the supply tube.

The cables of Layer 1 and 2 are connected at the inner surface of the supply tubes (segment C) while the cables of layers 3 and 4 are connected at the outer surface.

As for the present detector [34], the fully assembled half-detectors including supply tubes and all connections, will be tested and repaired as necessary at the integration site of the swiss consortium. This test will be made on a sector-by-sector basis using a slice of the CMS pixel power supply and data-acquisition system. The fully assembled and tested pixel barrel system will be transported to CERN. No transport damages occurred in the present detector, but the sector-wise test will be repeated upon arrival using the same or an identical slice of the DAQ and power-supply system.

Chapter 5

Front End Chips & Readout Chain

The current readout chain has been designed for operation at 25 ns bunch spacing and luminosities up to $1 \times 10^{34} \text{ cm}^{-2} \text{ s}^{-1}$. Given the current LHC operational experience it appears that the present readout chain of the pixel system has to be modified for efficient readout at $2 \times 10^{34} \text{ cm}^{-2} \text{ s}^{-1}$ operation and potential 50 ns bunch spacing. Keeping the 100 kHz L1 rate results in a considerable enhancement of data rates that requires modifications in the readout chip and the link speed. The net result is a factor of four higher data volume compared to the original LHC design goals. Under these conditions, the data links of the innermost layer of the current pixel system would reach their maximum throughput rate, resulting in a dramatic drop of readout efficiencies to 50% or less. The reduction of the innermost layer radius from 44 mm

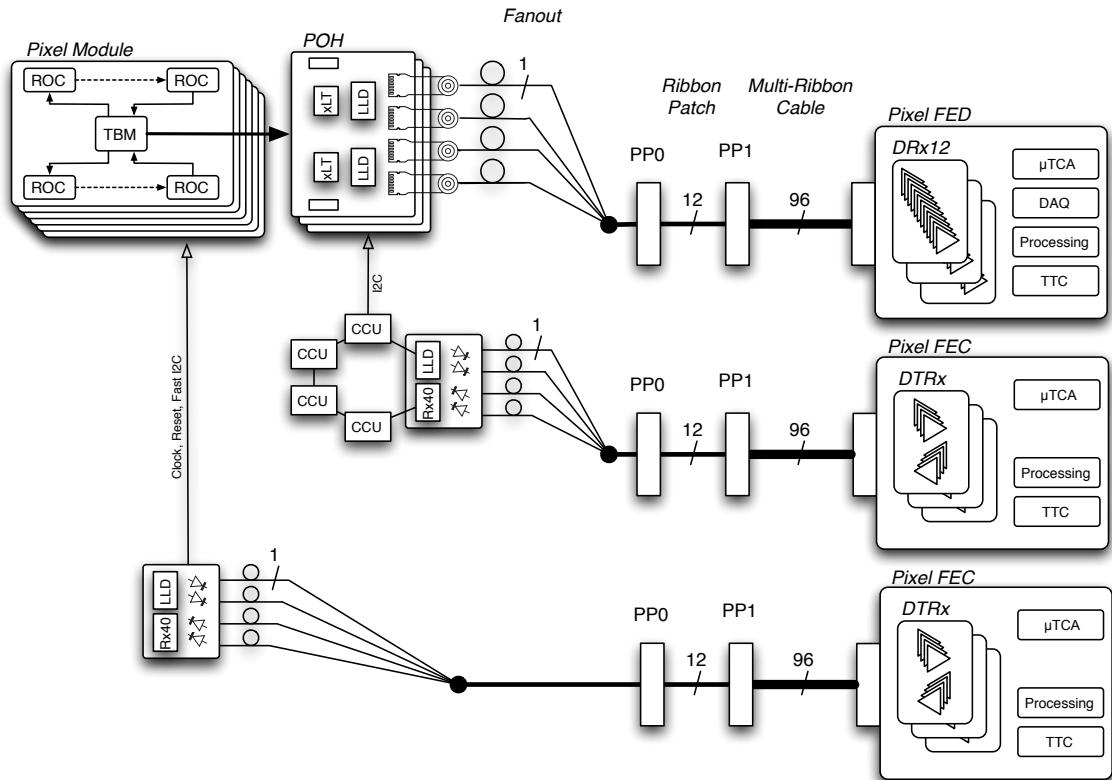


Figure 5.1: Pixel readout and control strings. All components up to PP0 are inside the pixel volume, PP0 is at the tracker bulkhead, PP1 is an intermediate patch-panel inside the vactank and the FEDs and FECs are in the service cavern.

to 29 mm leads to an additional increase in the data rate requirements. In the new system this situation is dealt with by going to a higher link speed with a digital protocol and dead time reducing changes inside the readout chip. In addition, we will increase the number of fibers in the pixel readout, drawing upon spare capacity installed in 2007.

The change of the readout protocol from the 40 MHz analog coded to 400 Mbit/s digital results in a doubling of the data throughput per fiber. For the outer layers (2-4) this provides sufficient reserve for the future expected LHC operations. For the innermost layer the number of fibers per module is in addition increased from two to four, resulting in an overall factor of 4 over the present layer 1 situation. A number of design modifications in the periphery of the readout chip allow efficient operation under these increased data rates. The changes in readout protocol and link speed also require modifications of the Token Bit Manager (TBM) ASIC, the optical link and the Front End Driver (FED).

An overview of the modified readout chain is given in Figure 5.1. A pixel hit in the silicon is registered in the Read Out Chip (ROC). The basic operation of the ROC is to store and output hit information for pixels with charge exceeding a set threshold. Hits consisting of an address, a pulse height and (shared) time stamp information are stored temporarily for each group (Double Column) of 160 pixels, until the read-out is triggered. The information from the ROC is sent to the TBM. The TBM serves as the central hub for downloading constants to each ROC, sending triggers and resets, and acquiring the hit information from each ROC it is connected to. From the TBM, the pixel data is sent via Optical Hybrids (POH) over long fibers to the optical receivers (DRx12) in the FED located in the service cavern. The FEDs buffer and decode the serial data streams from many TBMs and send it to the central DAQ. Control data and trigger signals originate in the Front End Controller (FEC) and are sent optically via a receiver/transmitter chip (DTRx) to the detector optical receiver/transmitter (DOH). One flavor of FEC is used to control the settings for the AOH's, DOH's (the AOH and DOH use the same Linear Laser Driver (LLD) chip), PLL's and delay settings via the Communication and Control Unit (CCU). The other flavor of FEC operates using a high speed I2C protocol for downloading information to the TBM and provides clock and fast control signals (e.g. resets).

5.1 ROC development

The current PSI46V2 chip used in running at CMS since 2007 is expected to have a data loss rate of 4% in the innermost barrel layer at design luminosity (115 MHz/cm² pixel hit rate). For the phase 1 upgrade detector, rates of nearly 600 MHz/cm² are anticipated and a new approach is warranted for the readout chip (ROC) and the readout chain. The new ROC has improvements in the internal data handling mechanisms and also in the readout approach. Column drain speed and width will be increased as will be the buffer depth for both the data (hits) and time stamp attached to the data.

The development of the new ROC is an evolution of the existing PSI46v2 chip. Table 5.1 shows a comparison of the old and new designs. This evolution allows us to benefit from the previous experience and infrastructure developed during production, testing and commissioning of the present readout system.

5.1.1 Performance and Limitation of current Pixel ROC

The basic operation of the ROC is to store and output hit information for pixels with charge exceeding a set threshold. Each hit, consisting of address, pulse height, and (shared) time stamp information, is stored temporarily for each group (Double Column) of 160 pixels, until the hit

Table 5.1: Comparison of the PSI46V2 and PSI46dig Readout chips. The values in parentheses for double column speed and data loss are for the advanced version of the PSI46dig chip for Layer-1.

	PSI46V2	PSI46DIG
ROC size	7.9 mm x 9.8 mm	7.9 mm x 10.2 mm
Pixel size	100 μm x 150 μm	100 μm x 150 μm
Smallest radius	4.3cm	2.9cm
Settable DACs / registers	26 / 2	19 / 2
Power Up condition	not defined	default values
pixel charge readout	analog	digitized, 8bit
Readout speed	40 MHz	160 Mbit/s
Time stamp Buffer size	12	24
Data Buffer size	32	80
Output Buffer FIFO	no	yes
Double column Speed	20 MHz	20 MHz (40 MHz)
Metal layers	5	6
Leakage current compensation	yes	no
in-time threshold	3500 e	< 2000 e
PLL	no	yes
Data loss at max Operating flux	$\sim 3.8\%$ at 120 MHz/cm ²	1.6% at 150 MHz/cm ² ($\sim 3\%$ at 580 MHz/cm ²)

information is read out. While at low pixel hit rates the system is almost dead time free, there are several data loss mechanisms inherent to the architecture which can become important with increasing hit rates and finally set a limit to the maximum luminosity at which the ROC can be operated. These mechanisms have been studied extensively with detailed simulations of the data flow in the present and future ROC. For luminosities beyond $1 \times 10^{34} \text{ cm}^{-2} \text{ s}^{-1}$ there are several data loss mechanisms which need to be reduced, the most important being overflows in time stamp and data buffers, speed limitation in the transfer of hits from the pixels to the double column periphery, dead time of a double column while waiting to be read out and the loss of data history after resets. The CMS pixel ROC is now very well studied under high data rates in the LHC. The performance of the chip compares well with expectations. In particular, there is no indication for a new, unexpected data loss mechanism.

5.1.2 Design improvements for upgraded Pixel ROC

The ROC for the upgraded pixel detector is an evolution of the present architecture. It will be manufactured in the same 250 nm CMOS process. The core of the architecture is maintained, with enhancement in the performance in three main areas:

1. *Readout protocol.* In order to increase the readout link speed a change in signaling was needed. The present pixel system relies on linear data links where pixel addresses are encoded in 6 different analog levels. Furthermore, the analog pulse height information is transmitted. This system has reached its limit in terms of speed. The new ROC uses a 160 Mbit/sec LVDS data link and several new blocks of the chip have been developed:
 - A 160 MHz clock needs to be generated within the ROC from the 40 MHz which is distributed over the module. A PLL is needed to lock with the correct

frequency and phase

- A data serializer running at 160 MHz
- Digital LVDS output drivers
- An on-chip 8 bit ADC to digitize the pulse height information running at 80 MHz.
- An event builder which generates the output data format. Each ROC readout consists of a 12 bit ROC header followed by 24 bits of data per pixel hit (pixel address and pulse height information). The header starts with a unique 9 bit pattern followed by a 3 bit ID field. There is an arbitrary payload bit in the ID field. This will be used to transmit status information from the ROC, like the result of an on-chip current measurement.

There are benefits beyond the increased rate for the ROC: the digital readout removes the need for the complex decoding of a multilevel analog signal.

2. *Reduced data loss.* As the number of pixel hits per unit time increases, the number of storage buffer cells for time stamps and pixel data has to be increased as well. The size of these buffers has been optimized with detailed data flow simulations in the ROC. The new ROC has 24 time stamp buffer cells (12 for the present ROC) and 80 data buffer cells (32 for the present ROC). The data loss due to buffer overflows at fluences up to 600 MPix/sec/cm² is less than 0.5%. An additional buffer stage on the ROC level has been introduced. Pixel hit data from the double columns start to be transferred to this new readout buffer immediately after the L1 trigger validation. After being digitized, data wait there for the module readout token. In this way, the retention time of validated data in the double columns and hence dead time of the double columns can be substantially reduced at high link occupancies.
3. *Enhanced analog performance.* Several measures have been taken to reduce the operational charge threshold. The present pixel system operates at a threshold of about 3500 electrons. There are two contributions to this:
 - (a) The lowest charge threshold with which the ROC can be operated. For the present system this is at about 2800 electrons. It is defined by internal crosstalk rather than the amplifier noise. Extensive studies of possible cross talk mechanisms have been performed. As a result the power distribution system in the ROC has changed substantially. A 6th metal layer has been added together with a thicker top metal layer. Decoupling of the power rails has been improved and sensitive analog nodes are better isolated. Several signals have been rerouted and better shielded. An absolute threshold well below 2000 electrons can be expected¹.
 - (b) The difference, ΔQ , between absolute and in-time threshold. The latter is the lowest charge threshold for which hits are still assigned to the correct bunch crossing. Lower charge signals are lost due to time-walk. This is mainly a characteristic of the comparator in the pixel cell. Measurements in agreement with simulations have shown that the present pixel system has a ΔQ of 700 electrons. The comparator of the new ROC has been redesigned to increase speed without additional power. From simulations, a ΔQ of 100 to 200 electrons is expected.

In addition, a few changes for ease of system operation have been made. The regulators for the analog power and sample and hold circuit are now current-referenced and independent

¹Values below 1800 electrons have already been established with the first digital chip submission.

of each other. A power-up reset circuit guarantees that the system starts up in a well defined low power state. Certain DACs have been removed and replaced by fixed voltages or currents where, in the PSI46v2 ROC, they have never modified from default values. The leakage current compensation circuitry has been removed, since the preamplifier has proven to be sufficiently tolerant to input leakage current.

The new digital ROC with these improvements was submitted to the foundry in January 2012 and is currently being tested. High rate proton beam tests will be performed. A second iteration of the design will be submitted in fall 2012. At the same time an advanced version of the design will be submitted. This is needed for the innermost barrel layer at a mean radius of 2.9 cm, which will receive roughly a factor of two more particles per second, per unit area, compared to the current innermost layer at 4.4 cm. The present column drain architecture becomes inadequate at these very high data rates. The limitations are twofold: firstly, the protocol for the transfer of pixel hits to the data buffer reaches its limit in terms of speed; secondly, the fact that the double column becomes insensitive while it keeps trigger validated data, and resets itself after readout, leads to an unacceptably high rate of data loss. Two new concepts will be introduced to overcome these limitations:

1. Column Drain Cluster (CDC) algorithm. After a hit, the column drain algorithm performs a dynamic 4-by-4 pixel cluster search. It then transfers the whole cluster in parallel to the double column periphery. This leads to a gain in data rate of a factor 1.8 compared to the present Column Drain mechanism. Another factor of two is gained by doubling the transfer clock speed to 40 MHz, which becomes possible due to the reduced number of clusters compared to single pixels.
2. More elaborate pointer logic in the buffer management. A check-out mechanism makes sure that data buffer cells containing trigger validated data are skipped in the column drain transfer. Once the hits are digitized and written to the ROC readout buffer, the cells are checked-in again. The pointer logic to the corresponding time stamps must be modified. This not only allows continuous data taking, it also makes double column resets after readouts unnecessary. Resets will still be kept in the system but downscaled by 2 orders of magnitude. Occasional resets are needed periodically to ensure recovery of logic failures due to SEUs.

The CDC architecture is currently under development.

5.1.3 Simulation results of upgraded Pixel ROCs

The ROC has several internal buffers to temporarily store pixel hit data before it is validated by a L1 trigger or it is read out. The filling level of these buffers depends on the track rate and density, the trigger latency, the trigger rate and the bandwidth of the readout links. To properly dimension the buffers, realistic simulations of all data flows inside the ROC are needed. It also needs to be verified that other data loss mechanisms not related to buffer overflows remain acceptable.

For this purpose a standalone software package has been developed to support the design procedure. Input data is produced within the standard CMS software framework CMSSW. Events are generated with the Pythia6 event generator using the Z2star tune. All particles are propagated through the detector and the charge generated inside the pixel sensor (sim hits) is simulated within CMSSW which makes use of the GEANT4 package. For pile up simulation sim hits for signal-like events (a mix of heavy quark, Z and W production) and minimum bias

events are added with the correct timing information. Then the charge appearing at the sensor surface after drifting in the electric field is calculated. These pixel charges are used as the input to the simulation program describing the whole readout chain from the ROC to the FED. This approach gives a conservative estimate of data losses at small radii. The Pythia event generator with the Z2star tune gives a radial dependency of the track density of $r^{-1.8}$ while both measured pixel rates with the current pixel detector and sensor leakage currents indicate rather a $r^{-1.25}$ dependency. This difference adds about 60% at $r = 2.9\text{cm}$ in the simulation compared to the observed data rate scaling.

The data flow program is written in C++ and simulates all data flow paths inside the ROC and a module. It closely follows the electronic CMOS architecture, from the pixel unit cells via column drain to the data and time stamp buffers, trigger verification, readout buffer and data readout. The latter includes the data transfer from ROCs to the TBM and further on to the FED via the optical link, simulating the full readout protocol.

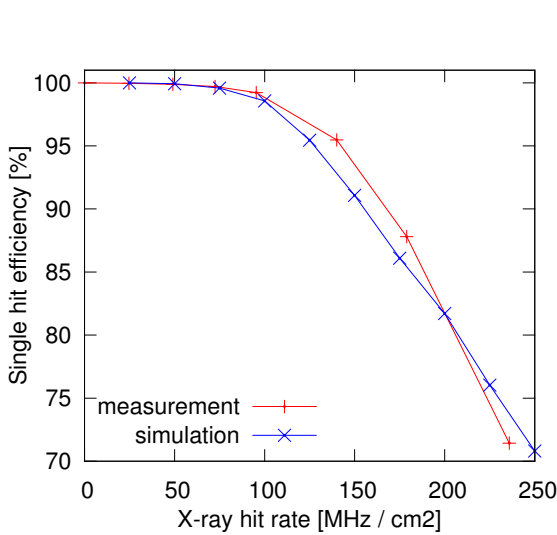


Figure 5.2: Comparison of measured and simulated single hit efficiency as a function of pixel fluence under X-ray irradiation for the current ROC PSI46V2.

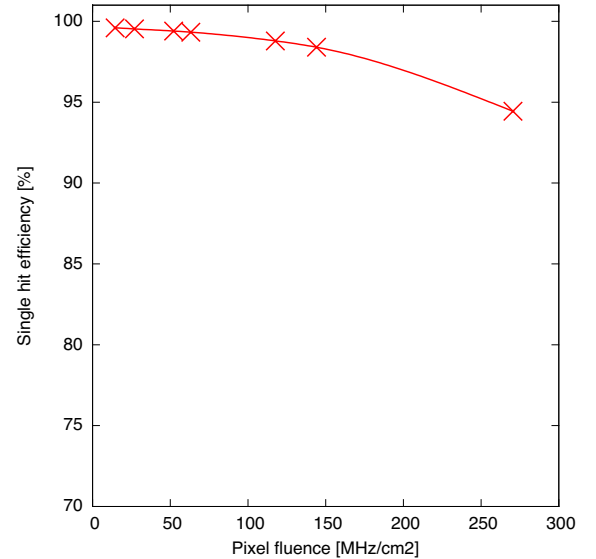


Figure 5.3: Simulated single hit efficiency as a function of pixel fluence for the new digital ROC (first submission not including the CDC modification) for events generated with Pythia using the Z2star tune.

Figure 5.2 shows as a cross-check the comparison of measured and simulated data losses for the current PSI46V2 ROC under X-ray irradiation. The single hit efficiency is shown as a function of the pixel fluence. The simulation is in fairly good agreement with the measurement. This plot cannot easily be compared with collision data, since X-rays produce mainly single pixel clusters and therefore produce more time stamps at the same pixel rate. Figure 5.3 shows the simulated single hit efficiency for the new digital ROC as a function of the pixel fluence. No detailed simulations for the advanced L1 ROC exist yet, since the architectural design process is still ongoing.

5.2 TBM development

The Token Bit Manager (TBM) controls the readout of a collection of ROC's and distributes clock, trigger, reset and is the interface for directing the downloading of ROC operating constants. The current TBM design must be modified, to accommodate the new digital readout of the ROC, as well as the increased data loads of the various layers of the detector. These various data loads require that three variations of the TBM be produced. The variations are as follows.

TBM07: This variation is for the outer rings of the forward pixel system. It contains a single TBM core, and will control one side of each blade. The output data of two of these chips will be combined by a DataKeeper chip into a single 400 MHz encoded data stream, sent through single fiber to the FED.

TBM08: This variation is for the inner ring of the forward pixels, and the outer layers of the barrel pixel. Due to the higher data rates, the TBM08 will contain the equivalent of two TBM07s, plus the Datakeeper chip on a single piece of silicon. It will output a single 400 MHz encoded data stream, sent through single fiber to the FED.

TBM 09: This variation is for the Inner two layers of the barrel, the inner most layer will require two TBM09s to handle the data rates. The TBM09 will contain the equivalent of two TBM07s, plus two Datakeeper chips on a single piece of silicon. It will output two 400 MHz encoded data streams, each stream will pass over a fiber to the FED.

Submission 1: January 2012. - TBM07

A TBM readout begins when the TBM sends out a header to the FED. As the Header completes, a token is transmitted to the first chip in the readout chain. That ROC now sends its data to the TBM, which in turn transmits it on to the FED. The Token is then passed to the next ROC, and so on. When the Token returns to TBM, a Trailer is transmitted to the FED, ending the event readout. If however, a ROC contains an excessive amount of data, the TBM has no way to interrupt that ROC. In order to limit the number of hits an event contains, a token out timer has been added. This timer can be set from 6.4 μ s to 1.3 ms. If the timer expires, before the Token returns, a Reset is transmitted to the ROCs, causing the ROCs to dump all remaining data. The TBM then sends a trailer, ending the current event, and making the event as an error. Any remaining events on the TBM stack are transmitted to the FED as "No Token Pass" events. This allows this TBM to catch up with other TBMs in the detector, while keeping this FED channel synchronized with all other channels.

The analog I/O section of the original TBM has been replaced. This new system increases the data rate by a factor of two, replacing the 40 MHz analog encoded digital signal, with a 160 MHz binary signal. This requires the inclusion of a 160 MHz PLL. The new header and trailer are modified to a 12 bit ID pattern (Header/Trailer), and 16 bits of data.

Under the old analog system, a simple summing amplifier could be used to combine the outputs of the various sets of ROCs and the TBM. With this digital system, the TBM needs to know which group of chips has the token, and therefore which input receiver to listen to. This is accomplished by routing the token back to a high impedance input on the TBM, each time the token switches from one group of ROCs to the next. It is envisioned that a version of this chip (designated TBM07) will be used on the Forward Pixel Pilot Blades described in Section 10.

Submission 2: Fall 2012

This upgraded pixel system is being designed to handle significantly higher data rates than its predecessor. This requires that each fiber carry more data. To accomplish this, the outputs

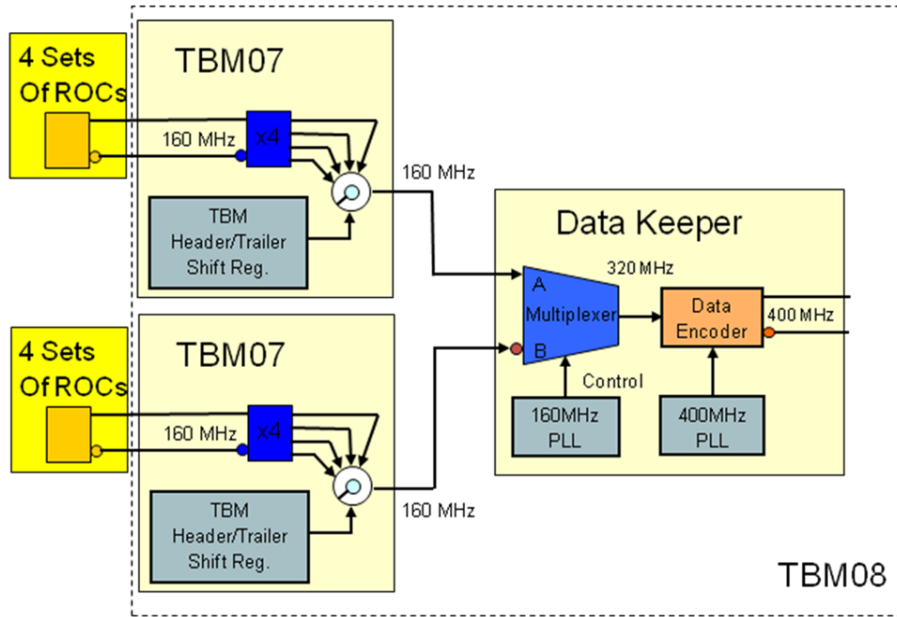


Figure 5.4: Two TBM07s with Data Keeper.

of two TBMs will be combined into one data stream, and encoded using a standard 4 to 5 bit NRZI encoding scheme to improve data transmission integrity. For this reason, the Forward Pixel system will require a Data Keeper chip, on a Port Card to combine the two streams and encode them at 400 Mbit/s (see Figure 5.4).

In regions of greater data rate, a single chip, combining two TBMs and a Data Keeper will be needed. The TBM08 will occupy the same space as a single TBM07, but handle twice the data rate.

Submission 3: Early 2013

In the region of highest data rate, a single fiber will be insufficient to handle the load. For this reason, the TBM08 will be modified to allow each TBM core inside to transmit encoded data from two groups of ROCs simultaneously (TBM09). Each core will have its own multiplexer/encoder at 400 MHz, and drive a signal to its own dedicated fiber up to the FED.

5.3 Opto-link

Due to the necessary changes to the ROC to reduce the inefficiencies in the present readout scheme, it quickly became obvious that the upgraded system should operate using digital readout. The data-rate generated by the new system has been calculated to be 320 Mbits/s per front-end module that houses 16 ROCs. Initially, it was thought that the Analog Opto-Hybrid (AOH) used in the present Pixel system could simply be rebuilt and used to transmit digital data at the increased rate. A key component of the AOH (its laser diode) is however no longer manufactured. It was thus decided to profit from the component selection studies being carried out in the framework of the Versatile Link project [35] that have identified both functionally-suitable and sufficiently radiation-tolerant candidate components that would be suitable for use in the phase 1 Pixel optical link. Component selection is important, as the single-mode optical fibers used in the present system must be re-used for the phase 1 upgrade. Figure 5.1 shows the layout of the optical link for the phase 1 upgrade of the CMS pixel detector.

Irradiation testing of components for use in the Versatile Transceiver [36] has shown that the

newer high-speed laser diodes are significantly more radiation resistant than the devices used on the current AOHs. Radiation testing with 300 MeV/c pions (which represent the dominant particle species in the inner regions of CMS) has shown that the newer devices are approximately a factor of four more resistant to radiation in terms of threshold damage and can thus withstand higher total fluences. The results of this test are shown in Figure 5.5. These newer devices are packaged as a Transmitter Optical Sub-Assembly (TOSA), which is a cylindrical package approximately 5 mm in diameter and 15 mm in length. The TOSA aligns the ferrule of an LC-type optical connector to the laser die. The TOSA contains a Fabry-Prot edge-emitting laser diode operating at 1310 nm, the die being the high-speed successor to the one used in the laserpill package currently installed in CMS.

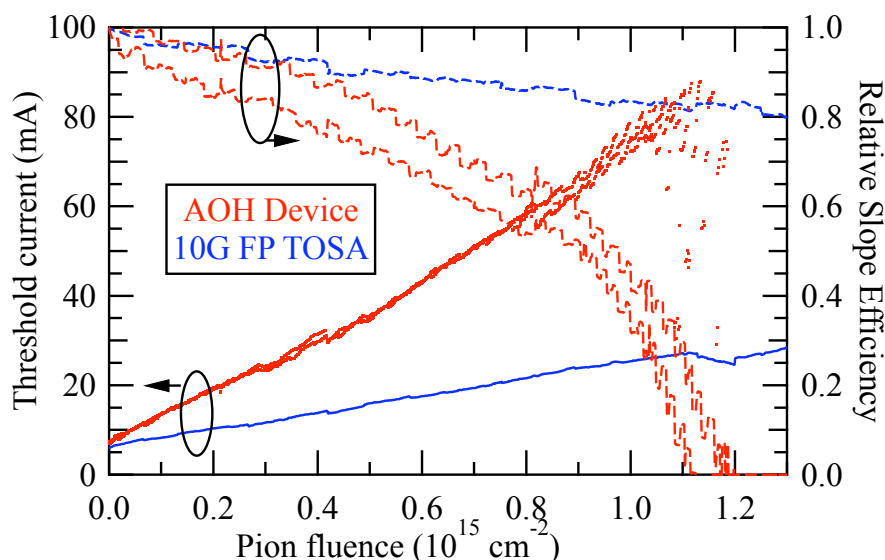


Figure 5.5: Comparison of radiation damage in between lasers used in the present AOH and lasers for the upgrade. The radiation damage effects are much smaller for the new devices.

The Pixel Optohybrid (POH) is a PCB designed to be mounted on the mechanical structure of the Pixel detector in the service tube. The POH receives input signals from the detector front-end that will be around 1 m away. The final system will require approximately 500 POH, of which one quarter is for the forward pixel and the remainder for the barrel pixel detector. With a candidate Transmitter Optical Sub-Assembly (TOSA) component identified by the Versatile Link project, a new Pixel Opto-Hybrid (POH) has been prototyped (Fig 5.6). Strict dimensional constraints on the POH come from the layout of the service tube in which the POH will be mounted. The prototype POH uses the same chipset as the present AOH, consisting of an Analogue Level Translator (ALT) and a Linear Laser Driver (LLD). An input matching network adapts the signals coming from the detector module via micro twisted pairs. The POH has two Analogue Level Translators (ALTs) and two LLDs, each driving two TOSAs for a total of four readout link transmitters per POH. The footprint of the two i/o connectors was kept compatible with the current AOH to ease in-system testing. This footprint and/or connector type may change in subsequent iterations of the design that may also be required to fully match new mechanical constraints as the overall system design evolves.

The ALT, which was designed to transmit an analogue signal at 40 MHz, has been measured to see if it is suitable for use as a level translator for a digital transmission at 400 Mbits/s. The eye diagrams obtained at 320 Mbits/s for two of the data patterns using POH prototypes with and without the ALT mounted (Figure 5.7) show a reduction in bandwidth with use of the ALT

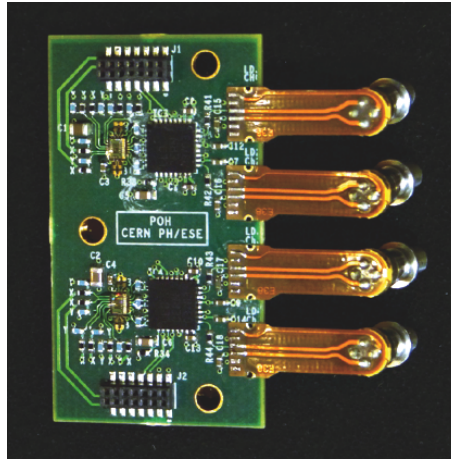


Figure 5.6: Photograph of a prototype POH.

that can be seen as an increased rise- and fall time in the eye, as well as a small amount of vertical eye closure. However, measuring the system BER for the two conditions there is little link power budget penalty when using the ALT at 400 Mbits/s as shown in Figure 5.7.

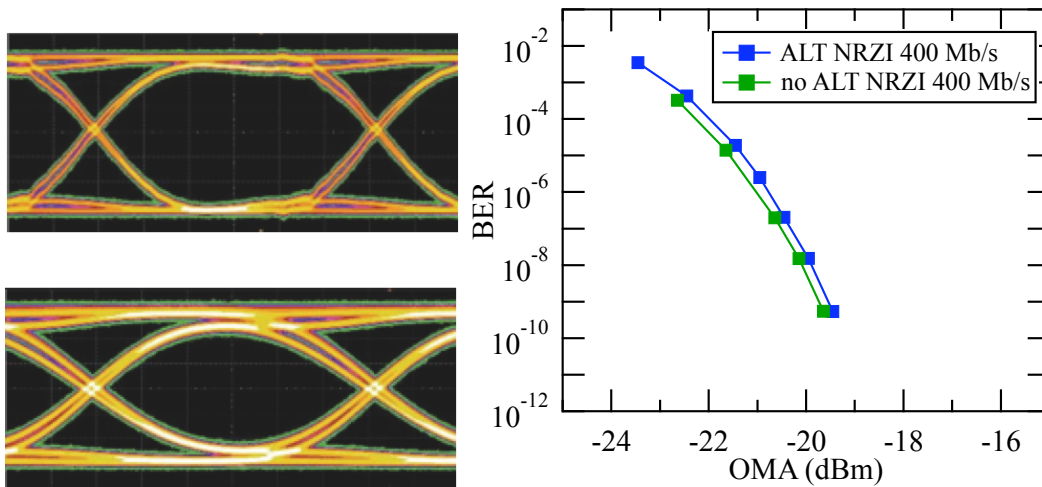


Figure 5.7: Eye diagrams of the POH operating at 400 Mbits/s without ALT (left-top) and with ALT (left-bottom); and (right) BER plots showing the minimal penalty associated with the lower-speed ALT.

Most digital optical receivers are sensitive to unbalanced codes as they typically operate AC-coupled and thus have an intrinsic low cut-off frequency. The raw data pattern from the TBM has a significant low-frequency content since it can contain a large number of consecutive bits at the same level. The eye diagram results obtained for the four data patterns clearly show pattern dependence in the receiver output due to the relatively low data-rate of the pixel optical link (see figure 5.8). It is also clear that the use of a line-coding scheme that improves the DC-balance of the raw detector data will be mandatory. The eye diagrams already indicate that the 4B/5B NRZI coding scheme should allow correct operation of the link at 400 Mbits/s. The eye diagram result is confirmed by the full link system BER measurements shown in Figure 5.9. Here we show that there is no additional penalty from operating the link at 400 Mbits/s with detector data encoded with 4B/5B NRZI with respect to a pseudo-random bitstream (PRBS7) at

320 Mbits/s. There would be an additional power penalty of 2.5-3 dB for using NRZ rather than NRZI on the 4B/5B encoded data, while for the raw data this penalty exceeds 10 dB. Optical power budget calculations [37] show that it is possible to reach a positive power margin and thus obtain a functional optical link. Use of the analogue ALT provides only a marginal link power budget (0.7 dB) which might easily be eroded by non-perfect signals being transmitted from the TBM to the POH. The power margin would be improved by using a level translator optimized for digital transmission at 400 Mbit/s. Design and prototyping of an ASIC for this purpose (DLT) is underway. Finally, it may still be possible to gain some additional margin by tightening the minimum slope efficiency specification of the laser and/or the minimum sensitivity specification of the receiver.

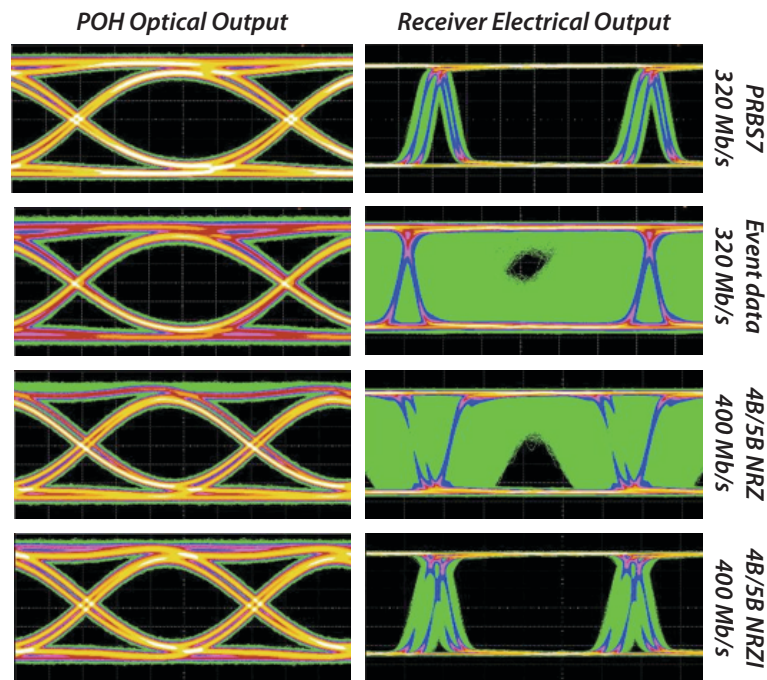


Figure 5.8: Full link eye diagram results for different data patterns.

The Optical Link project for the phase I Pixel Detector upgrade has three main partners: CERN, Fermilab, and PSI. The project will deliver the building blocks of the optical readout and control systems for the new phase I Pixel Detector, namely:

1. Pixel Optohybrid (POH) - the four-channel optohybrid that transmits readout data from the detector volume to the remote counting room.
2. Digital Optohybrid (DOH) - the two variants used in the original CMS pixel system to control the on-detector electronics.
3. Fiber plant - Optical fanout cables to connect the new POH & DOH to the CMS PP1 (Patch Panel 1 at the end of the CMS vacuum tank).
4. Digital Receiver Module (DRx12) - the twelve-channel digital receiver module that will sit on an upgraded Pixel FED in USC55

Deliverable 1 is the responsibility of Fermilab, while deliverables 2, 3 & 4 are the responsibility of CERN. An overview of the project flow is shown in Figure 5.10 and the attendant PBS is

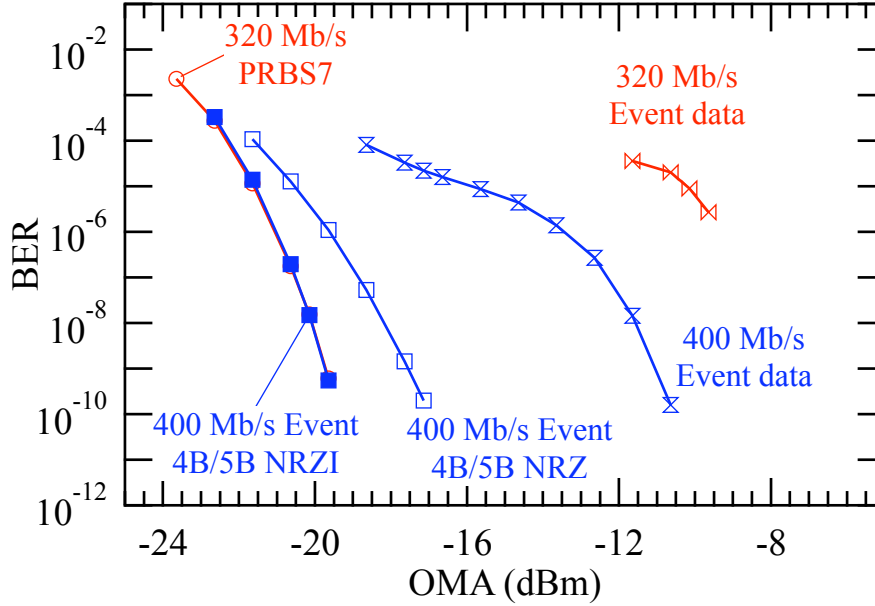


Figure 5.9: BER of full prototype link with different data patterns showing the need for a DC-balanced data encoding scheme such as 4B/5B NRZI.

shown in Table 5.2. The first part of the project, the demonstration of feasibility of the POH concept, has been carried out by CERN. The design has been handed over to Fermilab for final implementation that will take into account the final dimensional and electrical specifications. Fermilab will be responsible for the qualification and production of the POH, along with carrying out the attendant Quality Assurance. A full system-level integration of the POH and the rest of the electronics in the readout chain remains to be carried out by the collaboration. Once the quantities are fully defined CERN will be responsible for the production of an appropriate number of new DOHs. CERN will be responsible for defining and handling the logistics of the procurement of the optical fiber plant that will be needed to connect the new detector to PP1. CERN will carry out an evaluation of commercially-available DRx12 modules from a number of vendors in order to identify candidates for use in this project. Once the final number of required modules is defined, CERN will carry out the commercial actions on behalf of the collaboration for the purchase of the modules. CERN will then carry out the DRx12 qualification and follow the production of the final quantity.

5.4 FED/FEC Development

The ROC for the new pixel detector uses on-chip pulse-height digitisation, and therefore the 40 MHz analogue readout used in the current CMS pixel detector is replaced by a digital readout, running at 400 Mbits/s. As a consequence, the current VME off-detector readout electronics (front-end drivers, FEDs) will not be suitable for this new transmission protocol and speed:

- the optical receiver is not suitable for 400 Mbits/s digital readout
- the bandwidth of the S-Link [38] interface to the global DAQ is insufficient for data rates expected at instantaneous luminosities following LS2

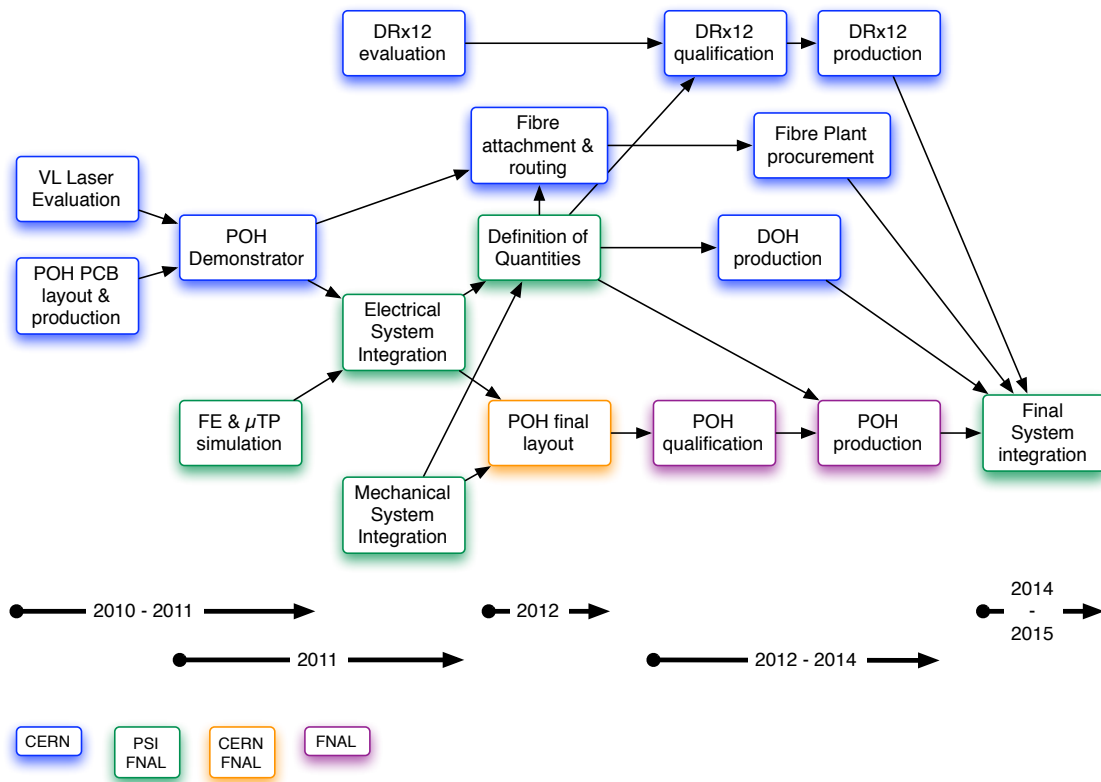


Figure 5.10: Optical Link Project Flow showing project partner responsibilities and approximate timescales.

An additional problem with the existing FEDs is that over time, the complexity of the firmware has increased beyond expectations, to the point where the ability to cope with detector occupancy and radiation related issues, including single event upsets (SEUs) and beam gas events, is now severely limited by lack of FPGA resources.

Table 5.3 estimates the number and bandwidth utilisation of active links for the Phase I pixel system. The bandwidth of the DAQ S-Link (5 Gbits/s theoretical maximum) would only just be sufficient to read out a 36 channel FED with perfect input link load balancing. A 48 channel FED with a 20 Gbits/s DAQ output link would instead be capable of reading a pixel detector with near fully saturated input links at 400 Mbits/s.

5.4.1 Phase I Pixel Data Acquisition

The baseline pixel DAQ project will deliver the replacement front-end DAQ for the Phase I pixel detector, the deliverables being;

1. FED — a replacement module in the counting room which captures, buffers, synchronises and packs readout data from the detector front-end before transmission to the CMS central DAQ system matching the requirements of the optical input link (Section 5.3), digital data format and high bandwidth output link.
2. DAQ Infrastructure — crates, power supplies, PCs and associated electronics to host the FEDs, including communication infrastructure required for local high bandwidth control and readout of FEDs.

Table 5.2: Project Breakdown Structure, responsibilities, deliverable quantities, start and end dates for the tasks. Dates are contingent upon funding being available.

PBS #	PBS Name	Institute	Deliverable	Start	End
1.1	VL Laser Evaluation	CERN	Doc.	Q1 2009	Q4 2011
1.2	POH PCB layout & fab.	CERN	2-5	Q4 2010	Q4 2010
1.3	POH Demonstrator	CERN	2-5	Q4 2010	Q1 2011
1.4	Fiber Attach & Route	CERN	Doc.	Q2 2011	Q3 2012
2.1	FE & μ TP simulation	PSI	Doc.	Q4 2010	Q1 2011
2.2	Electrical Sys. Integration	PSI	Signoff	Q1 2011	Q3 2011
2.3	Mechanical Sys. Integration (B)	PSI	Signoff	Q1 2011	Q3 2011
2.4	Mechanical Sys. Integration (F)	FNAL	Signoff	Q1 2011	Q3 2011
2.5	Definition of Quantities	PSI & FNAL	Doc.	Q4 2010	Q1 2011
3.1	POH Final Layout	FNAL	2-5	Q4 2011	Q1 2012
3.2	POH Qualification	FNAL	Doc.	Q2 2012	Q1 2013
3.3	POH Production	FNAL	304 (B),84 (F)	Q2 2013	Q1 2014
4.1	Fiber plant procurement	CERN	TBD	Q2 2011	Q1 2014
5.1	DOH Production	CERN	64+8 (B),(F)	Q2 2011	Q1 2014
6.1	DRx12 Evaluation	CERN	Doc.	Q1 2011	Q4 2011
6.2	DRx12 Qualification	CERN	Doc.	Q2 2012	Q1 2013
6.3	DRx12 Production	CERN	TBD	Q2 2011	Q1 2014
7.1	Final System integration	PSI & FNAL	Doc.	Q3 2014	Q4 2015

Layer/Disk	Radius	Modules	ROCs	Links	Bandwidth/Link
Layer 1	29 mm	96	1,536	384	285 Mbits/s
Layer 2	68 mm	224	3,584	448	120 Mbits/s
Layer 3	109 mm	352	5,632	352	108 Mbits/s
Layer 4	160 mm	512	8,192	512	50 Mbits/s
	Total Barrel	1,184	18,994	1,696	134 Mbits/s
Disk 1 Inner	45–110 mm	88	1408	88	210 Mbits/s
Disk 2 Inner	45–110 mm	88	1408	88	215 Mbits/s
Disk 3 Inner	45–110 mm	88	1408	88	215 Mbits/s
Disk 1 Outer	96–161 mm	136	2176	68	191 Mbits/s
Disk 2 Outer	96–161 mm	136	2176	68	194 Mbits/s
Disk 3 Outer	96–161 mm	136	2176	68	195 Mbits/s
	Total Endcaps	672	10,752	468	200 Mbits/s

Table 5.3: Estimate for Phase I pixel detector link requirements. Bandwidth estimates are an average per layer or disk and are based on GEANT4 simulations using the Pythia Z2 tune at $2.5 \times 10^{34} \text{ cm}^{-2}\text{s}^{-1}$ peak luminosity, 50 ns bunch spacing and 100 kHz L1 trigger rate.

3. Prototype System for Pilot Blades — a small scale prototype system for the readout of pilot modules after LS1.

An additional deliverable and extension to the project will be subject to a final review in April 2015:

4. FEC - a replacement module in the counting room for front-end module control with a high bandwidth communication path to the FED, in order to reduce the latency of the pixel module control feedback loop (Section 5.4.2).

The responsibility for deliverables 1-3 will be divided between all four CMS-UK groups (Bristol, Brunel, Imperial College and RAL). IPHC Strasbourg, in coordination with CMS-UK groups, will be responsible for the R&D towards deliverable 4. For this phase CMS-UK groups will provide a microTCA motherboard as a generic basis. IPHC will provide the mezzanines, firmware and software needed to utilize this motherboard as a microTCA FEC. The UK groups will also be responsible for developing, delivering and maintaining the firmware required to operate the new FEDs under high luminosity conditions. IPHC Strasbourg and the CMS-UK groups will be jointly responsible for developing, delivering and maintaining the online software required to operate the new FEDs and FECs under high luminosity conditions. CMS-UK expects to provide a significant contribution to the commissioning effort of the new pixel detector both before and after installation.

5.4.1.1 DAQ System Overview

To reduce the hardware design effort and build on the success of recent developments in this area, the prototype FED will be heavily based on the design of the MP7 [39] (Figure 5.11); a high bandwidth μ TCA processing card proposed for use in the Phase I calorimeter trigger upgrade. A first series of these boards is in manufacture, and testing is expected to be completed by fall 2012.

By replacing the optical inputs and outputs of the MP7 with devices matching the pixel system requirements, a fully functional pixel FED can be built with a limited hardware design effort. For prototyping, the FED will be implemented as an FMC carrier and locate the optical links on mezzanine cards, providing a modular and flexible approach to testing.

There are elements of the pixel DAQ which are not yet fully specified or designed and will require close coordination within CMS. An optical receiver for the readout links has not yet been selected which prevents a final specification of the system. In the short term, this challenge will be addressed with the prototype FED which, via the mezzanine cards, will provide flexibility and a testing platform for the receiver. Depending on the number of receivers a FED can host, we expect the output bandwidth to be between 10–20 Gbits/s, exceeding the maximum output bandwidth needed to read out a FED with fully saturated input links. This ensures that the DAQ links of the FED will never limit the system throughput. The replacement DAQ link is likely to be based on 10 Gigabit Ethernet but has not yet been fully specified and will be a focus of the initial testing plan.

The main parameters of the pixel DAQ system are summarised in Table 5.4 as a function of the number of input links per FED. A schematic of the system is provided in Figure 5.12.

5.4.1.2 Prototype FED Overview

The Phase I pixel FED prototype will be implemented as a double width, full height Advanced Mezzanine Card (AMC) compatible with the μ TCA crate system being developed for CMS up-

Links/FED	# FEDs BPIX	# FEDs FPIX	Bandwidth/FED Max
36	54	11	6.7 Gbits/s
48	40	8	9.0 Gbits/s
60	32	7	11.2 Gbits/s

Table 5.4: Estimates for the Phase I pixel DAQ system assuming an 88% optical ribbon occupancy. Maximum bandwidth estimates are extrapolated from Table 5.3 with a 32 bit hit encoding scheme and realistic load balancing.

grades. There are many advantages of pursuing a μ TCA based system including: a flexible, high density and high performance backplane that can be based on many of the serial standards in use today, e.g. Gigabit Ethernet (GbE), PCIe, SATA, etc.; advanced crate management capabilities, including hot swapping of hardware, power management and system monitoring and control; and power supply redundancy. Rack power and cooling requirements are expected to be similar to VME racks.

The FED will utilise the same PCB substrate and trace constraints as the MP7 in order to guarantee high speed signal integrity for links up to 10 Gbits/s. To mitigate risk and make use of the MP7s advanced functionality, the FED will also share many of the system components including the CPLD (complex programmable logic device), MMC microcontroller, Flash PROM, power regulators and sensors. Utilising the MP7 architecture for the microcontroller and peripherals would provide local non-volatile storage of firmware and detector calibration constants on the FED via a high capacity microSDHC card. Features such as these will help to reduce detector setup and commissioning time.

For prototyping and pilot blade readout, the FED will be implemented as a double front-facing FMC carrier using High Pin Count (HPC) connectors. The 12-channel digital optical receivers (DRx12) will therefore be located on FMC mezzanine cards. A FMC compatible FED will also allow the use of specialised or commercial test cards with electrical, as well as optical, links to perform read out of chips or modules. A single width FMC mezzanine could reasonably accommodate at least two 12-channel optical receivers, and possibly more, subject to the dimensions of the final DRx12 selected. Therefore, a baseline system of 48 input channels (links) per FED is proposed.

The aggregate output bandwidth of a 48 channel FED would be around 10 Gbits/s depending on the instantaneous luminosity and bunch crossing rate, data packing format, link utilisation and the balancing of the data load across the input links. In the present system, the FED short distance link to the DAQ is implemented as an electrical 64 bit parallel bus (S-Link) with a theoretical maximum output bandwidth of no more than 5 Gbits/s. Transmission of data from each μ TCA FED will rather be via one or two 10 Gbits/s optical links, using commercial off-the-shelf components (i.e. SFP+ transceivers), with a transfer protocol and DAQ optical receiver card yet to be defined. While the link definition and components fall under the scope of CMS central DAQ upgrades and maintenance, the FMC compatible FED lends itself well to testing and prototyping of the new link, especially as there are many commercial 10 Gbits/s SFP+ FMC mezzanines available on the market.

As in the MP7, the FED prototype will be served by a single Xilinx Series 7 FPGA, with the exact choice of part to be based on availability and cost. A Series 7 FPGA is well matched to the development timescale, supplies enough I/O to service the high density FMC interconnect and peripherals, supports multi-gigabit (including 10 Gbits/s) serialiser/deserializers and multiple

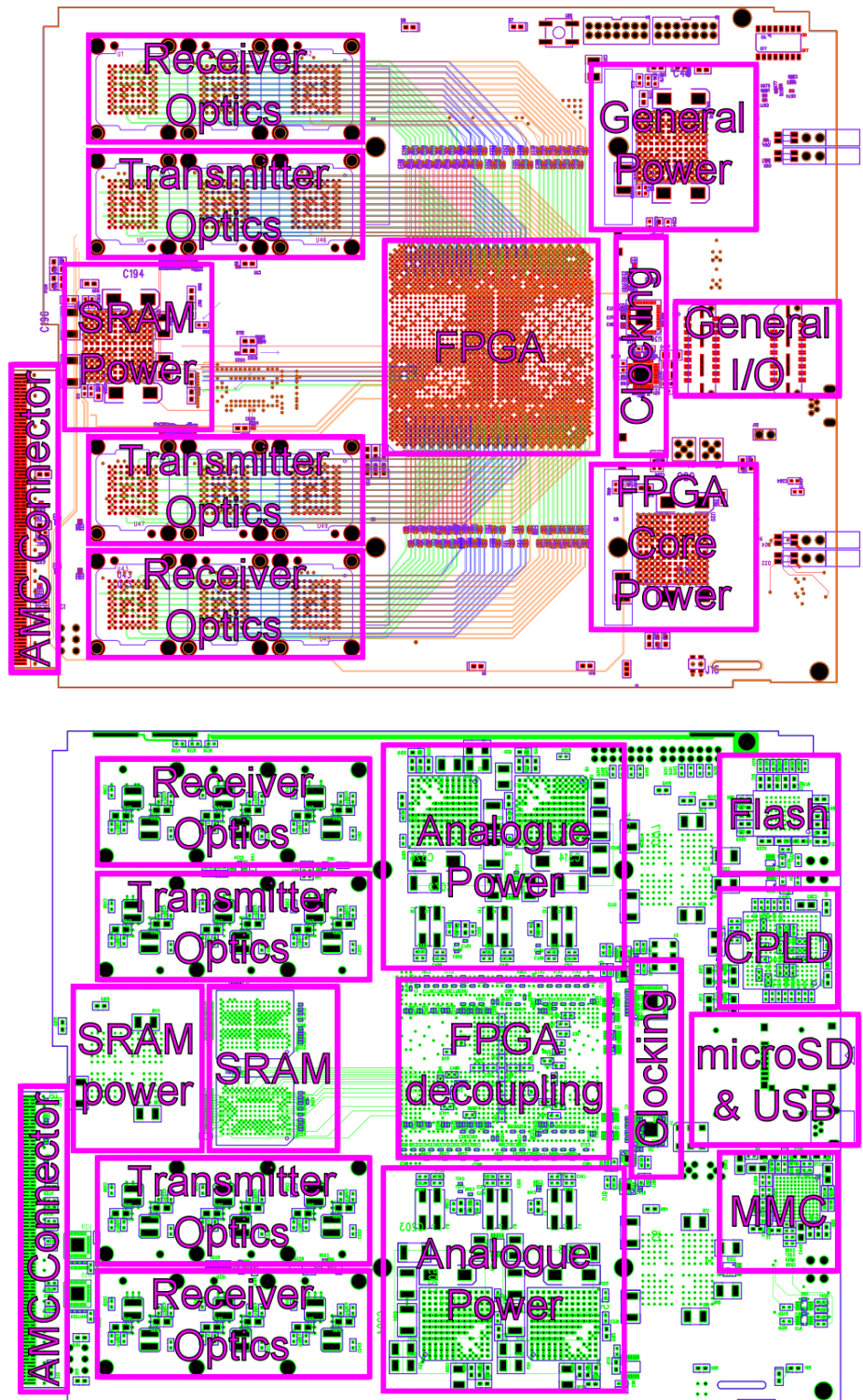


Figure 5.11: Layout of the MP7 trigger processor board (top: top surface, bottom: bottom surface). The Phase I pixel FED prototype will be derived from this board, where receiver/transmitter optics will be removed and the FPGA will be placed further back (towards the AMC connector). The layout on the underside will be virtually unchanged, while the top surface will require the power regulators to be moved back in order to accommodate space for two FMC sites on the front panel.

communication protocol standards and provides a 100 fold increase in logic resources over those used in the existing FED. The choice of FPGA for the final board will also be affected by the final system specification, including the design and implementation of the DAQ link. Since a Xilinx Series 7 FPGA offers a significant increase in block RAM resources with respect to the current FED, external RAM may not be a necessity, which could reduce the cost of the system. On the other hand, the choice of DAQ link could adversely increase the buffering requirements, which would dictate the capacity and bandwidth of the external RAM and influence the final FPGA choice.

5.4.1.3 System Interfaces Technical Description

The low level system logic for control, register access and monitoring will be based on the architecture developed for trigger and HCAL μ TCA hardware. The MMC microcontroller and CPLD architecture for implementing the necessary Intelligent Platform Management Interface (IPMI) and board management interface as well as the System Peripherals Interface (for monitoring, USB2.0 communication, flash memory access, JTAG boundary scan and boot-time programming of the FPGA) replicates the design used for the MP7 and will not be described here.

The FED will be able to communicate with the controller PC, and with the other boards in the crate, via the μ TCA backplane. While in principle the backplane topology is flexible and can be chosen to suit the application requirements, the μ TCA pixel crate will employ the same dual star backplane fabric and architecture as those specified in the trigger upgrade system. The backplane will provide the FED with both +12 V payload and +3.3 V management power, multiple bidirectional clocks, system management via IPMI and JTAG, and 21 user assigned high speed bidirectional serial ports capable of communication at up to 10 Gbits/s.

Certain port assignments, including those of the telecom and fabric clocks, have been standardised in CMS for system cross compatibility. Communication with the FEDs in a crate will be via the Gigabit Ethernet channel (Port0) from the backplane direct to the FPGA, distributed by a single commercially available MicroTCA Carrier Hub (MCH) located in the crate. The MCH provides the advanced management and data switching required in any μ TCA system including IPMI controlled power management, clock distribution, electronic keying, hot swapping of AMCs and switching functionality for backplane communication. A CMS-standard protocol (IPbus) [40], encompassing firmware logic to wrap an asynchronous 32 bit address/32 bit data bus into UDP/IP packets for GbE transmission and a compatible C++ hardware access library (uHAL), will be used for board read/write access.

Each FED will require a TTC clock input in order to extract the data from the front-end synchronously. The encoded TTC clock and control signal will be provided optically to a single AMC13 [41], a single width AMC module used in both the HCAL and calorimeter trigger upgrades, located in each μ TCA crate. The AMC13 will issue the 40.08 MHz TTC clock to the FEDs as one of the backplane clocks, while a fixed latency control line will transmit commands (L1A, TTC Resets, B channel) at 80 Mbits/s on Port 3. Additionally, the FEDs must communicate a fast feedback status (buffer occupancy, sync status, board errors) back to the TTC system for trigger throttling and reset control. For compatibility, this will probably take the form of the current sTTS feedback codes[42] which will be delivered back to the AMC13 on Port 3 for status merging and optical transmission to the trigger control system. The AMC13 also offers an alternative DAQ pathway to allow local readout of a FED crate for commissioning or spy data acquisition. This is available to the FED via a < 6 Gbits/s serial link on Port 1 (limited by the AMC13 SERDES). The current version of the AMC13 limits the local DAQ bandwidth to 12 Gbits/s (2 x 6 Gbits/s SFP+ transceivers) per crate which would be sufficient for most com-

missioning and spy acquisition needs, although this could be extended to 20–30 Gbits/s in the future. A receiver card for the AMC13 with 10 Gigabit Ethernet output is in development and the steps towards a multi-gigabit DAQ architecture including common protocols and hardware are under discussion with the CMS central DAQ (cDAQ) group.

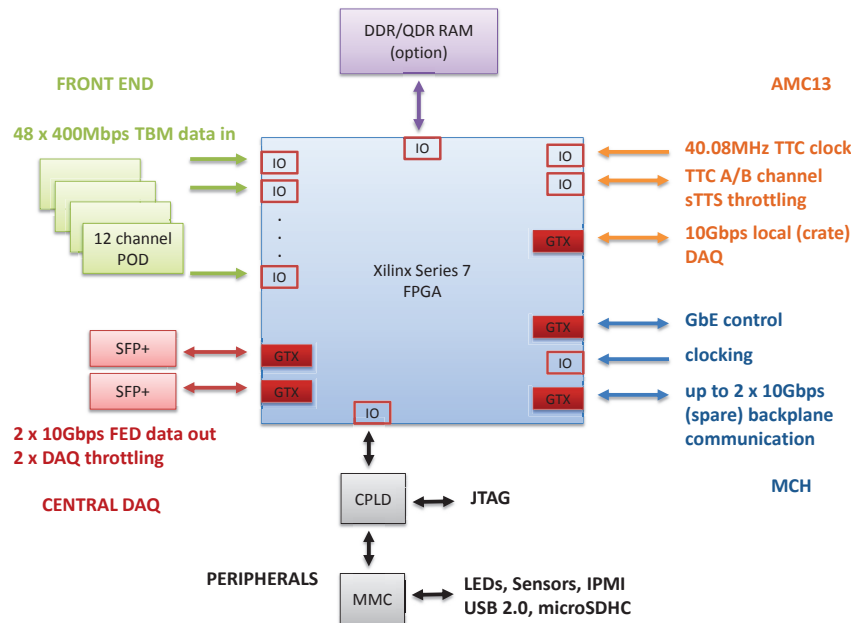


Figure 5.12: Block schematic of the pixel FED board and I/O.

Communication over the μ TCA backplane fabric can be extended using Ports 2 and 4 to implement high speed serial (SATA/PCIe) links via the MCH switch and additional high speed ports can be used for inter-crate communication via a custom cross-point switch mezzanine card on the AMC13. This flexibility will be implemented in the FED design in case it is required. One possible use could be to provide fast feedback to a new FEC implemented as a μ TCA card in the same crate, speeding up commissioning tasks and reducing the impact of front-end errors on the readout chain.

A double width, 12 slot, μ TCA crate could read out 8 BPIX sectors, accommodating 10 48-channel FEDs, 1 MCH, 1 AMC13 and dual redundant power modules. A single crate including fan tray would require 7U of rack space. The BPIX could be served by 4 crates while the FPIX would only need 1 crate.

5.4.2 Replacement of the Pixel Front End Control System (FECs)

A full redesign of the FED system opens opportunities beyond a simple replication of the functionality of the existing system.

The separation of detector control and detector readout into separate boards (FEC and FED) has led to problems in recovering from SEUs due to the lack of direct communication between FEC and FED. Calibrations of the pixel detector are too slow to be done routinely, again due to restrictions on the ability to transfer data between FED and FEC via the CMS online database. Since the FECs face similar end-of-life issues as the existing FEDs, it has been suggested that it might be beneficial for the replacement DAQ to include replacement of the control system with a more unified architecture.

WBS	due by	milestone
M1	Oct 2013	prototype FMC-FED hardware available
M2	Oct 2014	standalone prototype FED, multi ROC readout
M3	Oct 2014	standalone prototype FEC, multi-module control
M4	Apr 2015	demonstrator FED & FEC with readout & control of pilot blades
D1	Apr 2015	front end control system replacement review
M5	Apr 2015	demonstrator fast link integrated with central DAQ hardware
M6	Jan 2016	final FED hardware ready for production
M7	Jul 2016	final firmware & software for full system ready for deployment
M8	Jan 2017	delivery of full Pixel DAQ

Table 5.5: List of milestones for the pixel upgrade DAQ project.

In one example, a new FEC implemented as another μ TCA card could sit alongside its corresponding FEDs in the same crate and communicate via the high speed backplane. Alternative ideas range from keeping the current control system but enabling a high speed communication link to the FECs via the AMC13 and a local crate PC, to replacing the current segregated architecture with one using integrated FED-FEC boards, each controlling and reading out its own group of modules.

Most of the hardware and development work for the FEC replacement can be shared with those from the DAQ upgrade project. Since the prototype μ TCA FEDs have their optical interfaces located on FMC mezzanine cards, they can easily be modified to accommodate a FEC optical interface. Firmware and software for FEC operation can be adapted from existing code and experience of using FEC prototypes alongside the FED prototypes will be gained during the pilot beam setup.

A final assessment of the cost and benefits of either replacing or updating the existing control system (i.e. committing to Deliverable 4) will be taken by D1 (Table 5.5).

5.4.3 Deliverables, Milestones and Strategy

The overall strategy for the pixel upgrade DAQ project is to reduce hardware design effort by modifying an existing μ TCA board design developed by Imperial College for the trigger upgrade. This also enables the use of existing firmware and software modules developed for these boards. Flexibility during the development phase will be ensured by use of optical interfaces on FMC mezzanine cards, easily allowing the evaluation of different channel configurations, plus prototyping of replacement FECs. A DAQ system based on these FMC carrier boards will then be verified under realistic conditions as part of the pixel pilot blade system. Final design decisions can then take the experience from actual data taking with the pilot blades into account.

A first and mostly complete set of firmware and software will be needed for running the prototype FEDs with pilot blades, but both firmware and software are expected to evolve considerably following the experience gained with actual data taking. Provision of a DAQ system for the pixel pilot blade system is thus the first major deliverable of the pixel upgrade DAQ project, followed a few years later by production FEDs and associated infrastructure (crates, power supplies, firmware, online software) as well as potentially, subject to review following the pilot blade project, new FECs. The pathway towards these deliverables is outlined in terms of major milestones in Table 5.5.

Figure 5.13 provides a more detailed breakdown of the planned activities. The initial proto-

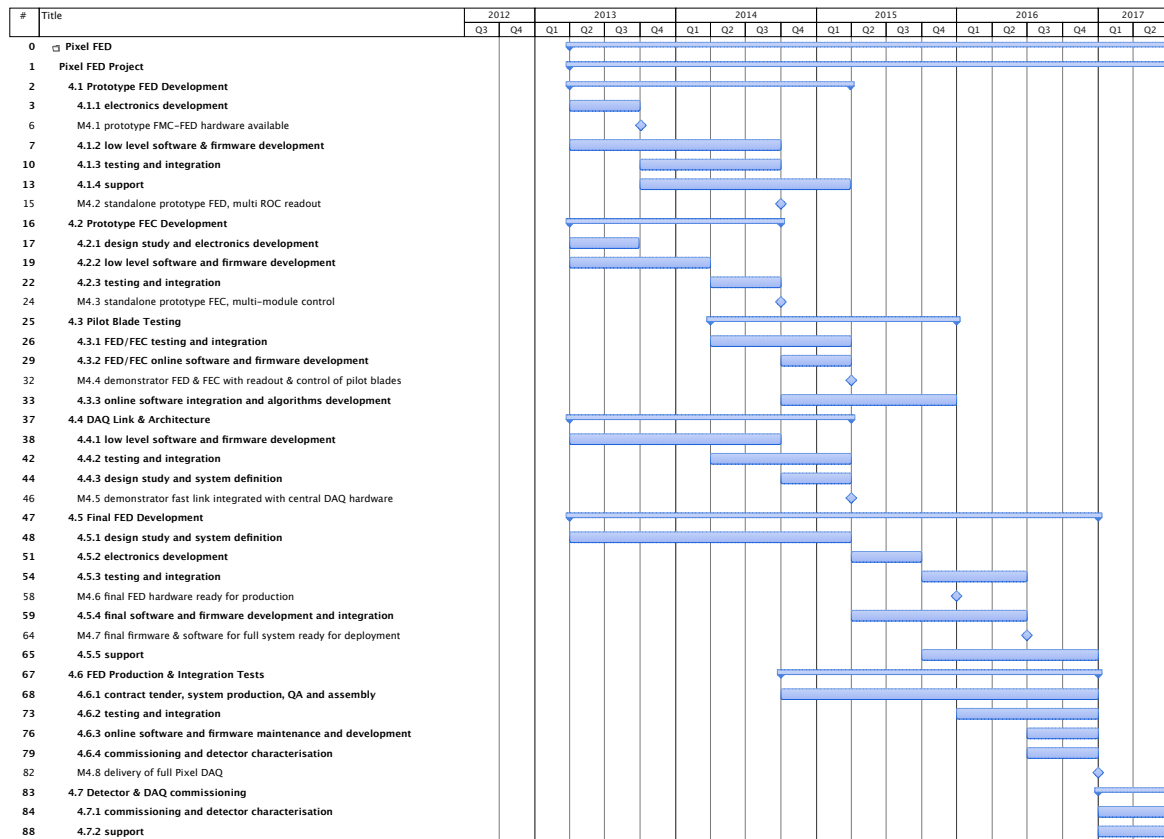


Figure 5.13: Provisional breakdown of the pixel DAQ upgrade project.

typing period is subdivided into five different areas. The prototype FED will dominate work during the first year and a half. The UK groups will produce prototypes and mezzanines and make them available to collaborators. The majority of effort will then be dedicated to firmware and software development and electrical and optical link ROC testing in the lab. Implementation of a prototype pixel FEC will be pursued in parallel, using the same hardware as the FED and porting existing FEC software and firmware to reduce development time and effort.

The first major system test will be part of the pixel pilot blade project, where prototype modules will be inserted into the existing detector and read out with a prototype FED and controlled by a prototype FEC. Testing in the period 2014-2016 will demonstrate readiness under realistic conditions and will be the proving ground for the majority of online software, firmware and algorithm development, and integration effort required. The final area of work in this period will be prototyping studies and definition of the replacement DAQ link requiring close collaboration with the CMS-central DAQ group.

The production and integration phase will follow on from successful prototype testing with pilot modules and the conclusion of the design study where the final system, including optical receiver, DAQ link and protocol and a decision on FED-FEC architecture, is defined. Effort is required to design and test the final board and integrate firmware and software from the DAQ link and pilot blade developments. The first final boards will replace pilot blade prototypes in the CMS service cavern to undergo integration testing with the global trigger and DAQ and timing systems where integration with the global DAQ and trigger and timing systems can take place. The full DAQ system will then be assembled at the Tracker Integration Facility (TIF) at

CERN where construction of the Phase I pixel detector is expected to be completed. This allows DAQ slice tests with the pixel detector in situ and detector commissioning and characterisation studies before installation.

Chapter 6

Pixel Modules

The upgraded pixel detector will have 1184 pixel modules in the barrel BPIX, compared to 768 modules in the present detector, with an increase in the pixel count from 48 million to 79 million. In the forward FPIX the number of modules will remain the same at 672. The new FPIX modules will be larger than in the present detector, increasing the pixel count from 18 million to approximately 45 million.

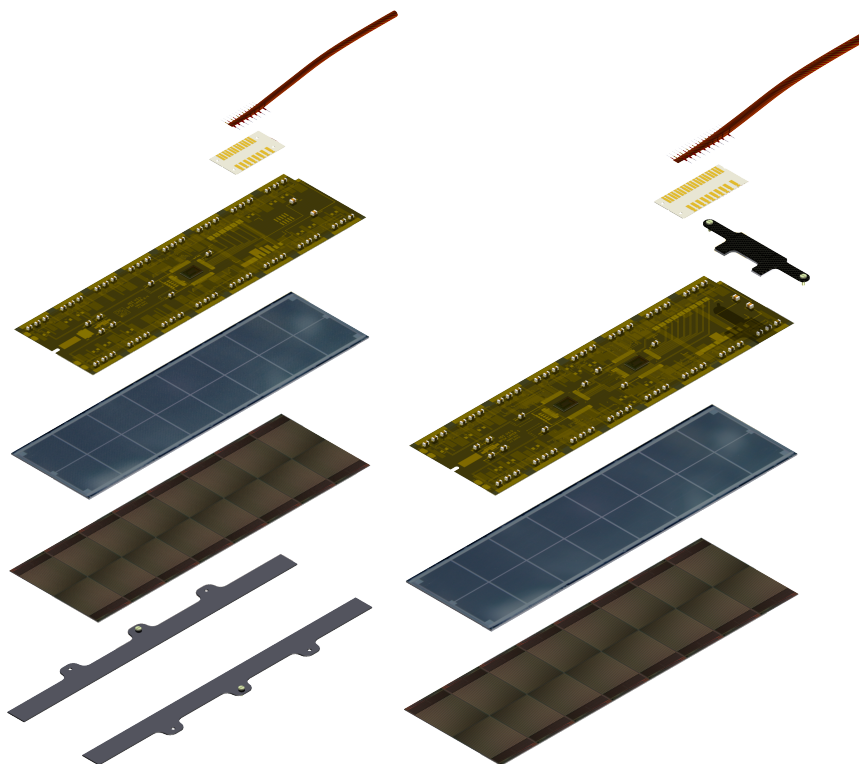


Figure 6.1: Upgrade BPIX modules: Layer 2 to 4 (left) and Layer 1 type (right).

The proposed upgraded pixel detector will have only one type of sensor module with two rows of 8 ROCs each. This will simplify sensor production, module assembly, and testing. The active area of the module is $16.2 \times 64.8 \text{ mm}^2$. The pixel size will remain the same as before, $100 \times 150 \text{ } \mu\text{m}^2$. The same n^+ -in-n technology as for the current detector [43] will be used for silicon sensors. The sensor is bump-bonded to 16 ROCs forming a detector unit with 66560 pixels. For the BPIX Layer 1 the ROCs will be thinned to $75 \text{ } \mu\text{m}$ thickness. For the BPIX Layers 2-4 and the FPIX end-cap disks, the ROCs will be thinned to about $180 \text{ } \mu\text{m}$ thickness. The ROC peripheries with wirebond pads extend 2 mm beyond the sensor along the two long sides of the module. A high density interconnect (HDI) is glued on top of the sensor with wirebond

pads to connect to the corresponding pads on the ROCs. The HDI provides signal and power distribution for the ROCs, the token bit manager chip (TBM) and decoupling capacitors. The TBM chips will be glued and wirebonded on the HDI. BPIX Layer 2-4 modules have $250\ \mu\text{m}$ thick Si_3N_4 base-strips glued to the back side of the ROCs that permits mounting the modules on the mechanical structure (Figure 6.1 left). There is no room for base strip and screws in the innermost layer. Instead, the modules will be held by carbon fiber clips attached to the mechanics with screws in the region of the z-gap between modules (Figure 6.1 right). FPIX modules are fastened to the support/cooling structure using screws through module end holders made of PEEK, with a thin layer of reworkable thermal interface material between the modules and support/cooling structure to improve heat transfer. All barrel module cables have the same length of $\simeq 95\ \text{cm}$. The cable consists of 20 copper-clad aluminium wires, 6 thin twisted pairs with $125\ \mu\text{m}$ diameter for signal transmission and 8 with $360\ \mu\text{m}$ diameter for power and detector bias. The cable for modules in Layer 1 has in addition three micro twisted pairs and two digital power wires. FPIX modules will be equipped with Kapton flat flex cables that are connected via a special connector placed on HDI as shown in Figure 6.2.

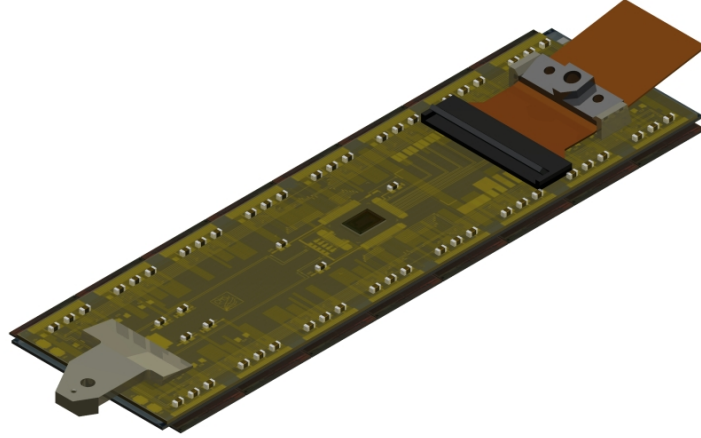


Figure 6.2: Upgrade FPIX modules.

6.1 Silicon sensor requirements

The new pixel detector will be ready to install in the year-end technical stop of 2016/17. During the subsequent years up to LS3, the LHC is expected to deliver about $500\ \text{fb}^{-1}$. Particle fluence has been estimated based on pixel cluster counting in the present detector. The average pixel cluster rate per cm^2 has been evaluated for the instantaneous luminosity of $10^{33}\ \text{cm}^{-2}\text{s}^{-1}$ using the measured number of pixel cluster per colliding bunches, the number of colliding bunches in an orbit and the orbit duration. The obtained number has been corrected for the detector radii and the colliding energy. As a result we estimated that a hadron fluence of $\Phi \simeq 3.0 \times 10^{15}\ \text{n}_{eq}/\text{cm}^2$ will be accumulated in the innermost pixel layer at $r=3\ \text{cm}$ for $500\ \text{fb}^{-1}$. This fluence is about factor of 2 higher than the operational limits of the proposed system requiring a replacement of the innermost barrel layer every $250\ \text{fb}^{-1}$. Barrel Layer 2 gets four times less

fluence and hence will stay operational for the entire period. The same is true for the FPIX inner disk modules that have the same (even about 10% less) pixel hit rate as the barrel Layer 2 modules.

6.1.1 Technological choice of sensor

As mentioned above, the sensors for the upgrade CMS pixel detector are n^+ -in- n as in the current detector. The collection of electrons is advantageous because of their higher mobility compared to holes, which causes a larger Lorentz drift of the signal charges. This drift leads to charge sharing between neighbouring pixels and thus improves the spatial resolution. Furthermore, the higher mobility of electrons makes them less prone to trapping, which leads to a higher signal charge after high fluences of charged particles. After irradiation induced space charge sign inversion, the highest electric field in the sensor is located close to the n^+ -electrodes used to collect the charge, which is also an advantage.

The choice of n -substrate requires a double sided sensor process, meaning that both sides of the sensor need photo-lithographic processing. This leads to higher costs compared to single sided p -in- n (or n -in- p) sensors. However, the double sided sensors have a guard ring scheme where all sensor edges are at a ground potential, which greatly simplifies the design of detector modules. This concept also ensures a high signal charge at moderate bias voltages (≤ 600 V) after high hadron fluences. The n -side isolation is implemented through a moderated p -spray technique with a punch through biasing grid (BPIX) and a partially open p -stop technology (FPIX). Figure 6.3 shows photographs of pixel cells for moderated p -spray technology and for open p -stop.

We plan to fabricate the sensors for the future pixel detector on 4 inch wafers that contain three sensors. The possibility of using 6 inch wafers is under serious consideration since, despite the higher mask and processing cost, this option could bring considerable savings with 8 sensors placed in on a wafer. There is also an optimisation underway to the pixel unit cell (PUC) design for FPIX sensors, that should be finalized in 2012. The design of the PUC should maximize charge collection efficiency for any point of impact of the particle across the $100 \times 150 \mu\text{m}^2$ area of the pixel and minimize the capacitive load for the front-end amplifier. An optimisation process is needed as these two goals are in conflict with each other.

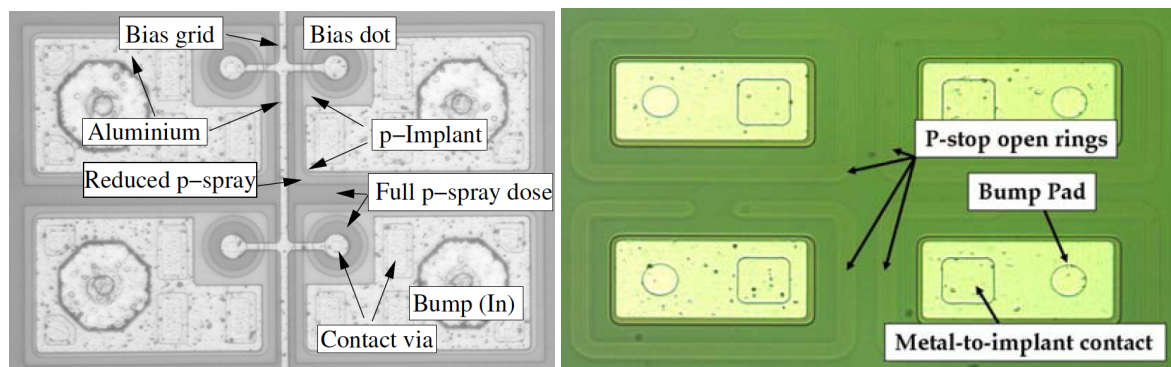


Figure 6.3: Photograph of four pixel cells in the same double column for BPIX (left) and FPIX (right).

6.1.2 Sensor radiation hardness

In order to provide track seeds, especially to the high level trigger, the hit detection efficiency should be as high as possible. With increasing hadron fluence the bias voltage to obtain the

full signal has to be increased to compensate for the changes in the sensor's internal electric field. Those changes are caused by radiation induced crystal defects which also act as trapping centers. Trapping reduces the maximum signal which is available, even if a sufficiently high electric field is present in the whole sensor volume. As the readout electronics have a detection threshold, a low signal can cause inefficiency. In order to predict the performance for high fluences, sensors have been irradiated and thoroughly investigated with a radioactive source [44] (BPIX) and at a beam test [45] (FPIX). In both cases the results confirmed that the sensors can tolerate the expected radiation doses and collect enough charge with a high efficiency. Below we describe in more details the test procedure and results reported in [44].

The sensor samples were taken from wafers of the main production run for the CMS pixel barrel which were processed on approximately $285\mu\text{m}$ thick n-doped diffusion oxygenated float zone silicon (DOFZ) according to the recommendation of the ROSE Collaboration [46]. The resistance of the material prior to irradiation was $3.7\text{ k}\Omega\text{cm}$ leading to an initial full depletion voltage of $V_{FD} \simeq 55\text{ V}$. Small sensors were produced on the same wafers as for the full modules. They were connected to readout chips using the bump-bonding process used for the module production for the CMS pixel barrel detector. As this procedure includes processing steps at temperatures above 200°C , it was done before irradiation. Therefore the sensors and readout chips were irradiated at the same time allowing a realistic testing of the performance after few years of operation at the LHC.

The sandwiches of sensor and readout chip were irradiated at the PSI-PiE1-beam line with positive pions of momentum $300\text{ MeV}/c$ to fluences up to $6 \times 10^{14}\text{ n}_{eq}/\text{cm}^2$, with $26\text{ GeV}/c$ protons at CERN-PS, or with 24 MeV protons in the irradiation facility of the Karlsruhe Institute for Technology up to $5 \times 10^{15}\text{ n}_{eq}/\text{cm}^2$.

A ^{90}Sr source has been used for inducing signals in the sensor. The β -spectrum of the daughter decay of ^{90}Y has an endpoint energy of about 2.3 MeV and therefore contains particles which approximate a minimum ionising particle. The testing and calibration procedure was similar to what is used for the qualification of CMS pixel barrel modules.

Data could be taken with all samples even the ones irradiated to the highest fluence. The high voltage capability was limited by connectors, narrow traces on the PCBs, etc. The most probable value of the signal charge as a function of the sensor bias is shown for all samples in Figure 6.4. For all fluences smaller than $10^{15}\text{ n}_{eq}/\text{cm}^2$ the signal clearly saturates for a bias larger than about 300 V , when the so-called full depletion is reached. Samples irradiated to $1.1 \times 10^{15}\text{ n}_{eq}/\text{cm}^2$ do not display a clear saturation of the signal up to a bias of 600 V . A higher bias was not applied for safety reasons. The samples irradiated to $2.8 \times 10^{15}\text{ n}_{eq}/\text{cm}^2$ were measured up to 1000 V . Also here, no saturation of the signal with bias was observed. The signal at 600 V is around 6000 electrons which is not sufficient for reliable operation with the present readout electronics, where the in-time threshold is around 3000 electrons. However, this fluence exceeds the expected $1.5 \times 10^{15}\text{ n}_{eq}/\text{cm}^2$, before Layer 1 substitution, almost by factor of two and the new ROC allows for a significantly lower threshold of 2000 electrons. Both these factors insure us that the Layer 1 modules can be efficiently operated during the expected lifetime with a bias voltage not higher than 600 V .

The good spatial resolution of the pixel detector is reached by an analogue interpolation method. The set of pixels showing a signal from the same particle is called a cluster. Interpolation between neighbours is only possible if the cluster size in each direction is at least two.

In the polar direction (orthogonal to the 3.8 T field) charge sharing is induced by the drift of charge carriers in the magnetic field. The value of this drift is given by the Lorentz angle which

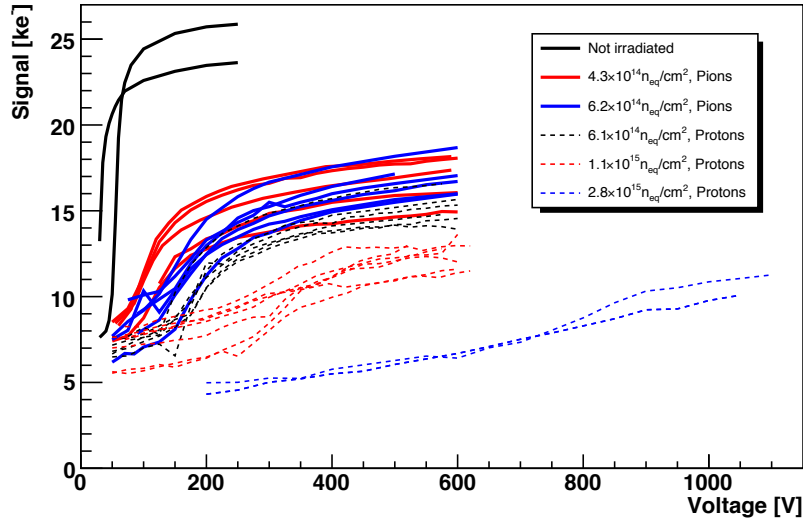


Figure 6.4: Charge collection in non-irradiated and irradiated sensors with different doses and different particle types (sensors of $285 \pm 15 \mu\text{m}$ thickness.)

is a function of the charge carrier mobility. The mobility is a function of the electric field and therefore of the sensor bias. Presently the pixel barrel modules are run at a bias of 150 V which results in a Lorentz angle of 22° and therefore a high fraction of two pixel clusters in $r - \phi$. This leads to a good spatial resolution of about $13 \mu\text{m}$.

With increasing radiation damage, the bias voltage should be increased to compensate for the increase of the space charge within the sensor bulk. Eventually the maximum bias provided by the power supplies (600 V) is needed to obtain sufficient signal charge. However, the increasing sensor bias decreases the Lorentz angle and the fraction of two pixel clusters. For a fluence of $1.1 \times 10^{15} \text{ n}_{eq}/\text{cm}^2$ and a bias voltage of 600 V the spatial resolution will be increased to about $20 \mu\text{m}$.

In the direction along the beam pipe (parallel to the magnetic field) charge sharing is not caused by the magnetic field, but by the tilt of the track. Therefore the region of the worst spatial resolution is the central part of the detector at a pseudorapidity $\eta=0$. Here particles penetrate the sensors in a normal angle and there is no charge sharing. Therefore, the point resolution is of the order of $150 \mu\text{m} / \sqrt{12} \simeq 40 \mu\text{m}$. For higher values of η , the angle, and therefore the fraction of two pixel clusters increases. At the angle where the average cluster length is exactly two (at $|\eta|=0.5$) the spatial resolution reaches the optimum value of about $16 \mu\text{m}$. With increasing incident angle the cluster length becomes larger. The internal pixels of long clusters do not contain spatial information and their fluctuations slightly degrades the position measurement.

In case of radiation induced trapping, the tracks with high incident angle suffer first from insufficient charge as the pixels are shorter ($150 \mu\text{m}$) than the thickness of the sensor ($285 \mu\text{m}$). For very long clusters, the probability that one pixel stays below the signal threshold of the readout electronics is high. The present reconstruction software processes this condition as being two separate clusters which leads to hit position reconstruction errors. This situation will be improved with the lower ROC thresholds, which is one of the objectives in the new ROC design.

6.2 Silicon sensor acceptance criteria

While in Section (6.1) the requirements concerning conception and design of the sensors like spatial resolution or radiation hardness are discussed, this section will describe the acceptance criteria for the parts delivered by the sensor vendor. The aim of those specifications is to ensure that the sensors were manufactured correctly and are not damaged. All can be verified with simple measurements.

For the pixel sensor Phosphorous-doped (n) FZ silicon will be used with resistivity of 2-5 k Ω cm. All wafers come from the same ingot, so the variation between the wafers is small. The wafer thickness is specified to be $285 \pm 5 \mu\text{m}$, polished on both sides ($\langle 111 \rangle$ crystal orientation). Necessary oxygen enrichment is achieved by keeping the ingot for 24 h at 1150 °C (DOFZ). Bow of the wafer after processing should not be more than 40 μm .

Some technology parameters will be checked with test structures. Full depletion voltage that is compatible with a resistivity of 2-5k Ω cm will be checked with simple diodes. The sheet resistance of the p^+ and n^+ implants measured with dedicated test structures should be lower than 500 Ω cm (typically <200 Ω cm). The parasitic current at the punch through structure is required to be less than 1 nA ($V_{DS} = 0.6 \text{ V}$, $V_{BIAS} = -150 \text{ V}$). Such a measurement involves contacts on both wafer faces, so it can only be done with a small number of devices.

Even on wafers that fulfil all requirements sensors might be broken due to local defects. In order to ensure that the sensors do not have scratches etc. an IV-curve has to be measured. Figure 6.5 shows a few IV-curves for accepted (black curves) and rejected (red curves) sensors from the previous production. The following criteria are used to decide whether a sensor is good:

- An operation voltage (V_{OP}) is defined as full depletion (V_{FD}) voltage plus 50 V and is at least 150 V.
- Leakage current $I(V_{OP}, T = +17^\circ\text{C}) < 2 \mu\text{A}$. This value was defined after a prototype production was measured and analysed to separate the good sensors from the "clearly faulty" ones. The value can be adjusted after a new test series was produced and analysed.
- No breakdown up to V_{OP} . A clear definition of breakdown is difficult. In the past the following specification was used as acceptance criterion: $I(V_{OP}) / I(V_{OP}-50 \text{ V}) < 2$.

Measuring an IV-curve is fast and easy. It shows quite clearly mechanical damages to the sensors that might occur at steps involving sensor handling. Therefore we plan to take the IV-curve of a sensor prior to bump-bonding shortly before the chip placement i.e. after dicing.

6.3 Module assembly

The module assembly procedure [47] comprises the following steps:

1. Build a bare module by bump-bonding 16 ROCs to the Si sensor;
2. Glue the base strips to the ROCs of the bare module (for BPIX Layers 2-4);
3. Apply a small amount of glue between the edge of the sensor and the ROCs to reinforce the connection near the wirebonding area;
4. Glue the pre-assembled HDI to the bare module;

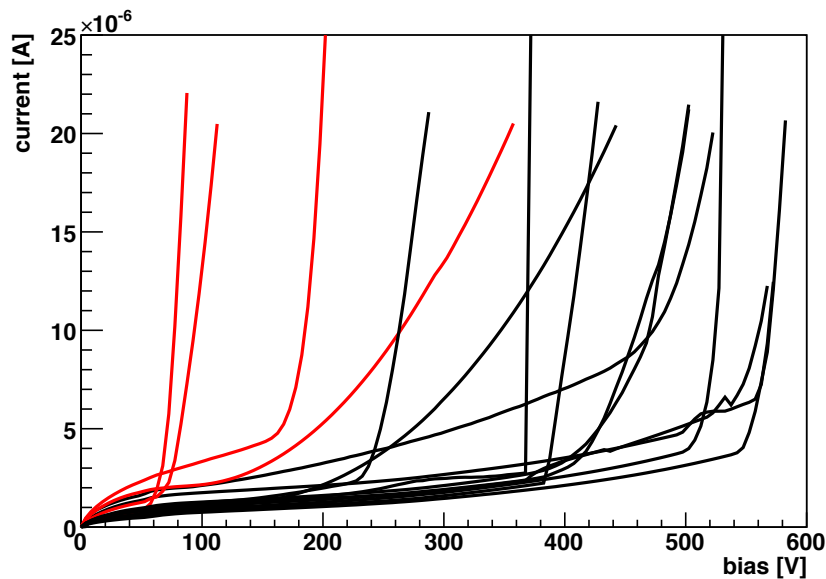


Figure 6.5: An example of IV-curves for sensors accepted (black) and rejected (red) in the previous production.

5. connect the HDI and the ROCs with wirebonds.

The most technologically challenging step is bump-bonding. Bump-bonding was a cost and schedule driver for the current pixel detector. For the present BPIX detector, bump-bonding was done by PSI whereas for FPIX the bump-bonding was performed by two commercial companies. Industry is progressing steadily on bump-bonding and lower cost processes for micro-bumps at 30 μm diameter and 100 μm pitch are becoming available. A survey of possible bump-bonding suppliers is ongoing.

6.3.1 Bare module assembly

To illustrate the process we briefly describe the bump-bonding procedure developed at PSI that will be used for production of Layers 1 and 2 modules. More details are available in [48]. In a first step, photo-lithographic and under-bump-metal (UBM) treatments of ROC and sensor wafers are performed. UBM is needed to make a robust connection between indium bumps and Al pads on the wafers. It is composed of thin layers of Ti, Ni and Au. Indium is then evaporated on both wafers. The next step is the lift-off of the photoresist. Then Si sensors and ROCs are cut out from the wafers. Finally, ROCs and Si sensors are re-flowed in an oven to make spherical bumps and the ROCs are placed and pressed to the sensors. Afterwards, the bare modules are reflowed again. The in-house fabricated bump-bonding machine provides a precision of 1 μm in placing ROCs on the sensors. The bare modules are qualified with a test including an IV-curve, ROC functionality tests and, on a sample basis, a pull test. In case of low quality bump-bonding, it is possible to rework a ROC. It is important to perform the bare module test to provide fast feedback to the bump-bonding process.

6.3.2 Assembly of HDI with TBM, power and signal cable

High density interconnects (HDI) will be visually inspected, looking for shorts and bridges, then probe tested to check the connectivity of all the traces. Accepted parts will then be equipped with the remaining components. For FPIX, the TBM, surface mount components

and a cable connector will be mounted, whilst for BPIX either one TBM (for layers 2 to 4) or two TBMs (for layer 1) will be mounted and the cable will be soldered to a special plate on the BPIX HDI. The assembled HDI is tested, checked the TBM functionality as well as checking for opens or shorts on the power and token passage lines. Thermal cycling is foreseen to check the ability of the HDI to withstand the expected environmental conditions inside CMS.

6.3.3 Complete module assembly

The construction of the BPIX module is completed in the following steps. The base strips are glued to the ROCs of the bare module (BPIX Layers 2-4 modules). A small amount of glue is applied between the edge of the sensor and the ROCs to reinforce the connection near the wirebonding area. The pre-assembled HDI is glued to the module. The HDI and the ROCs are connected with wirebonds.

All gluing procedures are done with standard two-component epoxy glue. Each gluing step is done on a separate jig that ensures the exact placement of the parts and keeps them in place with vacuum until the glue has cured. Instead of using a glue disperser to apply the desired small quantities of glue, the glue is applied with a stamp that is lowered into a glue bath and matches the form of the gluing area. This method is an easy but well-defined way to apply the glue exactly where it is needed. In order to apply the very small amount of glue in between the ROCs and the sensor, the stamping technique is used in a different way. Here, the stamp is replaced with Kapton flaps that bring the glue in the opening between the sensor and the ROCs.

For FPIX, robotic pick-and-place machines, with integrated optics, pattern recognition, and glue dispensing, will be used to join the HDI to bare modules, improving the uniformity of the production technique and reducing the risk of idle staff if there are delays in the supply of components. The module assembly sequence begins by manually placing pre-tested, known good bare modules and HDI on vacuum chucks on the baseplate of the pick-and-place machine. The machine program successively moves the camera (fixed to the machine motion head) to view the fiducials on the sensors and HDI and acquires the fiducial locations using pattern recognition, picks up a stamping tool from a tool rack, dips the stamp in the glue bath, and stamps epoxy on the sensors, returns the stamping tool to the tool rack, picks up a vacuum tool from the tool rack to pick-and-place individual HDI onto sensors (making adjustments based on the actual part locations in the machine to accurately align and join the components), and returns the vacuum tool to the tool rack. Module end holders are also aligned and glued to the modules using custom tooling and the pick-and-place machine.

Following mechanical assembly, HDI are wirebonded to the ROCs using semi-automated ultrasonic wirebonding machines. Routine pull tests of sample wirebonds will be performed for quality control. The wirebonds will be encapsulated with an elastomeric compound using semi-automated dispensing equipment. The module assembly sites will also be responsible for the testing and characterisation of the assembled pixel modules. Short flex cable connector savers will be connected to the FPIX modules and used for all FPIX module testing.

6.4 Module test

The goal of the module tests is to verify that all pixels function correctly, that each ROC can be programmed properly, and that all calibrations of a module produce reasonable results. The task is a challenge due to the large number of channels (124 M pixels) and the multidimensional parameter space: each ROC has 19 DACs and 2 control registers to be set, and several of them

have to be tuned for each ROC individually.

Another complication results from the unknown temperature at which the pixel detector will eventually be operated and the missing knowledge of the module behaviour after thermal cycling. Therefore, the full test procedure described below will be performed twice at $-20\text{ }^{\circ}\text{C}$ (before and after 10 thermal cycles between $+17\text{ }^{\circ}\text{C}$ and $-20\text{ }^{\circ}\text{C}$) and then, repeated at a temperature of $+17\text{ }^{\circ}\text{C}$. The complete test procedure and the analysis of test results will be fully automated: human intervention is reduced to placing modules in the cooling box, starting a program that supervises all procedures and browsing results that appear on an automatically generated web page.

The test setup is composed of a programmable cooling box in which four modules can be tested at a time, four custom test boards connected to a PC via the USB interface and a high voltage supply. The test board includes a field-programmable gate array (FPGA), which controls the tests, and two ADCs.

6.4.1 Module test procedure in a cooling box

The test and qualification process is divided into three main steps. First, all ROCs have to be set into an operational state: the analog current is set to the nominal value of 24 mA, and the signal threshold and the timing of the internal calibrate signal are tuned to a stable state. In the second step, the functioning of the pixel readout circuits and their electrical connections to the sensor pixels are checked. The following procedures are performed:

- check that each pixel responds to the internal calibrate signal,
- test the functionality of the four trim bits that are used for a threshold unification of all pixels in a ROC,
- determine the bump-bonding quality by checking for the presence of a bump-bond connection for every pixel,
- verify that each pixel readout circuit responds with the correct pixel address.

In the third step, the main characteristics of a module are determined by performing the following tests:

- measure the noise for each pixel,
- set the threshold of each pixel to obtain a uniform response over the whole module (trimming),
- establish the dependency of the pulse height on the injected charge,
- verify the absence of sensor breakdown and high leakage current (measurement of IV-curve).

In the following section, the most important tests and calibrations are briefly described.

6.4.2 Pixel defects

As part of the standard test, the readout circuits and the electrical connection to the sensor pixel are tested for each pixel. A pixel is counted as defective, if one or several of the following tests failed: pixel readout test (including test for mask defects when a pixel responds even when disabled), bump-bonding test, trim bit test, and pixel noise measurement.

The functionality of each pixel is checked by inducing a signal via an internal calibration capacitance. First, the masked (disabled) pixel is tested to determine if it responds to a calibration

Grade	A	B	C
Noise [e^-]	< 500	< 1000	> 1000
Relative gain width	$< 10\%$	$< 20\%$	$> 20\%$
Pedestal spread [e^-]	< 2500	< 5000	> 5000
Threshold width [e^-]	< 200	< 400	> 400
$I^{meas}(+17^\circ\text{C}, 150\text{V})$	$< 2\mu\text{A}$	$< 10\mu\text{A}$	$> 10\mu\text{A}$
$I^{calc}(-10^\circ\text{C}, 150\text{V})$	$< 3\mu\text{A}$	$< 15\mu\text{A}$	$> 15\mu\text{A}$

Table 6.1: Grading criteria based on ROC performance and sensor leakage current established in the previous barrel module production

signal. Second, for the enabled pixel 10 calibration signals are sent and the number of output signals is registered. The pixel is fully working if all signals are registered. The pixel is defective, if no output signal is registered.

In addition to the pixel defects listed above, a pixel is counted as defective if

- the pixel is noisy (above $1000 e^-$) or shows a strange noise behaviour (below $50 e^-$)
- the pixel could not be trimmed to a threshold of $V_{Cal} = 60$, i.e. a pixel with threshold below 50 DAC or above 70 DAC
- if the linear fit of the pulse height curve failed, i.e. the gain is below 1.0 ADC/DAC
- if the pixel saturated in the low V_{Cal} range, i.e. parameter $p1$ of the hyperbolic tangent fit to the pulse height curve is above 1.5

A module is graded as “A” if the fraction of pixel defects is less than 1%, graded as “B” if the fraction is in the 1-4% range, and graded as “C” in case the fraction of defective pixels is above 4%. If at least one pixel has a mask defect, such a module is graded as C. Grade A modules will be placed in the innermost layers of BPIX and the inner disks of FPIX. Grade B modules will be mounted in the outer layers and disks. Grade C modules will not be used in the upgraded pixel detector.

6.4.3 ROC performance

Missing charge has an impact on the hit resolution. The charge information depends on the pixel threshold and on the pulse height calibration. In the case of a calibration based on the average per double column or even per chip, the variation of gains and pedestals on a chip should be limited. To ensure a uniform response of all pixels on a chip, restrictions will be also applied to the average noise and the width of the trimmed threshold. The choice of performance based grading criteria was mainly determined during the module qualification tests performed for the present pixel detector [49], and are shown in Table 6.1.

In order to unify the physical thresholds of all pixels on a readout chip, the global chip threshold can be fine-tuned for each pixel by the use of four trim bits. After trimming, the RMS of the pixel threshold distribution should not exceed 400 electrons.

The correlation of the pulse height and the amplitude of an injected calibration signal can be described by a linear function over a large range. The slope of this function is called the gain, and the offset is called the pedestal. The relative gain width is calculated by dividing the RMS of the gain distribution by the mean. The pedestal spread is converted into electrons by using the calibration from the test-beam. The spread in both parameters is acceptable if the mis-calibration contribution to the track and vertex reconstruction is less than the effects of

multiple scattering. The tolerable variation of the gains is about 20% and the pedestal RMS is required to be less than 5000 electrons.

6.4.4 Sensor leakage current requirements

To detect eventual sensor damage during assembly, limits on the leakage current are defined as shown in Table 6.1. The leakage current at the initial operational voltage of 150 V should not exceed $10\ \mu\text{A}$ at $T=+17\ ^\circ\text{C}$. With increasing radiation damage, the module sensors will be operated at increasing depletion voltage V_{OP} . In order to ensure reasonable behaviour at higher operating voltages, a limit is set on the slope of the IV-curves: $I(V_{OP})/I(V_{OP}-50\ \text{V}) < 2$.

The grading criteria for the sensor leakage current are defined at the room temperature. Therefore the leakage current measured at $-20\ ^\circ\text{C}$ has to be converted to the corresponding leakage current at $+17\ ^\circ\text{C}$. In Table 6.1 we show the grading criteria used for the previous production, when modules were qualified at $-10\ ^\circ\text{C}$ due to less expected radiation damage. The mean of the ratio of converted to and measured current at the room temperature is around 1.5. Consequently the limit for the current measured at $-10\ ^\circ\text{C}$ is set 1.5 times higher than for the current measured at $+17\ ^\circ\text{C}$.

6.4.5 Module tests and calibration with X-rays

Module tests and calibration with X-rays has a twofold purpose: the testing of the module response to charge injected in the silicon sensor at high rate, and the calibration of the internal signal (VCal DAC) of each ROC. For these purposes, dedicated X-ray test stations will be built at each module qualification center.

High rate tests with X-rays are currently being developed. The details of the programme of x-ray tests to be used during module production remains to be decided, whilst the following tests are already available:

- pixel hit efficiency versus the hit rate
- double column readout uniformity
- bump-bonding quality test
- pixel noise measurements versus the hit rate

To determine the ROC threshold in electrons one needs to calibrate the VCal DAC value. This will be done with several fluorescent lines. The primary X-ray beam hits a selectable target and excites the emission line(s). In such a way one produces a monochromatic X-ray beam. A comparator threshold will be determined for each energy and then the VCal DAC will be found that corresponds to the established threshold.

In the future, we will decide which tests will be used for evaluating every module during pixel upgrade detector production.

6.5 Construction Database

The main purpose of the Construction Data Base (DB) is to keep track of the

- inventory of all module components
- component and modules test results
- assembly and mounting status
- shipping and storage information

FPIX is planning to use the same DB developed in the past for the current detector. BPIX is considering using either the same DB as FPIX, or developing a new DB similar to the one that has been used in the past.

6.5.1 FPIX DB

The Construction DB will reside in the CMS Online Database environment at P5 that provides high performance, very reliable service, high availability, and a secure environment. It will use the same database schema as that used very reliably for construction and online operations of the CMS Pixels and HCAL detectors since 2005. Interfaces exist for users to access the database remotely for loading and retrieving data. Database loads are very restricted, but read access is more widely available.

The Pixel databases began as a construction database and was later deployed for detector configuration and monitoring. The FPIX DB group has had the unique experience of using the Pixel Construction database to successfully coordinate the efforts of multiple institutions in different geographical locations to construct the present CMS Forward Pixels. Since then, a considerable amount of effort has gone into developing database interfaces for users to both load and access data remotely. These interfaces can be readily used for implementing an efficient and dependable pixel detector construction process distributed across multiple geographical locations. The standard procedure for users to load information is to produce data in predefined XML formats and copy them to a spool area in P5, where a dedicated database loader picks it up and writes the data to the database. As for data retrieval, a preferred mode is to retrieve data from the database using the CMS WBM interface.

6.5.2 BPIX DB

The BPIX DB design is based on similar projects previously used for the current BPIX detector and for the Tracker Inner Barrel/Disk (TIB/TID) detector assembly. A single DB instance running at CERN will serve all production centers and should be filled either by authenticated clients running at the various centers and/or via a web interface running at CERN. Frequent (few times per day) DB back-ups will be performed automatically.

The key point of such a DB is its strong integration with the testing procedures of the various components. The applications used in the testing centers to steer the testing procedures should integrate DB clients capabilities and fill the relevant DB tables. Dedicated DB tables will be created for each type of test integrating a common set of information about the performed test (such as the list of tested objects, an overall score for the outcome of the test, the center performing the test, the date, etc...) with a test-specific set of information. The test-specific information are for example the list of defects found in the test, the physical properties measured (e.g. IV values), and any other quantitative result that can be obtained in the test and later processed for statistical analysis. The concrete content of the test-specific tables will be developed in parallel with the definition of the various testing steps. A first prototype implementation is being developed for the tests performed for the current pixel barrel detector construction.

In addition to pre-processed test-specific results, the DB will also contain links to web URLs or grid PFN with the raw data of the performed test. This should allow central reprocessing of the test data in case new analysis and grading procedures are defined after the initial tests. A centralised analysis, opposed to analysis done at a local test center, can also be used as standard *modus operandi*. This was the approach used in the TIB/TID assembly process and provided uniformity of the test results across the three different integration centers (Pisa, Firenze and Torino).

Mounting and positioning information is also stored in the database. This is done by defining a logical position numbering scheme and associating the module ID to it. The current CMS DetID numbering schema, modified to include the additional layers, can be used to avoid later complications in matching of different conventions and to simplify the integration with existing CMS software and visualisation tools. While these tables only contain the current snapshot of the detector mounting, the historical view of the assembly operations is stored in a dedicated table containing all mounting and unmounting steps for each module or component.

A DB prototype is being tested using MySQL as backend and the python-storm object oriented library to define the clients API. Templates of tables for inventory of components (sensor, HDI, ROC) and compound objects (bare modules, full modules) have been defined for testing purposes. Fake test-specific tables have also been prepared while the procedures for the actual tests are finalized. A transfers handling system based on what was used for TIB/TID has also been created.

Chapter 7

The Power System

The power system of the Phase-1 upgrade to the pixel detector will also have to be modified. As in the other aspects of this upgrade, existing infrastructure will be reused as much as possible to minimize cost and installation time. Replacing all the pixel cables in the existing cable plant would be a significant task in terms of time, and adding new cables on top of what is already present would be very difficult given that space is at a premium in the cable trays from the YB0 to the PP0. However, the existing cable plant to the detector can be reused and is sufficient for the increased demands of a four-layer, three-disk detector if higher voltage can be supplied on the existing cables and is stepped down using custom DC-DC converters in the pixel service cylinders on-detector. In this chapter, we describe the custom electronics and the chip (ASIC) needed to accomplish this task.

7.1 System Parameters and Conception

In total, four different voltages are required to power the front-end electronics of the pixel system: two low voltages for operation of the module readout electronics; the bias voltage, to deplete the silicon sensor; and an “auxiliary” low voltage for electronic components that are located on the supply tube. A simplified view of the new pixel power supply system is shown in Figure 7.1. The power system of the current detector is described in detail in [43].

The present PSI46 readout chip requires 1.6 V for the analog and 2.2 V for the digital part. Six on-chip voltage regulators compensate for variations due to different voltage drops on the cables, and improve power supply noise rejection. Internally the chip operates with 1.4 V and 2.0 V. For the original analog version of the chip, the analog current per ROC amounts to 26.1 mA, while the static digital current per ROC is 29.9 mA. These static analog and digital ROC currents were used to predict the currents in the individual cables of the current detector, and the predicted values were compared with the measured values, with excellent agreement. The digital current has also a dynamic component that depends on the chip activity. The total digital current is thus a function of the particle fluence rate, R , which scales with instantaneous luminosity. A functional dependence of $I_{dig} = (29.9 + 0.1 \times R \text{ [MHz/cm}^2\text{)]) mA}$ was deduced from measurements with the real detector at various instantaneous luminosities during the first half of 2012. This rate dependence was confirmed in lab measurements on single modules using x-rays. The rate-dependent part of the digital power consumption is dominated by the transportation of hits from the pixel unit cell to the double column periphery, which happens independently from the bunch crossing rate. The digital readout activity upon receipt of a trigger is expected to be higher for a bunch crossing interval of 50 ns, as events contain more hits compared to 25 ns bunch crossing. However, this contribution is sub-dominant and the above quoted number is based on measurements with 50 ns bunch crossing. Therefore in the remainder of this chapter no distinction between the two bunch crossing scenarios is made.

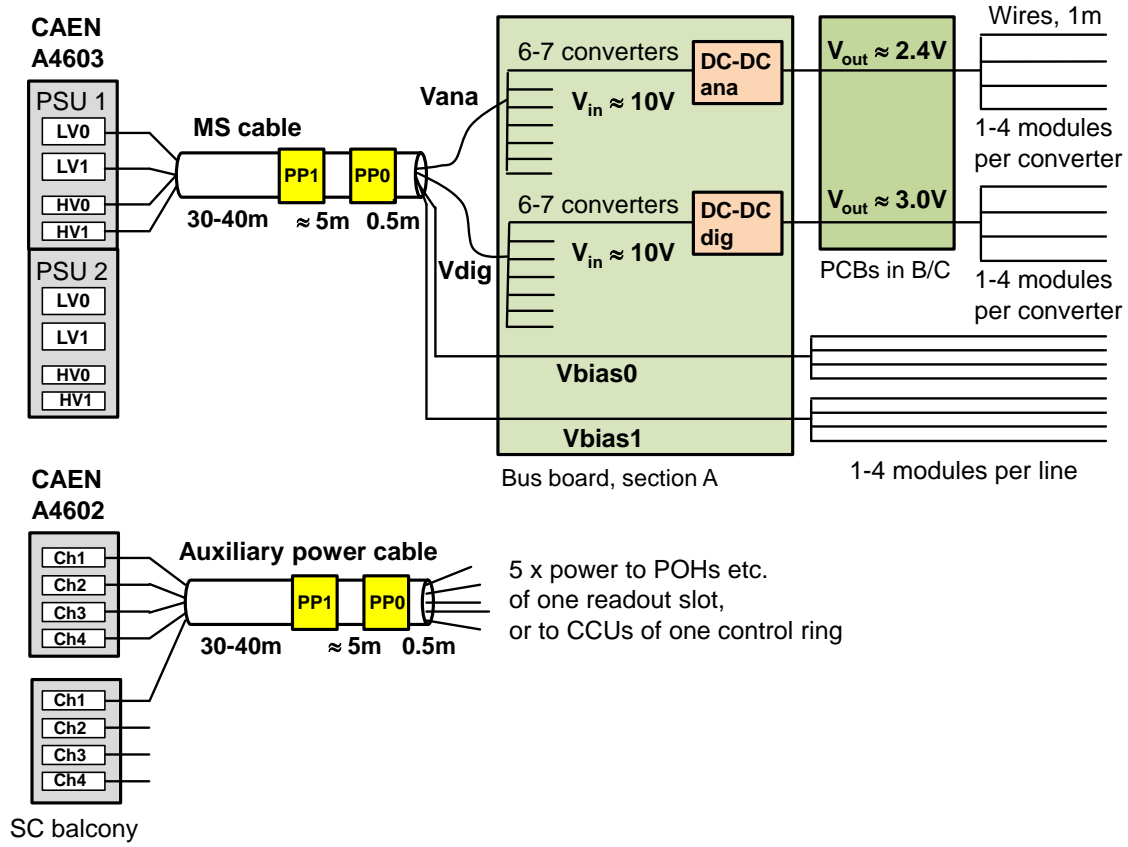


Figure 7.1: Simplified schematic of the pixel power supply system. It shows the connectivity of one unit of a A4603 power supply, and how two A4602 power supplies provide together the five independent channels of one auxiliary power cable. The digital and analog voltages, V_{dig} and V_{ana} , are supplied by the low voltage channels $LV0$ and $LV1$, respectively, while the high voltage to bias the sensors, V_{bias} , is supplied by two independent channels, indicated by $HV0$ and $HV1$, in each power supply unit. Cable break points are in patch panels 0 and 1 (PP0 and PP1).

An increase of the power consumption for the new PSI46dig chip is not expected. This will have to be confirmed by measurements; preliminary measurements of the static and dynamic currents do not indicate an increase. The digital current per module has been calculated based on measured cluster rates and widths for BPIX, and based on simulated particle fluence rates for FPIX (as a detailed extraction from data has not yet been done for FPIX), for all layers and disks. Required analog and digital currents per module are summarized in Table 7.1.

The digital voltage is also used to operate the TBM chip. The current per TBM chip amounts to about 35 mA.

The high or “bias” voltage is required to deplete the silicon sensor. The depletion voltage is about 50 V for an unirradiated sensor, but increases over the detector lifetime, as more particle fluence is collected. The CMS pixel modules, cables, connectors and power supplies have been laid out for a bias voltage of down to -600 V. The innermost layer of the BPIX will be exchanged after accumulation of 250 fb^{-1} , corresponding to a fluence of about $1.6 \times 10^{15} \text{ n}_{eq}/\text{cm}^2$. At this point the sensors in the BPIX inner layer will no longer be fully depleted. However, the detector is designed to work well also with partially depleted sensors. The bias current increases linearly with fluence. In addition, the required current depends exponentially on the sensor

Layer / disk	Analog current [A]	Digital current [A]
Layer 1	0.42	1.32
Layer 2	0.42	0.71
Layer 3	0.42	0.61
Layer 4	0.42	0.58
Disk 1 inner / outer	0.42 / 0.42	0.63 / 0.53
Disk 2 inner / outer	0.42 / 0.42	0.63 / 0.53
Disk 3 inner / outer	0.42 / 0.42	0.63 / 0.53

Table 7.1: Currents per pixel module (16 ROCs) for the analog (1.6 V) and digital (2.2 V) line, for layer 1-4 of the barrel and the inner and outer ring of disks 1-3. An instantaneous luminosity of $2 \times 10^{34} \text{ cm}^{-2}\text{s}^{-1}$ is assumed. The digital current includes 35 mA per module for the TBM chip. For simplicity, BPIX currents based on pseudo-rapidity averaged cluster rates and widths are shown in the table. If the pseudo-rapidity dependence of the cluster rate and width is included, the currents depend on the module's pseudo-rapidity and are slightly lower.

temperature. A temperature drop of 8 K decreases the current by a factor of about 2. Details depend on the annealing scenario. Based on measurements of the leakage currents after up to 5.5 fb^{-1} of data acquired in 2011 at $\sqrt{s} = 7 \text{ TeV}$, and using a scaling factor of 1.13 to account for the increase of fluence with center-of-mass energy, as deduced from measurements at three different values of \sqrt{s} , the current per module at $\sqrt{s} = 14 \text{ TeV}$ can be estimated as a function of the integrated luminosity and sensor temperature. For 250 fb^{-1} and a sensor temperature of 0°C (-4°C), the bias current of a module will amount to about 4.1 mA (2.7 mA) for layer 1 and 0.47 mA (0.31 mA) for layer 4.

Finally, an auxiliary voltage of 2.5 V is needed to operate the detector control electronics independently from the front-end. This includes the CCU25 ASICs, the Pixel Opto-Hybrids, and the PLL chips. All these components are located on the supply tube.

7.1.1 Power Supplies

The pixel detector is powered via the CAEN EASY 4000 power supply system. The system is controlled from a SY1527 mainframe, which contains three A1676A branch controllers. Six two-channel A3486H supplies transform 400 V_{AC} into 48 V_{DC} and can deliver up to 2 kW per channel. Magnetic field and radiation tolerant modules of types A4603 and A4602 transform the 48 V into the low, bias and control voltages. One A4603 module consists of two identical units, which deliver two low voltages ($90\text{W} + 40\text{W}$ at 8-12 V, Section 7.3), plus two independent bias voltages (-600 V , 20 mA) each. In total, 32 and 24 A4603 supplies are used by BPIX and FPIX, respectively. The A4602 power supplies are 4-channel devices. Sixteen such modules are used in the pixel system. The whole system fits into two power racks.

7.1.2 Power Cables

Two types of cables exist: “multi-service (MS) cables”, which carry the low and bias voltages, and “auxiliary power cables” for the auxiliary power. All cables are split into three parts: a 30-40 m long cable, which connects the power supply to Patch Panel 1 (PP1); a 5 m long cable, which runs from PP1 to the tracker bulkhead (PP0); and a 0.5 m long cable, which goes from there to the end flange of the supply tube. The conductor material is copper in all cases.

The 144 custom multi-service cables contain $6 \times 4 \text{ mm}^2$ low voltage conductors, ten AWG30 wires for the bias voltage, and two pairs of AWG28 wires for low voltage sensing. From the six low voltage conductors, four (two for power and two for return) are used for the digital

voltage, where larger currents are required, and two (one for power, one for return) for the analog voltage. The total resistance is typically $0.5\ \Omega$ on the analog line and half of that on the digital line (both for power plus return). The ten bias lines are arranged in two independent bias channels, each with four power lines and one common return line.

The twelve auxiliary power cables are standard cables with $26 \times$ AWG20 conductors, plus five pairs of AWG28 wires for sensing. The 26 conductors are arranged in five independent channels: four channels with six lines (three power, three return) each, which are connected to one A4602 supply and provide power to the pixel opto-hybrids and other supply tube electronics, and one channel with two lines, which is connected to another A4602 supply, and is used to power the CCUs of one control ring.

7.1.3 Modularity for BPIX

Each barrel half shell is powered by 16 MS cables and two auxiliary power cables, corresponding to 10 independent auxiliary power channels. Two MS cables are routed through one “slot” of the supply tube and power either 35 or 39 detector modules. Each MS cable includes eight bias voltage lines, which are connected to between one and four pixel modules each. The eight bias lines are grouped into two independent bias channels.

One auxiliary power channel powers the control components corresponding to one barrel read-out slot, or the CCUs of one control ring.

7.1.4 Modularity for FPIX

Each half disk is powered by four MS cables; and one MS cable powers either 5 or 6 modules of the inner ring, plus 9 or 8 modules of the outer ring, i.e. 14 modules in total. Each bias line serves 1-2 pixel modules.

One auxiliary power cable powers one half cylinder. One channel powers the control components corresponding to a 45° sector in ϕ , or the CCUs of one control ring.

7.1.5 Upgrade of the Power System

The upgrade of the pixel detector poses a considerable challenge for the power system. The increase in the number of readout channels by a factor of 1.9 with respect to the original pixel detector configuration increases the front-end power consumption by the same factor. Resistive power losses scale with the current squared, and are significant due to the sizeable resistance of the long supply cables. The required amount of additional or thicker cables cannot be installed, due to lack of space both in the cable channels and the connector areas (PP1 and PP0). Supplying the required power through the existing cable plant could cause overheating of the cable channels. In addition, the required total analog and digital power, i.e. front-end power consumption plus losses in supply cables, surpasses the power capacity of the CAEN A4603 power supplies. DC-DC step-down converters will be used to overcome both problems. These devices will allow to transmit the power at a higher voltage but lower current. The conversion ratio, r , is defined as the ratio of input voltage, V_{in} , to output voltage, V_{out} , i.e. $r = V_{in}/V_{out}$. With an input voltage of 9-10 V and analog and digital output voltages of 2.4 V and 3.0 V, respectively, conversion ratios of 3-4 will be reached, which decreases resistive power losses by a factor of around 10. The DC-DC converter output voltages are higher than the ROC operating voltages to compensate for the voltage drops in the power PCBs and the module power cables. The DC-DC converters and their integration into the pixel detector will be described in detail in the next section.

Layer / disk	Modules per converter pair	Analog current [A]	Digital current [A]
Layer 1	1	0.42	1.32
Layer 2	1 / 2 / 3	0.42 / 0.84 / 1.25	0.71 / 1.42 / 2.13
Layer 3	4	1.67	2.44
Layer 4	4	1.67	2.32
Disk 1	2+2 / 1+2 / 1+3	1.67 / 1.25 / 1.67	2.30 / 1.68 / 2.21
Disk 2	2+2 / 1+2 / 1+3	1.67 / 1.25 / 1.67	2.32 / 1.68 / 2.22
Disk 3	2+2 / 1+2 / 1+3	1.67 / 1.25 / 1.67	2.32 / 1.69 / 2.22

Table 7.2: Number of modules connected to a DC-DC converter pair, consisting of one converter for the analog and one for the digital voltage; and output currents per DC-DC converter. An instantaneous luminosity of $2 \times 10^{34} \text{ cm}^{-2}\text{s}^{-1}$ is assumed. For the disks, the two numbers in the sums are the numbers of inner and outer modules, respectively. In the disks as well as in barrel layer 2 three modularity variants exist. For example, one, two or three modules are connected to one pair of DC-DC converters in the second barrel layer.

Each pixel module is connected to one pair of converters. The number of modules per converter pair depends on the digital current and thus on the location of the modules in the detector. The envisaged modularity is summarized in Table 7.2. One power cable, corresponding to one A4603 power supply unit, will be connected to 6-7 (4) pairs of DC-DC converters for BPIX (FPIX). No DC-DC converters are required to supply the bias voltage and auxiliary power.

7.2 DC-DC Converters

7.2.1 Working Principle

The DC-DC step-down converters foreseen for the pixel detector are of the “buck” type. The basic schematics is shown in Figure 7.2. Two power transistors T_1 and T_2 act as switches. They are periodically switched on and off with a switching frequency f_s , such that during a time t_{on} transistor T_1 is conducting and T_2 is open, while during time $T - t_{on}$, where $T = 1/f_s$, T_2 is conducting and T_1 is open. In this way the load is periodically connected to and disconnected from the power supply. The ratio t_{on}/T is the duty cycle D of the converter and corresponds for an ideal, lossless converter to the inverse of the conversion ratio, $D = 1/r$. An inductor stores energy during the time t_{on} and releases it during time $T - t_{on}$. The core of the inductor has to be made of non-magnetic material, since all ferrites would saturate in the 3.8 T magnetic field present in the CMS tracking volume. Capacitors at the in- and output of the converter bypass AC components, such that a DC voltage is delivered to the load. A feedback loop based on the Pulse Width Modulation technique (not shown in the figure) stabilizes the output voltage at a hardware-programmable value.

The challenges for the application of DC-DC buck converters in high energy physics are to achieve sufficient radiation and magnetic field tolerance, high efficiency, low ripple, low electromagnetic emissions, low mass, low volume, all at the same time.

7.2.2 Specification for DC-DC Converters

The specifications for the DC-DC converters to be used in the CMS pixel upgrade project are summarized in Table 7.3.

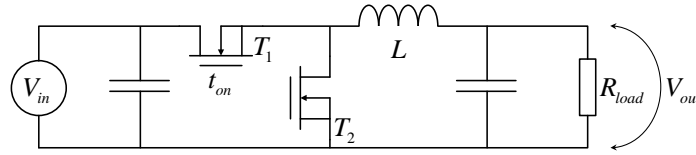


Figure 7.2: Simplified schematics of a buck converter. The feedback control loop is not shown.

Input voltage	9-10 V
Output voltage	2.4-2.5 V or 3.0-3.3 V
Conversion ratio	3-4
Maximum output current	3-4 A
Efficiency	At least 75%, at nominal operating conditions
Maximal dimensions	3.0 cm x 2.0 cm x 1.4 cm
Radiation tolerance (500 fb ⁻¹)	100 kGy and 2×10^{14} n _{eq} /cm ²
Protection features	Over-temperature, over-current and under-voltage protection
Control features	Remote disabling and status information
Special requirements	Stable operation under large and fast load variations
Total number required	1184
Total number including spares	1800

Table 7.3: Specifications for DC-DC converters for the CMS pixel upgrade.

7.2.3 ASIC Development

The semiconductor technology must provide both standard CMOS low-voltage transistors to realize the driving and control circuitry, as well as the high-voltage tolerant power transistors. While deep-submicron CMOS transistors are known to be relatively radiation-hard, the radiation tolerance of the high-voltage transistors, which are typically Laterally Diffused MOS (LDMOS) transistors, has been evaluated in dedicated studies [50]. The Total Ionizing Dose (TID) can induce threshold shifts and leakage current increase, while fluence induced displacement damage effects include an increase of the transistor on-resistance. A special transistor design is necessary to make the transistors sufficiently radiation-tolerant for the application in the CMS Tracker.

Radiation-tolerant buck converter ASICs have been developed in the PH-ESE group of CERN, using the 0.35 μm I3T80 technology from ON Semiconductor (previously AMIS). The most recent prototype ASIC in this technology is the AMIS4 [51]. This is a fully integrated synchronous buck converter which includes all required linear regulators, a bandgap reference, adaptive logic for dead-time handling, as well as measures against Single Event Effects. Protections against over-current, over-temperature and under-voltage states as well as a soft-start procedure are implemented and handled via a Finite State Machine. The converter can be switched on and off remotely and outputs a status signal. The chip is optimized for inductances of 200-500 nH and switching frequencies of 1-3 MHz. The device is specified to work with input voltages of up to 10 V, and to deliver output currents of up to 3 A. Currents up to 4 A can be delivered when the converter is properly cooled (even when the coolant is at room temperature). Based on the layout of the future AMIS5 chip, it was checked that electro-migration will not be an issue for currents of 4 A and any realistic chip temperatures. For example, a safety margin in current density of about 3 is found for a chip temperature of +50 °C.

Radiation tests both with protons and x-ray photons have been performed on single transistors

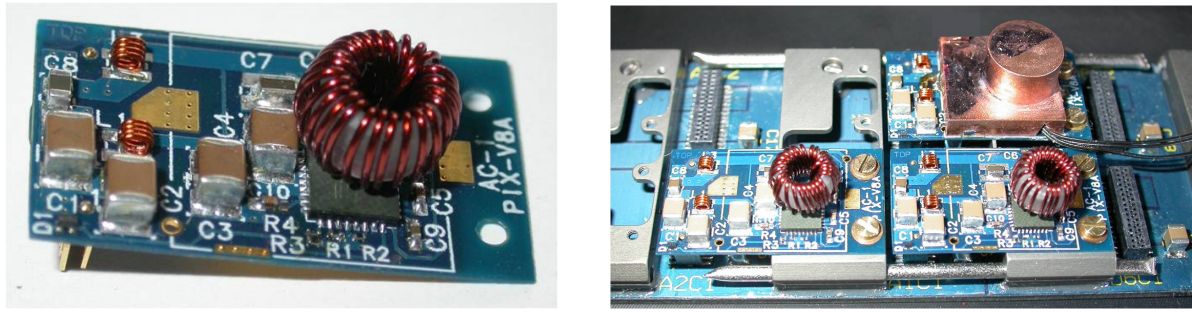


Figure 7.3: The AC_PIX.V8 DC-DC converter (left), and a part of the bus board with three DC-DC converters (one with a prototype shield; the cables coming out of the shield belong to thermistors), cooling bridges and dummy cooling pipes (right).

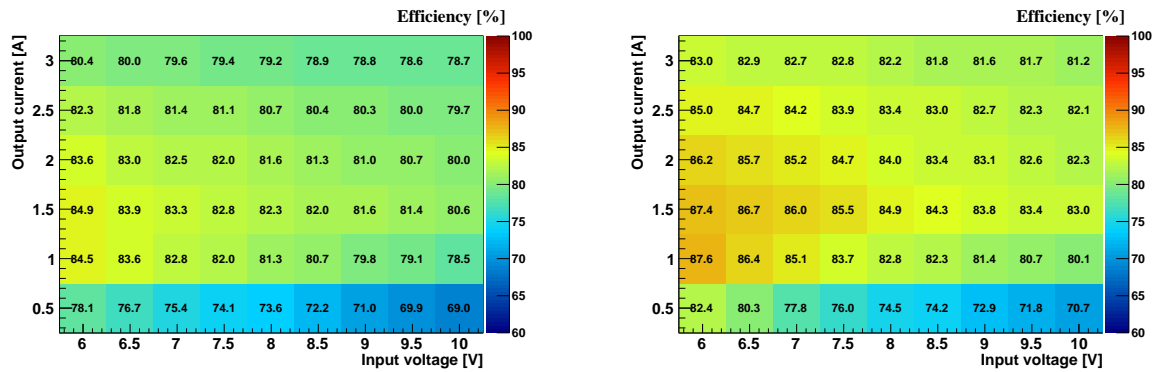


Figure 7.4: Power efficiency of the AC_PIX.V8 DC-DC converter as function of the input voltage and output current, for an output voltage of 2.5 V (left) and 3.3 V (right).

and prototype chips. The AMIS4 chip was functioning up to a Total Ionizing Dose of about 1 MGy [51], with an efficiency drop of about 2%. Both single transistors and full chips have been successfully tested up to fluences of about $1 \times 10^{15} n_{eq}/cm^2$. The efficiency was found to increase slightly with fluence. At the installation position of the DC-DC converters (a radius of about 20 cm and $z \approx 200$ cm) a TID of about 100 kGy and a fluence of $2 \times 10^{14} n_{eq}/cm^2$ is expected for a luminosity of $500 fb^{-1}$ [52].

In summer 2012, the next version of the chip, AMIS5, will become available. Functional differences between AMIS4 and AMIS5 are mainly related to details of the implementation of the control signal logic (status signal and remote control). AMIS5 will also implement changes to a certain type of on-chip pre-regulator, to improve the stability of the chip.

7.2.4 DC-DC Converter Development and Performance

The AMIS4 and its predecessor, the AMIS2 [53], were used to develop buck converters tailored to the application in the CMS pixel detector. In the following, results based on the most recent prototype converter, AC_PIX.V8, with the AMIS4 ASIC will be described, unless it is explicitly stated that results have been obtained with AC_PIX.V7 converters, which are equipped with AMIS2. The AMIS2 ASIC is similar to AMIS4, but does not yet implement the safety and control features. Dead times are fixed and an external 3.3 V supply is required.

In Figure 7.3 the AC_PIX.V8 converter is shown. The 2-layer PCB is equipped with the AMIS4 chip in a QFN32 package, a custom toroid inductor with a plastic core and an inductance of

450 nH, and pi-filters at the input and output ($L = 12.1$ nH, $C1 = C2 = 20$ μ F). The switching frequency is set to 1.5 MHz and the output voltage is either 3.3 V or 2.5 V. Slightly lower output voltages of 3.0 and 2.4 V are currently foreseen to be used in the detector. The comparison between measurement results of the 3.3 and 2.5 V converters show that a change of the output voltage by 5-10% will have an insignificant influence on the converter performance. The converters will be equipped with a shield, which serves three purposes: it reduces radiated magnetic emissions, it segregates noisy parts on the PCB from quiet parts, and it serves as a cooling contact for the coil. The preferred technology for the shield is a plastic body onto which a 30 μ m thick copper layer is galvanically deposited. The total copper thickness is therefore 60 μ m. Shields milled out of Aluminium (90 μ m thickness) are an alternative. The shield is connected to ground potential. The footprint of the DC-DC converter is 28×16 mm², and the height, including shield and connector, amounts to 13 mm.

The power efficiency, P_{out}/P_{in} , of the AC_PIX_V8 converter has been evaluated as a function of input voltage and load current. As is visible from Figure 7.4, the efficiency for input voltages of 9-10 V and output currents of 2-3 A, as expected in the pixel application, reaches about 80% for an output voltage of 2.5 V and about 82% for an output voltage of 3.3 V. The statistical uncertainty of these measurements are 0.5% (absolute). Only for output currents of well below 1 A efficiencies are significantly lower with values of about 70%, with an uncertainty of 1% (absolute). All quoted efficiencies have been determined at room temperature. A decrease of the cooling temperature by 1 K increases the efficiency by about 0.05% (absolute).

Even with optimal PCB and filter design a DC-DC converter will always produce a certain amount of conductive noise, i.e. noise currents propagating through the cables, due to its switching nature. Both Differential Mode noise, manifesting itself as voltage ripple, and Common Mode noise is created. Noise spectra have been measured with a classical EMC set-up: the noise signal is induced in a magnetic pick-up probe, which is clamped around the power and ground conductors in the incoming or outgoing cable. The pick-up noise signal is measured with a spectrum analyzer. A lot of effort has been invested to optimize the PCB layout and the filter design for low-noise performance [54, 55]. As mentioned above, one function of the shield is to segregate the “noisy” part of the PCB from sensitive components like the inductor of the output pi-filter. This is documented in [56, 57].

The flow of large fast-changing currents through the air-core inductor leads to magnetic emissions (radiated noise). The magnetic radiation has been minimized through optimized coil design, using FE simulations [58]. The remaining field is reduced to a negligible level by the shield. This can be seen from Figure 7.5, where the emissions with and without shield are compared for AC_PIX_V7 converters. For these measurements, the magnetic emissions of the powered DC-DC converter are scanned with a magnetic probe, in a plane parallel to the PCB, and at a distance that corresponds to a height of 1.5 mm above the shielding.

Due to its inefficiency of about 20%, the DC-DC converter dissipates heat, which has to be removed by active cooling. The critical components are the ASIC and the inductor. The chip is glued with heat-conductive glue into its package, and is connected through vias to a large copper ground area on the PCB backside, which will be in contact with a cold surface. The shield is exploited to cool the inductor. It is filled with cured heat-conductive paste, to ensure that the inductor transmits its heat to the metal-coated inner surface. By thermal conduction the heat is then brought through four solder connections from the shield to the backside ground area. This concept has been studied both with FE simulations and measurements, using an infrared camera for measurements without shield and thermistors for measurements with shield [57]. For an output current of 3 A, the chip package temperature is about 25 K above the cooling

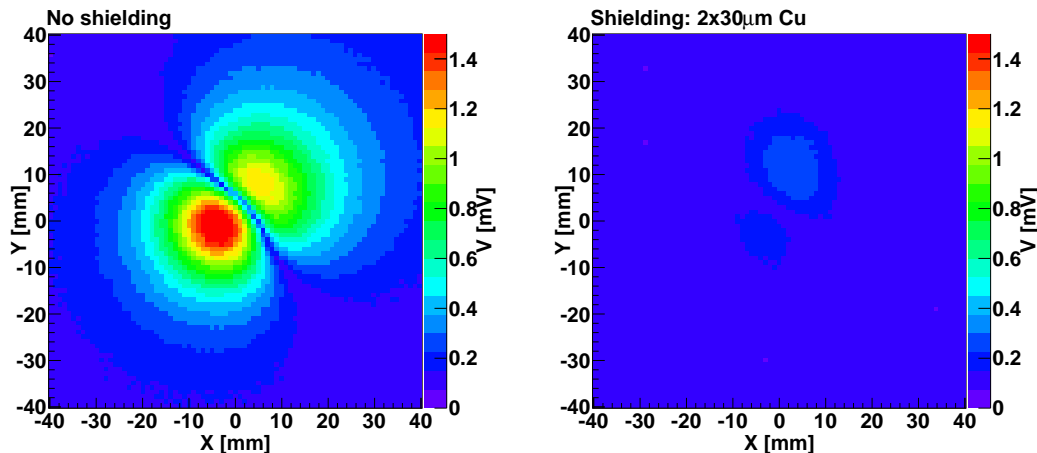


Figure 7.5: Magnetic emissions of the AC.PIX.V7 DC-DC converter, at a distance corresponding to a height of 1.5 mm above the shield. The field component perpendicular to the PCB plane is presented. The colour-coding shows the voltage induced in a magnetic near field probe. Left: without shield, right: with a plastic shield coated with a 30 μm thick copper layer (60 μm in total). Both measurements have been performed with an input voltage of 8.5 V and an output voltage of 2.5 V.

temperature. Without the shield, the inductor temperature was rising to temperatures of up to 70 K above the cooling temperature, for an output current of 3 A. Under the same condition, but with the shield in place, the inductor temperature is at most 40 K above the temperature of the cooling block. Resulting temperatures both for chip and coil are uncritical even for cooling at room temperature. The over-temperature protection of AMIS5 will set in at 120 °C.

The magnetic field tolerance of DC-DC buck converters has been tested in 2008 in a 7 T Nuclear Magnetic Resonance magnet at Forschungszentrum Jülich, using DC-DC converters both with an early custom prototype chip (AMIS1) and with commercial chips, with ferrite and air-core inductors. The efficiency of converters with air-core inductors changed by at most 5%, while devices with ferrite inductors showed a drastic drop of efficiency by up to 80%. The AMIS5 boards will be tested for magnetic field tolerance in 2013.

7.2.5 Integration of DC-DC Converters

In BPIX and FPIX the same DC-DC converters will be used. In both cases they are located outside of the sensitive tracking volume, and far away from the sensitive front-end electronics. The requirements in terms of low-mass and low-noise design are therefore relaxed with respect to a potential installation close to the front-end chips.

7.2.5.1 Control Communication

The DC-DC converters will require two control lines: one input line for the enable/disable signal, and an output line with the binary status information (status good or bad). The parallel PIO ports of the CCU25 ASIC [59] will be used for the control communication. To limit the number of connections, pairs of converters powering the same modules will be controlled together. The status signal will be delivered as open-drain, to allow for a wired-OR of the output signals.

7.2.5.2 Integration for BPIX

For BPIX the DC-DC converters will be located in segment A of the supply tube (Figure 4.10), at $\eta \approx 4$ and $z = 200 - 230$ cm.

Up to 13 pairs of DC-DC converters will be plugged to a bus board (Figure 7.3). This 8-layer PCB with dimensions 488 mm x 40 mm x 1.6 mm will distribute power and control signals for the DC-DC converters. The bias voltage will also be transmitted through this PCB. The board will be connected to a 0.5 m long multi-service cable on the far end, and will be plugged to other power distribution boards at the near end. These boards bring the power from segment A to segment C, from where it is transmitted via copper clad aluminium cables of 360 μm diameter and 1 m length across segment D to each individual pixel module.

Based on the layout of a prototype bus PCB, and with realistic assumptions for the power boards in segments B/C and the cables in segment D, voltage drops between the DC-DC converters and the pixel modules have been estimated in a DC analysis for an input voltage of 10 V and realistic output currents. Voltage drops on power plus return are typically 600 mV, with the largest single contribution coming from the wires in segment D. With respect to nominal module input voltages of 1.6 V and 2.2 V, the voltage margin amounts to 150-300 mV for DC-DC output voltages of 2.4 and 3.0 V.

In the current BPIX system, eight real and one “dummy” CCU are used per half shell, i.e. one CCU per readout slot, and all CCUs are located in the central slot of the supply tube. The CCUs will be relocated to the A/B transition regions of their respective readout slots, from where they will communicate with their DC-DC converters, POHs, DOHs, etc. The control ring signals between CCUs will be transmitted with a new flexible ring cable.

The geometry of the DC-DC converters, in particular the shape of the shield, has been optimized such that 13 pairs fit into each supply tube slot. CAD studies have shown that the remaining volume is sufficient to house all other required services (optical fibers, cooling pipes, etc.).

The DC-DC bus board will be fixed by four screws to the supply tube. Long holes will allow for thermal expansion. A heat dissipation of about 30 W is expected from the DC-DC converters in one supply tube slot. The CO₂ cooling pipes, which are routed from the end flanges to the pixel detector through the supply tube slots, will be used for cooling of the DC-DC converters. In fact, the heat from both DC-DC converters and opto-hybrids is used to pre-heat the CO₂ liquid, such that a two-phase flow is created. The DC-DC converters are cooled through their backside, which will be in contact with aluminum cooling bridges. Each converter is fixed with two screws to a cooling bridge. One bridge serves one converter pair. The bridges are made out of two parts. The lower part will be glued precisely to the bus PCB, and will support the cooling pipe. Once the cooling pipe is in place, the upper parts can be screwed to the lower parts. Cut-outs in the bridges minimize their mass. To insulate the electrical DC-DC ground from the cooling system, the cooling bridges will be anodized all around.

7.2.5.3 Integration for FPIX

The DC-DC converters for FPIX will be installed at the inside of the service cylinders (Figure 1.10), between the end flange and the port cards. Bus boards will carry four pairs of DC-DC converters, where one pair delivers power to three or four pixel modules. Each bus board will serve one port card, corresponding to one readout group respectively 1/4th of a half disk. Twelve bus boards will be required per half cylinder. The voltage margin has been estimated and is very similar to the BPIX case. From the bus boards, low voltages will be transmitted

via cables to the port cards, and from there via 75 cm long flexible aluminium readout/power cables to the pixel modules on the disks.

Bias voltages will be transmitted directly from filtering cards to the port cards and then through the aluminium readout/power cables to the pixel modules.

Similar to the BPIX case, the CO₂ detector cooling loops will be used to cool the DC-DC converters.

7.2.6 Future Developments

During 2012, testing of DC-DC converters with the AMIS4 chip will continue, including e.g. system tests similar to those described in Section 7.4, tests of the cooling performance and radiation tolerance. Once the final geometry has been chosen, the production of the shield and inductor will be transferred to industry. Electrical and thermal tests of fully equipped bus boards are under preparation. Passive and active thermal cycling of the converters will be done to test and prove their reliability.

The AMIS5 ASIC will become available in summer 2012. This chip will implement the final properties, and, if fully functional, would be used in the pixel upgrade. The AMIS5 chip will have to be tested very carefully, including tests of magnetic field and radiation tolerance. A pre-series of 200 DC-DC converters of the final design will be produced with the vendors selected for mass production.

In total, 800 DC-DC converters are required for BPIX and 384 for FPIX. Packaged untested chips will be delivered to CMS. Converter PCBs will be produced, equipped and tested for functionality in industry. Further functionality and performance tests as well as thermal cycling will happen at RWTH Aachen University. The actual mass production is expected to take place during 2014.

7.3 Power Supply Modification

In their original version the A4603 pixel power supplies are incompatible with the envisioned DC-DC conversion scheme, due to a limitation of their output voltage to 7 V for the digital part and 5.8 V for the analog part. However, with a relatively simple and low-cost modification the existing CAEN A4603 power supplies will be made compatible.

The maximum output voltages will be increased from their current values to 12 V for both channels. The output voltage will be software-programmable in the range of 8 to 12 V, such that the conversion ratio for the DC-DC converters can still be adjusted as desired. Stabilization of the output voltage in the presence of DC-DC converters, which represent a negative-impedance load for the power supplies, could be difficult, and is not required, as the DC-DC converters regulate their output voltage themselves. Therefore, after successful tests (Section 7.4), remote sensing has been dropped in favour of a simple local sensing at the power supply output. Voltage drops on supply cables will therefore reduce the DC-DC converter input voltages, with respect to the PS output voltage. All other parameters, in particular the total output power, set precision, read-back precision and voltage ripple, will stay as they are.

The modification includes the exchange of components on the motherboard itself as well as the exchange of mezzanine cards, followed by firmware upgrades and a recalibration. Nevertheless the modification will be implemented in a modular way, such that the installation of “modification kits” can be performed at CERN, if required. In total, 66 power supply modules will be modified. The first four prototypes will be delivered until July 2012. If thorough

Layer	Bias current [mA], -4°C	Bias current [mA], -2°C
Layer 1	8.1	10.0
Layer 2	7.4	9.1
Layer 3	6.1	7.5
Layer 4	5.0	6.1

Table 7.4: Estimates for the current per power supply bias channel at two different sensor temperatures, for the four barrel layers. An integrated luminosity of 250 fb^{-1} is assumed.

tests are successful, the modification kits will be delivered by October 2013, and installed by the supplier when required by the pixel project. A burn-in of the modified power supplies, i.e. operation under load for a specific period, likely to be between half-a-day and several days, depending on the amount of changes required to the motherboard, will be performed. This can happen in batches, and is expected to be feasible during the available shutdown time.

The safety margin of the power supplies has been estimated, based on previously mentioned currents per ROC, assuming DC-DC converter output voltages of 2.4-2.5 V and 3.0 V, and using channel-by-channel calculations of power losses on cables and on the supply tube, as well as the measured DC-DC converter efficiencies. In the following, all margins are calculated with respect to the nominal capability (in terms of power or current) of the power supply. For an analog DC-DC converter output voltage of 2.4 V (2.5 V), the maximum required analog power of any power supply is 28.7 W (30.1 W), while the available analog power per power supply is 40 W. This corresponds to a safety margin of 28% (25%). The optimal value for the analog voltage can only be decided once voltage drops on the supply tube are known with more precision. For the digital power, the maximal required power of any power supply is 57.3 W and 61.8 W for instantaneous luminosities of 2.0 and $2.5 \times 10^{34} \text{ cm}^{-2} \text{ s}^{-1}$, respectively. Compared to the available 90 W per power supply, this corresponds to safety margins of 36% and 31%, respectively. The calculation behind these margins is very detailed, but it includes assumptions, simplifications and extrapolations. Uncertainties arise e.g. from the DC-DC efficiency, supply tube voltage drops, power consumption of the future chip, irradiation effects on DC-DC converters and the ROC, dependence of the hit rate on center-of-mass energy, and a potential beam displacement. Critical parameters have been varied individually within their uncertainty and the effect on the margins has been determined. Typically the margins change by a couple of per cent.

The currents per power supply bias channel have been calculated as well, taking into account the connectivity of modules to bias channels. Per channel, 20 mA can be supplied. Required currents per channel are shown in Table 7.4 for all layers, for an integrated luminosity of 250 fb^{-1} and two typical sensor temperatures. The exchange of the innermost layer is currently foreseen after 250 fb^{-1} . Operation up to 250 fb^{-1} is possible with a safety margin of 50% or better (depending on the sensor temperature). Operation up to 500 fb^{-1} , with twice the bias currents required, is possible with a safety margin of 19%, if a sensor temperature of -4°C can be reached. The safety margin of layer 2 amounts to 26% and 9% for 500 fb^{-1} and temperatures of -4°C and -2°C , respectively.

A number of additional (modified) power supplies will be ordered, to allow for system tests and commissioning of new detector components to be performed in parallel to the operation of the current pixel detector during 2014-2016. Modified power supplies could in principle be down-graded and then be used again in the current detector, if spares are needed during that period.

7.3.1 Further developments

While detailed calculations based on the input data available to-date show that the modified A4603 power supplies can be used up to LS3, as detailed above, a number of further studies and projects have been launched, aiming at either decreasing the power consumption or at increasing the capabilities of the power system. If successful, these measures would be beneficial if the luminosity increases faster than currently projected, or if LS3 would be delayed. In the following, some of these projects are outlined.

- Slow control of the power supply output voltage. The DC-DC chip foundry does not recommend permanent operation with voltages above 10 V, but the application of voltages up to 12 V for short periods will not do any harm to the DC-DC chip. Currently in all estimates the power supply output voltage is chosen such that the maximum DC-DC converter input voltage does not surpass 10 V even for zero current. Consequently for realistic currents the digital voltage will be somewhat lower than 10 V, due to voltage drops over the supply cables. The sense wires could be used to measure the input voltage of the DC-DC converter, and this information could be used to adjust the power supply output voltage such that the voltage drop is compensated. This would increase the safety margin on the digital power by about 5% (relative) for $2.5 \times 10^{34} \text{ cm}^{-2} \text{ s}^{-1}$.
- Shielding of the power supplies. The power supply output power is currently limited by the requirement of compatibility with the substantial magnetic fringe fields present at the location of the power supply racks. For a magnetic field below about 50 mT, a more efficient material could be used in the transformer core. Previous shielding campaigns for the tracker cooling plant motors indicate that the magnetic field can be reduced to below that level by local shielding.
- Installation of additional cables. The possibility to install and connect a limited number (at most 16) of additional pixel multi-service cables is being studied. The advantage of this measure would be two-fold: the pixel modules could be distributed onto more cables, and these cables plus their corresponding power supplies could be laid out for a higher bias voltage (e.g. 1000 V), to provide full depletion up to higher fluences. While details are complex and have to be worked out, these cables will have to be pulled already during LS1. It has therefore been decided to prepare for this, irrespective of the future decision on the actual usage of these cables.
- Operation of pixel multi-service cables up to 1000 V. Tests will be carried out on spare cables to understand if they could be operated up to, for example, 1000 V. Both the trip limit (loss of insulation) and a potential degradation should be studied. If successful, tests should be repeated on irradiated cables. A similar program is underway for the outer tracker.
- Development of new power supplies. As detailed above, the power supply system is expected to work up to an instantaneous luminosity of $2.5 \times 10^{34} \text{ cm}^{-2} \text{ s}^{-1}$ with a safety margin of about 30%, a number that is considered sufficient to accommodate the uncertainties in the power calculations. However, as of today, the date of LS3 is not fixed, and the luminosity projection up to LS3 is uncertain. A larger instantaneous luminosity and therefore a reduction of the safety margin in late Phase-1 cannot be excluded. New, and more powerful, power supplies will increase considerably the margin of the power system. They will also allow the provision of a higher bias voltage. Given the long development time of new power supplies, estimated to be five to six years, including specification, qualification, ordering and

production, the development of these devices has to start already now. New power supplies are also required for the “Phase-2 pixel detector”, a completely new device to be installed in LS3. The specification of the new power supplies should therefore be compatible with both the Phase-1 and Phase-2 pixel requirements. The specification of these new power supplies has started, but several key parameters for Phase-2 (such as the future pixel size) are not yet fixed. The new power supplies could be available already in LS2, and will in any case be available well before LS3.

Since an operation with bias voltages of up to 1000 V is desired and could be made possible by several of the above described measures, this has already to be taken into account for the design of components that carry the bias voltage, both on the supply tube and the modules. It has to be noted that an increase of the bias voltage from the nominal maximum value of 600 V up to e.g. 1000 V would lead to a slight increase of the bias currents.

7.4 Power System Tests

7.4.1 Pixel Module Noise with DC-DC Converters

The noise spectra of DC-DC converters have been measured with a classical EMC set-up, which allows for comparison and optimization of the converters. However, only system tests with real pixel detector modules can tell if the performance of the detector would be compromised by the use of DC-DC converters. Since pixel modules with the new ROC are not available yet, all system tests have been performed with present pixel modules, which are, however, very similar to the future ones.

Present barrel pixel modules with 16 ROCs have been powered with AC_PIX_V8 DC-DC converters, based on the AMIS4 ASIC, which provided the required 3.3 V and 2.5 V. The DC-DC converters were plugged to a prototype bus board and connected to the pixel module with 1 m long aluminium power cable prototypes, as foreseen for the final detector. A CAEN A4603 power supply with the original back-board was used to power the DC-DC converters. The PS was modified such that it can deliver the required input voltages for the DC-DC converters when operated with a voltage divider on the sense line. The connection between the power supply and the DC-DC converters was realized with an original multi-service cable of 40 m length. A USB-based lab readout board, as routinely used for module qualification, served as data acquisition system. The “PSI46 expert” software was used to program the DACs, to perform standard detector calibration procedures, and to read out the data. A threshold scan was performed, and the S-curve of each pixel was fit with an error function to determine its width, as a measure of the pixel noise. Arrangements with one or two pixel modules and up to eight DC-DC converters (corresponding to four pairs) were studied. In measurements with two pixel modules, these were powered either both from the same pair of DC-DC converters, or each from its own pair. All measurements are compared with measurements in which the modules were powered conventionally, i.e. directly from the A4603 power supply. Up to now, no significant increase of the module noise was observed. Figure 7.6 shows the resulting histograms (black curves) for a measurement with two modules and four pairs of DC-DC converters, of which one pair was used to power the two modules. The noise amounts to 157.0 electrons without (left plot) and 157.2 electrons with (right plot) DC-DC converters. The difference is not significant. This is the largest set-up studied so far.

To simulate the situation when the DC-DC converters are connected to several modules and operate under full load, an additional constant load of 2 A is connected in parallel to the modules and also to the other digital voltage lines. As visible from the red curves in Figure 7.6, also

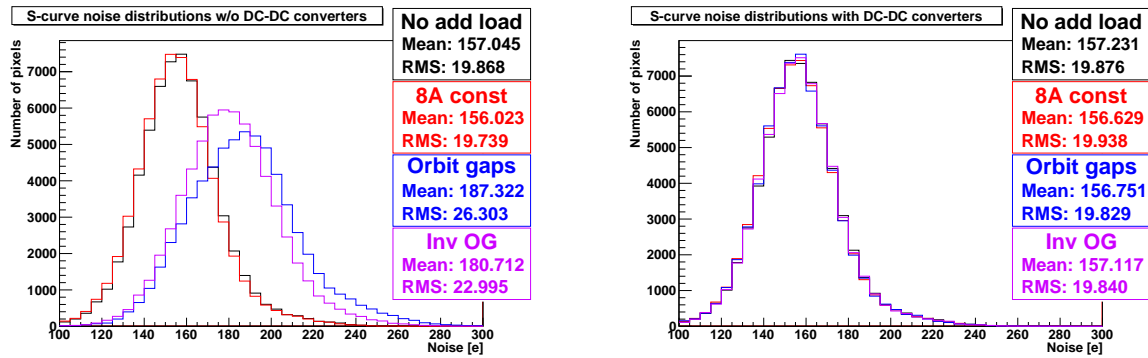


Figure 7.6: Distributions of the noise (width of the S-curve) of all pixels of one pixel module, in an arrangement with eight DC-DC converters, from which one pair was used to power two pixel modules. Measurements have been performed without (left) and with (right) DC-DC converters, for the following four cases: no additional load (black); an additional constant load of 2A on each digital line (red); a variable load as expected due to orbit gaps on each digital line (blue); and a variable load corresponding to an inverted orbit gap pattern on each digital line (pink).

in this case no negative effect due to the powering via DC-DC converters is observed.

Several tests were performed with AC_PIX_V7 DC-DC converters with AMIS2 ASICs.

The effect of the converter's switching frequency has been investigated. While per default the switching frequency of AC_PIX_V7 is 1.3 MHz, it has been varied between 1.0 and 3.0 MHz, i.e. over the whole accessible range. The difference in the mean of the noise histograms is below 1%.

To simulate a potential low impedance AC connection between pixel modules and DC-DC converters due to e.g. carbon fiber support structures, which could alter in particular the Common Mode noise path, the components were arranged on a large solid copper support plane. The AC coupling to this plane did not lead to any negative effect.

System tests have also been performed with an FPIX panel, comprising 21 ROCs, and AC_PIX_V7 DC-DC converters on an independent set-up. Again, the noise behaviour of the panel was not compromised.

7.4.2 System Tests with LHC Time Structure

The same set-up was used to investigate a potential effect due to the time structure of the LHC beam: every $89 \mu\text{s}$ there is a $3 \mu\text{s}$ long so-called abort gap, which allows the beam to be dumped. Due to the sparsified readout scheme of the PSI46 ROC the corresponding drop in digital activity leads to large and fast load changes. The current drawn from the digital converter drops within a few bunch cycle periods by up to 1 A for $2 \times 10^{34} \text{ cm}^{-2}\text{s}^{-1}$. An active load was used to mimic fast load changes, both with the orbit gap pattern and with its opposite, i.e. assuming just a few filled bunches. A load switching between 2.0 A and 0.0 A was connected in parallel to the pixel modules and also to all other digital voltage lines, and the pixel modules were powered either conventionally or with AC_PIX_V8 DC-DC converters. As visible from the blue and pink curves in Figure 7.6, the pixel noise is much less affected when the module is powered from DC-DC converters. The DC-DC converters' regulation and additional filters present on the DC-DC converters contribute to the stability of the power supply chain.

7.4.3 Remote versus Local Sensing

The remote sensing technique is currently used to compensate for large voltage drops over the supply cables, to ensure that the correct voltage is applied to the pixel modules. Since the DC-DC converters, located relatively close to the pixel modules, provide a (locally) regulated output voltage, this is not required anymore. Due to the negative impedance characteristics of DC-DC converters, remote sensing could even lead to instabilities. Tests have been performed to compare the system behaviour with remote sensing, as realized in all measurements presented so far, to local sensing directly at the power supply. The same set-up as described above was used. Sensing was either performed at the input of the AC.PIX_V8 DC-DC converters, or at the back of the power supply. No significant differences between the means of the noise histograms were observed, even with a dynamic load with LHC-like time structure. The sense lines, which cannot be removed from the cables anyway, can still be used to measure the voltages at the supply tube. This measurement will happen inside the power supplies, to which these wires will still be connected.

7.4.4 Future Tests

Several further tests are under preparation. These include:

- tests with more pixel modules;
- operation of DC-DC converters at lower temperatures;
- system tests with more advanced prototypes of the bus board;
- studies of the power distribution in one supply tube channel including the boards of segments B and C;
- characterization of the cooling properties when using a CO₂ cooling system;
- and tests with modified power supplies.

Tests with new pixel modules will be performed as soon as these are available. In the pixel pilot system (Chapter 10), half of the modules will be powered with DC-DC converters and a modified power supply. This test will be crucial to investigate and address a potential negative influence of DC-DC converters at the system level, e.g. via cross-talk. In particular, it will be verified that the performance of the surrounding strip detector is not compromised.

Chapter 8

Beam Pipe & Early Installation Preparations

To improve the physics performance of the pixel detector in terms of impact parameter resolution and vertex resolution, the first active layer of the Pixel detector will be at 2.9 cm from the beam line. This distance is not compatible with the diameter of the present central section of the beam pipe and a smaller diameter beam pipe has been designed and submitted for construction.

The smaller beam pipe diameter needs to be balanced against the safe and efficient operation of the accelerator requiring beam stability with minimum background in the experiment. In addition, for the safety of the detector, the experimental section of the beam pipe should never be an aperture limitation for the beam and this should be true for all possible beam conditions and expected beam optics configurations. Finally, the minimum beam pipe diameter and wall thickness is also constrained by the mechanical stability under vacuum.

8.1 CMS Beam Pipe System

The CMS beam pipe spans over ± 18 m from the interaction point to both ends of the experimental cavern. It is segmented into a central section and 4 sections on each end. The central section is 6.2 m long and consists of a cylindrical part of 3.8 m length with conical ends. The present cylindrical piece has an inner diameter of 58 mm and is made out of 0.8 mm thick beryllium, while the conical parts are made out of stainless steel also 0.8 mm thick. The design of the CMS beam pipe system and especially the central section has been the subject of extensive studies leading to the conclusion that a cylindrical central part followed by a conical section at each end is the most favorable in terms of reducing backgrounds since it minimizes the solid angle with heavy material as seen by particles produced at the IP [60], [61], [62]. The conical section of the present central portion of the beam pipe starts at ± 1.9 m and follows the $\eta = 4.9$ cone, it extends into the end-cap portion of the pipe and terminates in a thin window before a flange at ± 10.7 m which couples it to the HF pipe. The HF pipe is almost 3 m long, also slightly conical, varying in diameter from 170 mm to 208 mm and is constructed from 1.2 mm thick stainless steel. It terminates in a thin window flange which carries 3 ion pumps and reduces the inner diameter to 58 mm, for coupling to the CASTOR-T2 (CT2) pipe. This cylindrical pipe again terminates in a flange and bellow system, which couples it to the cylindrical, stainless steel forward pipe, 2.4 m long, which terminates at the junction to the TAS absorber at 18 m. The schematic of the present as well as the final drawings of the future beam pipe can be seen in Figure 8.1

The main features of the CMS beam pipe system are:

- The Be central section which presents minimal material to particles emerging from the interaction point.

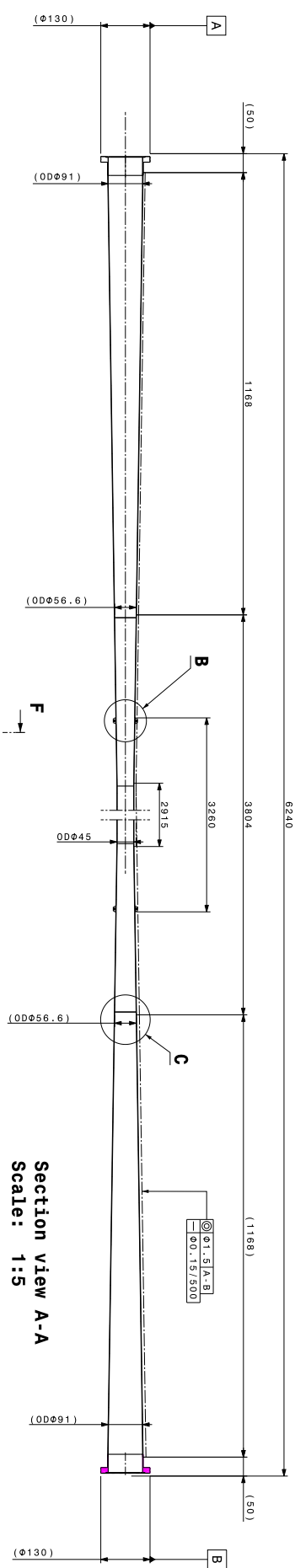


Figure 8.1: The upper schematic shows the elements of the beam pipe system of CMS (present central section). In comparison, the lower presents the final drawing of the CMS new central beam pipe.

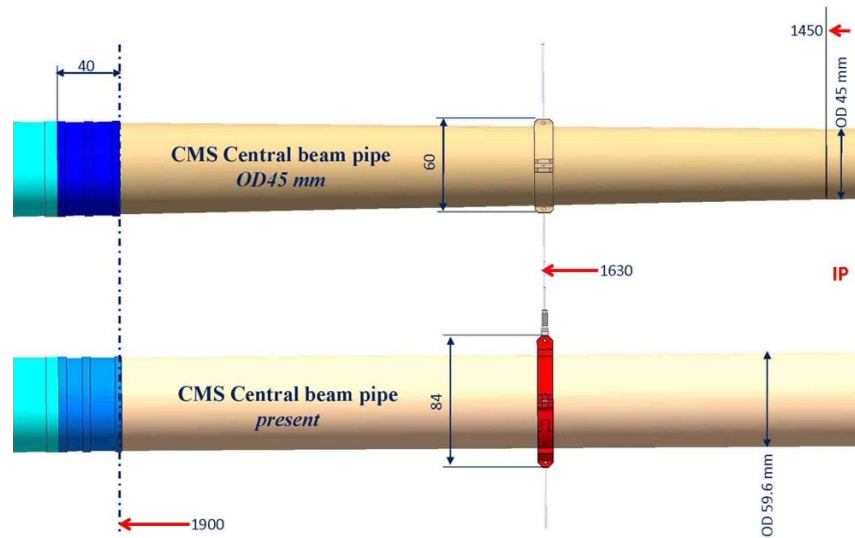


Figure 8.2: Sketch of the new (top) and old (bottom) beam pipe. For the new pipe notice the conical part extending to $z=1450$ mm in order to achieve a smaller diameter on the cylindrical part of 45 mm.

- The conical outer sections along lines of constant η (allowing the use of stainless steel while still minimizing background in the muon system).
- The thin reducing window at the end of the endcap pipe.
- The HF and CT2 pipes which allow forward calorimetry up to $\eta = 7$, external to the return yoke.
- The placement of pumps and flanges out of the detector acceptance.

The radius and thickness of the central beryllium section are important parameters affecting the physics performance of the CMS tracking system. The impact parameter resolution and vertex resolution could be substantially improved by a re-designed pixel tracker, which has an additional fourth tracking layer within the limited space between the beam pipe and the strip tracker, ensuring also that the first measured point, given by the radius of the first layer, is as close to the beam line as possible. The support system proposed for the upgraded pixel tracker, would allow such a 4-layer system to be installed, but with installation tolerances so small as to pose a substantial risk. Reduced risk and better performance can be obtained if the beam pipe radius can be reduced. This requirement has to be balanced against assuring safe and efficient operation of the accelerator and minimizing background in the experiment.

8.2 New Central Beam Pipe Design

8.2.1 Design Constraints

As already pointed out, the main reason to change the beam pipe design is to allow a new Pixel detector to be mounted closer to the interaction point. This can only be achieved by reducing the outer diameter of the cylindrical part of the beam pipe (see Figure 8.2).

As the new Pixel detector features the innermost barrel layer at 29 mm from the beam line, taking into account mechanical tolerances and the 2 mm "stay clear" region for ease of installation and adjustments, the outer diameter of the cylindrical part of the beam pipe cannot exceed

45 mm. A certain number of mechanical and physical characteristics of the old beam pipe design need to be maintained:

- The overall length of 6240 mm
- the longitudinal extension of the pure Beryllium section of the beam pipe (length = 3804 mm)
- the cone angle of the conical section (current η value of 4.9).
- the support position at ± 1630 mm

With all these constraints in mind, the new beam pipe is defined by simply extending the conical part following the $\eta=4.9$ line closer to the center until the cylindrical part can start with an outer diameter of 45 mm. The transition from conical to cylindrical now occurs at $z=1457$ mm from IP. As a consequence, the inner conical section already starts within the pure Beryllium part of the beam pipe and the support at $z=1630$ mm finds itself in the conical part. The only other parameters left free for optimization are the inner radius of the cylindrical part for a length now of 2915 mm and the material to be used for the outer conical part. Consequently, a study was carried out by which the minimal inner radius of the beam pipe was determined to be 21.7 mm with a wall thickness of 0.8 mm (see Section 8.2.3 for further details).

8.2.2 Choice of Materials

For the choice of the beam pipe material for the outer conical part, three options were investigated. The first option is to keep the material unchanged by using Stainless Steel as was done for the current beam pipe design. Secondly, two other alloys were considered, type 2219 Aluminum (93%) and Aluminum/Beryllium composite (AlBeMet® [63]).

The Stainless Steel option was discarded, since this material is heavy, it gets easily activated and in addition, some of its isotopes have a rather long half-life. As a consequence, significant effort would be required to shield the Stainless Steel pipe during opening and maintenance of the detector, a feature which is not in accordance with the ALARA principle for radiation protection. Aluminum (type 2219) on the other hand, although easily activated as well, results in radioactive isotopes with short half-lives and, just after one month cool down period, the activation level drops by about a factor of three. Aluminum beam pipes are widely used in the LHC experimental areas and present very little technical risks.

Finally, the AlBeMet® composite performs best in terms of activation and material density, since 62% of this alloy is made of pure Beryllium and in addition its mechanical properties are nearly as favourable as the Aluminum alloy type 2219. However, in spite of these obvious advantages, not a lot of experience exists with beam pipes built out of this material, it has never been used for LHC experimental beam pipes and in fact only short pipes have ever been built with it (at DESY). AlBeMet® is very brittle and some of its properties, such as notch sensitivity, are not very well known. Technical and schedule risks were considered higher for AlBeMet® with respect to Aluminum and it comes at a substantial higher cost. All of these facts were considered during the CMS central beam pipe Engineering Design Review (EDR held at CERN on March 5th 2012) and resulted in the recommendation of using Aluminum as material of choice for the external conical part, 1630 mm support collars and end flanges.

However the committee recognized the future potential of AlBeMet® (for instance in rebuilding the stainless steel, conical end cap beam pipe sections in CMS using a material less susceptible to activation) and suggested that a R&D program for future AlBeMet® beam pipes should be started soon in collaboration with the CERN-TE department.

8.2.3 Beam Pipe Support Structure

The central beam pipe is attached to the Tracker structure by means of a pair of 4 stainless steel wires (two vertical and two horizontal). The attachment points are located 1630 mm away from the interaction point, resulting in a span of 3260 mm.

Since with the new design of the beam pipe the attachment points now fall on the conical part of the pipe, the design features a short cylindrical section (width = 12 mm) around these points to allow for the needed support adjustments and slack. It is planned to redesign these supports, moving away from Stainless Steel clamps to Aluminum in order to significantly reduce the amount of material. The detail design should take into account not only the primary function of supporting the beam pipe without introducing stress to the structure, but also the need to maximize clearances to the Barrel and Forward detectors during the insertion and removal processes.

8.3 Central Beam Pipe Tolerances and Aperture Calculations

The required beam aperture determines the theoretically minimum inner diameter for any new beam pipe. During injection the beam occupies the largest aperture in the vertical plane and in case of an asynchronous beam dump the beam is largest in the horizontal plane. The dimension of the beam pipe must be chosen such that, taking into account all possible mechanical tolerances of the beam pipe, all installation tolerances and all possible movements of the pipe during operation, the wall of the pipe can never approach the beam closer than the limiting distance required by the beam aperture. As a prudent precaution for the safety of the detector, no element of the beam-pipe within it should have a smaller aperture than the closest machine element to the interaction region, which in the CMS case is the TAS absorber, situated at 18 m and having an inner radius of 18 mm.

During the design of the LHC experimental beam pipes currently installed, conservative aperture estimates lead to the request for a "stay-clear" cylinder of 14 mm radius around the nominal beam line close to the interaction point. The following mechanical factors have been considered to contribute to limiting the practicably achievable minimum inner pipe radius, such that the "stay-clear" cylinder is always contained within the physical pipe:

- Construction tolerances causing the pipe radius to be less than nominal.
- Mechanical sagging of the pipe between supports.
- The precision with which the pipe can be surveyed into place.
- Time-dependent movements of the beam pipe supports (attached through the Tracker, Tracker support and barrel Hadron Calorimeter to the central yoke wheel). These may be caused by displacements of the whole cavern with respect to the plane of the LHC machine, settling or flattening of the central yoke wheel, or distortions due to the magnetic field.

In Table 8.1 the original estimates of these mechanical contributions are compared with the values or upper limits inferred from measurements of the installed system.

As it can be seen from the final linear sum of the tolerances, there are significant improvements in minimizing the uncertainty of the beam pipe envelope with respect to the ideal beam line believed to be achievable for the new beam pipe. This in turn allows to significantly lower the limit on the minimum diameter of the cylindrical portion of the pipe (see next paragraph).

Major improvements in being able to better constraint the final tolerances come from:

Quantity	2005	after LS1	after LS1 +1 year	after LS1 + 3 years	Comments
Construction tolerances (circularity)	2.6 mm	0.4 mm	0.4 mm	0.4 mm	Deviation from circular cross-section at any point
Concentricity tolerances, including sag between supports	2.2 mm	0.75 mm	0.75 mm	0.75 mm	Deviation from ideal cylinder axis in the cylindrical region of ± 1.45 m
Installation alignment to beam line and/or TAS	2.6 mm	1.6 mm	1.6 mm	1.6 mm	Survey estimate based on as-achievement
Quad fiducials to beam line uncertainty	0.0 mm	0.5 mm	0.5 mm	0.5 mm	Only if alignment with beam line. Possibly time-dependent.
Load transfer	0.0 mm	0.2 mm	0.2 mm	0.2 mm	Measured limit
Field induced yoke movement	1.2 mm	0.5 mm	0.5 mm	0.5 mm	2011 results from Nuclear interaction tomography
YB0 yoke distortion	1.4 mm		0.2 mm	0.6 mm	From survey and Nuclear interaction tomography
Cavern and YB0 yoke movements	5.0 mm		0.5 mm	1.5 mm	From survey as measured, over last 2 years, projected to 1 year or 3 years
Tolerances Linear Sum	15.0 mm	3.95 mm	4.65 mm	6.05 mm	

Table 8.1: Quantities contributing to the total tolerance.

1. Measurements made on the present as-built pipe, confirming the excellent quality control of the processes critical for the final mechanical precision achieved by the manufacturing company (first 2 quantities). These values are part of the tolerances requested and accepted for the new beam pipe.
2. Better estimate based on as-achieved alignment of the various survey elements and reference frames, leading to a very good precision in the final position of the beam pipe itself (3rd quantity).
3. Precise measurement of the beam pipe movement with and without magnetic field by means of nuclear interaction tomography [64] allowed to reduce significantly the tolerance for magnetic field induced movement of the YB0 yoke (hence of the beam pipe).
4. Finally many measurements were taken during the last few years in order to establish the variation of the cavern floor and YB0 yoke relative to the beam line. These measurements show a stabilizing effect with time of the cavern floor position under the heavy load of the YB0 yoke. However, not enough time has passed since the lowering of YB0 (February 2007) and it is conservatively assumed here that there will still be some stabilization ongoing at the level of 0.5 mm per year.

It is important to note that the last 2 quantities ("YB0 yoke distortion" and "Cavern and YB0 yoke movements") are considered to be time dependent. Both can be monitored either by the use of nuclear interaction tomography and/or by direct survey during normal operation periods. These quantities could then be reset to zero if so deemed necessary, providing enough time is granted to access the beam pipe support elements inside the YB0 yoke. As no such time is presently foreseen during the three years following the end of LS1, the last value of 6.05 mm is considered as input for the final aperture calculations.

8.3.1 Aperture Calculations

New aperture calculations were made by machine experts in order to establish whether the smaller diameter central beam pipe section would still be compatible with safe and stable beam operation for various machine optics and energies. Relevant inputs to the aperture calculations are:

1. The final value of 6.05 mm as the linear sum of the tolerances for the position of the beam pipe with respect to the ideal beam line. Since no intervention is foreseen between LS1 and LS2, the LS1+3 years value is considered.
2. "Stay clear" region of 14.00 mm around the beam. This quantity is to be added to the 6.05 mm linear sum of the tolerances already presented from the LS1+3 years column of Table 8.1.
3. New beam pipe radius in the central cylindrical section is assumed to be 21.7 mm.
4. Closed orbit tolerance of 4 mm at nominal injection energy and optics (170 μ rad crossing angle, 2 mm beams separation and 3.75 μ m nominal normalized transverse emittance)
5. Beta-beating of 20%.

The output of the aperture calculation is a quantity called $n1$ defined as the largest setting in sigma of primary collimators such that the local aperture is protected from secondary halo [65].

	Injection (450 GeV)		Flat top (7 TeV)	
Central beam pipe radius (mm)	29	21.7	29	21.7
Tolerances (mm)	11	6.55	11	6.55
n_1 (σ) at IP5	26.4	19.8	567	454

Table 8.2: Results of the aperture calculations for the new beam pipe. For the aperture calculation represented in this table, the tolerance used was 6.55. It turned out later that indeed we can have 6.05 mm instead due to a better understanding of our survey data.

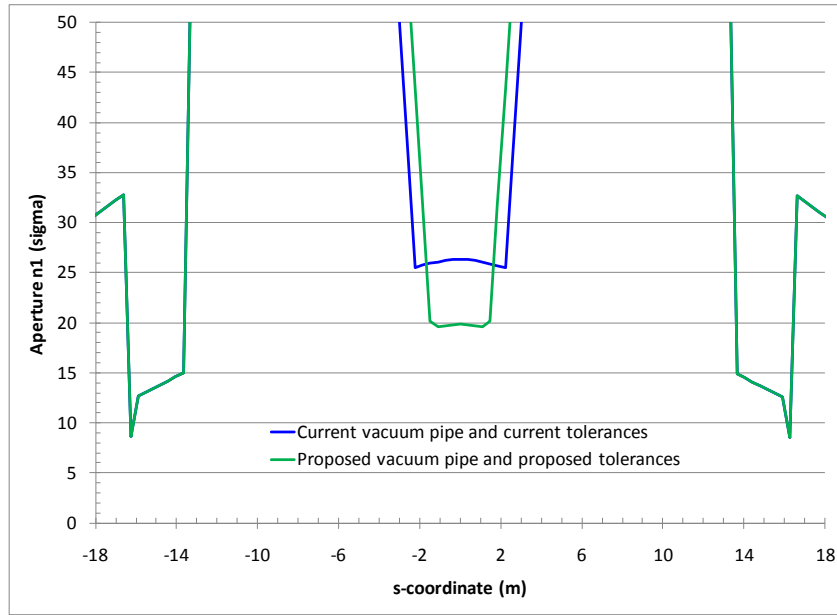


Figure 8.3: Aperture calculations at injection in n_1 (sigma) for the new central beam pipe radius of 21.7 mm and new tolerances from Table 8.1 (green) compared with the old beam pipe and tolerances (blue).

Taking into account also operational margins, the primary aperture of the LHC needs to stay at $n_1 > 7.0$. This value of n_1 is the criterion for the geometrical acceptance for all elements in the ring. Details about the aperture calculations are summarized in table 8.2.

From this point of view, the most stringent conditions are at injection energy and optics as the beam size is larger and still un-squeezed at the IP. Figure 8.3 shows the results of the n_1 calculation for the new beam pipe design with new tolerances as compared to the old design and old tolerances both at injection. It can be seen how the new design is still well within the geometrical limits having an n_1 value around 20σ . Outside the central region the old and new CMS beam pipe system coincides and the closest aperture limit is at ± 16.4 m from the IP in the bellow module transition between the forward and CT2 sections of the pipe.

Special considerations should be made for the very high β^* optics conditions (i.e. greater than a kilometer). In these conditions the reduced central section of the pipe may become an aperture limitation.

Although not clear to what extent the high beta-star scenario will be pursued during the future LHC physics program, the agreed solution consists in ensuring that, for the duration of this specific program, the central beam pipe position stays at all time in the shadow of the TAS. As the TAS inner radius is 18 mm, taking into account the 14 mm "stay clear" region, this

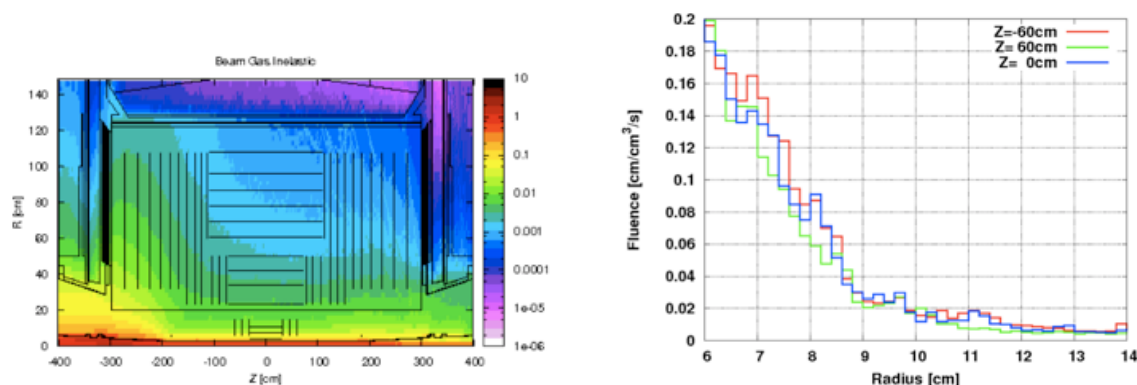


Figure 8.4: Fluka simulation of a beam-gas interaction coming from the right end side of the CMS long straight section. On the left (a) the resulting shower profile in the pixel and silicon strip tracker region opening up in the magnetic field toward the left side. On the right (b) the radial profile at three Z locations in the region covered by the Pixel detector. A cut-off of 9 cm is clearly evident.

implies that the total uncertainty in the position of the central beam pipe should stay below 4 mm. From Table 8.1 it can be seen that this is guaranteed at time = 0 from the last survey and adjustment of the beam pipe (for example just after LS1). High beta-star operation of the machine is then possible with no limitation in its value, providing enough time is granted to survey and possibly re-adjust the position of the central pipe.

8.4 Beam Background Simulations

During 2010-2011 data taking periods, extensive studies were made on the impact of machine induced background events in CMS. One important aspect of the new beam pipe is the measure of its impact on the machine induced background events showering the central portion of the detector.

Machine Induced Background events (MIB) were simulated in the LHC detectors focusing on two main sources: tertiary beam halo and beam-gas interactions. Particle fluxes originating from these operational beam losses were calculated with the MARS15 [66] code (later also with FLUKA [67]) and presented at the entrance to the ATLAS and CMS experimental halls (about 22 m from IP). It is found that background rates in detector subsystems strongly depend on the origin of MIB, particle energy and type. Using this source term, instantaneous and integrated loads on the detectors and impact on the detector performance can be further derived. The latter was done for CMS using both GEANT4 [68], [69] (with the standard CMSSW based full detector simulation) and FLUKA (which uses a somewhat simplified version of the CMS geometry) simulation codes. Material and shape of the central section of the pipe have an impact on how the MIB events are seen by the CMS detectors close to the beam line (mainly Pixel, inner portion of the silicon strip tracker, HF, BCM1 and PLT).

Figure 8.4(a) shows the hit density released on the inner portion of the CMS detector as a result of a primary beam-gas interaction along the LSS5.

As primary beam-gas events further interact along their path toward CMS (coming from the right in Figure 8.4(a)), they enter the detector region still well collimated and open up in the presence of the magnetic field reaching higher radii when exiting the detector. In the pixel region these events are well confined below a radius of about 8-9 cm (Figure 8.4(b)). Of relevance

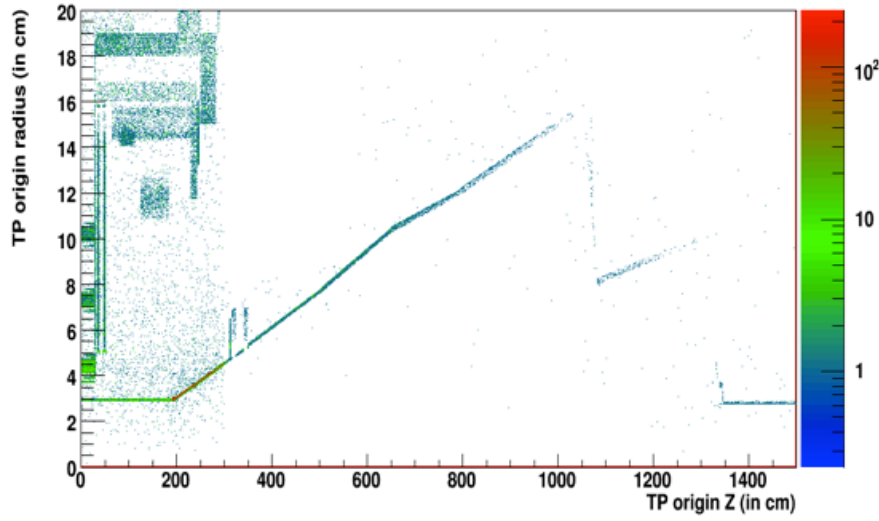


Figure 8.5: GEANT simulation of hit density in proximity of CMS for events where primary beam-gas interaction occurred along LSS5. As expected, the highest values are found at the end of the conical section of the pipe between 200 mm and 250 mm from IP5.

for CMS in this context are mostly beam-gas events interacting with the beam-pipe and beam-pipe elements in the proximity of the interaction region, hence superimposing to the innermost detectors showering particles to the normal p-p interaction products originated from the IP. Especially for the Pixel, these extra particles, being almost parallel to the silicon modules, may leave a large number of hits and, if the event is triggered at L1, causing at present sizeable dead-time for the experiment (long time to readout and clear). Figure 8.5 shows the interaction map for events which primary beam-gas interaction occurred along LSS5. As can be seen from the colored density map, the beam pipe material is a source of many of these interactions and in particular the region where from conical it becomes cylindrical at around 2 m from the IP which scores the highest density in the map.

The shape and mostly the material in the conical section of the of the beam pipe plays a major role in determining the amount of showering particles from beam-gas interactions which eventually make their way in the inner region of the CMS detector.

8.4.1 Geant4-based Simulations

The effect of replacing the stainless steel conical part of the CMS beam pipe by either AlBeMet® or Aluminum components was tested using beam-gas Monte-Carlo samples (beam gas events coming from 3.5 TeV proton beams) recently generated with FLUKA.

The new beam pipe geometry was described in the Geant4-based simulation with the option of 0.8 mm AlBeMet® or 1.2 mm thick Aluminum for the conical parts extending beyond 1900 mm from the IP, while the Pixel detector description stays the same (present Pixel). These samples were passed into CMS Geant4-based simulation, and the resulting activity in the Pixel was measured for the different pipe configurations and materials.

It is evident from the results of Figure 8.6 that there is a substantial gain in the new beam pipe when using AlBeMet® instead of stainless steel in terms of total number of clusters (Figure 8.6(a)) and cluster density at lower radii (Figure 8.6(b)).

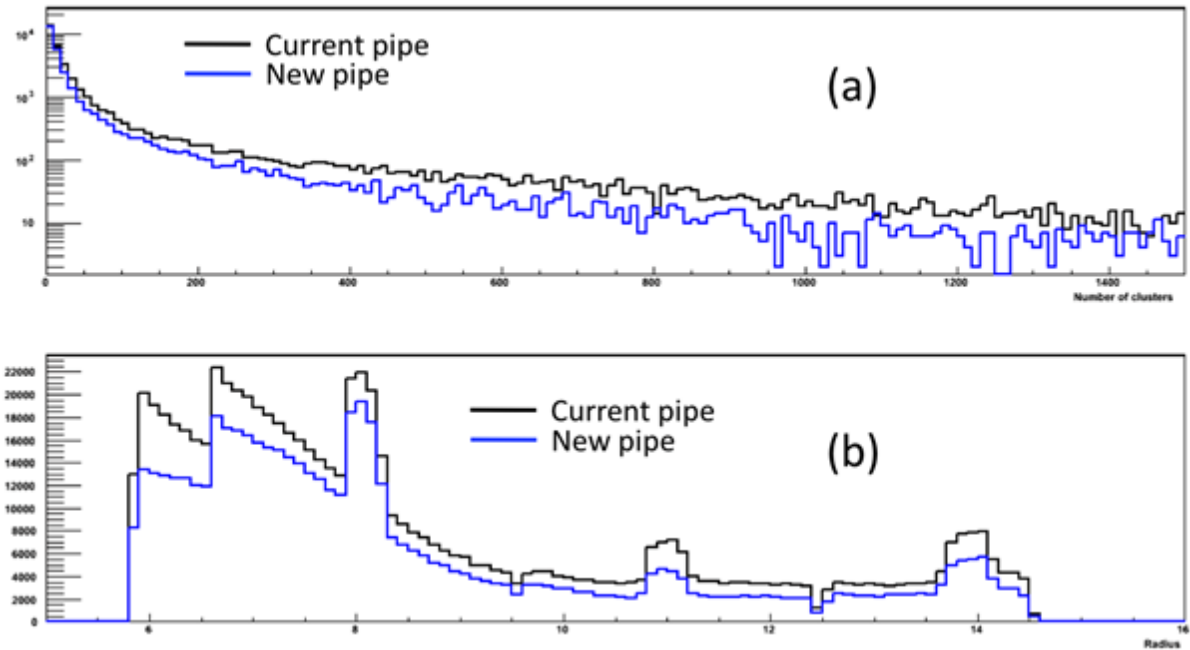


Figure 8.6: GEANT simulation of the whole Pixel cluster multiplicity (a) and radial cluster distribution in the forward disks (b) as result of beam-gas interactions for Beam 1. Here the new pipe is assumed to be with AlBeMet®.

Beam-gas induced clusters (RECO) based on 4M events	AlBeMet®	Aluminum
Events with >1 Pixel cluster	0.89	0.95
Events with >100 Pixel clusters	0.65	0.72

Table 8.3: Beam-gas induced Pixel clusters for the AlBeMet® and Aluminum options as compared to Stainless Steel.

At the simulation level, when comparing Aluminum and AlBeMet® to stainless steel, one observes 60% less hits in the pixel barrel layers, and 40% less in the forward disks.

As mentioned previously (Figure 8.5) most of the beam-gas induced hits in the pixel volume come from interactions with the central beam pipe; as the new materials have a much lower density, it is not surprising to observe a lower activity in the pixels. A further positive effect shown here is the pronounced reduction of resulting hits at low radii (i.e. with the new pipe the rise to low radii of Figure 8.4(b) is less steep).

These results are confirmed at the reconstruction level. Table 8.3 summarizes the benefit of the new beam pipe as compared with the old one for both AlBeMet® and Aluminum. Most relevant is the gain for events leading to high Pixel cluster multiplicities (greater than 100 Pixel clusters) for which we are expecting a reduction of $\sim 35\%$ and $\sim 30\%$ in the AlBeMet® and Aluminum case respectively, leading to the expectation of a substantial reduction on the experiment dead-time for the same beam conditions.

8.4.2 FLUKA-based Simulations

A parallel effort was also launched using the FLUKA based CMS geometry description taking as inputs the original beam-gas events generated using MARS15. In this case we studied the

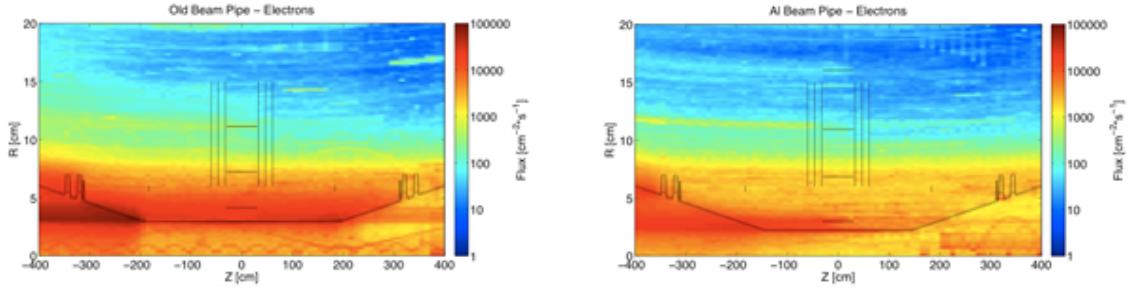


Figure 8.7: Fluka simulation of the hit density for electrons emerging from the interaction of primary beam-gas events (entering from the right) with detector material for the old beam pipe (left) and the new aluminum beam pipe (right).

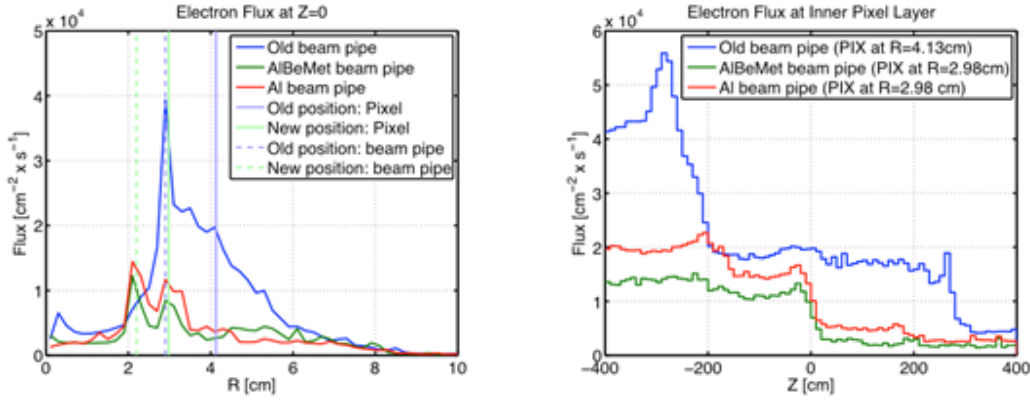


Figure 8.8: Fluka simulation of the electron flux for electrons emerging from the interaction of primary beam-gas events (entering from the right) with detector material as a function of radius (left) and Z (right).

effect of the new beam pipe layout and material on beam induced background activity for the old Pixel and also implemented and studied the new Pixel phase I upgrade geometry.

Results show that while hadron and neutron densities are not affected too much by the change in beam pipe layout and material, the electron density, which by far dominates the overall background, does (Figure 8.7). This is explained by reduced electromagnetic showers in the conical part of the beam pipe due to lighter material. Figure 8.8 shows the electrons flux as a function of radius and along the beam line for the various cases examined. Notice how, in spite of the reduced beam pipe radius and innermost layer position of the Pixel detector, the electron flux is now about a factor of 2 less with respect to the present pipe and larger radial position of the present Pixel detector. The longitudinal distribution also shows a substantial reduced electron flux along the Pixel detector coverage.

8.5 Spare beam pipe and strategies

Given the very high cost of the new beam pipe in Be and Aluminum, there will be no purchasing of a spare part. To cope with the unlikely scenario of a damaged or un-usable pipe we are faced with a few options:

1. Purchase a second identical pipe but entirely in Stainless Steel

2. Re-use the old 59.6 mm diameter beam pipe

The first option has the advantage of requiring no modification to the new Pixel detector, but the big disadvantage of having a massive amount of material between the interaction point and the Pixel detector itself, heavily spoiling the physics performance of the whole CMS detector. Furthermore in that location stainless steel will soon activate further spoiling our physics results and it will represent an almost impossible challenge for the management and minimization of radiation exposure during maintenance operations.

Although far from optimal, the second option is more favorable but is obviously not compatible with the present layout of the Pixel detector. Two further options are then possible: either remove the innermost layer and continue to use the outer three or prepare a 16 faceted innermost layer at 39 mm (as described in the Technical Proposal) from the beam line in exchange to the present 12 faceted layer at 29 mm. The latter seems the best possible solution and provisions will be made such that the present mechanical design stays compatible with this option.

Chapter 9

CO₂ Cooling

The introduction of CO₂ two-phase cooling is a major innovation of the pixel upgrade project, compared to the C₆F₁₄ liquid cooling of the present detector; it greatly contributes to the reduction of the passive material in the tracking volume, and hence to the improvement of the tracking performance.

Evaporative cooling is an appealing technology, in particular for tracking detectors with high power density, as it provides high cooling efficiency with minimal amount of material. The choice of CO₂ as refrigerant is particularly advantageous, because of its excellent thermodynamical properties, that allow the use of very small pipes, and because of its low density. In addition CO₂ is substantially cheaper than fluorocarbon refrigerants, and has much lower impact on the environment.

The main aspects of the implementation of CO₂ two-phase cooling for the CMS pixel detector are discussed in this chapter.

9.1 The 2PACL Method

The process design chosen for the CMS pixel cooling system is the 2-Phase Accumulator Controlled Loop (2PACL) [70], originally developed for the AMS Tracker Thermal Control System [71], and later implemented in the LHCb VELO Thermal Control System [72].

This cooling method is characterized by the absence of any active components inside the detector. The process is completely controlled from the cooling plant, that can be located at a relatively large distance from the detector (ideally in an accessible and radiation-free zone), while only small-diameter tubing is required inside the detector volume.

The main components of the cooling plant are a vessel, a pump, a heat exchanger and a “primary” cold source (a chiller, or another circuit in turn cooled by a chiller). A scheme of the process is shown on the left side of Figure 9.1. The vessel (called accumulator) is used to store a saturated liquid/vapor mixture of carbon dioxide. The mixture is liquefied in a heat exchanger (condenser), which is cooled by the primary system. The liquid is then pumped through the transfer lines up to the detector, where it evaporates inside small tubes (evaporators), and then returns into the accumulator. Pressure (and temperature) regulation inside the accumulator sets the evaporation temperature inside the detector.

9.1.1 Thermodynamic Process Details

The right plot of Figure 9.1 illustrates the 2-phase process that the CO₂ undergoes inside the cooling circuit. A pump increases the pressure of sub-cooled CO₂ that is sent to the evaporators inside the detector (A-B). On its way to the detector the CO₂ liquid is heated up by a

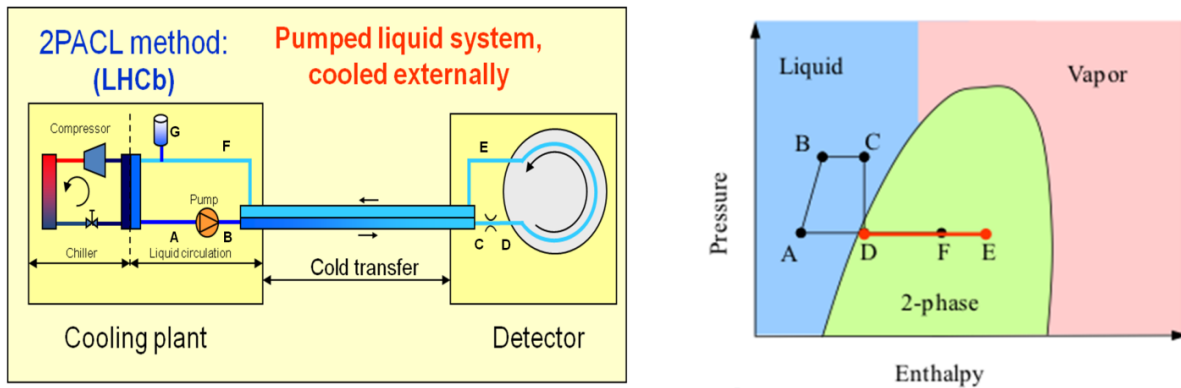


Figure 9.1: Left: scheme of the 2-PACL process. Right: the 2-PACL thermodynamic cycle.

thermal contact with the returning CO₂ vapor mixture (B-C liquid flowing to the detector, E-F liquid/vapor mixture returning from the detector). At the detector inlet, the CO₂ is distributed to the parallel evaporators by capillaries (C-D), which provide the necessary pressure drop to reach the onset of evaporation. Inside the detector pipes (the evaporators) the heat is absorbed from the detector (D-E) and a fraction of the CO₂ progressively evaporates. The liquid/vapor mixture is then transferred back to the cooling plant (E-F) into the accumulator vessel (G), where the regulation of the process takes place (see below). The CO₂ is then liquefied and sub-cooled by passing through a heat exchanger, the condenser, into which the refrigerant of the primary circuit circulates in counterflow; after that, the CO₂ is ready to be pumped again into the detector. The primary circuit needs to run typically at a temperature about 10 °C lower than the minimum operating temperature of the CO₂ 2-PACL.

The element of the system where the process is controlled is the accumulator (G). The volume of the accumulator is at the same pressure¹ as the entire portion of the circuit from the inlet of the detector (after the capillaries) to the inlet of the condenser. A cooling spiral and a heater inside the vessel regulate its pressure, and hence the evaporation temperature inside the detector. In addition, the regulation of the flow of the primary fluid inside the condenser controls the temperature of the sub-cooled liquid CO₂, ensuring correct operation of the pump.

The relatively simple control system, not requiring any active component inside the detector volume, is a key aspect of the 2-PACL concept, that contributes to maximizing the reliability and safety of the overall system.

9.1.2 Implementation in Existing Systems

The first CO₂ cooling system designed for a particle detector was the AMS system. AMS was designed to operate on the International Space Station (ISS); operation in space implies demanding requirements in terms of robustness and reliability, since access is normally impossible, maintenance and repair are excluded. The quality required to operate in space can only be achieved by a very rigorous approach during design, production and qualification. Among the basic rules, we can list: (i) keep the design as simple as possible, (ii) select components of the highest quality, with specifications that exceed the operation requirements by ample margins; (iii) use certified assembly techniques; (iv) perform thorough tests during assembly and on the complete system, with no tolerance for any defect.

The second CO₂ system based on the 2-PACL concept was designed for the LHCb VELO. Part

¹In this simplified scheme the pressure drop in the transfer lines and in the evaporators is neglected.

of this system is inside the vacuum of the LHC machine, and therefore even a microscopic leak in that part would stop the operation of the LHC. The system was designed using the same “aerospace quality” as the AMS one, and has now been running for three years without a slightest problem, and almost without any maintenance.

For the CMS system we plan to use the same approach. Malfunctioning of the cooling system is likely to generate severe problems to the detector and to the data taking. CMS can be opened for maintenance at most once per year, and opening is a costly and somewhat risky operation, that will become in future more and more complicated to manage due to the increased radiation levels in the cavern. Therefore the approach outlined above, although it implies some cost increase, is fully justified for CMS.

9.2 The CMS Pixel System

9.2.1 Requirements and Constraints

The cooling system needs to remove the thermal load from the detectors as well as the heat leaking from ambient to the cold parts of the system. Contributions to the latter are given by the heat leaks through the insulated pipe bundles between the cooling plant and the detector and into the cooling station and manifolds. At present, the maximum power estimates are: 6 kW for BPIX, 3 kW for FPIX and 1-2 kW for the heat leak into the pipe bundles. The design value for the cooling plant targets therefore 15 kW of total cooling capacity, thus providing ample safety margin.

The CO₂ cooling will re-use the copper pipes joining the cooling distribution racks on the cavern balconies with the first patch panel located inside the CMS detector, named “PP1”; such pipes are now delivering the liquid C₆F₁₄ to the present pixel detector. The relatively small layer (18 mm) of insulation installed around those pipe bundles was designed and qualified to ensure operation without any condensation for coolant temperatures of -20°C ; for lower temperatures condensation cannot be excluded.

Two operation scenarios define the range of temperatures required for the coolant: the commissioning phase and the long-term operation.

During commissioning the detector volume may not be sealed yet, and therefore the operating temperature has to remain above the ambient dew point, to avoid any condensation. Taking into account the average dew point of the CMS experimental cavern, a temperature of 15°C is chosen as upper value of the operation range.

During long-term operation, the silicon sensors need to be kept below -4°C , to mitigate radiation damage effects. To fulfill such requirement, a coolant temperature of -20°C is chosen as a lower limit of the operation range, while the on-detector cooling design will ensure a temperature difference sufficiently small between the sensors and the coolant. Such a choice is compatible with the properties of the insulation of the cooling channels, described above.

The CO₂ cooling plant will rely on available services at P5. As cold source, the plant will use the primary chiller of the C₆F₁₄ system. The performance limitations of the fluorocarbon system have been tested during the end of year technical stop in 2011/2012. Test results showed that the primary chiller has enough power to cope with the CO₂ needs. The upgrade works that will be executed during the LS1 will be needed only for the improving the present C₆F₁₄ system performances at the present detector.

At the same time, during LS1, consolidation of the dry air and nitrogen plants is planned, to

increase the flow available to CMS and its auxiliary systems. The planned modifications take into account the needs of the new CO₂ plant.

9.2.2 Cooling Plant Design

As shown in Figure 9.2, the cooling system for the pixel detector upgrade consists of two identical units. Each unit is designed to provide sufficient cooling power for the entire detector, i.e. 15 kW. Under normal operating conditions BPIX and FPIX use each a separate unit, but they can be connected to the same unit in case of need. The two units allow BPIX and FPIX to operate at different temperatures, if needed, and at the same time the design offers a two-fold redundancy, which can be useful in case of technical problems, or for maintenance.

Liquid CO₂ is pumped to the detector through long transfer lines (Section 9.3), using the copper pipes already installed on the CMS central wheel. Heating or cooling of the accumulator volume regulates the evaporation temperature at the detector. The plants will be also equipped with an independent storage system. In this way the volume of the accumulator can be dimensioned to optimize the regulation, while the much larger volume needed to empty the plants is provided by the additional storage system.

The cooling system delivers a constant flow to the detector. Manual regulation valves are implemented on the main manifolds, to balance the flow in the different cooling lines. Variations of thermal loads inside the detector can affect the flow balance: if the heat load decreases in a given line, its flow resistance decreases, hence that line will see a larger flow, and the flow to the other lines will correspondingly decrease, which may lead to a feedback loop. In order to keep the balancing stable and independent of variations of the thermal loads inside the detector (e.g. due to powering/un-powering different parts), each cooling line is equipped with a capillary at the inlet of the detector. The capillaries provide a pressure drop that is large compared to the pressure drop variations expected inside the detector, thus making the system stable. The capillaries will be placed outside the active volume, which offers possibility of access in case of need, and avoids adding material in the tracking volume.

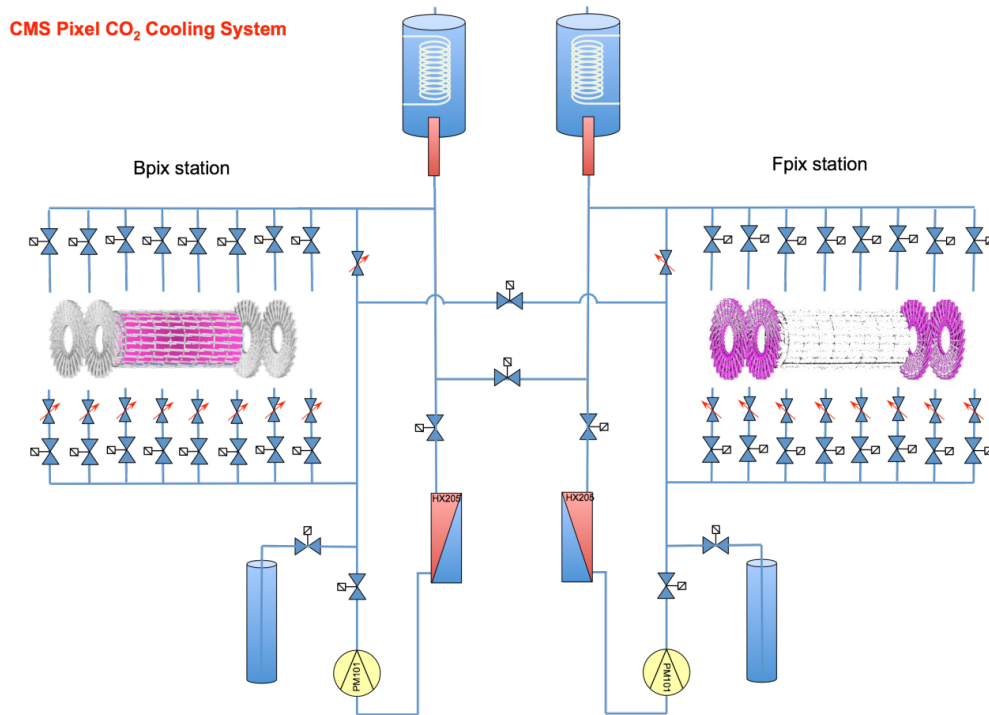
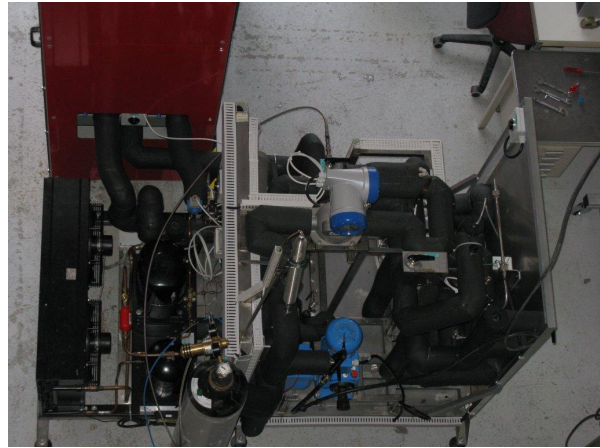
As mentioned in 9.2.1, the CO₂ system will use the primary circuit of the C₆F₁₄ system as cold source, which has proven to be adequate during the performance test.

The control system for the plant process will be developed using PVSS, using the UNICOS standard developed at CERN, which is the basis for the controls of the LHC and the experiments cryogenics. Based on the experience gained with the prototype plants (described below in Section 9.2.3) the system will implement all the control functionalities, as well as the monitoring of the main cooling plant parameters, which will be transmitted to the Detector Control System (DCS).

9.2.3 Prototyping Steps

Based on the experience of the CO₂ systems of AMS and the LHCb VELO, several prototypes and small-scale systems have been recently designed, built and operated at CERN. The developments have been carried out by a CO₂ cooling team composed of engineers and technicians from the Detector Technology Group, the CMS Group and the ATLAS Group of the CERN Physics Department, and from the Cryogenics Group of the Technology Department.

The first CO₂ system that was built is the "CORA" unit: CO₂ Research Apparatus (Figure 9.3). It is a system aiming at testing and qualifying components to be used for the construction of other cooling plants, and for "system tests" with detector mock-ups. The plant can provide a cooling power of 2 kW at -35 °C. In the last months the CORA unit has been dedicated

Figure 9.2: Layout of the Pixel CO₂ cooling system.Figure 9.3: CORA: CO₂ Research Apparatus.

to a full-scale test of the CMS transfer lines (discussed in Section 9.5). The system, including mechanical part and controls, was designed and built with contributions from the whole CO₂ team, which holds the responsibility for its operation. The accumulator has been built by an external company, on a design developed jointly by CERN and NIKHEF.

Based on the CORA design, the 1kW cooling system "MARCO" (Multipurpose Apparatus for Research on CO₂, shown in Figure 9.4) has been developed and built by the CERN Detector Technology Group for the IBbelle experiment, and will be used as a design basis for the ATLAS Inner B Layer system.

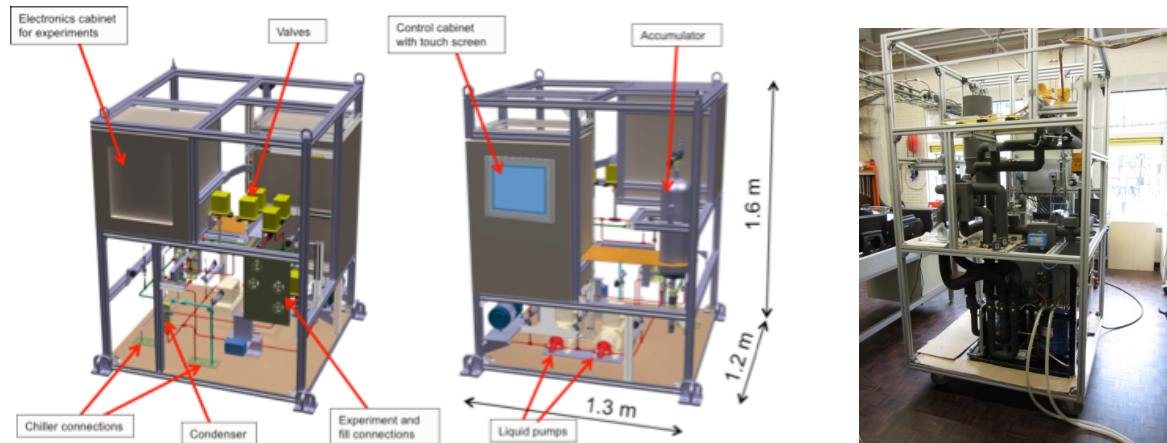


Figure 9.4: MARCO: Multipurpose Apparatus for Research on CO₂. Left: 3d model; Right: the plant during assembly.

For small-scale testing (modules, etc.), the Detector Technology Group also developed an optimized design for a 100 W unit. Two such units have been built so far, and they are in use in the LHCb and ATLAS Collaborations. The design is available and easily reproducible.

During the design and construction of these systems a lot of attention and a large effort has been devoted to identifying and qualifying components that can serve as standards for future projects: a set of valves, pumps, heat exchangers, filters, etc. have been qualified for CO₂ applications and can now be used in systems of different size. A similar concept of standardization has been applied to the control systems, based on UNICOS and PVSS. The design and construction of the cooling plants for the CMS Pixel Upgrade will be based on those standards.

9.2.4 Construction Plans, Schedule, Resources

9.2.4.1 Construction Plans

Two cooling systems will be built in the context of the Pixel detector upgrade project.

The first system will be installed in the Tracker Integration Facility (TIF), a large clean room in the Meyrin site, originally built for the integration and commissioning of the CMS Silicon Strip Tracker. It is foreseen that the final integration and commissioning of the pixel detector will take place in the TIF.

The TIF cooling system will be half-size compared to the final Pixel system, i.e. it will be composed of one of the two identical units that form the final system (see again Figure 9.2). The purpose of this auxiliary system is to perform full-scale cooling tests using detector mock-ups, hence providing the final validation of the cooling system, and support the commissioning of the detector before installation. It will then remain as auxiliary setup for any further activity after detector installation.

As a primary cold source the TIF plant will use the C₆F₁₄ cooling system that served the Silicon Strip Tracker commissioning, connecting either to the chiller or to the fluorocarbon circuit, depending on the scheme chosen for the P5 system. The chiller currently installed can support operation at -30°C , but with limited power. An upgraded chiller will be installed in Autumn 2012 to allow operation with up to 15 kW load, which is the nominal figure for a single cooling unit. A dry air plant and the rest of the services needed are already available.

The commissioning of the cooling plant will include the fine-tuning of the control system, that

will be identical to the one for the P5, also implementing the ability to simulate the presence of the second unit and test the redundancy concept.

The final system for P5 will be installed after the commissioning of the TIF system. Details of the services needed and of the installation sequence are discussed later in this chapter.

9.2.4.2 Resources

The construction of the plants will be done at CERN, with contributions from external companies for some of the assembly tasks and construction of specific components (accumulators). In addition, external companies will also be employed to support some of the installation work.

The CERN team in charge of the project includes personnel from the CMS and Detector Technology groups of the Physics Department who have participated in the conception, design, construction and commissioning of the prototype systems described above in Section 9.2.3. The team is composed of a core of engineers (4 FTE), along with substantial technical support. The CERN responsibilities include choice of the cooling plant components, guidelines for the design, coordination of construction and installation, design and implementation of the controls, commissioning of the system and interface to the DCS.

The group from IN2P3 Lyon is in charge of the engineering design of the cooling plant, including participation in the sizing and choice of components, full 3D modeling of the system and realization of the construction drawings. The designers will then provide assistance and supervision for the assembly of the plants.

BPIX and FPIX engineers participate in the cooling plant design process by providing input on performance requirements, design of the on-detector part of the system, and definition of the instrumentation for the process monitoring.

9.2.4.3 Schedule

A coarse planning for the construction of the two systems is shown in Figure 9.5.

The design phase for the two systems will be completed by mid 2012 and the procurement of the components will start as soon as they are fully defined, so that construction can advance during the last part of the year. The design work is common to the P5 and the TIF systems, and the procurement of the parts will be done in parallel for both.

The system for the TIF will be built in the second half of 2012, and it is expected to be operational in early 2013. It will be first thoroughly tested in standalone mode, and then it will be exploited for full-scale tests with detector mock-ups and realistic power loads. Afterwards it will remain available to support the detector integration and commissioning.

In 2013, in parallel with the commissioning and operation of the TIF plant, the system for P5 will be assembled, and will be ready by the end of the year. Installation and commissioning at P5 is planned for the first half of 2014. Given the two-fold modularity of the P5 system, it could also be considered to build, install and commission the two halves sequentially rather than in parallel, if that turned out to be more compatible with the overall schedule of the different activities at P5.

9.3 Design of the Cooling Lines

The current Pixel detector and the outer Strip Tracker are cooled down by a system based on liquid C_6F_{14} , operating at pressures around 3 and 6 bar for the two detectors, respectively. The

Construction schedule	2011			2012				2013				2014			
	2/4	3/4	4/4	1/4	2/4	3/4	4/4	1/4	2/4	3/4	4/4	1/4	2/4	3/4	4/4
Continue R&D															
System conceptual design defined			★												
Engineering design of cooling plants															
Procurement of components															
Construction of TIF cooling plant															
Commissioning at TIF															
Construction of P5 cooling plant															
P5 cooling plant ready for installation															
Installation and commissioning at P5															

Figure 9.5: Planning for the design, construction, installation and commissioning of the Pixel CO₂ cooling systems.

supply and return lines connecting the cooling plant to the detector are made of 12 mm inner diameter copper tubes, laid along the CMS central wheel in 2008. Such pipes were qualified by a pressure test at 20 bar. After qualification, the tubes have been covered by several thousand cables and optical fibers; replacing them would be an extremely time-consuming and risky operation. It was therefore chosen to investigate the option of re-using the existing pipes with CO₂, re-qualifying them for higher pressure.

One of the main advantages of evaporative cooling systems is the efficient heat transfer that the fluid provides while boiling. The design of the system must ensure that the onset of evaporation happens before the inlet to the detector, but not too much before, so that the full latent heat of vaporization can be used for detector cooling. On the other hand, the vapor quality (e.g. the mass ratio of vapor and liquid) at the exit of a detector loop should never exceed a value of 0.5-0.6 in order to prevent the "dryout", i.e. a significant loss of cooling performance due to the absence of liquid along the pipe walls.

The rest of this section explains how the transfer lines and the evaporators will be optimized to guarantee operation in correct thermodynamic conditions.

9.3.1 The Cooling Loops on YB0

The present Pixel detector is cooled with liquid C₆F₁₄ at low pressure (3.5 bar). Four bundles each containing 9 copper pipes with 12 mm inner diameter (two bundles for inlet, two for outlet) run along the central CMS wheel (YB0, Figure 9.6), bringing the coolant from the cooling plants to the cryostat region and back (Figure 9.7). Each bundle is insulated with two 9 mm layers of SpaceLoft®.

In the new CO₂ system, 8 out of 9 pipes will be used in each bundle, 4 for inlet pipes, containing liquid, and 4 for return pipes, carrying a mixture of liquid and vapor. Three main aspects have to be addressed to adapt the existing pipes to the new system.

1. The YB0 section of the copper pipes was qualified up to 20 bar after installation in 2007. With CO₂ evaporative cooling the range of operating pressures will be between 20 and 70 bar (the CO₂ saturation pressure is 70 bar at 30 °C and 20 bar at -20 °C). The pipes have been re-qualified for operation at 70 bar, as reported in Section 9.3.1.1.
2. The cross section of the pipes is large compared to the CO₂ flow required to cool down the detector; that translates to a small fluid velocity, which could cause boiling in the inlet

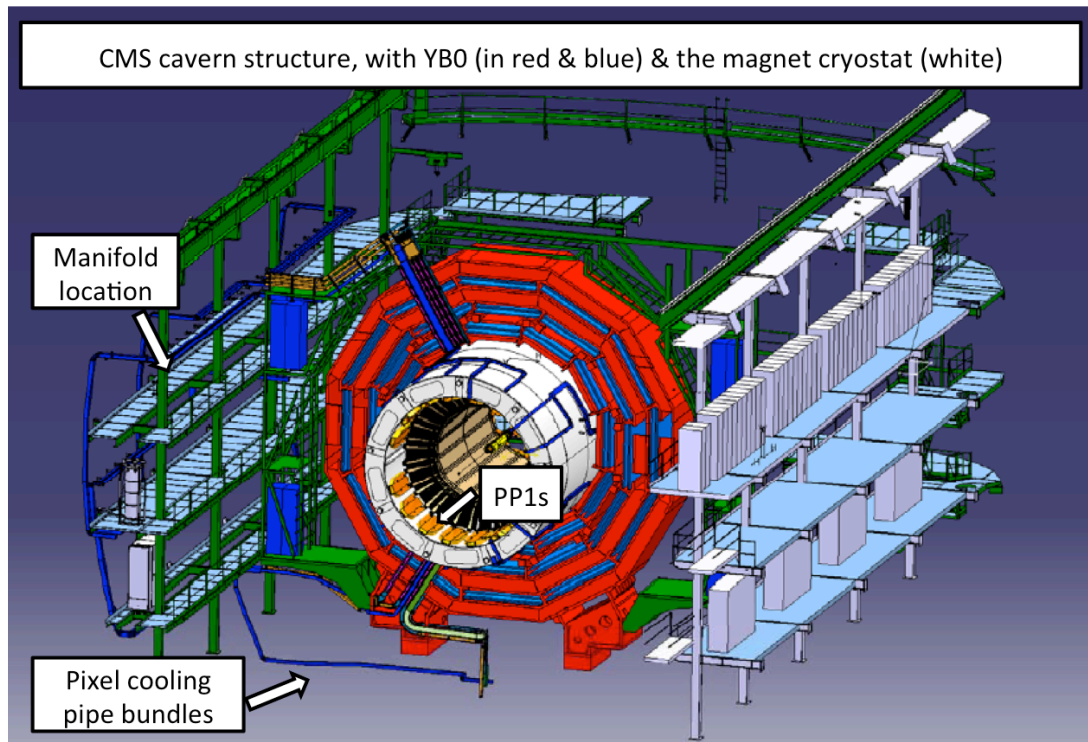


Figure 9.6: CMS experimental cavern structures, with YB0 and the magnet cryostat, including the pipe bundles for the pixel cooling.

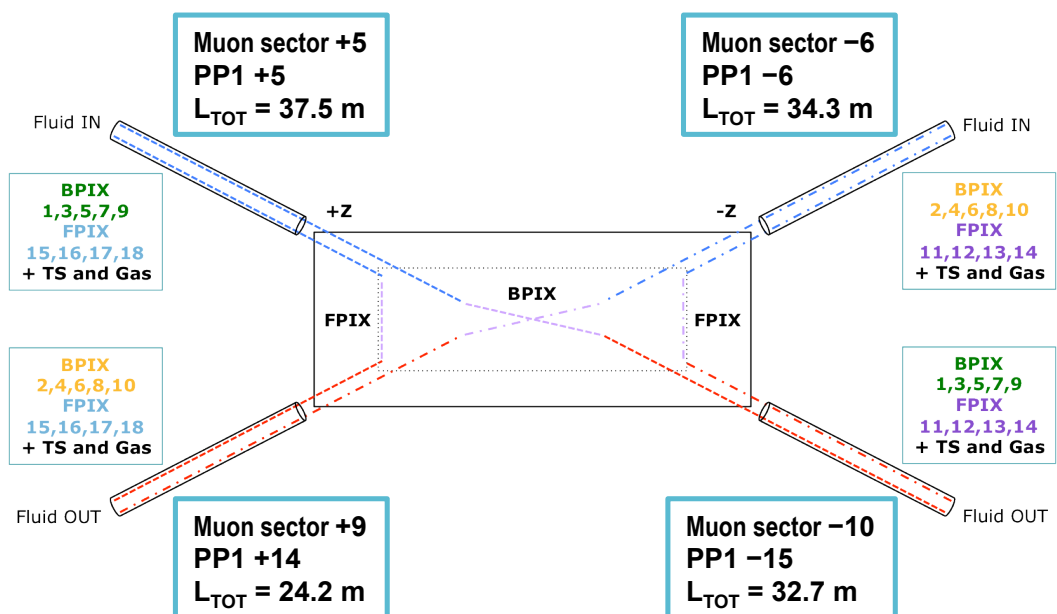


Figure 9.7: The four bundles of cooling pipes serving the Pixel detector.

pipes. If that was the case, higher flow could be obtained by implementing by-passes in PP1, in order to maintain the design pressure and temperature conditions at the inlet of the detector.

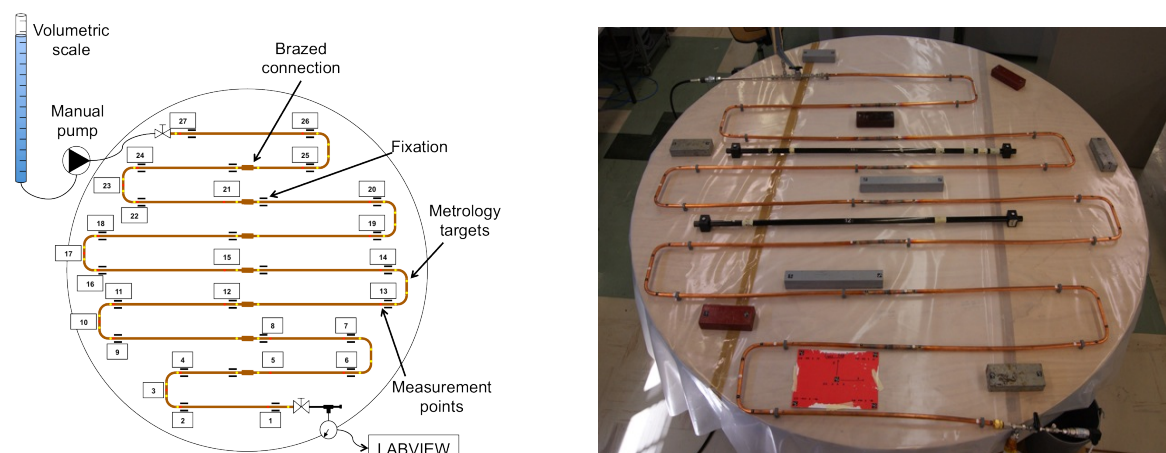


Figure 9.8: The test set-up for full cooling loop qualification.

3. The 2PACL system requires that inlet and outlet pipes be at the same temperature. If the heat transfer inside the bundles is not enough, the section between PP1 and PP0 can be replaced by new pipework designed to maximize the heat transfer efficiency.

In order to address the issues (2) and (3) mentioned above, a dedicated setup has been built and appropriate tests are planned, as discussed in Section 9.3.1.2.

9.3.1.1 Qualification for Operation up to 70 Bar

The pipes have been qualified in two steps: (i) reproducibility and single connection strength for the brazed connections and (ii) deformation under pressure (up to rupture) of an entire cooling loop with typical geometry.

Several samples of pipe sections brazed together were produced and tested in 2011 with the same methods and procedures used during the cooling system construction in 2007. Burst tests with water and tensile tests showed a perfect reproducibility of the results, with a rupture pressure of about 240 bar and a tensile strength of 245 MPa. On top of the destructive tests, metallographic investigations were performed on some of the samples, showing a full reproducibility of the qualification criteria issued during installation in 2007 [73].

Once the reproducibility and the maximum sustainable pressure of the joints was verified, a more complex test set up was built, to evaluate the elastic limit, the deformation range and the maximum sustainable pressure of a full cooling loop.

The mock-up of the cooling circuit was made of 8 U-shape pipe sections brazed together and bent with the same tool used during installation in CMS in 2007 (Figure 9.8). The set-up was about 16 m long, for a volume of 1.84 l. It was fixed to the table with plastic brackets that allow movements of the pipes. One side of the pipe was equipped with a pressure sensor connected to an acquisition system and the other side to a manual pump for pressurization.

Water was injected in the pipes while monitoring its pressure and volume, the deformation of the pipe diameter at various points and the elongation of different pipe segments. Several cycles were performed, in which water was injected to reach a chosen pressure value, and then the pressure was released. The change in volume observed in the cycle is shown in Figure 9.9 as a function of pressure. Permanent deformations of the pipes were detected for pressures higher than 120 bar, which is therefore identified as the elastic limit. The same analysis based on the

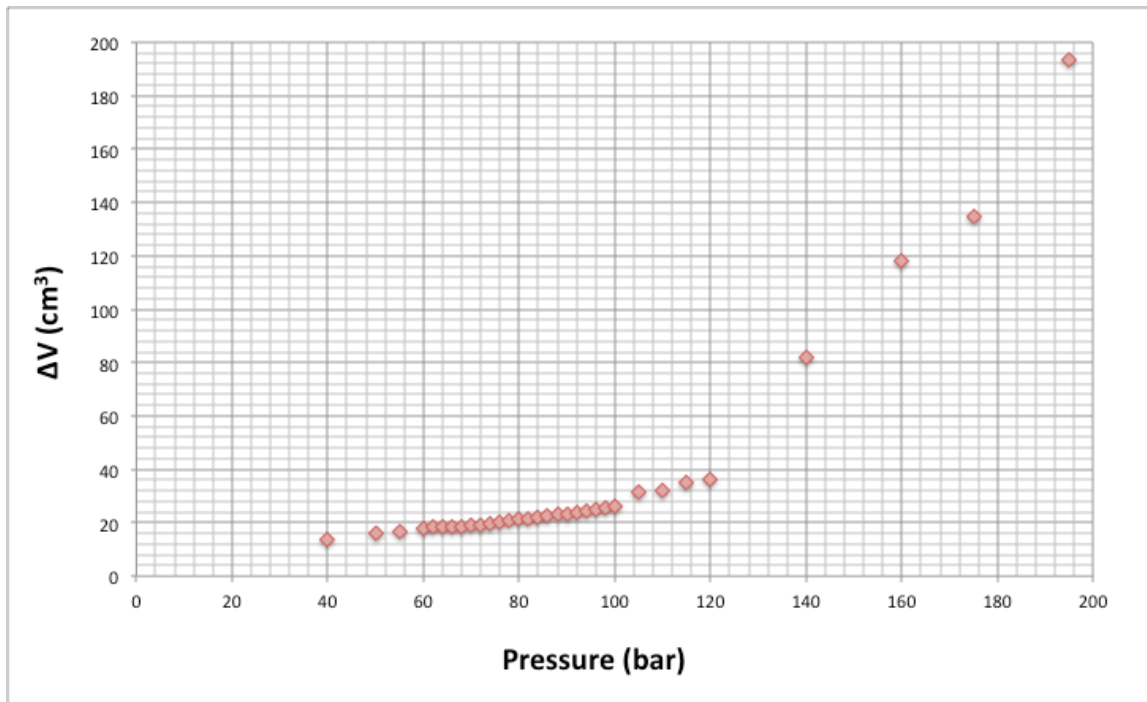


Figure 9.9: Total volume changes on the pipes after a load cycle.

change in pipe diameter yielded the same result. Up to 195 bar the elongation was found to be lower than 0.05% for the longest pipe sections. After measuring the elastic limit, the pressure test was continued up to rupture, which happened at 247 bar.

The results of these tests show that the pipes can be operated safely with the CO₂ system at 70 bar, and the necessary certificate was obtained from the CERN Safety Commission [74].

To ensure that the limit of 70 bar cannot be exceeded even in case of accidental overheating (above 30 °C), any section of the piping that can be isolated from the rest of the circuit (including the detector circuits) will be protected by safety valves or burst disks.

Before operating the system in CMS, each pipe will have to be qualified following the procedures detailed in Section 9.5.

9.3.1.2 Full Scale Piping Test Set-up

A full-scale mock-up of two CMS cooling loops has been built at CERN, in the proximity of the 2 kW CO₂ cooling system CORA. On each cooling loop, a dummy heater of 1 kW is mounted to simulate a part of the detector load. The four pipes (two inlet and two return) are routed along a wall, reproducing all the height differences, the inclinations and the bending radii that can be found on the copper pipe bundles at P5. Insulation equivalent to the one present in YB0 is being installed. An acquisition system with a PVSS interface allows recording pressure and temperature at different spots along the circuits (see schematics in Fig 9.10), and the flow is measured by the control system of the cooling plant.

This set-up will be used to measure the performance of the cooling lines in the whole range of possible operating temperatures and thermal loads, for different values of the coolant flow. The test will allow to define whether the flow in the transfer lines needs to be larger than in the detector, in which case by-passes will be implemented in PP1. The test will also provide

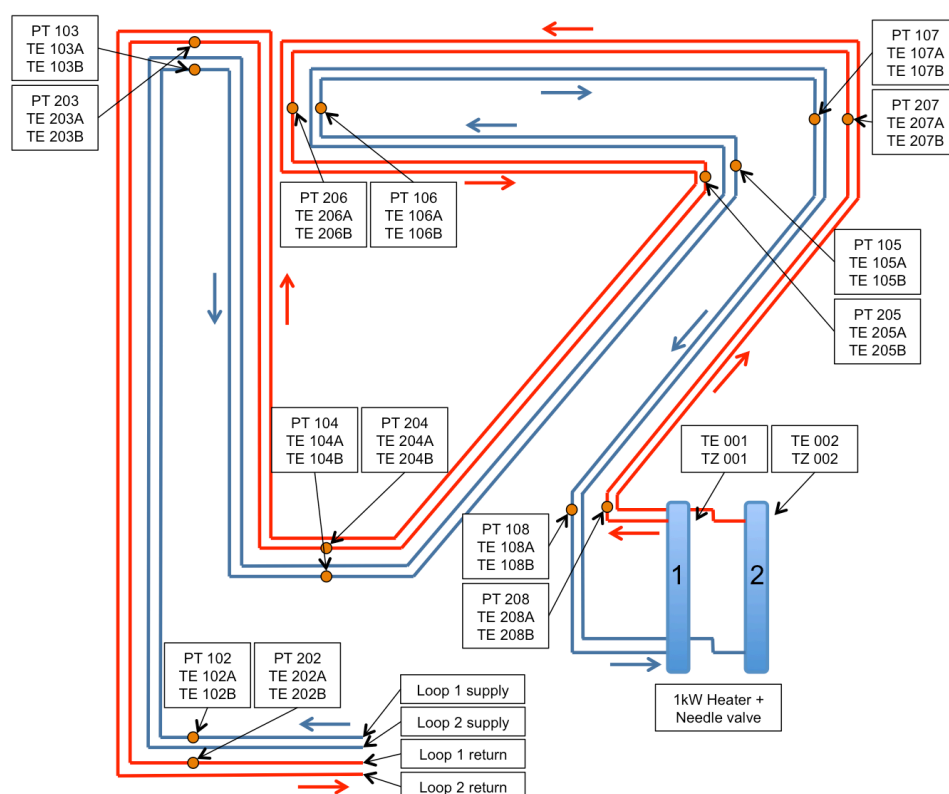


Figure 9.10: The cooling loop full-scale mock-up schematics, with the pressure transmitters (PT) and temperature sensors (TE) used to monitor the process..

a precise measurement of heat transfer efficiency inside a pipe bundle, which will be used as input for a possible re-design of the section from PP1 to PP0 (see below in Section 9.3.2).

The test is expected to be completed by Fall 2012. Preliminary results show that the heat transfer between the inlet and outlet pipes is enough to maintain the adequate temperature set point in a wide range of flow rates around the nominal flow required to operate the detector. The part list of the TIF system has been defined based on such results.

9.3.2 The Region Inside the CMS Cryostat

While the cooling pipes between the plant and PP1 are buried under a large amount of services, the lines between PP1 and the detector are relatively easy to access and can be replaced if needed.

In this section of the cooling lines, the electrical breaks also referred to as “dielectric fittings” need to be re-qualified for the new CO₂ systems. They consist of ceramic couplings that were designed and tested for the low pressure C₆F₁₄ system, and are composed of ceramic and metal, hence material compatibility with CO₂ is not a concern. Following the concept used for the qualification of the YB0 copper pipes, a representative series of samples will be tested for high-pressure to assess their suitability for the new system.

On the detector end, special “Lancashire” fittings connect to the detector pipes. These fittings were chosen as they can be assembled without the use of tools. They contain rubber O-rings and are therefore not compatible with CO₂. They will be replaced by Swagelok VCR fittings.

The pipes themselves are of the same type as the YB0 sections, with smaller diameter and same

Layer	Loop	Tubing length [mm]		Power [W]					
		Supply Tube	BPIX	Supply Tube		BPIX			
				S.by	HL	Startup		500 fb ⁻¹	
						S.by	HL	S.by	HL
1	1	6965	2242	38	50	39	112	97	170
2	2	6965	4514	38	50	118	174	155	211
3	1	9468	3376	75	99	71	87	80	96
3	4	9468	3381	75	99	87	106	98	117
4	2	7199	4514	39	51	126	141	134	150
4	3	7199	4514	39	51	126	141	134	150

Table 9.1: Barrel Pixel cooling loop design. Lengths and power estimates are given separately for the pipe sections on the supply tube and those inside the detector. The power consumption of the detector depends on the instantaneous particle rate, and increases with irradiation: in order to give the full range of figures, estimates are provided for the detector in standby (S.by) and operating at high luminosity (HL), at startup and after having collected 500 fb⁻¹.

wall thickness, therefore the re-qualification for high pressure performed for the YB0 pipes applies here, with larger safety margins. The other aspect to consider is the overall heat exchange efficiency between supply and return lines. If the heat exchange inside the YB0 bundles turns out to be adequate, the pipes between PP1 and PP0 could be reused, replacing only the Lancashire fittings and possibly the dielectric fittings. If, instead, the heat exchange efficiency needs to be improved, the pipes between PP1 and PP0 will be replaced by a concentric tube assembly that functions as a heat exchanger. In this case the supply line will be inside the return line, thereby being isolated from environmental heat input and will be cooled by the two-phase fluid in the return line to a temperature below the saturation temperature. This assures that the supply line contains only liquid phase, which is necessary in order to guarantee a correct flow distribution through the capillaries.

The test described above in Section 9.3.1.2 will provide all the necessary information to define the details for which open questions remain.

9.3.3 The Barrel Pixel Cooling Layout

In the Barrel Pixel detector, each of the four layers will be connected to two separate cooling lines from the cooling plant, one arriving to the detector on the +z end of CMS and the other on the -z end. Before entering the Pixel support tube each main cooling line will be split into the numerous detector-cooling loops, following the segmentation described in Table 9.1.

Each detector loop will cool down the full barrel length over a given azimuthal range, and its inlet and outlet pipes will be located on the same z-side (Figure 9.11). All inlet pipes, mounted on the supply tube shells, will be used to cool down the electronic devices there. In this way, the CO₂ will reach saturation and start boiling before entering the detector section of the cooling loop.

Detector loops connected to a single main line (also called “parallel loops”) are designed to have similar operation parameters also under changing thermal load conditions. The capillaries installed after the manifolds contribute to minimizing the differences, as discussed above in Section 9.2.2.

The expected performance of this cooling system is shown for one of the two layer-1 cooling loops in Figure 9.12, where the temperatures of the CO₂ and of the tube inside the detector

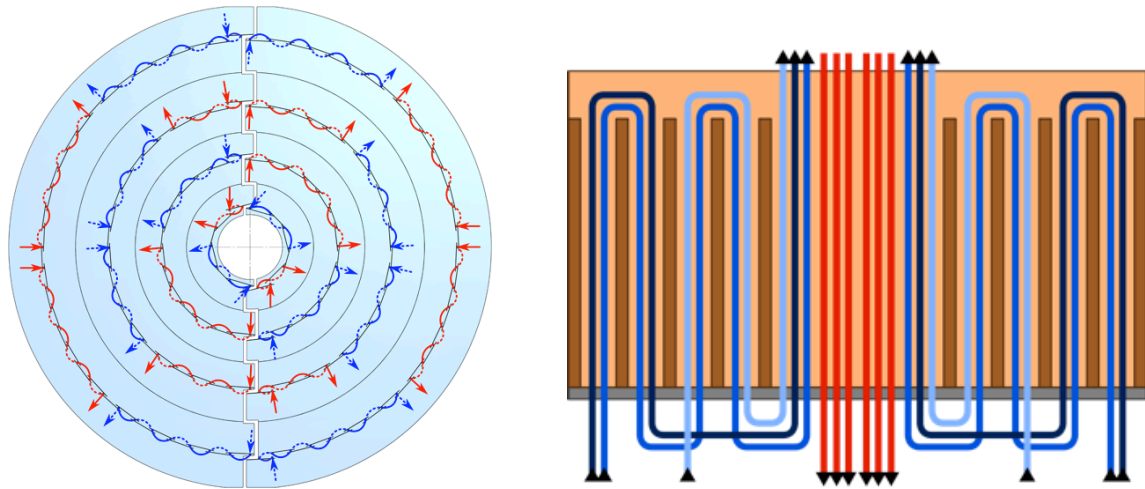


Figure 9.11: Barrel Pixel cooling loop schematics; x-y plane section (left) and view along z on the supply tube (right).

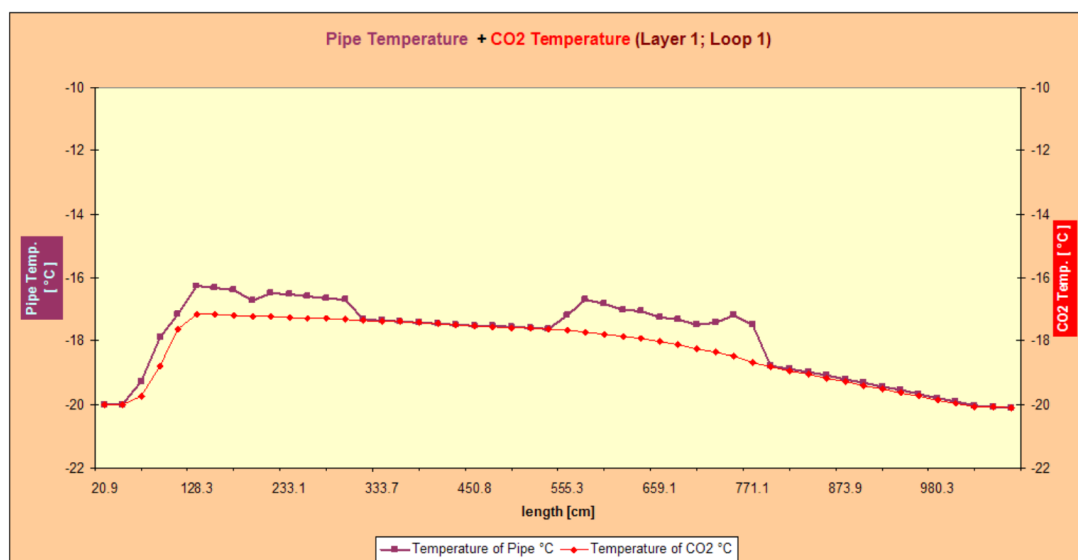


Figure 9.12: Calculated temperature of CO₂, fluid and tube, over the length of a selected Pixel barrel detector loop, under typical operation conditions. The segments where the pipe temperature is higher than the CO₂ temperature are those where heat is dissipated in the pipe, namely the section on the support tube with the DC-DC converters, and the detector section with the front-end electronics.

are plotted along the full cooling loop length. It is calculated that the tube surface temperature will not exceed $-16\text{ }^{\circ}\text{C}$ when the CO₂ inlet temperature is $-20\text{ }^{\circ}\text{C}$. The calculations shown are those for one of the worst cases in terms of power density (BPIX Layer 1) and results can be considered as representative and conservative for the other circuits. The full heat transfer chain, including the thermal contact with the detector sensors, needs to be optimized and then qualified experimentally. Such tests are foreseen during the second half of 2012.

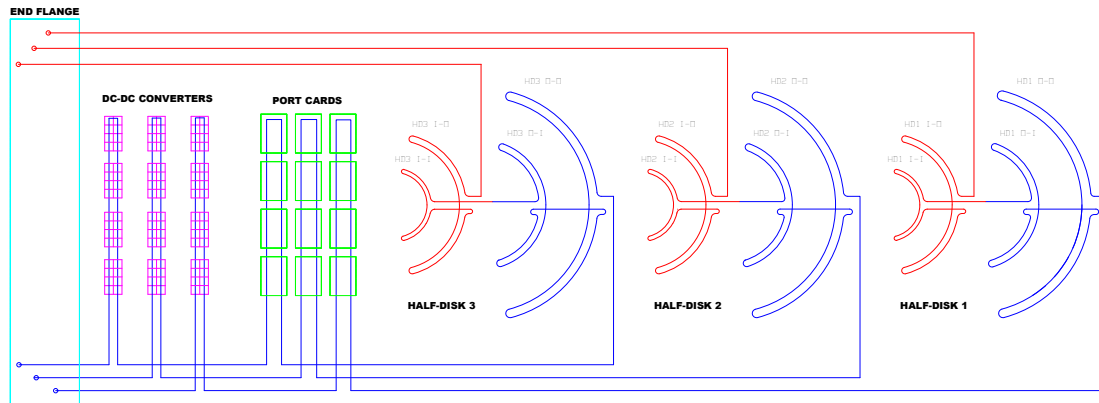


Figure 9.13: Pipe routing for one Forward Pixel detector half cylinder.

9.3.4 The Forward Pixel Cooling Layout

In the Forward Pixel detector, each disk is cooled down independently by two loops, serving the two halves of the disk, on $+X$ and $-X$ respectively. The single half-disk cooling tube is routed along the four carbon fiber structures supporting the detector blades. A schematic of the tubes on one half disk is given in Figure 9.13.

The cooling pipe arriving from the plant is split into a manifold at the detector support tube; each detector loop is routed below the DC-DC converters and the electronic port cards. In this region, the CO_2 reaches the saturation point and evaporation begins.

In Figure 9.14, the calculated values for the CO_2 temperature (liquid and pipe) and pressure are reported, in case of a typical load, for the cooling loop on the half disk number 1. Such calculations show that at the inlet of the detector the tube temperature is about -17°C . As for the Barrel Pixel, the full heat transfer chain, including the thermal contact with the detector sensors, will be finalized and validated in the second half of 2012.

9.4 Integration of the Cooling Plant in CMS

Two possible locations have been identified for the cooling plant: the service cavern (USC), or the experimental cavern (UXC). In USC, the cooling plant could be accessible also during beam time, thus allowing for an easier preventive and corrective maintenance. In addition, the environmental conditions in the USC cavern are much less harsh than in UXC (no radiation, no magnetic field), resulting in less stringent requirements in the choice of components, hence a larger commercial range. Integration in USC requires a longer transfer line between the plant and the accumulator (located in USC), and the manifold, which would be installed in UXC; for this solution radiation protection studies need to be completed, to quantify the possible activation of the fluid circulating at a small radius around the particle interaction point.

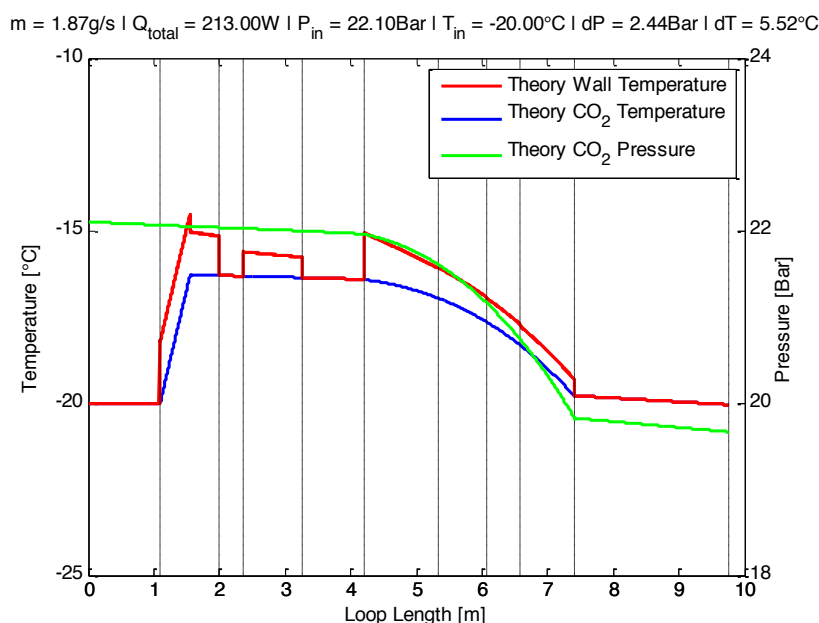


Figure 9.14: Pressure and temperature of CO₂ liquid and tube over the length of a selected Forward Pixel detector loop under typical operation conditions.

9.4.1 Preliminary Studies on Radiation Protection Issues

Preliminary studies on radiation protection issues have been launched at the end of 2011. The mass of the fluid exposed to irradiation has been estimated to be about 1% of the total mass in the plant; for this calculation, it has been considered as exposed fluid that contained in the cooling circuits inside the vacuum tank of CMS, i.e. the volume of pipes from PP1 to PP0 plus the volume inside the Pixel support tube and detector circuits; the case of the Barrel Pixel has been taken, where the volumes exposed to irradiation are bigger than for the Forward Pixel, hence deriving a safe conservative estimate. The total absorbed dose on the irradiated mass is calculated to be 200 kGy for an integrated luminosity of 500fb^{-1} , as shown in Figure 9.15, which translates to 2.4 kGy on the whole CO₂ mass. On the basis of these estimates, the CERN Radio-Protection is performing activation studies in order to assess whether the plant needs to be in a controlled area: the result of such studies will guide the choice of location.

9.4.2 Cooling Plant Layout and Installation Issues

Two identical CO₂ plant cores will compose the integrated cooling system for the Phase-1 pixel upgrade. These cores supply independent cooling to the FPIX and BPIX systems, but also ensure a built-in redundancy into the system as each has the capacity to cool the entire system at a given set point. Each one of these units will fit into an ad hoc insulated box, accessible through “fridge” type doors, so that the internal volume can be kept cold and dry through adequate flushing of dry air. The two cooling unit boxes will be located next to each other, and will be connected by two pipes that allow the backup of one sub-detector on the other sub-detector unit. The envelope assigned for each unit is about $1.2\text{m} \times 1\text{m} \times 1.8\text{m}$ ($l \times w \times h$). A preliminary arrangement of the hydraulic components inside the boxes is given in Figure 9.16. Next to the cooling plant cores two accumulators will be installed, with a volume of 135 l each (preliminary estimate). Two manifolds will distribute the coolant to the eight cooling loops of BPIX and FPIX, respectively. These manifolds will also be contained in an insulated box, and will be instrumented with inlet and outlet pneumatic shut-off valves, two burst disks calibrated

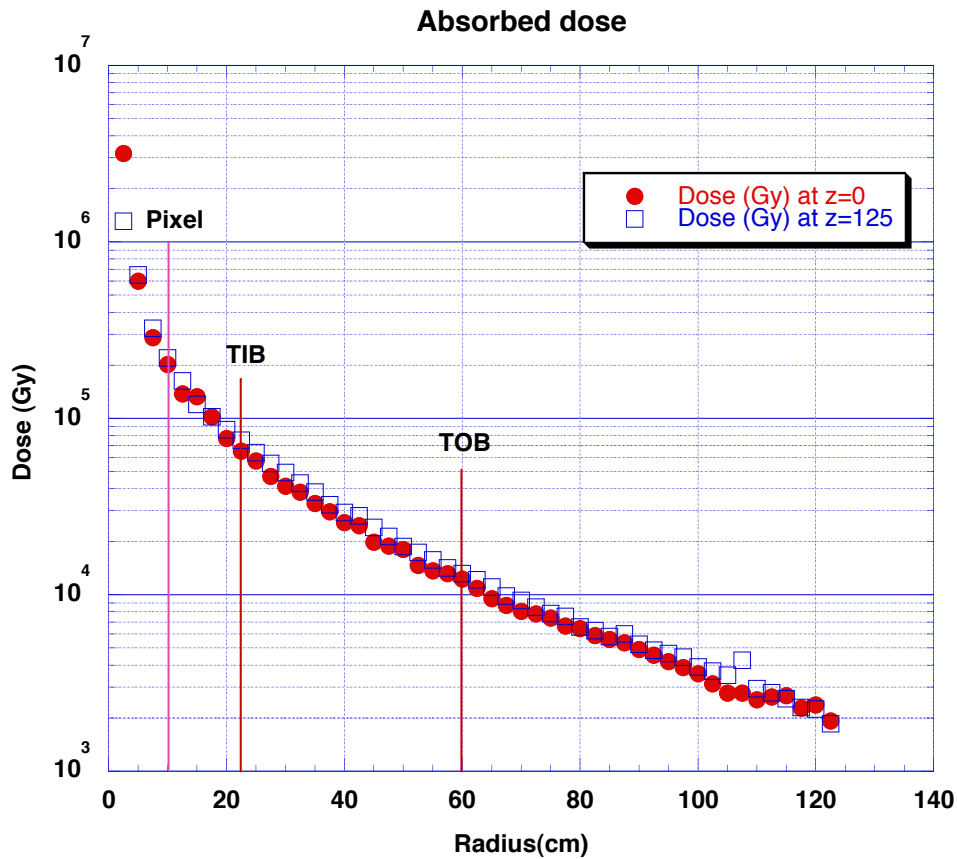


Figure 9.15: Absorbed ionizing dose as a function of distance from the beam line for two different values of z : $z=125$ cm corresponds to the position of the first TEC disk. The three vertical lines show the average Pixel position, the innermost TIB layer and the innermost TOB layer.

at 88 bar (Maximum Design Pressure), inlet and outlet temperature and pressure probes, and a flow meter.

As mentioned in the previous section, the cooling plant cores and the accumulators could be integrated either in the USC or in the UXC cavern, depending on the outcome of the radio-protection studies. The manifolds will be located in UXC, in proximity of the cooling pipes already installed and connecting the detector to the present C_6F_{14} cooling system. The cooling plant will be connected to the manifolds with 1" insulated pipes. If the plant is installed in USC, the most practical routing for these pipes would be the tunnel housing the magnet cryogenic lines. As mentioned in earlier, the cold source for the plant condensers and accumulators will be the chiller of the C_6F_{14} system, if the plant is installed in USC, or the primary fluorocarbon circuit, if the plant is installed in UXC. In either case, the length of the connections to the primary cold source will be minimized.

9.5 Qualifications of the Copper Lines on YB0

The pipe material and joints of the lines connecting the first patch panels PP1 inside the CMS vacuum tank to the balconies of the UXC cavern have been fully qualified for operation with the CO_2 system, and will be reused. The pipes will have to be reshuffled on the balconies to implement the new connection scheme, and a dedicated in-situ qualification will be applied.

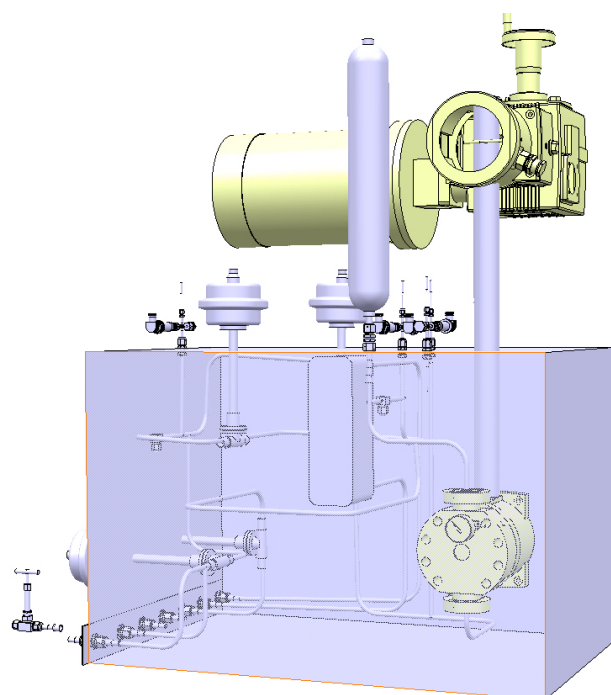


Figure 9.16: Preliminary layout of one cooling plant core.

The existing distribution network is organized in four bundles of 9 pipes each; two bundles are used for the C₆F₁₄ supply and the other two for the fluid return (see Figure 9.7). In the new application, inlet and return pipes will be routed together. Out of the 36 existing pipes, only 32 will be used. In each bundle, 4 inlet and 4 return pipes will serve the same sub-detector, leading to 2 pipe bundles, one on each Z end, for BPIX and 2 for FPIX.

Because of the direct relation between the temperature inside the detector and the pressure at the inlet of the detector, it is desirable to equalize the length and the static height on all cooling pipes serving the same sub-detector. Based on the available data from the as-built model of the CMS cooling system, studies are on-going to optimize the selections of pipe bundles to be coupled together. Before circulating CO₂ in the system, the installed pipework will be pressure tested at 1.25 times the Maximum Design Pressure of 70 bar (that is ~88 bar), as required by the CERN Safety Commission. This test pressure is significantly lower than the elastic limit of 120 bar, and at this pressure the measured deformations of the pipes are negligible.

The pressure test will be done on all 9 pipes of each bundle, so that one can be kept as a spare and possibly used with no need for further testing. The test will be done after the existing detector has been disconnected from the cooling system, as the detector pipes cannot be operated at the required pressure. The test will be done with liquid C₆F₁₄, in order to reduce the stored energy in the system and avoid the necessity to evacuate the PP1 and balcony areas during the test. An ad-hoc simple manifold will be prepared for the connection on the balcony side, where the pumping system will be located, and plugs will be put on the pipes at PP1.

The test will consist of the following sequence of operations:

- drain C₆F₁₄ from the existing plant, possibly by vacuum (4 hours)

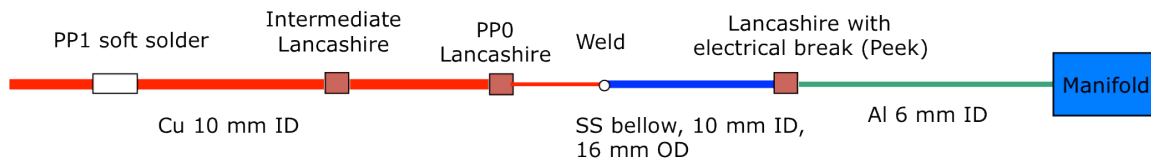


Figure 9.17: Layout of C_6F_{14} cooling distribution from PP1 to the Pixel detector.

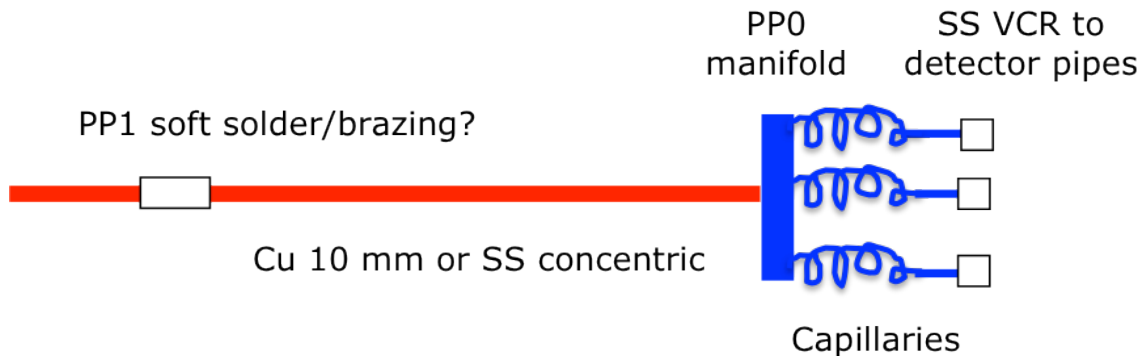


Figure 9.18: Layout of CO_2 cooling distribution from PP1 to the Pixel detector.

- disconnect the copper pipes from the detector at PP0 (1 hour per PP0)
- cut the copper pipes at PP1 and put in place the plugs (2 hours per PP1)
- disconnect the copper pipes from the C_6F_{14} cooling plant manifold (1 day)
- connect the pipe bundles to the pumping station for pressure test at the balconies (1 hour per bundle)
- pump C_6F_{14} liquid into the pipes at the nominal test pressure and verify the tightness (2 hours per bundle)

The last two operations are typically done per each bundle, i.e. repeated 4 times, but can also be grouped to operate more bundles simultaneously, by building a suitable manifold dedicated to the pressure test. After the liquid C_6F_{14} pressure test is executed, a complete draining of the pipes is needed, preferably using vacuum pumping. This step can take about 3 days, after the caps are removed at PP1.

9.6 Cooling Lines from PP1 to Detector

On the existing cooling circuit, the layout of the pipes between PP1 and the detector follows the schematics of Figure 9.17. At PP1 a ceramic element, vacuum brazed to copper connectors, is used to connect the pipes arriving from the balconies (Cu 12 mm ID) with the pre-bent pipes installed inside PP1 (Cu, 10 mm ID). This connection is done via soft soldering and its resistance to the pressures needed for CO_2 operation is to be verified. A test bench is ready and the qualification program will be started in summer 2012. After the 10 mm Cu pre-bent pipes, still before PP0, an intermediate Lancashire fitting, containing a rubber joint, will have to be removed for operation with CO_2 .

In the new configuration, the connection at PP1 may be replaced (if needed) as well as the pipe between PP1 and PP0, which may be substituted by a concentric pipe, in order to increase the heat exchanged between in-going and out-going CO_2 . In any case, at PP0 there will be a small

manifold for each line arriving from the plant. Each manifold will distribute the coolant into a maximum of 4 detector cooling loops and will have capillaries at their exit, in order to balance the flow between the detector loops. The new parts to be installed between PP1 and PP0 will be prepared and tested for leaks in advance, so that they can be installed as pre-assembled pieces before the new detector. Stainless steel VCR connectors will be used to connect the manifold capillaries to the detector pipes at the support tube (sketch of Figure 9.18).

9.7 Plan for Cooling Plant Installation and Commissioning

In 2014, the final system for the P5 operation will be installed in the P5 caverns. Necessary services (power, dry air for instrumented valves and for drying, cold source) will be prepared in advance in the chosen location (see Section 9.4). The necessary tests to qualify the present primary system have been performed during the winter stop 2011/2012 and they have shown the need of some refurbishment for the primary fluorocarbon circuit. Such changes (replacement of some heat exchangers, upgrade of the pumping system) will be executed at the beginning of the LS1. Power and dry air systems will also be upgraded. For the dry air, the work will be done during LS1, in order to increase the total flushing capacity for the CMS detector. An additional quantity of dry air covering the needs of the CO₂ cooling system is taken into account in the specifications. After the installation in P5, the CO₂ cooling plant will not be immediately connected to the detector cooling lines, since those will still be operated with the present C₆F₁₄ system and the existing detector. Dummy thermal loads can be implemented at the level of the manifolds to test and commission the new CO₂ cooling system while the present pixel detector is still in operation.

9.7.1 Preliminary Installation Scenario & Qualification Tests in Stand-alone

The integration of the cooling system at P5 involves improvement and consolidation of existing services and infrastructure that will be done in advance, and a program of installation and commissioning activities for the cooling plant itself. In this section we describe, as an example, the installation plan for the option in which the plants are located in USC.

The following preparation work is planned:

- dry air consolidation and preparation of connection pipes at the USC and UXC locations (manifold and plant flushing, pneumatic valves piloting); for the manifold valve piloting, multipipes will be installed between the location in USC chosen for the electro-pneumatic rack and the manifold location in UXC;
- installation of electrical cabinet (USC);
- consolidation of the primary system and preparation of connections: the latter activity requires the primary fluorocarbon circuit to be empty, so it has to be performed during the consolidation works at the beginning of LS1;
- reinforcement of the floor in the location chosen for the plant cores and the accumulators;
- installation of the connection pipes between the cooling plant cores and the manifolds (this will require at least 1 month if the plant is located in USC).

Having prepared the necessary infrastructure, the installation plan includes, for USC55, the following activities:

- installation and connection of the cooling plant cores and the accumulators;

- pressure and leak test of both accumulators and plant cores;
- installation and connection of the control cabinet;
- installation and connection of the electro-pneumatic cabinet;
- connection of cooling plant to the primary cold source.

In the experimental cavern, UXC55, the work includes:

- installation of the manifolds;
- pressure and leak test of stand-alone manifolds;
- connection of manifolds to electro-pneumatic cabinet;
- connections of manifold to the control cabinet.

Once the cooling system is fully installed, it can be connected either to the final detector and detector pipes, or else to temporary pipes and dummy thermal loads for commissioning. Details of the connection and test procedures follow.

9.7.2 Connection to the Detector and Qualification Procedure

The manifolds installed in the UXC cavern will be equipped with Swagelok VCR connectors in stainless steel, plugged with caps for the pressure and leak test of the manifolds in stand-alone. Whenever the long transfer lines need to be connected, caps will be removed. Copper pipe extensions connecting the manifolds to the existing YB0 copper pipes in the location of the C_6F_{14} plant will be installed in advance and left in the proper position for connection. In order to connect the existing pipes to the manifolds, the pipes need to be disconnected from the present detector and qualified for operation in pressure, as specified in Section 9.5.

Once this is achieved and the manifolds are installed and pressure tested in stand-alone mode on the balconies, the following tasks will be executed:

- brazing of the “extension” copper pipes to the existing ones (3 days);
- VCR connection of such pipes to the manifolds (2 hours);
- installation of the PP1 to PP0 pipes and manifolds, as described in Section 9.6.

After the full path from the manifold to PP1 is completed, a pressure test will be done on the copper pipes, in order to guarantee their safe operation with CO_2 . This can be performed using the manifold of the cooling plant as injection system, and must be performed with gas (Argon or CO_2), thus it will imply to evacuate the area for a couple of hours of test. After pipes are qualified at 88 bar, the pressure will be lowered to 80 bar and sniffing mode leak search performed at the level of the new connections: manifold VCRs, copper pipes brazed connection in the previous manifold location and PP0. One day should be reserved for such tests, with at least three sniffing systems available: one on the balconies, and one on each end of the detector at PP1.

Chapter 10

Pilot System & Early Integration into CMS DAQ

For the CMS pixel phase 1 upgrade, we will introduce some new concepts to the detector readout and powering such as digital readout at 400 Mbps, new Pixel Optohybrids, new FEDs, and DC-DC converters. This will require changes to the data acquisition system (DAQ), detector control and monitoring system (DCS), data quality monitoring (DQM), and offline reconstruction. The current plan is to be ready to install and commission the phase 1 pixel detector with modified DAQ and DCS systems during an extended Year-end-Technical-Stop near the end of 2016 and to have the new detector fully operational soon after. To be best prepared for a short commissioning period and to take advantage of the long shutdown during LS1, we will build a small pilot system of a few prototype modules incorporating the new readout chain, which will be installed in available space in the existing FPIX half cylinders in late 2013. The new μ TCA FED system will be used, otherwise the baseline plan is a hybrid solution with new daughter-boards on the existing FEDs to readout the new fully digital pixel system. When the LHC delivers beams again in late 2014, we will use this pilot system to learn in the actual collision environment of CMS how the readout, control, and offline systems perform. This will provide valuable experience for the operation of the new pixel detector as well as enabling an early start for the modifications that are required for the DAQ, DCS, and DQM.

It is essential that installation and operation of the pilot system should have minimal effect on the operation of the current pixel detector. The present FPIX was designed for possible installation of a third disk, thus sufficient infrastructure (optical fibers, power cables, and cooling) is available to accommodate the pilot system in these locations. Since the existing mechanical support as well as the cooling lines should not be modified to accommodate the pilot system, we are constrained to use the current C_6F_{14} instead of CO_2 cooling for the pilot system. The pilot system can be mounted on a spare FPIX half-disk support structure at the location of the third disk on one of the current FPIX half cylinders. The prototype modules would be placed on brazed aluminum cooling channels connected to the existing FPIX cooling manifolds. Mounting a few prototype modules on the half disk will give only partial azimuthal coverage, but still allowing for integration into the offline tracking software for efficiency and other studies.

The goals of the pilot system are:

- Gain operational experience with the new ROCs and TBM with digital transmission and readout in the FED at P5, providing long-term tests of stability over days, weeks, and months.
- Get a head start on required DAQ modifications: FED firmware and software and calibration procedures.
- Test the DC-DC conversion powering, test for possible electrical interference to nearby

subdetectors (Tracker Inner Barrel), and get a head start on required modifications to DCS.

- Study how the TBM and FED handle conditions present in P5, including high-occupancy background events from beam-gas collisions (machine induced background, or MIB) and single-event upsets to front-end electronics.
- Demonstrate improved hit efficiency for the new ROC in the high-rate environment of the LHC, using tracks projected to the pilot system from the present pixel and strip tracker.
- Provide a fully integrated and realistic test bed for prototype μ TCA pixel FED and FEC electronics when such become available.

10.1 Description of the Pilot System

The half-disk pilot system will have four 2x8 modules mounted on the brazed aluminum cooling channels, which are attached to the aluminum half-disk support structure. Figure 10.1 shows how the modules will be mounted. The pixel modules will be oriented perpendicular to the beam axis, covering from 6.1 cm to about 13 cm. The geometrical configuration is similar to the FPIX upgrade detector. The half ring will then be mounted as a third disk on one of the half cylinders. The 2x8 pixel module will be constructed exactly like the new FPIX module, with a HDI glued to the back of the sensor module. We will use the pre-production PSI46digV1 chip, which is designed for barrel layers 2–4 and the forward disks. (If the PSI46dig+ chip designed for barrel layer 1 is available, some modules will be equipped with these.) A new TBM will be attached to the HDI. To test both speed variants of the TBM to Port Card connection, some modules can be equipped with a 160 Mbps TBM07, as planned for the outer disks of the FPIX, and others can be equipped with a 400 Mbps TBM08, as in the inner disks and barrel layers 3–4. (The TBM is described in Section 5.2.) From the HDI, a prototype Aluminum flex-cable developed for the FPIX upgrade will transmit the output signal from the TBM to a prototype phase 1 FPIX Port Card, to which a Pixel Optohybrid board (POH) and supporting electronics are mounted. The output from two TBM07 modules is combined on the Port Card in the Data Keeper ASIC, which multiplexes two 160 Mbps data streams from the TBMs and includes a 4-bit to 5-bit encoding scheme for stability of the optical transmission, giving output in the same protocol as a TBM08. The 400 Mbps output of the Data Keeper or a TBM08 will be transmitted by a single channel of the POH over fiber to the downstream FEDs.

For powering of the pixel module, in principle, since we have all power cables already in place for the third disk, we do not need to use DC-DC conversion. However, since DC-DC conversion is an important element to the upgraded pixel detector (c.f. Section 7), we intend to have some modules powered by a prototype DC-DC converter board using AMIS5 chips (c.f. Section 7.2.3) for the digital and analog power of the ROCs. This will also allow evaluation of the impact of any electrical interference from the DC-DC converters inside of CMS, either within the pixel system or to other subdetectors. For maximum flexibility, it is envisaged that we will build two pilot system half disks, one powered by the conventional CAEN power supply modules (A4603), and the other one by DC-DC converters. The prototype DC-DC converter bus board will be thermally connected to the existing cooling lines on the half cylinder for cooling and controlled via a CCU board, which has spare channels available.

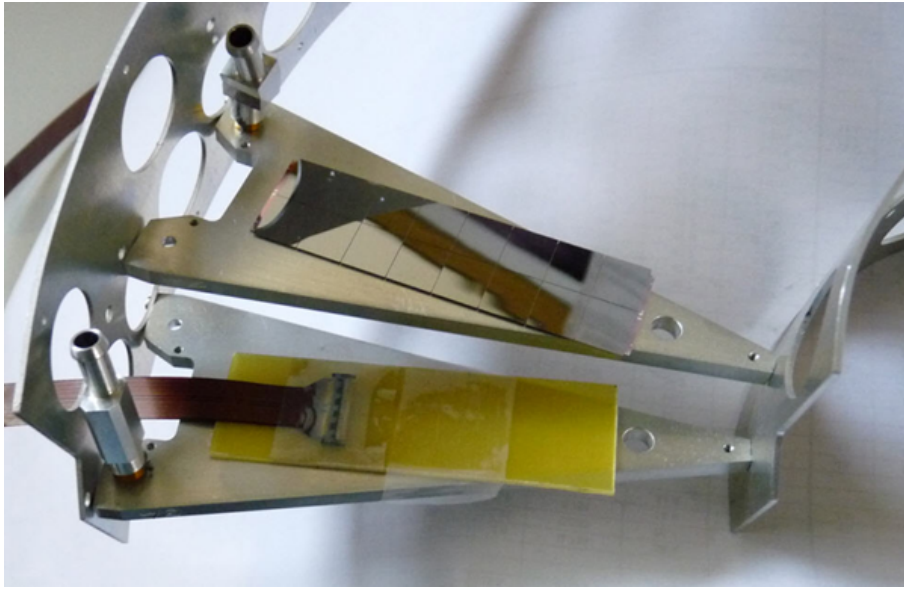


Figure 10.1: Picture showing how the pilot system pixel modules will be attached to the existing Al brazed Cooling channel and half ring support structure.

10.1.1 Parts Needed

For the pilot system, we will use prototype or pre-series versions of the various new electronic circuits that will be used for the upgraded FPIX detector as described in previous chapters. These include the PSI46dig ROC, TBM07, sensor modules, Aluminum flex cable, Pixel Optohybrids, Port Card, DC-DC converter bus board, AMIS5 chips, and the modified FED. In addition the present pixel FEC and tracker FEC VME boards will be reused for phase 1 and the pilot system. We will use the spare Aluminum half-ring support structures and the brazed aluminum channels. No other mechanical support or cooling lines are required.

For trunk power cables, power filtering boards, and power cables within the half cylinder, we will use the spares left over from the construction of the FPIX detector. A modified CAEN power supply unit will be used for powering the modules with DC-DC converter.

Bump-bonding of the new ROCs to the new 2x8 modules will be done in industry. An additional benefit of the pilot system is to allow us to start working with our industrial partners and have their processes verified early.

10.1.2 Development of New Components

All the required components will be tested electrically and functionally. The ROC and TBM wafers will be probe tested with known good dies marked. Likewise, the sensor wafers will be probe tested, and only good sensors and ROCs will be used for bump bonding. The prototype aluminum flex cable, Port Card, and POHs will be fully tested before installation. The HDIs will be probe tested, and the accepted ones will then have the TBMs glued to them. Then the assembled HDIs will be electrically and functionally tested which may include a thermal cycling stress test.

The new μ TCA pixel FED hardware and firmware that can receive and decode the new digital data format is under development as described in chapter 5. To ensure the capability to read out the pilot blades earlier than the μ TCA system might be fully operational, prototype versions of daughter boards for the existing FED, and firmware, will be available at the time of integration at CERN.

For this small-scale intermediate DAQ upgrade, a plug-in board is made that fits into the present FED. The plug-in is essentially a mini-FED, with provisions for one 12-channel fast optical receiver, a 10 Gb Ethernet output to the downstream DAQ, a USB2 interface to the FPGA, and a large FPGA. A large FPGA will allow us to spy on the internal operations and help in debugging firmware issues, a capability not available in the present FED. We foresee maintaining the operation of the plug-in FED with the current VME infrastructure and keeping the capability for the present readout links into the downstream DAQ. Therefore, during early operations, the pilot detector will use the plug-in FED plus the infrastructure that already exists for calibrating and operating the present pixel detector with as small an impact as possible.

A diagram of the stage one FED is shown in Figure 10.2 . Note that the board is for testing purposes and component choices are not final.

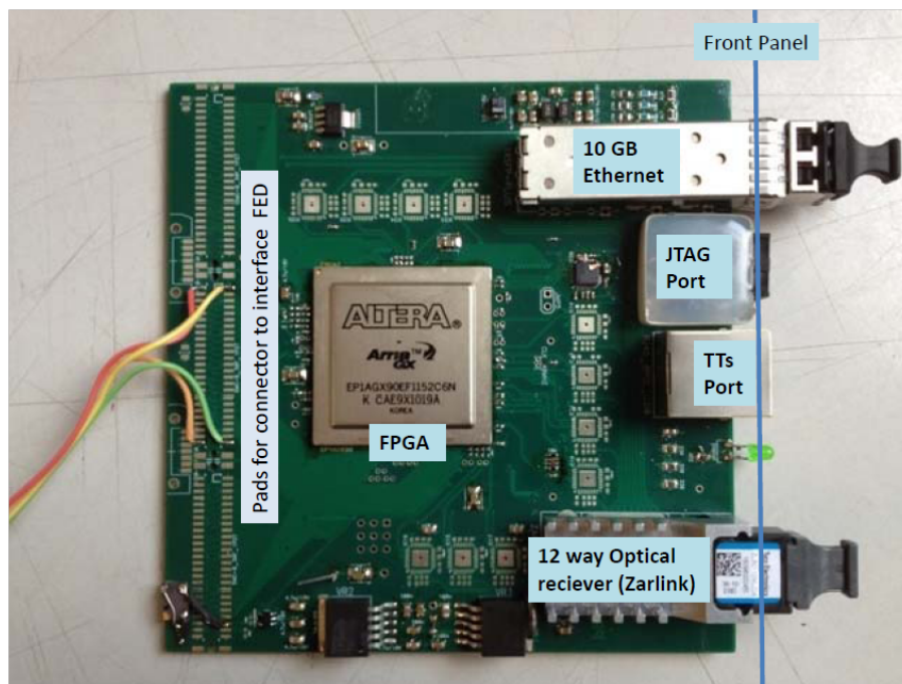


Figure 10.2: Prototype FED for the digital TBM data. Each of these plug in cards is essentially an autonomous FED since there are individual 12 way optical inputs, a 10 Gb Ethernet output and an RJ-45 port for the Trigger Throttling system (TTs). Additionally, the JTAG port allows realtime inspection of the FPGA.

10.1.3 Assembly and Testing

Bump-bonded pixel modules will be delivered to two sites for assembly and testing. These are Purdue University and University of Nebraska at Lincoln. Both have acquired a new gantry system and will use the modules to fully check out their assembly procedure. The assembly includes gluing the HDI to the pixel modules. The assembled pixel modules will then be tested for functionality and then fully characterized in terms of performance (pixel alive, S-curve, trimming, gain calibration) before accelerated aging tests. Pixel modules that pass all the acceptance criteria will be shipped from the assembly sites to Fermilab for assembly on the half ring support structure. The assembled half disk will then be shipped to CERN for installation in the FPIX half cylinder and further testing.

10.2 Installation, Commissioning and Monitoring

The existing FPIX half cylinders have services and mechanical structures to support a third disk. Each of the two pilot system half disks will be installed in these locations and provided with the necessary cooling, power, and optical fiber connections for control and readout. The pilot system half disks will be integrated into the existing FPIX half cylinders and commissioned using a test stand running the modified pixel online software at CERN. Commissioning of the hardware and software begins with functional tests of the communication and readout using the modified software. Parameters for the ROCs will initially be taken from module test results. The online software calibration procedures will be used to tune front-end electronics settings as required, due to fiber connections, timing changes, and temperature differences. Prototype detector calibration procedures as implemented in the online software will be validated on the full readout chain prior to installation in CMS.

The pilot system will be installed with the present FPIX half cylinders in to CMS when required by the LS1 schedule. The installation into CMS at P5 follows the identical procedure for the initial installation of the FPIX detector, performed in 2008 and repeated after repairs in 2009. No changes to the installation procedure are required to accommodate the pilot system, apart from connection of a few additional cables and fibers between the half-cylinder and Patch Panel 0.

10.2.1 Integration into DAQ

The pilot system will require addition of new hardware to the pixel DAQ system at P5. (DAQ system changes for the phase 1 pixel detector are described in chapter 5.) To minimize the impact on operation of the existing pixel detector, it is advantageous to deploy a separate parallel system as far as possible. The pilot system will be initially controlled and readout from dedicated VME boards placed in existing crates (spare slots are available) or, preferably, in a dedicated pilot system VME crate. Rack space is available for a dedicated crate. Clocks, triggers, and control commands will be distributed from the TTC system by one pixel FEC motherboard with two mezzanine mFECs, one connected to each of the pilot system half-disks, which are serviced by separate optical fiber ribbons. The pixel FEC should be a unique VME board, to allow possible firmware changes if necessary to match the new TBMs. Devices on the Port Card and the DC-DC converter card will be programmed by a separate tracker FEC with two mFECs, each connected to new prototype CCU boards in each half cylinder. While spare tracker FEC channels exist in the present pixel system, operating with an independent board allows complete separation of the present pixel detector and the pilot system. One modified FED card with two daughter boards (or two 12-channel inputs) is needed to receive the optical links from the two pilot system half-disks. One S-link connection to the central CMS DAQ event builder allows readout of the pilot system FED in the usual data stream. When available, prototype μ TCA FED/FEC electronics will also be used with the pilot system.

10.2.2 Modification Needed to Existing DAQ and Detector Control System

To accommodate the pilot system in the pixel data acquisition system at P5, some modest changes are required to online software that can be accommodated within the present software framework. Existing low-level interfaces can be cloned and modified to program parameters to the new devices present in the phase 1 readout chain. This includes programming of new ROCs and TBMs, accessed through the pixel FEC, and new devices on the Port Card (Pixel Optohybrid and Data Keeper) and DC-DC converter card, accessed through I2C programming via the tracker FEC. The nature of these changes are minor (e.g. hardware addresses and functions)

and can be made with minimal development within the existing software framework.

The existing software framework also supports numerous local calibration runs that are used to optimize front-end electronics parameters. Many of these procedures can be used directly or with small modifications. For example, threshold adjustments and gain (ADC to charge) calibrations should work identically with the new ROC. Additional scans and optimization procedures appropriate to the new readout chain can be developed within the software framework in a straight-forward manner. One anticipated change is the optimal set up of the digital optical links, which can follow existing scans of linear laser driver set points used for the analog optical links. Commissioning of the pilot system and pixel online software at P5 includes development of needed calibrations, to be further specified as the readout chain is tested and operational experience dictates.

Likewise, the changes required to the Detector Control System (DCS) are relatively minor changes related to details of hardware changes or additional channels for control and monitoring. They will be achieved within the existing framework. Of particular note are the modifications to the CAEN power supplies for use with DC-DC conversion based powering. The pilot system with DC-DC conversion will provide a test case for the required changes.

10.2.3 Monitoring

Operation of the pilot system within CMS will also allow development of Data Quality Monitoring (DQM) for the new phase 1 detector in advance of the installation of the full detector. Beginning with the current pixel system, adding a few additional monitoring elements (e.g. histograms) will be a simple way to begin. Monitoring of the error stream from the new FED channels will require modifications to the software to interpret error conditions from the new FED. Other monitoring elements based on higher-level data objects, e.g. cluster position, cluster size and charge, will be identical once data is decoded in the DQM framework, and no changes will be required apart from adding the new monitoring elements. As in the case of the DAQ and DCS, operational experience will lead to additional ideas to be implemented during operations of the pilot system.

10.2.4 Integration into Offline Reconstruction

The pilot system will be integrated into the CMS tracking software. The data will be present in the CMSSW framework when the prototype FED is included in data taking. Local reconstruction of hits (clustering) on the new modules is a simple extension to the list of detectors in the pixel system. Once clusters are available, the hits on the pilot system detectors may easily be added in the tracking finding algorithms. To perform efficiency studies of the new ROC, tracks found using the present tracker (i.e. excluding the pilot system) can be swum to the position of the new modules using existing software and correlated with clusters on the new detectors. This is a simple extension of detector performance studies already performed for efficiency studies in the present tracker.

Chapter 11

Installation, Testing and Commissioning

The basic installation and testing sequence is similar to what has already been done twice with the current pixel detector, which gives us a well documented, precise plan of action.

This chapter describes the chronological sequence of the various steps necessary for the installation of the phase 1 upgrade to the pixel system. The process of installation and testing starts with the removal of the present pixel system and ends with the go-ahead to the experiment to start the closure procedure of CMS. The goal is to deliver a system that is fully certified as functional and is ready for commissioning and integration with the experiment. Due to the limited time allowed, limited tests will be performed to assure that no more interventions on the soon-to-be inaccessible hardware connections are needed.

Following installation, a significant amount of further work will be required to prepare the detector for physics data taking. During this phase, the detector will be calibrated and tuned to a reasonable level of performance, integrated with the rest of CMS and timed in with cosmic data taking. This procedure was successfully applied previously with the current detector. The time estimates for the whole process will be refined based on the experience we gain with the up-coming extraction and re-insertion of the present pixel detector that is planned for LS1. Furthermore, still during LS1, we plan to exercise the insertion procedure of the new system with a dedicated detailed mockup.

Table 11.1 shows the outline of the installation and checkout sequence.

11.1 Considerations on Radiation Protection for Future Pixel Detector Maintenance

After extended periods of operation of the LHC at high luminosity, radiation protection needs to be considered for any work to be carried out in the inner volume of the cryostat of the CMS solenoid. The beam pipe, the bulkhead of the tracker and the ECAL are the main sources of radiation due to activation. The amount of radiation from the preshower detector (ES) and ECAL end-cap (EE) reaching the inside of the vac-tank depends on the opening of YE1. If YE1 is rolled away by 5 m or more it will not contribute significantly to the radiation in the tracker region [75]. However, the expected level of activation depends on the peak luminosity, the running time of LHC and the cool down time before accessing the area.

As the running scenarios and the performance of LHC are very hard to predict all calculations will have significant uncertainties. The shielding design is based on calculations assuming 10 years of LHC operation at design luminosity: $1 \times 10^{34} \text{ cm}^{-2}\text{s}^{-1}$. After this irradiation, the activation level inside the vac-tank is expected to be between $15 \mu\text{Sv/h}$ and $50 \mu\text{Sv/h}$, approximately equally shared by radiation from the beam pipe, the bulkhead region and the ECAL [75].

Task ID	Description	Min (days)	Max (days)	Integrated (days)
1	Prerequisites	4	4	4
2	Extraction of present system	4	4	8
3	Work on cooling pipes	7	10	15 to 18
4	Insertion of BPIX and checkout of connections	5	7	20 to 25
5	Insertion of FPIX and checkout of connections	4	6	24 to 31
6	Insert BCM/PLT and close the Pixel volume	3	3	27 to 34
7	Reach nominal cooling and give the go ahead for closing CMS	1	1	28 to 35
8	Calibration and commissioning in local	20	30	48 to 65
9	Commissioning with the rest of CMS	5	5	53 to 70

Table 11.1: Sequence of steps for the installation, testing and commissioning of the Phase 1 Pixel detector. The table shows the estimated duration according to previous experience with the present system and the maximum time for each step where contingency is added. The contingency is not a fixed percentage but it is weighted according to the difficulty of the tasks and the capability to extrapolate the present experience to the new system. The units are working days.

The bulkhead shielding disk will be 2 cm of lead, resulting in a reduction factor of 5 for this source. The beam pipe will be shielded also by 2 cm lead except around pumps and flanges where the thickness will be 4 cm. With these in place, the overall reduction factor for radiation will be larger than 5.

Activation and radiation levels will also be better understood at the beginning of LS1. However, the expected radiation levels in LS1 will be much smaller: 5 – 15 $\mu\text{Sv/h}$. At this stage there will be no shielding. Shielding will be ready to be used for any access after the end of LS1.

Beam energy, peak luminosity, integrated luminosity and cooling time before accessing the region will determine the level of activation. Therefore, after any opening of the YE1 disk, the radiation level inside the vac-tank will be measured by, or under supervision, of the radiation protection department of CERN. All work in this area has to be planned to minimize the exposure of personnel to radiation. This applies for both the individual and the collective dosage. All working procedures have to be reviewed under participation of radiation protection experts before being carried out. Depending on the measured radiation levels, the radiation detection department will request different levels of details in work preparation and documentation.

To maintain the unique feature of CMS of allowing fast access to all detector components and to respect the ALARA principle of radiation protection, a modular system of shielding is under construction that can be adapted to all foreseeable maintenance scenarios. For the work at the pixel detector the following scenarios are foreseen.

1. Work on the bulkhead, as connection or disconnection of services after installation or before removal of the pixel detector, or for any repair or maintenance of the services at the bulkhead. In this case the beam pipe inside the vac-tank will be covered with lead shielding and a shielding disk will be set up about 10 cm in front of the bulkhead. The shielding disk will extend in radius far enough to shield the radiation from the ECAL and will have the possibility to be partly opened to give access to the bulkhead area actually worked on. The details of the sectioning of the shielding disk are currently under discussion with the experts from pixel, tracker, BRM (Beam Radiation Monitor) and PLT (Pixel Luminosity Telescope).
2. The extraction or insertion of the pixel detector will be done without shielding. It is limited in duration, but requires all the space close to the beam pipe.
3. Work inside the PP1. The shielding is compatible with the insertion of the special so-called “Surkov frame.” This frame allows easy access to all PP1s except the lower two. For accessing these, all shielding will be removed and a U-shaped shielding will be mounted underneath the beam pipe, supported by the Surkov-Frame.

A general layout of the shielding is shown in Figure 11.1.

11.2 Prerequisites for Pixel Removal and Installation

The configuration of the CMS experiment for pixel installation is shown in Figure 11.2. Both endcaps should be in the 10.6 m open position. There are several prerequisites that need to be met before starting pixel activities:

- Necessary Beam Pipe (BP) supports and protections:

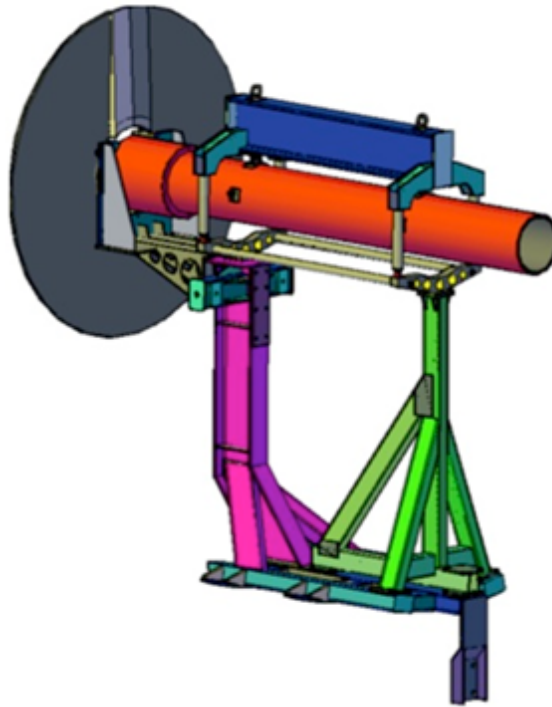


Figure 11.1: General layout of the beam pipe and bulkhead shielding.

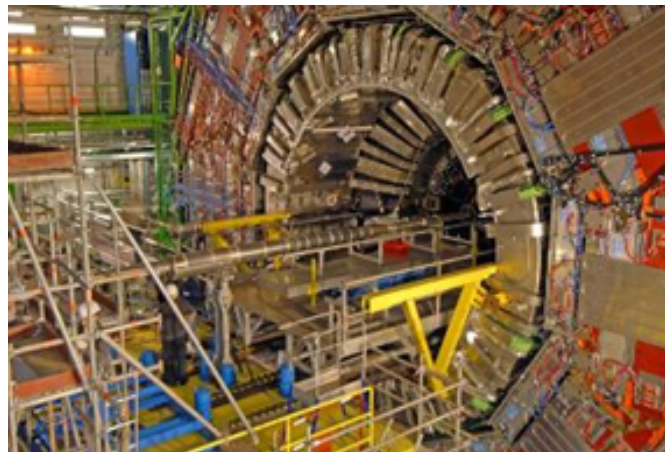


Figure 11.2: CMS configuration for pixel installation and removal.

- The Beam pipe column support must be installed at 10.7 m from the interaction point (IP). This can be adapted with the column displaced by 80 cm and additional horizontal extension (nose) if parallel activities are planned on the preshower (ES).
- The additional "spider-wire" beam pipe support must be installed at 6 m from the IP.
- Standard beam pipe mechanical protections must be installed. They will be partially removed only during extraction/insertion of the pixel system in the part of the beam pipe closer to the interaction point.
- Necessary platforms:

- Main installation platform. Two options are available for pixel activity:
 1. Heavy-weight platform (20 ton) for contemporary EE, ES, and pixel activities (this platform is also called GASPROM platform);
 2. Light-weight platform (10 ton) for pixel activities only.
- Pixel platform. This is the platform that is installed partially inside the vac-tank. It extends from the CMS Tracker bulkhead to ~ 7 m in Z over the main installation platform. This platform rests on four support beams that are fixed to the magnet solenoid structure. The total estimated time for the installation of beams and platform is one working day.
- Beam pipe and bulkhead shielding. This is described in the previous section. The estimated time to install the shielding is one working day.
- Pixel scissor table. The table base with rails is screwed on the pixel platform floor. This table has to be precisely aligned in all three directions with respect to the rail system inside the inner bore of the Strip-tracker. It supports the pixel system during removal/insertion. The estimated time for its installation is four hours.
- Others:
 - Alignment ring. The alignment ring is to be removed. This implies the disconnection, installation of a temporary support and guiding rails, moving the alignment ring to higher Z and locking the alignment ring in its garage location. The estimated time for this operation is two hours.
 - Nose shell. The Nose shell is to be removed. This device is the humidity barrier between the pixel volume and the outside environment. Once it is removed the pixel cooling system should have a setting point for the fluid above the dewpoint of UXC. The estimated time for this operation is one half of an hour.
 - Beam pipe support at 3.5 m. The BP support at 3.5 m is to be modified for BCM (Beam Condition Monitor) extraction. The carbon fiber support at 3.5 m is to be completely removed and replaced with the aluminum stiffener support while the one at 3.2 m should be removed only on the bottom half. At this point it is safe to open the inner ring of the bulkhead. The estimated time for this operation is two hours.
 - Beam Conditions Monitor. The BCM is to be completely removed, placed inside the transport boxes and carried away from the installation platform. The estimated time of this operation is one half of a day per end.
 - Horizontal wires. The Horizontal Wires at 3.2 m should be released and secured on the bellow protection and the two horizontal pulley supports should be retracted. The estimated time for this operation is one half of an hour.
 - Beam pipe support at 3.2 m. The top part of the beam pipe support at 3.2 m is to be removed and replaced with the aluminum stiffener support. The estimated time for this operation is two hours.
 - Beam pipe survey and tools preparation. The survey of the central beam pipe collars with theodolite and precision alignment of the pixel scissor table. The estimated time for this operation is four hours as no personal is allowed on any of the platforms during the beam pipe survey.

Most of these actions can be performed in parallel on the plus and minus ends of the CMS experiment. The total time to reach this configuration is 4-5 working days.

At this point the pixel system can be removed.

In parallel to preparation of the volume inside the vac-tank there are several other activities that have to take place between the end of operation with beam and the insertion of the new pixel detector. These actions can take place while CMS is opening following operation with beam in the first few weeks of the extended technical stop.

CMS balcony X2 in UXC:

- Cooling system. The C_6F_{14} cooling system and pipes need to be drained to the best possible level (within the pressure tolerances of the Pixel detector). Following drainage the copper pipes from the balconies (X2) to the vac-tank need to be cut from the present C_6F_{14} cooling plant and reconnected to the new CO_2 systems.
- Power system. The CAEN power supplies (A4602 and A4603) will be upgraded to be compatible with the specification of the new pixel detector. (See Chapter 7.)

CMS S1 in USC:

- VME electronics. The VME electronics in S1G01-4 need to be upgraded to the one compatible with the new digital readout. In particular all FEDs need to be replaced with the new boards based on microTCA (see Section 5.4). This work will take place in the service cavern (USC) and can start as soon as the last beam is dumped before the technical stop. This activity should have no impact on the schedule of work in the UXC.
- Pixel PLCs and DCS. The pixel PLC system located in S1G02 needs to be expanded with extra modules to readout the larger number of sensors foreseen for the upgraded pixel detector. The following steps will have been done before the installation of the pixel detectors.
 - Connect RTD/HMX simulators at PP0 and read back with the PLC, make sure all channels are giving correct values and the cable mapping is correct.
 - Read the values from PVSS make sure that each channel data point is reading the correct channel.
 - Turn on/off CAEN modules from PVSS and make sure all PVSS controls of the CAEN supply working.
 - Connect simulated (passive) loads at PP0 and read back from PVSS. Make sure cable mapping is correct and PVSS data points has correct channel address.
 - Test the interlock for each interlock group and see that the corresponding CAEN power modules turned off.
 - Connect simulated loads and RTD/HMX humidity sensors at PP0 patch panel on the Tracker bulkhead, corresponding to each half cylinder. Test the functionality of the PVSS controls (finite state machine, activating interlocks for over-temperature, humidity).

All these activities can be performed either before the present pixel system is extracted or while there is work on the Pixel cooling pipes (See Section 11.3) before the insertion of the upgraded detector and after the extraction of the present one (these activities require access to PP0).

	Activity	End	
1	Disconnect cooling pipes and electrical/optical cables	Minus	half shift
2	Setup and extract FPIX	Minus	1 shift
3	Disconnect cooling pipes and electrical/optical connection	Plus	half shift
4	Setup and extract FPIX	Plus	1 shift
5	Setup and extract BPIX	Minus	1 shift
6	Pack and crane all removed objects to the surface for storage in the RP area	Both	Off critical-path

Table 11.2: List of steps for the removal of the present pixel system.

11.3 Extraction of the Present Pixel System and Other Preparatory Work

The removal of the present pixel system will follow well established procedures. Such procedure has been developed during the 2008-2009 YETS when the present forward pixel system has been removed and will be further tuned during LS1 when the present pixel system (both Barrel and Forward) will be extracted and reinserted. During this period it will be crucial to understand the potential interferences associated with operation in a challenging radiation environment like drainage of the irradiated cooling fluid from the system and mechanical interferences with the radiation shields. These steps are outlined in Table 11.2.

Once the old Pixel detector is removed the work on replacing the cooling pipes between PP1 and PP0 can start. This work is necessary due to the ceramic electrical decoupler. The copper cooling pipes will be disconnected at PP1 and the sections between PP1 and PP0 will be removed. Further drainage and cleaning of any remaining C_6F_{14} should be performed on the remaining copper lines. The new pipes should be installed and capped on the PP0 side and connected to the existing copper lines at PP1. The new cooling system has very different operating pressures than the present one. This demands for thorough testing of all components before connections to the detector. Once the new pipes are connected to the new cooling system we deem necessary to pressure test with argon the full system up to the PP0 connections before installing the detector. This activity implies work on both ends of the detector on the top and the bottom of the vac-tank (4 different muon sectors). The estimated time to complete this task is 7-10 days and it will be better evaluated during LS1 when a detailed inspection of the vac-tank should provide the details to optimize the operation.

11.4 Phase 1 Pixel Installation

The installation of the new pixel detector will be very similar to what has been already done for the present pixel system. The list below show the sequence of the various steps for the Barrel. The choice to start from the MINUS END is completely arbitrary. The same procedure should then be followed for the Forward Disks system, but since they are inserted one end at the time, an extra day should be added to the schedule.

1. Insert and test BPIX:

- (a) Insert BPIX from the MINUS end. This will be done one half-barrel at the time and it is going to take 1 day per half-barrel.

- (b) Connect BPIX on both ends estimated another day (half day on each end).
- (c) Gas (argon) pressure test the cooling lines. Estimated one day.
- (d) Establish cooling to the detector (estimated half day).
 - i. One line at the time checking temperature behavior in the BPIX via DCS (this is DCS-to-cooling mapping).
 - ii. Coolant temperature should be chosen somewhere between 15 °C and 20 °C in order to avoid any problem with condensation (UXC dewpoint is guaranteed below 13 °C).
- (e) Test of the connection (electrical and optical) Estimated a couple of days.
 - i. Detector should be powered one power supply at a time and corresponding temperature should be monitored via DCS (CAEN to DCS mapping)
 - ii. Detector parameters from pre-insertion testing should be used to configure the detector.
 - iii. The most critical step in this process is to establish the quality of the optical connections.

Figure 11.3 shows a picture of the bulkhead inner part without the carbon fiber panels so that all the pixel connection to the services are visible.

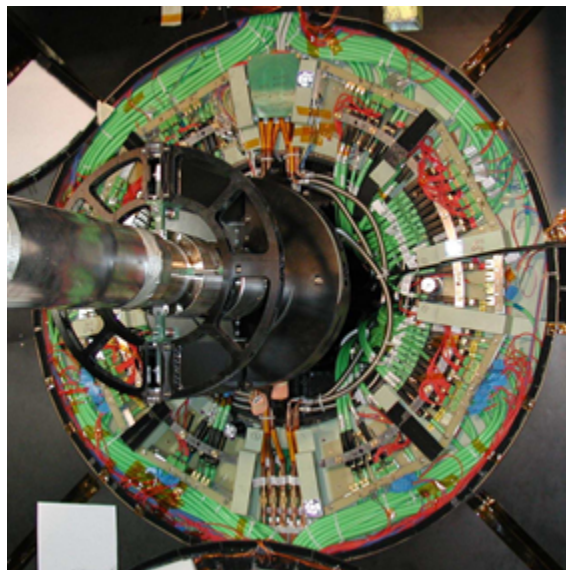


Figure 11.3: Picture showing the bulkhead with the inner rail without the covers and with all connection in place.

11.5 Other Activities Within the Pixel Volume

With the new pixel detector installed and cabled correctly, the BCM carriage that also contain the PLT is to be installed. The whole process is quite similar to the Pixel installation and testing. The BRM and PLT installation consists of:

- Mechanical installation
- Electrical and optical connections

- Connections check out.

The estimated duration of this process is 1 working day for both PLUS and MINUS ends. The tight alignment requirements for the PLT system imply that the final adjustment of the PLT location is to be done as an iterative process with the survey team. A half-day on each end should be sufficient.

The last activity in the vac-tank is the closure of the humidity seal of the pixel volume, which can be seen in Figure 11.4. The carbon fiber panels for the inner bulkhead need to be placed

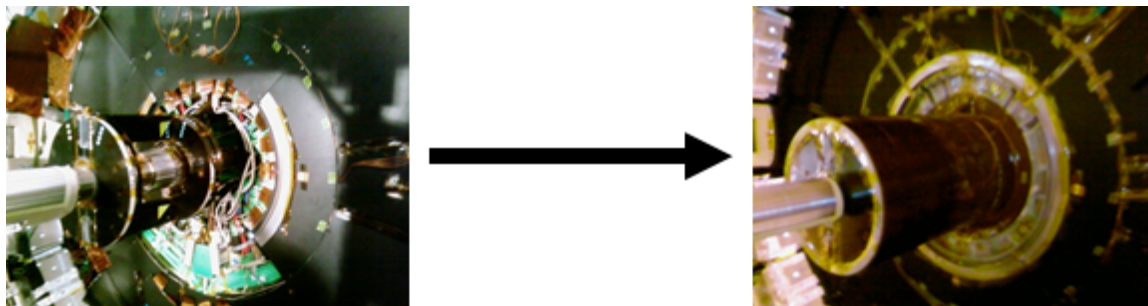


Figure 11.4: Closure of the pixel volume with the humidity seal.

on top of the connection region up to a radius of 625 mm and sealed with Velcro and Kapton tape. The bulkhead nose shell will be installed over the beam pipe carbon fiber supports. The arrangement acts as a seal between the pixel volume and the outside environment, and hosts the heating foils to avoid condensation on the outer surface of the seal itself.

The effectiveness of the seal must be tested by monitoring the dew point inside the pixel volume with the following conditions:

1. Establishing the nominal flow of dry gas (either dry air or Nitrogen at 1-2 volume exchange per hour).
2. Bringing the cooling system temperature setpoint to nominal (-20°C).
3. Powering up the detector.
4. Checking the stability versus time overnight with different power conditions for the detector.

Official signoff that the pixel work in the vac-tank is finished. At this point the alignment ring can be put back in place and infrastructure and tooling can be removed.

The total estimated time for this activity is 1 to 2 days.

11.6 Other General Considerations

To minimize the long-term effects of radiation damage on silicon sensor, it is recommended to keep them cold after exposure to irradiation. During the replacement of the CMS pixel detector it is desirable to minimize the amount of time with the silicon strip tracker at room temperature. The plan is to install a humidity seal between the pixel and the strip volume during LS1 that should guarantee the necessary decoupling between the pixel and the strip environment.

The most likely scenario is that one end of CMS (preferably the MINUS end) will be opened before the other as tools and trained personnel are not sufficiently available to open both ends of CMS at the same time. The impact on the schedule of parallelizing work on both ends is quite minimal and it could be accounted as no more than a couple of days.

The activity levels of the inner part of the CMS detector requires installation of radiation shielding in the vac-tank region. Installation and removal of the shielding is estimated to add a day at the beginning of the schedule and a day at the end of it. The shielding is being designed such to minimize the interference with Pixel replacement/maintenance and the impact on the time-estimates for the affected activities will be assessed.

11.7 System Calibration, Integration and Commissioning

The phase 1 pixel detector is very similar to the present pixel system. Up to this date the present pixel system has been calibrated and re-commissioned two times:

- The first following the installation (total calibration time of two months)
- The second following the year-end technical stop between 2011 and 2012 (total calibration time of three weeks).

In terms of commissioning, the differences between the two systems are mainly on the readout electronics. The data will be transmitted in a digital format (see Chapter 5) over new optical links to the service cavern, received and processed with the upgraded FEDs.

The main challenges for the calibration and commissioning are identified in the analog and digital parts of the front-end electronics (ROC). Threshold minimization and gain optimization are the most critical calibration for the detector. The procedures will be very similar to the one already in place at CMS. The most noticeable difference is that for the phase 1 pixel system we are planning to pre-calibrate the modules during their production phase so that the detector will be installed with a pre-existing database configuration for the foreseen temperature of operation. Such approach should shrink the necessary time to calibrate the detector standalone (local calibration) as most of the calibrations are iterative processes and the time for their completion strongly depends on the starting configuration.

The list of the major local calibrations are:

- Bias and gain of optical links.
- Power consumption tuning (power DACs).
- FED parameter tuning (optoreceiver and delay).
- TBM parameter tuning (gain).
- ROC parameters tuning (threshold and gain).
- Pixel trimming.

Following the calibration in local mode the new pixel system should join the rest of CMS in the central DAQ and participate in global runs. The experience gained with the operation of the pilot blade system in the previous three years will be crucial for the successful and timely completion of this process. The pixel detector, DCS and DAQ will be tested for their compatibility with the overall experiment. There are three phases that we foresee:

- High trigger rates test with random triggers.
- Cosmic data taking for the gross time alignment of the pixel system with the rest of

the experiment.

- Data taking with p-p collision for the fine and final time alignment.

Both cosmic data and early collision data will be crucial for the alignment of the detector and for measurements of various other parameters important for tracking like the Lorentz angle.

Chapter 12

Project Organisation, Responsibilities, Planning and Costs

The community involved in the Pixel Phase 1 Upgrade project is much larger than the community that originally built the present Pixel detector, its size being nearly that of the entire present Tracker community (Tracker = Pixel + Strips detectors).

There are 46 institutions participating, widely distributed over the world, with about 400 physicists, engineers, senior technicians and doctoral students involved into this construction. These include both the people who are committed to carry out the construction of the upgraded detector and those mainly working on software aspects, including study of the physics case and detector response simulations.

12.1 Participating Institutes and Collaborators

1. **Institut für Hochenergiephysik der OeAW, Wien, AUSTRIA**
M. Friedl, J. Hrubec, H. Steininger
2. **Department of Physics, University of Helsinki, Helsinki, FINLAND**
P. Eerola
3. **Helsinki Institute of Physics, Helsinki, FINLAND**
D. Fusi, J. Härkönen, P. Luukka, T. Mäenpää, T. Peltola, E. Tuominen, E. Tuovinen
4. **Institut Pluridisciplinaire Hubert Curien, Université de Strasbourg, Université de Haute Alsace Mulhouse, CNRS/IN2P3, Strasbourg, FRANCE**
R. Baumann, D. Bloch, C. Bonnini, E. Chabert, E. Chambit, L. Charles, L. Gross, J. Hosselet
5. **Université de Lyon, Université Claude Bernard Lyon 1, CNRS-IN2P3, Institut de Physique Nucléaire de Lyon, Villeurbanne, FRANCE**
D. Contardo, A. Eynard, J. C. Ianigro, N. Lumb, L. Mirabito, S. Viret
6. **RWTH Aachen University, I. Physikalisches Institut, Aachen, GERMANY**
H. Esser, L. Feld, W. Karpinski, K. Klein, I. Özen, G. Pierschel, J. Sammet, S. Schmitz, M. Wlochal
7. **Deutsches Elektronen-Synchrotron, Hamburg, GERMANY**
M. Aldaya, A. Burgmeier, L. Calligaris, G. Eckerlin, D. Eckstein, T. Eichhorn, S. Habib, J. Hansen, K. Hansen, J. Hampe, H. Maser, C. Muhl, J. Olzem, H. Perrey, A. Petrukhin, D. Pitzl, A. Zuber

8. **University of Hamburg, Hamburg, GERMANY**
L. Bergerm, M. Centis Vignali, B. Frensch, E. Garutti, J. Haller, T. Hermanns, T. Lapsien, M. Matysek, C. Sander, J. Sibille, P. Schleper, S. Schuwalow, G. Steinbrück
9. **Institut für Experimentelle Kernphysik, Karlsruhe, GERMANY**
T. Barvich, Th. Blank, F. Bögelspacher, M. Caselle, A. Dierlamm, F. Hartmann, S. Heindl, U. Husemann, A. Kornmayer, Th. Müller, H.J. Simonis, P. Steck, M. Weber, Th. Weiler
10. **INFN Sezione di Bari, Università di Bari, and Politecnico di Bari, Bari, ITALY**
P. Cariola, D. Creanza, M. de Palma, R. Ferorelli, L. Fiore, S. My, N. Pacifico, A. Pompili, G. Sala, L. Silvestris
11. **INFN Sezione di Catania and Università di Catania, Catania, ITALY**
S. Albergo, S. Costa, N. Giudice, N. Guardone, F. Librizzi, F. Noto, A. Tricomi, C. Tuvè
12. **INFN Sezione di Firenze and Università di Firenze, Firenze, ITALY**
V. Ciulli, C. Civinini, E. Focardi, G. Sguazzoni, A. Tropiano
13. **INFN Sezione di Genova and Università di Genova, Genova, ITALY**
R. Ferretti, F. Ferro, M. Lo Vetere, S. Minutoli, R. Monge, E. Robutti, S. Tosi
14. **INFN Sezione di Milano-Bicocca and Università di Milano-Bicocca, Milano, ITALY**
P. D'Angelo, S. Gennai, S. Malvezzi, D. Menasce, L. Moroni, D. Pedrini, S. Sala
15. **INFN Sezione di Padova and Università di Padova, Padova, ITALY**
N. Bacchetta, D. Bisello, P. Giubilato, D. Pantano, N. Pozzobon, M. Tosi, A. Zucchetta
16. **INFN Sezione di Perugia and Università di Perugia, Perugia, ITALY**
G.M. Bilei, S. Bizzaglia, M. Bizzarri, B. Checcucci, E. Conti, G. Farnesini, L. Fanò, M. Menichelli, S. Meroli, P. Placidi, A. Papi, D. Passeri, A. Saha, A. Santocchia, G. Scolieri, L. Servoli, S. Taroni
17. **INFN Sezione di Pisa and Università di Pisa, Pisa, ITALY**
P. Azzurri, G. Bagliesi, A. Basti, R. Beccherle, J. Bernardini, T. Boccali, F. Bosi, G. Broccolo, R. Castaldi, D. Caiulo, M.A. Ciocci, R.T. D'Agnolo, R. Dell'Orso, S. Donato, F. Fiori, L. Foà, A. Giassi, M.T. Grippo, A. Kraan, F. Ligabue, T. Lomtadze, P. Mammini, L. Martini, A. Messineo, A. Moggi, C.S. Moon, F. Palla, F. Palmonari, A. Profeti, A. Rizzi, A. Savoy-Navarro, A.T. Serban, P. Spagnolo, F. Raffaelli, P. Squillacioti, R. Tenchini, G. Tonelli, A. Venturi, P.G. Verdini, C. Vernieri
18. **INFN Sezione di Torino and Università di Torino, Torino, ITALY**
M. Costa, D. Dattola, G. Dellacasa, N. Demaria, G. Mazza, E. Migliore, M. Musich, L. Pacher, A. Potenza, A. Rivetti, P. Trapani
19. **CERN, European Organization for Nuclear Research, Geneva, SWITZERLAND**
D. Abbaneo, I. Ahmed, E. Albert, G. Blanchot, J. Daguin, S. Detraz, D. Deyrail, F. Faccio, N. Frank, K. Gill, T. Katopodis, A. Kornmayer, L. Kottelat, A. Koukovinis, S. Mersi, S. Michelis, J. Noite, A. Peisert, J.-F. Pernot, P. Petagna, H. Postema, P. Tropea, J. Troska, A. Tsiros, F. Vasey, B. Verlaet, L. Zwalinski
20. **Paul Scherrer Institut, Villigen, SWITZERLAND**
W. Bertl, W. Erdmann, R. Horisberger, H.-C. Kaestli, D. Kotlinski, U. Langenegger, B. Meier, T. Rohe, S. Streuli

21. **Institute for Particle Physics, ETH Zurich, Zurich, SWITZERLAND**
F. Bachmair, R. Becker, M. Donega, P. Eller, D. Hits, U. Horisberger, U. Roeser, M. Rossini, A. Starodumov, H. P. von Gunten, R. Wallny
22. **Universität Zürich, Zurich, SWITZERLAND**
K. Boesiger, V. Chiochia, B. Kilminster, R. Maier, P. Robmann
23. **National Taiwan University, Taipei, TAIWAN**
P.-H. Chen, C. Dietz, U. Grundler, W.-S. Hou, J.-J. Liao, S.-H. Lin, R.-S. Lu, D. Majumder, X. Shi
24. **University of Bristol, Bristol, UNITED KINGDOM**
J.J. Brooke, D. Cussans, H. Flacher, R. Frazier, J. Goldstein, M. Grimes, G.P. Heath, H.F. Heath, D.M. Newbold
25. **Rutherford Appleton Laboratory, Didcot, UNITED KINGDOM**
K.W. Bell, C. Brew, D.J.A. Cockerill, J.A. Coughlan, K. Harder, S. Harper, E. Olaiya, D. Petyt, C.H. Shepherd-Themistocleous, I.R. Tomalin
26. **Imperial College, London, UNITED KINGDOM**
R. Bainbridge, R. Beuselinck, O. Buchmuller, D. Colling, P. Dauncey, G. Davies, J. Fulcher, D. Futyan, G. Hall, G. Iles, G. Karapostoli, A.M. Magnan, J. Marrouche, J. Nash, A. Nikitenko, M. Pesaresi, M. Pioppi
27. **Brunel University, Uxbridge, UNITED KINGDOM**
J.E. Cole, P.R. Hobson, A. Khan, P. Kyberd, D. Leslie, I.D. Reid, L. Teodorescu
28. **University of Illinois at Chicago, Chicago, Illinois, USA**
M. Adams, C. Gerber, B. Kapustka, D. Strom, P. Turner
29. **University of Colorado at Boulder, Boulder, Colorado, USA**
J. Cumalat, K. Stenson, S.R. Wagner
30. **Fermi National Accelerator Laboratory, Batavia, Illinois, USA**
J. Andresen, J.N. Butler, D. Butler, H.W.K. Cheung, J. Chramowicz, D. Christian, G. Dep-tuch, G. Derylo, H. Gonzalez, J. Howell, U. Joshi, S. Kwan, C.M. Lei, S. Los, M. Matulik, A. Prosser, R. Rivera, P. Tan, L. Uplegger, E. Voirin, J.C. Yun
31. **Johns Hopkins University, Baltimore, Maryland, USA**
A.V. Gritsan, P. Maksimovic, M. Swartz
32. **Kansas State University, Manhattan, Kansas, USA**
A. Ivanov, R. Taylor
33. **The University of Kansas, Lawrence, Kansas, USA**
A. Bean, W. Burg, M. Everhart, J. Herman, D. Noonan, J. Orcutt, C. Pfannenstiehl, J. Sibille, R. Stringer, G. Tinti, J. Worth, R. Young
34. **University of Mississippi, University, Mississippi, USA**
L. Cremaldi, L. Perera, D.A. Sanders, D. Summers
35. **University of Nebraska-Lincoln, Lincoln, Nebraska, USA**
K. Bloom, C. Bravo, A. Dominguez, S. Emmel, C. Fangmeier, B. Farleigh, W. Frederick, J. Kelty, D. Knowlton, J.A. Monroy

36. **Princeton University, Princeton, New Jersey, USA**
B. Harrop, D. Marlow
37. **University of Puerto Rico, Mayaguez, Puerto Rico, USA**
J. Acosta, E. Brownson, J.C. Cuevas, A. M. Lopez, C. Malca, H. Mendez, S. Oliveros, C. Pollack, J. E. Ramirez, J. Siado, I. Vergara
38. **Purdue University, West Lafayette, Indiana, USA**
E. Alagoz, K. Arndt, G. Bolla, D. Bortoletto, M. Bubna, M. Cervantes, I. Christie, Y. Ding, K. Khan, M. Kress, A. Krzywda, G. Lockwood, V. Noe-Kim, I. Shipsey, D. Snyder, J. Sun
39. **Purdue University Calumet, Hammond, Indiana, USA**
N. Parashar
40. **Rice University, Houston, Texas, USA**
K.M. Ecklund, J. Zabel
41. **Rutgers, the State University of New Jersey, Piscataway, New Jersey, USA**
E. Bartz, J.P. Chou, Y. Gershtein, E. Halkiadakis, A. Lath, S. Schnetzer, S. Somalwar, R. Stone
42. **State University of New York at Buffalo, Buffalo, New York, USA**
A. Kharchilava, A. Kumar
43. **Texas A&M University, College Station, Texas, USA**
R. Eusebi, I. Osipenkov, S. Sengupta
44. **University of California, Davis, Davis, California, USA**
M. Chertok, J. Conway, F. Ricci-Tam
45. **University of California, Riverside, Riverside, California, USA**
K. Burt, M.E. Dinardo, F. Giordano, G. Hanson, J. Ellison
46. **Vanderbilt University, Nashville, Tennessee, USA**
W. Johns

12.2 Project Organisation

The Phase 1 Pixel upgrade is a subproject of the overall CMS Tracker Project. Therefore, its organization fits within the general organization of the Tracker project. The general Tracker project organization is shown for reference in Figure 12.1. Names of people holding the different roles are the ones at the time of writing.

In compliance with the CMS Constitution and with the Tracker project Constitution, the Tracker Institution Board is the highest decision-making body in the Tracker Project. The Tracker Project Manager, appointed by the CMS Spokesperson, heads the project and is assisted by two deputies and the Tracker Resource Manager.

A number of Boards oversee, steer, endorse, etc., as appropriate, specific managerial, organizational or technical matters. Among these boards, the one specifically concerned with the management of the Pixel Phase 1 Upgrade project is the **Phase 1 Upgrade Management Board (Phase-1 MB)**.

From the construction organization point of view, the Phase 1 Pixel detector can be subdivided into three main areas:

1. the Forward Pixel (**FPIX**) system, including all in-detector parts, structures and components specific to the end Disks;
2. the Barrel Pixel (**BPIX**) system, including all in-detector parts, structures and components specific to the Barrel;
3. Common Systems and Integration (**CSI**), including all in-detector parts and components which are the same in FPIX or BIX or are however procured through a single common procedure, the off-detector services (such as power supplies and cooling plants) and all the integration interfaces. CSI is also the interface to the CMS Technical Coordination.

The construction activities in the three main areas are each coordinated by a specific **Technical Coordinator**.

This structure is indicated in Figure 12.1. Each Phase 1 Upgrade technical Coordinator coordinates and oversees the actual day-to-day work of different Working Groups and Production Centres, distributed across most of the participating Institutes.

Tracker Organisational Chart

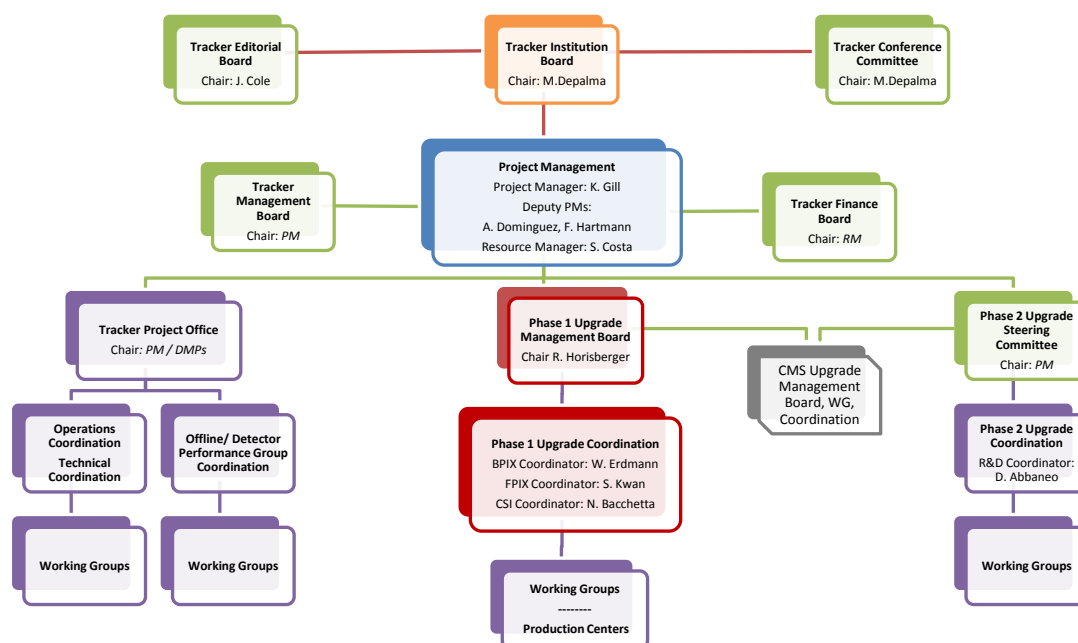


Figure 12.1: Tracker organizational chart.

12.2.1 Phase 1 Upgrade Management Board (Phase-1 MB)

This board evolved from a previously existing (up to January 2011) and now phased out Tracker Upgrade Steering Committee, which had steered the physics studies, simulations, and R&D activities leading to the Pixel-related sections of the CMS Upgrade Technical Proposal. Its members are the link persons to the Funding Agencies (FAs) supporting the construction of the

upgraded Pixel detectors either with financial funds for Materials and Services (M&S), or with manpower available at the home Institutes, or both. This board is completed by a number of *ex-officio* members: the full Tracker Management Team, the Chairman of the Tracker Institution Board, the present Pixel detector Operation Managers, and the CMS Technical Coordinator.

The concept that inspired the composition of this board is that representatives of the main Funding Agencies in the Pixel Phase 1 Upgrade project share a common commitment and responsibility to deliver the upgraded detector. The responsibility for managing the project is shared by these agency representatives and with the Tracker Project Management team through their combined involvement in the Phase-1 MB.

The Phase-1 MB supervises, reviews progress and defines planning and strategy for the Phase-1 Upgrade project; defines and manages the scope, the budget and the milestones of the project, as well as the sharing and responsibilities between different Funding Agencies involved resulting in an internal MoU. The Phase-1 MB meets several times a year, at least during CMS and Tracker weeks. Decisions are taken by consensus whenever possible.

In any important areas where consensus cannot be reached, or where there is a significant impact on the wider Tracker project, the Tracker PM can bring these matters to the Tracker Management Board for resolution.

12.2.2 Phase 1 Upgrade Project Leader

The Chairperson of the Phase-1 MB is selected among the members, by the members themselves (*ex-officio* members do not vote and cannot be selected) and is the *de-facto* Project Leader of the Phase 1 Upgrade subproject within the Tracker project.

The Chairperson represents the project on the CMS Upgrade Project Office. The Chairperson is endorsed by the Tracker PM, Tracker Institutions Board and CMS Upgrade Managers.

The Phase-1 MB Chairperson/Project Leader role is characterized by the following charge and deliverables:

- To lead the Phase-1 MB to define and manage the scope, cost and budget for the pixel upgrade, taking into account the LHC schedule, available resources, and interests of the groups involved.
- To lead the MB to define a set of project milestones and then steer the project to meet them, assuring the necessary flow of resources and information throughout the project.
- To work closely with the Phase-1 BPIX, FPIX and CSI Coordinators to review technical progress; manage the planning and strategy to deal well with problems and opportunities; establish and use appropriate documentation with reliable archiving for all relevant technical specifications of parts and interfaces, QA procedures, QC procedures and logistics.
- To prepare for reviews of important technical, engineering and procurement decisions, normally chaired by CMS Technical Coordination.
- To chair the Phase-1 MB, organize meetings, agendas, objectives, and follow-up with reports to the TIB.
- To work in partnership with the Tracker PM team to assure proper consideration of all decisions, including their impact on the Tracker project as a whole, with appropriate preparation of points for endorsement by the TIB.

- To work closely with the Tracker Resource Manager on all resource-related matters.
- To represent the Tracker Phase-1 Upgrade in the CMS Upgrade Project Office as well as in CMS Management and LHCC meetings.

Last but not least, the Phase-1 MB Chairperson has been responsible for assembling an editorial team and publishing this TDR.

12.2.3 Phase 1 Upgrade Technical Coordination Team

This team is composed of two detector construction Coordinators, one for BPIX, one for FPIX, and the Common Systems and Integration (CSI) Coordinator. These people lead the technical activities within the project. The Coordinators act as a team to ensure that:

- Realistic and detailed plans are prepared.
- Adequate resources and supervision are committed to the different activity lines.
- The planning is consistent with the project milestones, quality objectives and budget.
- Progress is properly monitored across the technical activities in all centres.
- Technical specifications for parts and interfaces between parts of the system are established, well defined, documented and followed.
- QA/QC procedures are established, well defined, documented and followed.
- Information flows properly within the project, to/from the Phase-1 MB and within the technical Coordination team, and that there is a central repository used to organize and archive project documents.

The CSI Coordinator will ensure that the common parts of the upgraded area, which are outside the normal supervision of the FPIX and BPIX Coordinators, are fully supported and properly integrated into the project such that the appropriate solutions are adopted by FPIX and BPIX. The Phase-1 BPIX and FPIX Coordinators, working together with the CSI Coordinator, should ensure that common solutions are implemented wherever it is appropriate.

The Coordinators convene technical steering groups of experts as necessary.

As seen in the global Tracker organizational chart, the Coordinators report to the Phase-1 MB, and the Tracker PM.

12.2.4 Role of the Resource Manager

The Resource Manager of the Tracker project has also the role of Resource Manager of the Phase 1 Upgrade subproject. His/her tasks include:

- Maintaining and updating the subproject Cost Book, starting initially from estimates of costs and funding, and progressively evolving it towards a detailed bookkeeping of actual expenses on one side, and FAs contributions on the other side.
- Elaborating and updating the cost time profile and the cost sharing among FAs.
- Taking care, together with the technical Coordinators and/or with the heads of Working Groups and/or the people responsible of the Production Centres, of procurements for the construction of the upgraded detector; specifically, the Resource Manager is responsible for the tendering process involved in common procurements performed centrally.
- Reporting regularly on construction expenditures to the Phase-1 MB, to the CMS FB, and preparing regular reports for the LHC RRB as required.

12.3 Construction Responsibilities

As already mentioned, the community committed to share the effort of constructing the upgraded Pixel detector is almost the size of the entire current full-Tracker community. Over the last few years, through a series of meetings and discussions of different official managerial boards within the Tracker and technical working groups, a responsibility sharing model has been outlined which stems from historical involvements in the construction of the present Pixel detector but has expanded into larger communities and consortia similar to the ones which successfully carried out the construction of the present Strip Tracker.

We now describe the sharing of responsibility for *delivery* of the different parts of the detector, discussing its historical evolution and some rationale behind it.

12.3.1 FPIX

The FPIX will be built in the USA, like the current Forward Pixel. The upgraded FPIX comprises 672 modules. The bumpbonding of Sensors to ROCs will be outsourced to commercial companies.

Concerning the production infrastructure, it will be the responsibility of the USA FAs to setup a network of Production Centres in the USA: modules will be assembled at Purdue University (infrastructure already exists) and University of Nebraska. Final assembly of the modules onto the half disks will be performed at Fermilab, which is basically already fully equipped since the production of the existing detector. Commissioning of each complete half cylinder will be done at Fermilab and then at the Tracker Integration Facility (TIF, in Building 186 at CERN).

12.3.2 BPIX

The BPIX, which for the present detector was under the full responsibility of a Swiss Consortium composed of PSI, ETH and the University of Zürich, will now be shared among four Europe-based consortia, one of which involves also Taiwan. Overall the upgraded BPIX comprises 1184 modules, plus additional 96 modules in the replacement Layer 1 (total 1280 modules to be built)

The mechanical structure, including the on-detector cooling tubes, the Supply Tube, and almost all services inside the latter, will be the responsibility of the Swiss Consortium, with specific parts or phases of the construction taking place in each of the three Institutes of the Zürich area, and with just a few specific components provided by other Countries/Agencies.

In addition, the Swiss Consortium will perform the module construction for Layer 1, Layer 2, and for a replacement of Layer 1.

The module construction for one-half Layer 3 will be performed in Italy by the INFN Consortium, involving five INFN Sections located at five Italian Universities.

The modules for the other one-half Layer 3 will be constructed at CERN by a Consortium composed of CERN itself, Taiwan and Finland.

The module construction for Layer 4 will be performed in Germany by a Consortium composed of DESY and several German Institutes funded by BMBF.

In the above-outlined sharing of BPIX module construction, the relevant quantities of module components are, as a general rule, procured at the expenses of the concerned Consortia, although the procurement processes may be handled at a central site, typically CERN, in a coordinated way.

Concerning the production infrastructure:

- The Swiss Production Centre is distributed across the three participating Institutes, basically already exists and is already fully equipped from the production of the existing detector. PSI will mainly concentrate on the construction of modules and services and on the Barrel mechanics, University of Zürich on the Supply Tube mechanical structures, ETH on testing equipment and operations.
- The INFN Production Centre will also be distributed, across five sites (Pisa, Padova, Catania, Bari and Perugia), with each specific construction operation taking place at a single site.
- The Production Centre of the CERN/Taiwan/Finland Consortium will be at CERN.
- The German Production Centre will consist of multiple laboratories as well: on the DESY Campus, in Karlsruhe and in Aachen. The module construction will take place at DESY for one half of Layer 4 and in Karlsruhe for the other half.

The internal organization of each Consortium derives from a number of considerations, some of which apply in differently manner to each Consortium. Mainly, the exploitation of existing infrastructure and expertise, the specific interests of groups for developing new expertise on particular items, and the minimization of overall construction costs (not just the M&S ones) for a Funding Agency comparing costs for moving parts from one site to another with costs for moving personnel from one site to another.

12.3.3 Common Systems

The Common Systems include a variety of detector, and even module, components which are identical in FPIX or BPIX, or are anyway procured through a common procedure, as well as the services "external" to the sensitive volume of the detector and common to its two partitions.

As a general approach, the common module components such as ROC and TBM wafers will be procured with a common initiative and distributed to the different laboratories as necessary, both in the USA and in Europe, and their cost will be shared among FAs proportionally to the fraction of modules of assigned to each Consortium.

The needed modification of the current power supplies is being developed jointly by the Swiss Consortium and the Aachen group, but will be paid for by most of the FAs funding this project. The DC-DC converters, which are a novel part of the power system with respect to the existing detector, will be the responsibility of the Groups who have developed them. These include the Aachen (funded by BMBF) and CERN groups. A contribution by the Swiss Consortium is also envisaged. The development of new power supplies will be again followed jointly by the Swiss Consortium and the Aachen group and if a replacement is needed it would be paid by most of the FAs funding this project.

The optical links will be taken care of and paid for for the most part by CERN, and for a minor part by the USA.

The DAQ system cards for the upgraded detector will be the responsibility of the UK. Austria will provide an interim DAQ solution for the FPIX pilot blade system. France will be involved in the DAQ software development. All have expertise and technical interest in this item from the existing Tracker.

Other major off-detector general services, namely the cooling system, interlocks and monitoring system, will be provided by CERN, but with a financial contribution by France which is

involved in the system design and will contribute to its assembly and commissioning.

A dedicated infrastructure for commissioning the detector during and after final integration at the Tracker Integration Facility (TIF, in Building 186 at CERN) will also be the main responsibility of CERN, with a substantial contribution by Taiwan and a small contribution by France for the cooling system at TIF.

Costs for final detector installation inside CMS will be paid in part by CERN and in part by the Swiss Consortium, e.g. through the development and construction of dedicated tools.

12.3.4 Institutional interests

In Figure 12.2 we show a synoptic view of the interests of the different participating Institutes on specific construction activities. Responsibility for the *delivery* of a given part of the detector or a given operation rests with the individual Institutes, whilst financial responsibility for the *procurement* of the parts needed to carry out any construction activity rests with the Funding Agencies, not the individual Institutes.

		Sensor testing	ROC wafer testing	TBM testing	HDI assembly and wirebonding	HDI testing	Bump bonding and bare module testing	Module assembly and wirebonding	Module testing	Mech structure	Supply Tube	Service Cylinder	System assembly	System testing	Pilot Blade System	Construction Database	Test Beams	Cooling System	DC-DC converters	Power Supply qualification	Data links	FED/FEC	Pixel DAQ sw	Interlocks & Monitoring	Commissioning at TIF and PS	Installation	Dev beyond Phase 1: Sensors	Dev beyond Phase 1: Electronics
Austria	HEPHY														X													
Finland	HELSINKI-HIP						H-L3																					
France	STRASBOURG																					X			X			
France	LVON																	X					X		X			
Germany	AACHEN-1																		X									
Germany	DESY						H-L4	H-L4	H-L4				L4	L4						X								
Germany	HAMBURG-UNIV	H-L4			H-L4	H-L4	H-L4	H-L4	H-L4																			
Germany	KARLSRUHE-IEKP	H-L4			H-L4	H-L4	H-L4	H-L4	H-L4																			
Italy	BARI							H-L3									X											
Italy	CATANIA				L3	L3																						
Italy	FIRENZE						H-L3																					
Italy	GENOVA																										X	
Italy	MILANO-BICOCCA																									X		
Italy	PADOVA		BPIX						H-L3								X											
Italy	PERUGIA								H-L3								X											
Italy	PISA	H-L3					H-L3										X											X
Italy	TORINO																X											X
Switzerland	CERN	H-L3						H-L3	H-L3								X	X	X		X			X	X	X	X	
Switzerland	PSI	L12+1	BPIX		L12+1	L12+1	L12+1	L12+1		BPIX										X			X		BPIX	BPIX		
Switzerland	ZURICH-ETH								L12+1								X						X		BPIX	BPIX		
Switzerland	ZURICH-UNIV									BPIX															BPIX	BPIX		
Taiwan	TAIPEI-NTU						H-L3	H-L3									X	X							X			
United Kingdom	BRISTOL																						X					
United Kingdom	RAL																						X					
United Kingdom	LONDON-IC																						X					
United Kingdom	BRUNEL																						X					
USA	CHICAGO-UIC				FPIX				FPIX								X											
USA	COLORADO																		FPIX						FPIX			
USA	FERMILAB	FPIX	FPIX	FPIX	FPIX	FPIX	FPIX			FPIX		FPIX	FPIX	FPIX	X	X	X		FPIX	FPIX	X				FPIX	FPIX	X	X
USA	JOHNS-HOPKINS																											
USA	KANSAS-STATE			X																		X	X					
USA	KANSAS-UNIV		X			FPIX									X													
USA	MISSISSIPPI																											
USA	NEBRASKA						FPIX	FPIX							X													
USA	PRINCETON																								FPIX			
USA	PUERTO_RICO														X											FPIX		
USA	PURDUE	FPIX					FPIX	FPIX	FPIX		FPIX					X	X	FPIX							FPIX	FPIX		
USA	PURDUE-CALUMET																											
USA	RICE																							FPIX				
USA	RUTGERS			X																			FPIX		FPIX			
USA	SUNY-BUFFALO																											
USA	TEXAS-TAMU																X								FPIX			
USA	UCDAVIS																									FPIX		
USA	UCRIVERSIDE												FPIX	FPIX	X										FPIX	FPIX		
USA	VANDERBILT														X													

Legend:

- X=interest in this item
- FPIX=interest in this item for FPIX
- BPIX=interest in this item for the entire BPIX
- L12+1=interest in this item for BPIX Layer1, Layer2 and replacement Layer1
- L3=interest in this item for BPIX Layer3
- H-L3=interest in this item for half BPIX Layer3
- L4=interest in this item for BPIX Layer4
- H-L4=interest in this item for half BPIX Layer4

Figure 12.2: Preliminary interests of participating Institutes on construction deliverables

In addition to the listed construction activities, many Institutes are involved in software tasks

to which the notion of M&S cost does not apply, namely in physics performance studies and simulations.

12.4 Construction Schedule

The construction schedule, up to installation, is shown at a glance in Table 12.1 and then with finer detail in Figures 12.3, 12.4 and 12.5, for the three areas (FPIX, BPIX, CSI) respectively.

This schedule aims at being ready for installation during a technical stop around the turn of the year 2016-2017.

Milestone	Date
Technical Design Report	9/2012
Start sensor production	10/2013
Submission of final ROC	10/2013
Re-installation of present detector and pilot blades	5/2014
Start of module production	5/2014
CO ₂ plant installed at Point 5	8/2014
uTCA FED readout of pilot blades	4/2015
Start of detector assembly and testing	6/2015
End of module production	2/2016
Pre-installation slice tests at CERN	6/2016
Ready for installation	9/2016

Table 12.1: Major milestones for the Pixel upgrade project

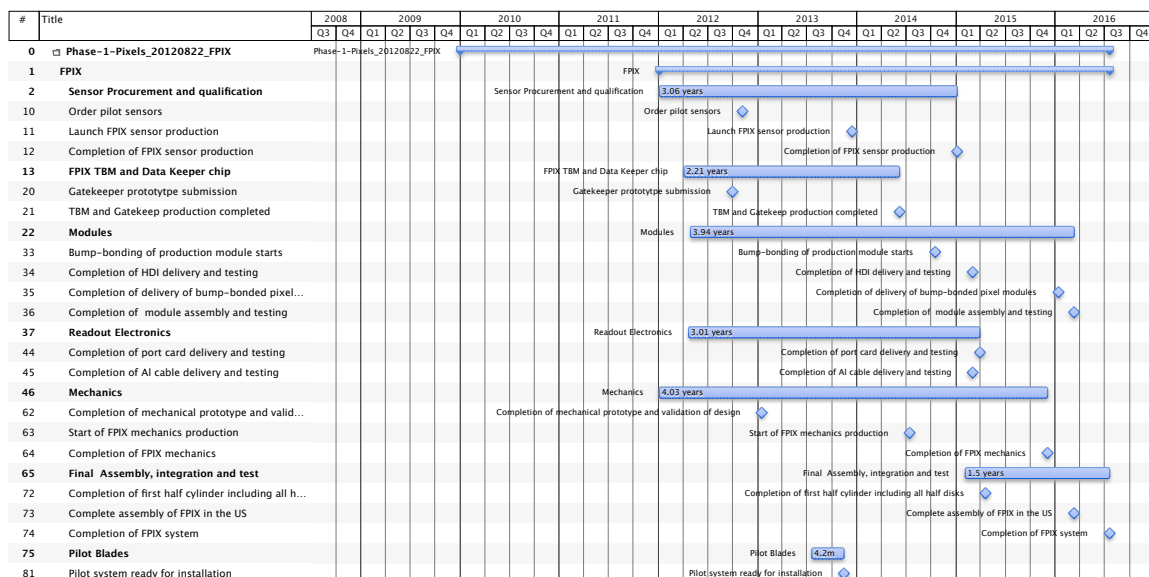


Figure 12.3: Construction schedule for FPIX.

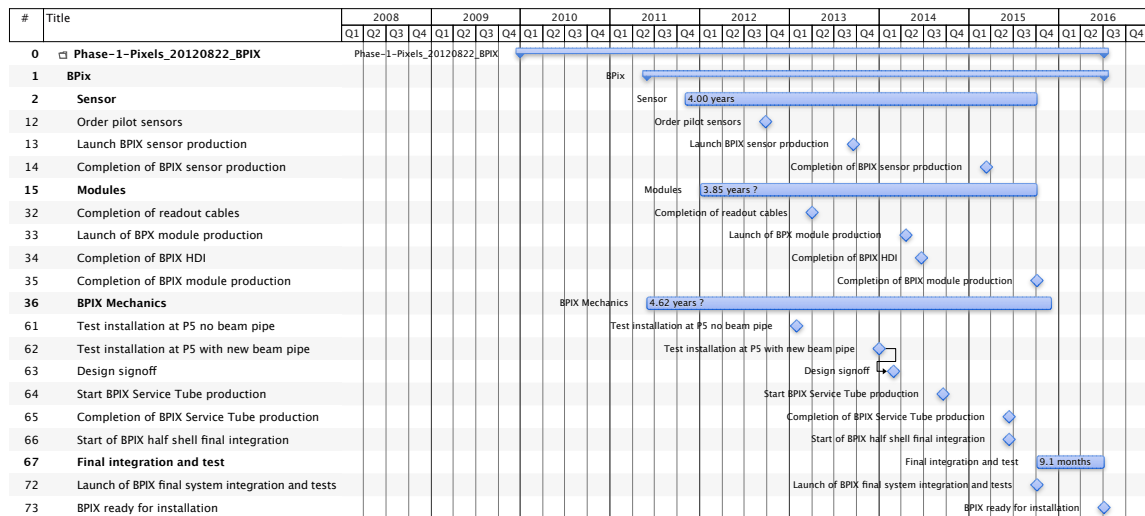


Figure 12.4: Construction schedule for BPIX.

12.5 Costs

12.5.1 Cost Estimate

The detailed cost estimate of the Phase-1 upgraded Pixel detector has been established, with about 200 individual items in the Cost Book, on four levels of a Work Breakdown Structure (WBS).

It should be noted that the cost estimates are for M&S only and concern only items which fall into the allowed expense group 4.6.3 as defined by the CORE (LHCC Cost Review Committee) and recently reformulated by the CMS Resource Manager specifically for the CMS Upgrade project as follows:

1. Final prototype or pre-production fabrication required to validate a final design or product quality, prior to production.
2. Engineering costs incurred during production at a vendor or contractor, not at a CMS member Institution.
3. Production fabrication and construction costs, including QA and system testing during the assembly process.
4. Transportation costs, integration and installation.

All quotes and estimates have been collected in calendar years 2010 and 2011 and verified around the beginning of 2012. Quotes and estimates have been provided in CHF, EUR, or USD, depending on the geographical location of Institutes, companies, vendors, or suppliers. In this chapter, all monetary values are expressed in CHF. The following conventional exchange rates have been used to convert EUR and USD to CHF:

- 1 USD = 1.0 CHF
- 1 EUR = 1.2 CHF

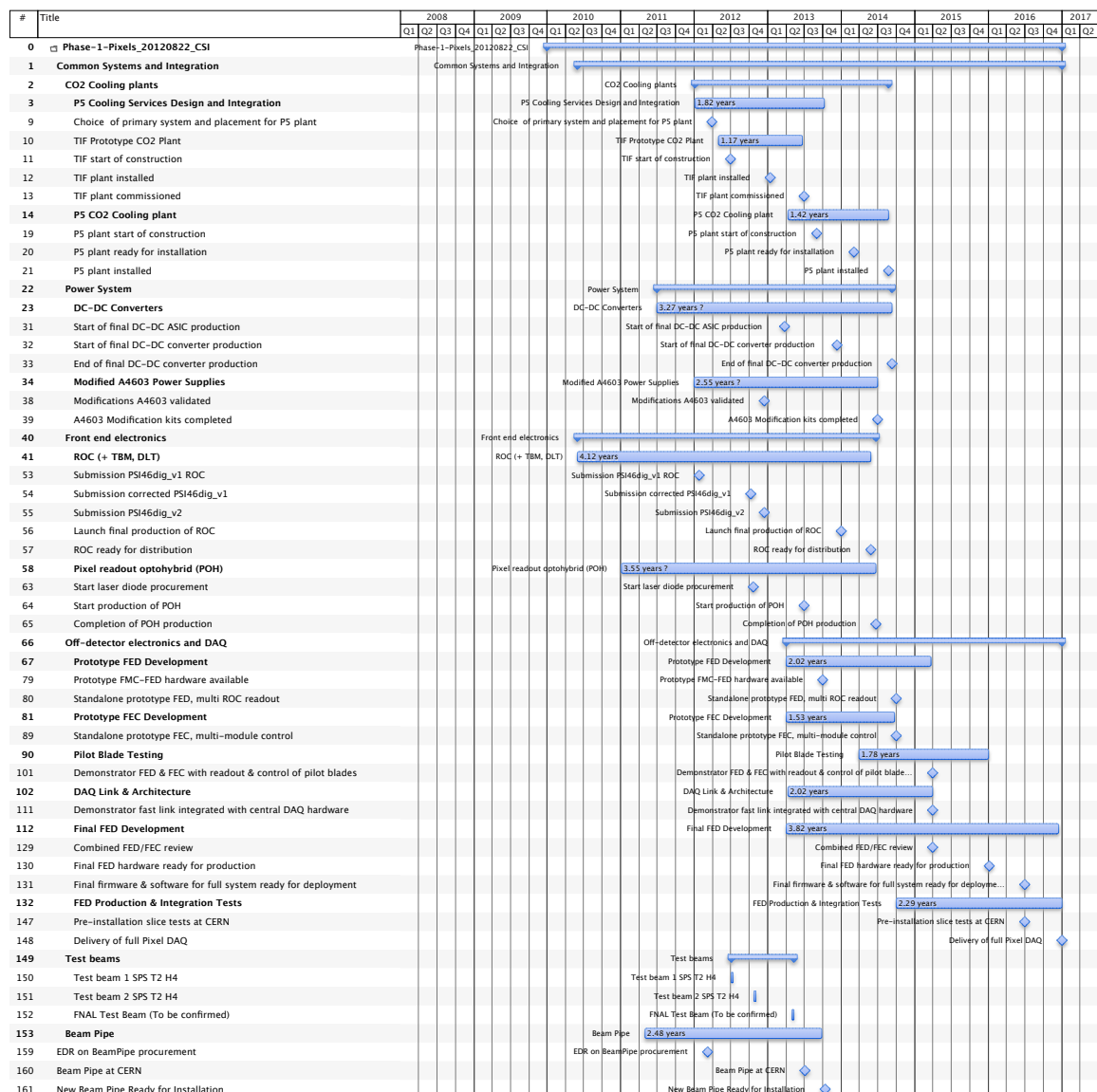


Figure 12.5: Construction schedule for common systems and integration.

As a general procedure, the cost of each individual item is estimated by using a unit cost and an estimate of the quantity needed. The quantity is the sum of: the actual quantity to be mounted on the detector; the additional quantity, varying from item to item, needed to compensate for expected yields of certain fabrication operations; the number of spares estimated as needed to a) safely overcome the assembly, integration, commissioning, and installation stages, when handling of parts may result into accidental damage of them, thus needing immediate replacement, and b) leave in the end on the shelf about 5% spares available for later maintenance of the detector.

Following CMS rules and guidelines, neither general contingency (for unexpected or unforeseen technical flaws or major accidents) nor financial contingency (for inflation, exchange rate variations, or general evolution of economy or market conditions which may alter the cost of procured materials and components) have been included in the estimates. For these issues, in case of cost increase, we will have no other choice than turning to CMS for help or, ultimately,

to the FAs with additional, *ad-hoc* requests for further funding.

The quality of the individual item cost estimates ranges from certain (i.e. a completed order – applies to some final prototypes and/or production centre setups) down to educated guesses. Whenever available, actual quotes already obtained from vendors and/or companies have been used. In some cases, educated interpolation of market surveys not yet evolved to the stage of a formal quote has been used. In other cases, careful extrapolations from similar parts of the existing detector were carried out by the experts, or groups thereof, who took care of the corresponding parts of the existing detectors.

In all cases, the uncertainty in the *unit* cost estimate of each individual item, in the currency in which it was provided, is believed to be quite small, not more than 5%. This because the quotes should be rather firm, but also the estimates based on extrapolations have been done so carefully that we are confident their uncertainty is not larger than 5%. However, the quantity needed may fluctuate a little more on some items for which the final technical solution has not been frozen yet. Furthermore, we cannot guarantee the stability of any costs against fluctuations of currency exchange rates or against market fluctuations for the base materials/components.

With these caveats in mind, we now proceed to show the estimated cost of the project. The global cost of the Pixel Phase 1 Upgrade project is estimated to be **17'100 kCHF** at the time of writing.

A breakdown of the global cost down to the second WBS level, is presented in Table 12.2.

Area	Item	Cost (kCHF)
FPIX	Detectors (incl. Bumpbonding)	2'224
	Module Electronics	276
	Module Mechanics	424
	Service Cylinder	221
	Module Production, Testing, Integration	222
FPIX Total		3'368
BPIX	Detectors (incl. Bumpbonding)	4'892
	Module Electronics	764
	Module Mechanics	314
	Supply Tube	704
	Module Production, Testing, Integration	555
BPIX Total		7'229
CSI	Cooling System	1'030
	Power System	1'110
	Readout Electronics and Data Links	2'415
	DAQ	900
	Interlocks & Monitoring	105
	Commissioning hw @TIF	616
	Installation @P5	147
	Transportation	180
CSI Total		6'503
Grand Total		17'100

Table 12.2: Estimated cost of the project

The fact that the BPIX costs nearly twice the FPIX is not a surprise, as BPIX has about twice

the number of modules of FPIX and the two areas conventionally contain mainly items whose quantity or dimensions scale with the number of modules. Systems and operations which do not scale linearly with the number of modules, such as for example the cooling plant, are in fact included in the CSI partition.

For both FPIX and BPIX areas, the "Detectors" costs include the Silicon sensor wafers, masks, prototypes for bump bonding qualification and, as indicated, the bumpbonding of Sensors to ROCs, but not the ROCs themselves. The main cost drivers are the sensor wafers and bump-bonding, while masks and prototypes are minor items costwise.

ROCs are included in the "Readout Electronics and Data Links" item along with TBMs, optical links (lasers, transmitters, receivers, transceivers) and fibers. The main cost drivers here are the optical links, followed by ROCs.

"Module Electronics" items include the HDI and the connector + cable connecting the module to power, control and readout units. This item's cost is dominated by the HDI.

Concerning the "Power System", about 2/3 of this item's cost refers to the possible replacement with new units after LS2, should this be eventually needed, while the initial modification of the present ones is expected to cost only 134 kCHF. The DC-DC converters account for ~25%. Regarding the "Commissioning hardware at TIF", more than 2/3 of the cost are due to the cooling system.

Any large production and major procurement will be preceded by dedicated Engineering Design Review and/or Procurement Readiness Review.

12.5.2 Expected Funding and Cost Sharing

The global cost of the project is expected to be borne by all institutions participating in the project.

Discussions with the Funding Agencies are ongoing to define the sharing of the total project cost. The commitments of each Funding Agency will be formalised in a signed Memorandum of Understanding (MoU).

Appendix A

Evolution of Pixel Detector

A.1 Introduction and Motivations

The Phase 1 pixel detector upgrade should provide good performance for the whole of Phase 1 operation, until LS3 when a new Pixel detector for High Luminosity (HL) LHC will be installed. To meet the challenges coming from the increasing performance of the machine, we plan to develop a new pixel detector that will be needed for the HL-LHC period, where an instantaneous luminosity of $5 \times 10^{34} \text{ cm}^{-2}\text{s}^{-1}$, a pile-up of 100 (25 ns) and an integrated luminosity of 270 fb^{-1} per year are foreseen. The most important areas of improvement that have been identified are:

- Increased radiation hardness of inner layers;
- Improved rate capability of the ROCs;
- Increased granularity, using smaller pixels;
- New trigger functionalities.

We have a 5-year development plan to focus on the critical technologies: the sensor, the ROC and also the complete pixel system. While this plan aims at establishing the choices for the HL-LHC pixel detector, it is also a path for continuous evolution of the pixel detector. Some of these developments could also possibly be used earlier, replacing the inner parts of the Phase 1 pixel detector, to extend its lifetime and/or enhance its performance, should this be required.

The main challenge for the sensor technology is the radiation hardness related to cumulative effects, linearly dependent on total integrated luminosity. Preliminary estimates based on present data give a fluence for the inner barrel layer above $10^{16} n_{eq}(1 \text{ MeV})/\text{cm}^2$ for ten years of HL-LHC at a total integrated luminosity of about 3000 fb^{-1} . R&D work is ongoing on three sensors technologies, namely: planar silicon, 3D silicon and diamonds. Development of monolithic pixel sensors on standard CMOS process is also underway: the qualification of these devices is still in progress, and therefore this option will not be described in further details in the following.

One of the main challenge for the pixel Read-Out Chip (ROC) is to record the maximum instantaneous luminosity. The ROC has to record with high efficiency ($>99\%$) signals at very high rate and store them for a time determined by the trigger latency. The flux of particles in the first barrel layer is expected to be higher than $500 \text{ MHz}/\text{cm}^2$. The trigger latency is expected to be at about $6.4 \mu\text{s}$, more than one and a half times the present value. Another challenge is to read out big events, considering a possible pile-up of 100 or higher, at a L1 trigger rate of at least 100 kHz . A new ROC must be capable of working with a significantly smaller threshold than present 3500 e^- , since all sensors featuring high radiation hardness are characterized by smaller signals.

At HL-LHC the CMS L1 trigger rates are expected to increase due to reduced rejection power at increased pile up. It will be important to combine calorimeter information with tracking information at a trigger level before the HLT. If a new pixel readout chip can be developed that supports fast “level 0” readout of parts of the pixel detector (a region of interest), this information may significantly improve the L1 electron/tau triggers and to multijet triggers at very high instantaneous luminosity. Preliminary studies show that multijet triggers can benefit from pixel information already with only one pixel layer.

Very high luminosity operation of the LHC involves tracking in dense jets, and two-track separation performance becomes very important. Increasing the granularity of the pixel detector allows an improvement of two-track separation. In particular, with the present detector, the b-tagging efficiency is limited by cluster merging in the high energy tail (b jets of a few hundred GeV and above) and becomes quite poor for jets produced in the decays of multi-TeV final states. Improving this limitation is a main goal for the high luminosity operation, which can be achieved implementing smaller pixel size in a suitably optimized sensor.

A.2 Sensor Development

A variety of solutions have been pursued to increase substantially the radiation hardness of sensors with respect to n-on-n silicon sensors foreseen for the Phase 1 pixel upgrade. These include diamond sensors, 3D silicon sensors, magnetic-Czochralski (MCZ) planar silicon detectors, epitaxial, p-type silicon wafers, and thin planar silicon detectors. These sensors, if proven to be practical, will be a major improvement for the lifetime of the inner parts of the pixel detector.

The current common understanding [76] shows that planar sensors are basically good up to $2 \times 10^{15} \text{ n}_{eq}(1 \text{ MeV})/\text{cm}^2$, while beyond this new materials or sensor concepts are interesting. 3D detectors offer a shorter collection distance that mitigates the limiting effect of charge trapping. Nevertheless, 3D devices have higher capacitance and are also insensitive to magnetic field [77] and the detector resolution in this case is determined by the track incidence angle, pixel size, and effective threshold. Diamond offers the advantage of small leakage current and lower dielectric constant, thus reducing the electronic noise, with the disadvantage of a smaller signal.

A.2.1 Thin Planar Sensors

Thinner sensors together with smaller pixel cell dimensions, will greatly moderate the problem of cluster merging. A ROC chip with a lower detection threshold also mitigates the loss of signal from the trapping of carriers and the overall radiation tolerance will improve. With reduced detector thickness, the carrier drift path is reduced, resulting in shorter drift times at constant bias and less carrier trapping, mitigating the reduction of signal due radiation damage.

Optimal $r\phi$ resolution is achieved when the pixel dimension is comparable to the Lorentz width, implying that optimal segmentation depends on sensor thickness. Radiation damage plays a role in the “breakage” of clusters at high rapidity where tracks traverse the pixel cells along the z (beam axis) direction producing long clusters. These clusters can “break” into separate clusters as more charge is lost. Decreasing the ratio of thickness to the pixel cell dimension in z helps limiting cluster breakage.

The PIXELAV [78] simulation was used to model data taken in the 2003-2005 CERN beam tests of pixel sensors irradiated at fluences up to $1.2 \times 10^{15} \text{ n}_{eq}(1 \text{ MeV})/\text{cm}^2$ and is currently used to generate information for the CMS pixel reconstruction algorithms. Linear but conservative extrapolations allow tuning of sensor thickness and cell size parameters vs. voltage and chip

parameters (e.g. threshold). Studies were done for two examples, with a low ROC threshold (1000 e^-) and a $100\text{ }\mu\text{m}$ z pixel dimension for a thickness of $220\text{ }\mu\text{m}$ and $100\text{ }\mu\text{m}$. Results are shown in figure A.1. The effect of radiation damage on a pixel geometry of $(75 \times 100 \times$

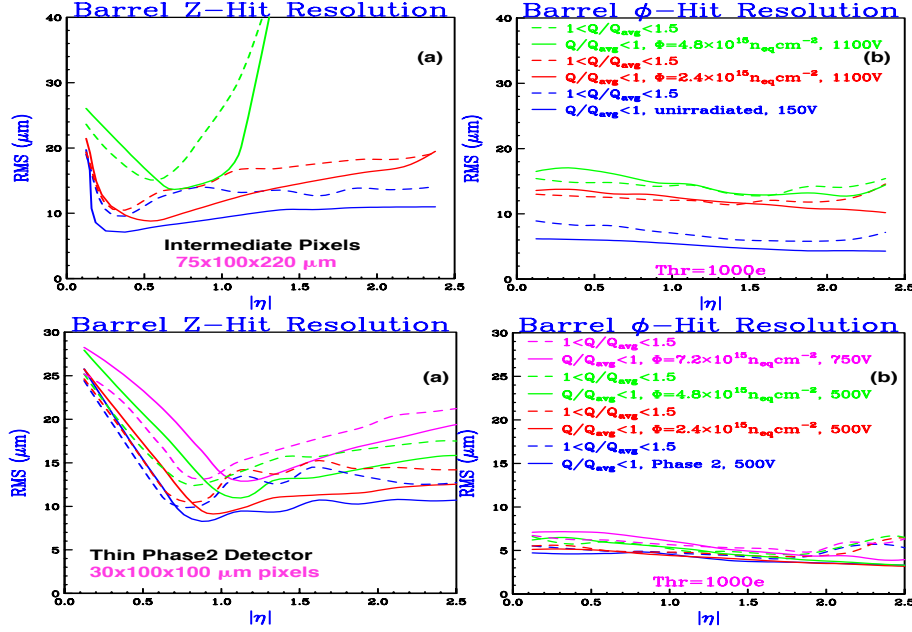


Figure A.1: Global-z (left) and azimuthal (right) resolution for the planar silicon sensors with $(30 \times 100 \times 100)\text{ }\mu\text{m}^3$ (upper plots) and $(75 \times 100 \times 220)\text{ }\mu\text{m}^3$ (lower plots) cells coupled to a low threshold ROC before and after irradiation.

$220\text{ }\mu\text{m}^3$ cell) is qualitatively similar to the current pixel geometry. This detector would still function at $2.4 \times 10^{15}\text{ n}_{eq}(1\text{ MeV})/\text{cm}^2$ with a loss of about 50% in resolution. The poor global-z resolution high-rapidity seen at $4.8 \times 10^{15}\text{ n}_{eq}(1\text{ MeV})/\text{cm}^2$ is evidence of cluster breakage. The thin geometry $(30 \times 100 \times 100)\text{ }\mu\text{m}^3$ cell) maintains instead good resolution up to the largest fluence.

In general, the thin planar detector concept is quite attractive if the threshold of the readout chip can be reduced to about 1000 e^- . Final parameters need to be established by simulations and real sensor beam test studies.

A.2.2 3D Pixel Sensors

Since 2010, CMS has an active 3D R&D program with several vendors and different geometry configurations. We received single-chip devices from SINTEF, FBK, and CNM. SINTEF fabricates 3D sensors with an active edge, manufactured using support wafers. The SINTEF sensors have both the n^+ (readout) and p^+ (ohmic) electrodes etched from the same side and penetrating through the entire wafer thickness. Double side Double Type Column (3D-DDTC) devices have been developed independently at FBK and CNM. They have n^+ and p^+ electrodes etched from the front and backside of the wafer respectively. Both electrode types completely pass through the silicon bulk.

Different pixel configurations were designed and manufactured, each of them compatible with the existing CMS pixel ROCs. The pixel configurations can have one (1E), two (2E), or four (4E) n-type electrodes per pixel. SINTEF has produced 2E and 4E sensors, while FBK and CNM have manufactured all types. The distance between n-type and p-type electrodes is of

great importance since it affects parameters such as capacitance and noise, depletion voltage and breakdown, charge collection, and radiation hardness. The inter-electrode distances in the 1E, 2E, and 4E configurations are $90\text{ }\mu\text{m}$, $62.5\text{ }\mu\text{m}$, and $45\text{ }\mu\text{m}$, respectively. The sensor thickness varies between 200 and $230\text{ }\mu\text{m}$. A thorough simulation [77], [79], [80] of all devices has been performed with the Synopsys TCAD. The sensors are diced and bump bonded to the CMS pixel ROC of the type PSI46v2 at IZM (Germany) and SELEX (Italy). The bump bonded sensors, assembled at Fermilab, Purdue University, and INFN Torino, have been irradiated.

Several SINTEF, CNM and FBK sensors with standard guard rings and with different electrode configurations were characterized with a ^{90}Sr radioactive source and then tested at Fermilab with a proton beam of $120\text{ GeV}/c$. Data were taken for various values of depletion voltages, detection thresholds, temperatures and angles with respect to the beam. Some of these devices were irradiated at Los Alamos National Laboratory (USA) with 800 MeV protons at fluences up to $5 \times 10^{15}\text{ n}_{eq}(1\text{ MeV})/\text{cm}^2$ and re-tested. The data analysis is presently ongoing. In Figure A.2,

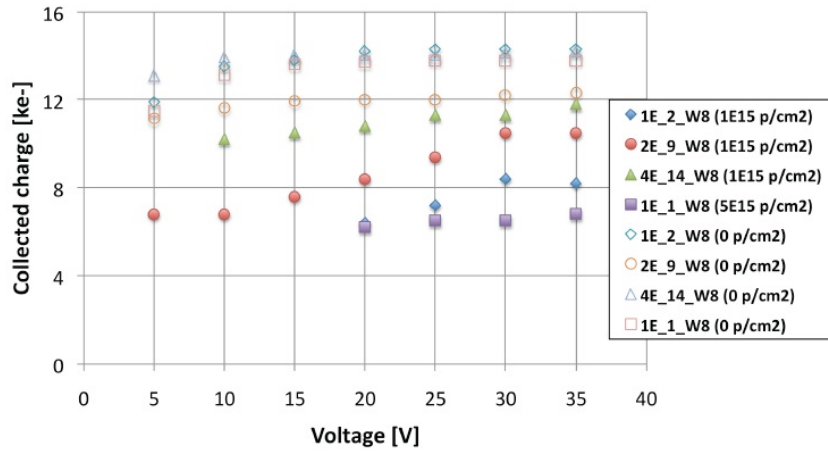


Figure A.2: Collected charge versus voltage for FBK 1E, 2E and 4E devices before and after irradiation.

we show preliminary measurements of collected charge as a function of bias voltage for the FBK sensors before and after irradiation. These devices are about $200\text{ }\mu\text{m}$ thick and have a depletion voltage lower than 10 V . The measurements show that we can collect almost 8000 e^- after an irradiation of $5 \times 10^{15}\text{ p}/\text{cm}^2$ by applying only 20 V . Operating the sensor at such low voltage is attractive, as it lowers the requirements on the power and cooling systems, and offers some potential for reducing the amount of inactive material as well.

A.2.3 Diamond

Diamond is a promising candidate for a highly radiation tolerant sensor for a pixel detector. Chemical Vapor Deposition (CVD) diamond sensors have been studied for about 20 years as extremely radiation hard tracking detectors. The quality of diamond sensors, as measured by their Charge Collection Distance (CCD), has improved tremendously. Mono-crystal sensors, which have essentially full charge collection (CCD thickness of sensor), are now a viable choice for some tracking applications, such as the CMS Pixel Luminosity Telescope (PLT).

Currently, the size of mono-crystal diamond is limited to $8 \times 8\text{ mm}^2$, about the size of a single PSI46 ROC. On the other hand, large size polycrystalline diamond module (e.g. a 2×8 module) is available. The best product on the market these days for polycrystalline diamond is $750\text{ }\mu\text{m}$ thickness with a $\text{CCD} > 250\text{ }\mu\text{m}$ (which gives a signal of $\sim 9000\text{ e}^-$). Both silicon and

carbon have a max in NIEL for neutrons at 25 MeV (170 MeV mb and 17 MeV mb, respectively) and large NIEL for protons at this energy (350 MeV mb and 52 MeV mb). It appears as if the charge loss due to irradiation is about a factor of 7-10 between Si and C across the spectrum. This means that the basic detecting performance of the sensor, expressed in CCD, deteriorates in diamond at a much slower rate than in silicon. Since the ionization released per radiation length by a MIP is a factor 2 larger in silicon, the signals detected by both sensors end up to be roughly comparable at doses around $10^{16} \text{ n}_{eq}(1 \text{ MeV})/\text{cm}^2$ as long as one can keep the silicon over-depleted. At this point, the additional advantages presented by diamond become decisive: on one side, the negligible leakage current, practically independent from the absorbed dose, and a factor two smaller capacitance of pixels (factor two smaller dielectric constant) translate into a superior S/N ratio. The high thermal conductivity can be exploited to directly cool the front-end electronics thus reducing the amount of material in the detector. Furthermore, diamond sensors can be safely operated at room temperature and, because of the higher carrier mobility, much faster signals can be delivered to the preamplifiers. In a strong magnetic field, the tiny leakage current is further reduced. The CMS PLT group has done tests of mono-crystal diamond in a magnetic field. Based on their results, one would expect a Lorentz angle of $13.4^\circ \pm 2.1^\circ$ in a 4 T field with an applied bias of $1 \text{ V}/\mu\text{m}$. Recent tests on irradiated sam-

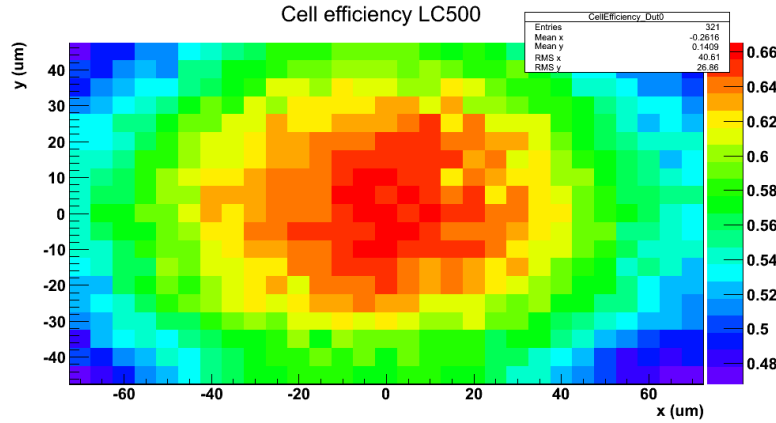


Figure A.3: Diamond detection efficiency as a function of the proton impact point within the $100 \times 150 \mu\text{m}^2$ pixel cell and current ROC: low efficiency due to the high threshold (about 2500 e^-)

ples have demonstrated that after $2 \times 10^{16} \text{ n}_{eq}(1 \text{ MeV})/\text{cm}^2$, diamond still collects more than 30% of its initial MIP signal. Several diamond pixel detectors, including large diamond pixel modules, have already been built and successfully tested with ATLAS or CMS readout chips. The performance of the pixel detector was recently tested at the Fermilab test-beam facility using a polycrystalline diamond with $500 \mu\text{m}$ thickness and a CCD around $200 \mu\text{m}$ at 500 V bias, bonded to the PSI46v2 ROC with a threshold setting of $\sim 2500 \text{ e}^-$. The detecting efficiency for normally incident 120 GeV protons on the detector is plotted in Figure A.3 as a function of X and Y-coordinates of the proton impact point within the pixel cells. The efficiency decreases moving from the centre and reaches its minimum at the cell corners. The low detection efficiency is due to the threshold-cut, which becomes even more important toward the edges just because the fraction of proton-induced signal shared with the nearby cells increases. With a lower threshold these effects will practically vanish or eventually be confined in a very small region near the corners. Recent results obtained with a low threshold of 1500 e^- (using FEI4 chip for ATLAS IBL[81]) show that order of 97% detection efficiencies can be achieved with polycrystalline sensors.

A.3 Trigger Studies

Studies of pixel detector contributions to the L1 trigger have started very recently. These early studies are nevertheless very useful to understand what capabilities can be required from the detector and the front-end electronics. Two different approaches have been investigated for a L1 trigger based on pixels to evaluate the possible impact on the design of the ROC.

The first scheme requires a Level-0 (L0) trigger from the calorimeter system that selects a fraction of the pixel detector to search for clusters to build up a L1 trigger. A second approach is based on self-triggered pixel chips, which detect nearby clusters of pixels from tracks coming from the same origin. In both cases the cluster size contains important information, especially along the z -direction since it is proportional to the tangent of the track dip angle. Shallow tracks coming from distant vertices result in larger clusters with respect to those tracks originating near-by. Similarly, tracks coming from the same vertex show a similar pattern along z , and this could be used for track isolation at L1. A desirable feature of a new ROC is to include cluster position and dimensions in the fast trigger readout.

A.4 Readout Chip

A new pixel ROC will be required to match the pixel size of a new pixel detector and cope with the hit rates expected for the high luminosity running of the LHC. The choice of pixel size is a delicate optimization between general physics requirements (required resolution, multiple scattering, etc.), the pixel sensor (segmentation, collected signal, radiation damage, etc.), bump bonding technology, and what can be implemented in IC technologies available to our community. Initial studies indicate that a pixel size of $\sim 50 \mu\text{m} \times 100 \mu\text{m}$ could be a good compromise in this optimization with an option of using smaller pixels (e.g. $50 \mu\text{m} \times 50 \mu\text{m}$ or equivalent pixel area).

Preliminary studies of the particle and pixel rates for these two pixel sizes are indicated in Figure A.4 for a 2D planar sensor in the inner most layer (highest rates) for different options of sensor thickness. It can be seen that a new pixel ASIC must be capable of sustaining hit rates up to $2 \text{ GHz}/\text{cm}^2$ with sufficient safety margins and the significant statistical fluctuations that can be expected from occasional very large events, e.g. due to beam gas interactions. A list of technical requirements for the new pixel ROC is summarized in Table A.1. In order to fulfil those, the architecture of the new pixel ROC has to be carefully optimized, with emphasis on the digital part. Low-noise analogue front-ends circuits in each pixel should have a low threshold, converting sensor signals as early as possible into the digital domain, where extensive buffering and intelligent logic enables the handling of hit rates in a high granularity chip.

A.4.1 Readout Chip Technology

The IC technology required for such a new pixel ROC development depends strongly on the pixel size, the required hit rates, data buffering and required trigger and readout functions and interfaces. In addition the technology must have a very high radiation tolerance (300 Mrad and $10^{16} \text{ n}_{eq} (1 \text{ MeV}) \text{ cm}^{-2}$) for a nearly 10 year lifetime in the hostile HL-LHC radiation environment. The technology must also be appropriate for the integration of many thousands of very low noise pre-amplifiers, shapers and discriminators together with large amounts of digital logic for data buffering and readout.

The current (and Phase 1 upgrade) CMS pixel detector ROC has been developed in a 250 nm CMOS technology that has been made sufficiently radiation hard by using special layout tech-

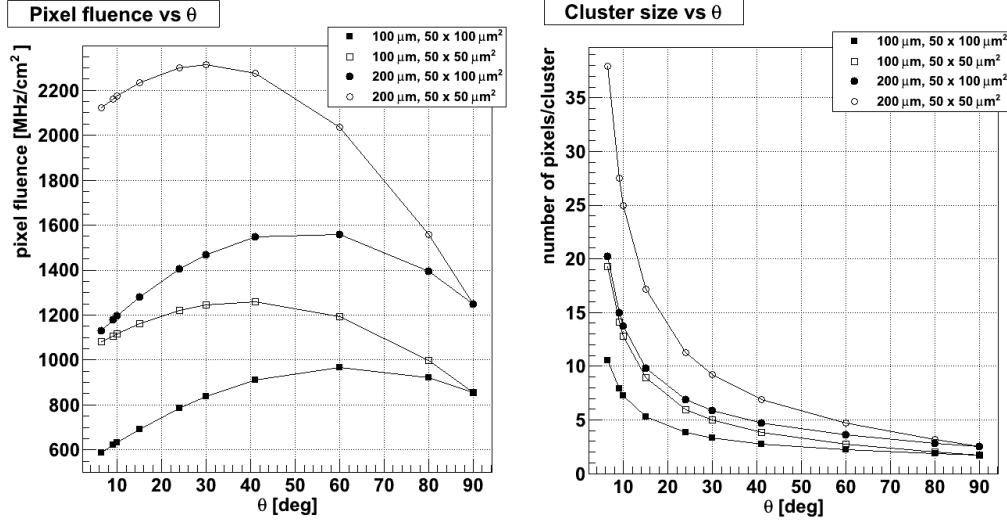


Figure A.4: Estimated pixel hit rates per cm^2 (left plot) and cluster width (right plot) versus theta for a planar 2D pixel detector in layer 1 for different sensor geometries: $50 \times 50\ \mu\text{m}^2$ (open) and $50 \times 100\ \mu\text{m}^2$ (black) pixel cell size for a thickness of $200\ \mu\text{m}$ (square) and $100\ \mu\text{m}$ (circle).

Track rate: $500\ \text{MHz}/\text{cm}^2$	Pixel deadtime: $< 50\ \text{ns}$ for MIPs
Efficiency: $> 99\%$ at $2\ \text{GHz}/\text{cm}^2$	Leakage current compensation
Threshold: $\approx 1000\text{--}1800\ e^-$	Power: $< 1\ \text{W}/\text{cm}^2$
Polarity: neg. & pos.	Trigger rate: Up to $200\ \text{KHz}$
Pixel size: $< 50 \times 100\ \mu\text{m}^2$	Trigger latency: $< 6.4\ \mu\text{s}$
Amplitude resolution: $\sim 4\ \text{bit}$	Readout: To LPGBT link chip
Time walk: $< 25\ \text{ns}$	Radiation hard: $300\ \text{Mrad}$ & $10^{16}\ n_{\text{eq}}(1\ \text{MeV})/\text{cm}^2$
Sensor: 2D Si, 3D Si, Diamond	Support for intermediate trigger with Region of interest information
Sensor capacitance: $< 200\ \text{fF}$	Modes: Triggered, Self triggered, Non triggered, Testing, Calibration
Front-end noise: $< 200\ e^-$	

Table A.1: General specifications of CMS pixel ROC.

niques (enclosed gate layout) for all transistors in both analogue and digital functions. To cope with the significantly increased requirements for a HL-LHC pixel detector a denser IC technology will be required. A $130\ \text{nm}$ CMOS technology, is currently used for several short-mid term pixel projects in the HEP community (ATLAS IBL, Medipix, LHCb VELO pixel, etc.), and has been considered as a possible option for the high luminosity CMS pixel upgrade. It is however estimated not to offer sufficient logic density to fulfill all the requirements for a HL-LHC pixel upgrade.

On the other hand, experience is currently being gained in the HEP community with $65\ \text{nm}$ CMOS technologies. It offers about four times higher logic density compared to the $130\ \text{nm}$ node and has recently been radiation qualified by CERN [82]. It is found not to require special layout of transistors in digital functions to tolerate the HL-LHC radiation environment. This gives an effective logic density gain of a factor nearly 30 compared to the $250\ \text{nm}$ technology.

The handling of radiation induced Single Event Upsets (SEU) in the 65 nm CMOS technology is the same as used in previous technologies, using triple modular redundancy (TMR) and Hamming encoding for critical functions. The SEU cross-section of the 65 nm technology is slightly better than previous technology generations, though with an increased risk of multiple bit upsets in neighbouring elements. This technology has in addition significantly lower power consumption for digital functions and also some power reduction for small dynamic range analogue functions. It will therefore allow the design of a pixel ROC implementation with significantly increased complexity and acceptable power dissipation. This has a direct impact on the required local infrastructure for cooling and powering and the material budget of the pixel detector.

The 65 nm technology node is known to be a mature and high yield modern technology that is expected to remain commercially available for the full time frame of the HL-LHC CMS upgrade. Demonstrator circuits of analogue pixel front-ends have been made in the context of the technology evaluation at CERN. A Pixel front-end has already been shown to have very good performance and radiation tolerance [83, 84]. The 65 nm CMOS technology has therefore been chosen as the baseline for a new ROC development.

A.4.2 Analog Front-end

To be capable of working with the different sensor options currently under evaluation, the analog front-end must have sufficiently low noise and sufficiently good threshold uniformity between pixels to function reliably with detection thresholds lower than $1800 e^-$ (ideally $\sim 1000 e^-$). The signal polarity must be programmable and active leakage current compensation is required in particular for the planar Si sensor options.

A four bit amplitude measurement for all hits above threshold is sufficient to perform centre of gravity calculations for hit clusters and also continuously monitor the optimal function of the pixel sensor. An amplitude measurement using the simple Time Over Threshold (TOT) principle is the baseline option if the related deadtime can be made sufficiently short (< 50 ns for minimum ionizing particles (MIPs)). An alternative option under evaluation is the use of a self triggered 4 bits Successive Approximation Register (SAR) ADC that can be implemented very efficiently in deep sub-micron CMOS technologies. It has been shown that the time walk requirement, to assure that all hits are correctly assigned to their bunch crossing (and thereby also the right trigger), will be a determining factor for the power consumption of the analog pixel front-end. The use of digital time walk compensation, based on the amplitude measurement, will enable the analog power consumption to be minimized. From initial test circuits of similar pixel front-ends in 65 nm, it is estimated that the analog front-end with its local threshold adjust DAC, biasing and configuration bits can possibly occupy an area of less than $(50 \times 50) \mu\text{m}^2$.

A.4.3 Pixel Groups

After the basic pixel signal discrimination and amplitude measurement all further signal processing and data storage will be fully digital. Hit information will need to be stored locally in the pixel cells until the arrival of the trigger determining which event data to read out. For the relatively small pixel size required, it will be marginal to fit sufficient logic and storage into the remaining area of each pixel, even in a 65 nm technology. Since pixel hits are highly clustered (average cluster size: ~ 4) an architecture based on local pixel regions can decrease significantly the amount of local buffering required. The use of pixel regions also enables functions and logic to be shared across pixels, making much more efficient use of the digital resources. This is especially beneficial for a pixel ROC that must be capable of working with various types of sensors

with good isolation between analog and digital functions. It is estimated that the power consumption of such a pixel ROC with an optimized architecture can be kept below 1 W/cm^2 in a 65 nm CMOS technology.

At the arrival of a positive trigger, each pixel region extracts address and amplitude measurement for each cell with a signal and sends them via column buses to the End Of Column (EOC) logic. Hit data from all columns are merged into a common data stream with appropriate formatting and encoding. The global pixel chip architecture with the main data buffering and data buses together with the general configuration and monitoring functions are shown in Figure A.5. The readout interface from the pixel ROC to the low power GBT optical link transmitter chip [85] will be done with local low power serial links with a programmable speed between 80 Mbits/s and 640 Mbits/s. Initial estimates for a $\sim 2 \text{ cm} \times 2 \text{ cm}$ pixel chip in the inner pixel layer indicates that $\sim 300 \text{ Mbits/s}$ bandwidth is required per chip for a 100 KHz trigger rate. This fits well with a pixel module having ten pixel chips and low power GBT link interface chip as indicated in Figure A.6. Local power converter/conditioning electronics and the electrical to optical conversion will most likely be located at $\sim 1 \text{ m}$ distance from the pixel detector module itself for reasons of material budget and radiation hardness, as in the case for the Phase 1 upgrade. For the inner pixel layer a pixel module consisting of only one row of 5 pixel chips may be mechanically more appropriate and will also ensure better data bandwidth margins for the readout link.

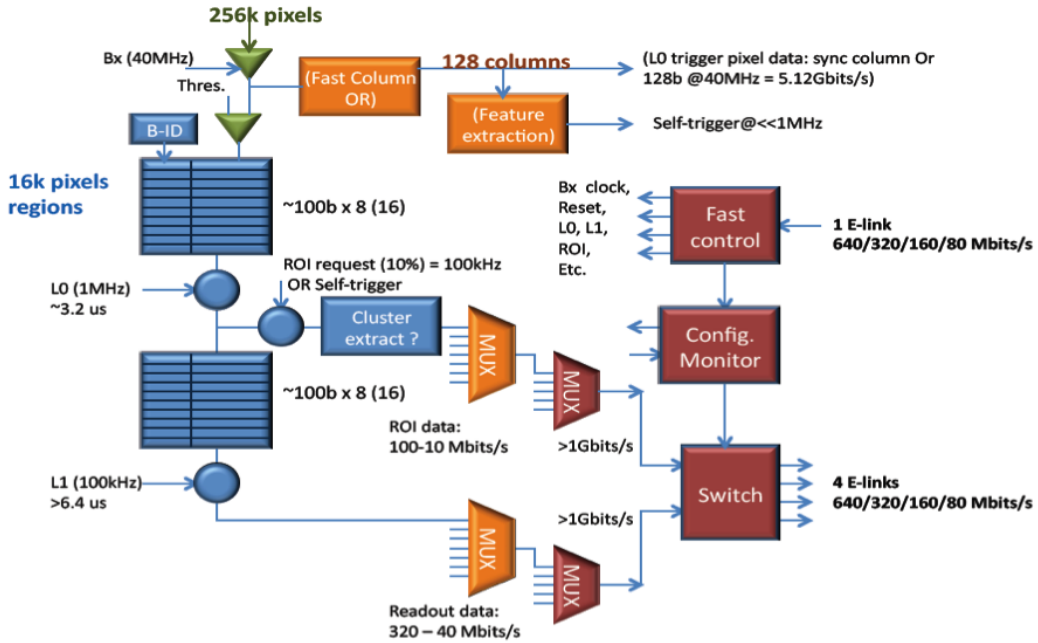


Figure A.7: General data flow with readout data and ROI data.

A.4.4 Pixel Trigger

The high-density 65 nm technology will, from first estimates, also offer the possibility that the pixel detector contributes Regions Of Interest (ROI) information to a two-stage trigger system. In this approach a fraction of the Pixel ROCs will, after a latency of about 100 clock cycles, be requested to send pixel information to the trigger system. At this level only relatively coarse pixel hit information will be required and the pixel address of the central hit in a cluster could

be sufficient. The data rate from each pixel chip is of the order of 100 Mbits/s for a scenario where the first stage trigger reduces the rate to ~ 1 MHz and $\sim 10\%$ of the ROCs are requested to send ROI data. A pixel ROC with 4 serial output ports of up to 640 Mbits/s each assures sufficient bandwidth and flexibility for the normal readout data and the optional ROI information. The global data flow in the pixel ASIC is indicated in Figure A.7, where the two levels of multiplexing shown are the shared column buses and the final data merging in the EOC logic. If required, one of the readout ports can be configured to use a readout protocol compatible with the current readout system.

Another option is to send direct synchronous data extracted locally in the ROC to the trigger system. This can be coarse hit information from OR'ed pixels in columns or basic counts of clusters and/or hits in each bunch crossing. More sophisticated data extraction analyzing the local configuration of clusters (e.g. cluster widths or groups of clusters) will also be studied in more detail.

A.5 Organization and Development Plan

A development plan is presented here covering the next 5 years, in parallel with the Phase 1 construction project. The plan takes into account a coherent effort toward the ultimate pixel detector for the HL-LHC, but should also be flexible to make use of any opportunity between LS2 and LS3 to improve the performance and the longevity of the pixel detector by replacing the innermost barrel layer. The main target is the development of the critical technologies, namely the sensor, the ROC and the electronic system

A.5.1 ROC Development

For the ROC development it is important to form a strong collaboration among several ASIC designers in a few research centers. Collaboration has begun between Fermilab, INFN Torino and Perugia, CERN and other European groups are also expressing their interest to participate.

Sharing of tools is essential for the collaborative effort of designing the new ROC. According to past experience, five years is considered a reasonable time to develop of a new ROC. The basic 5-year plan is shown in Figure A.8. During the first years, several Multi Project Wafer (MPW) submissions will be made via Europractice, and only at a later and more mature stage will a full engineering run be made.

The first MPW submission will be focused on studying analog building blocks for the ROC, including a pixel front-end and an ADC. The second submission will be a small-scale prototype, bondable to a sensor. A third MPW will include a complete pixel column with full analogue and digital functions in the pixel cells/regions, made as a folded column so it can fit within a limited sized test chip. The definition of the whole architecture of the chip is developed in parallel, and tested with architecture simulation tools among the different centers with ASIC expertise. The goal is to define the architecture of the ROC in two years, during which time also the pixel dimensions will be defined following simulation and performance studies.

The third MPW prototype will adopt the chosen pixel geometry and architecture, with a simplified end of column logic. The aim is to be able to test a full column of the ROC chip. All submissions will be tested in laboratory, with the prototype bonded to a sensor measured in a test beam. Irradiation tests will be essential to understand the radiation hardness of the chip design. Other groups, in addition to those involved to the ROC design, are interested to join in the testing, characterization and irradiation studies of the chip.

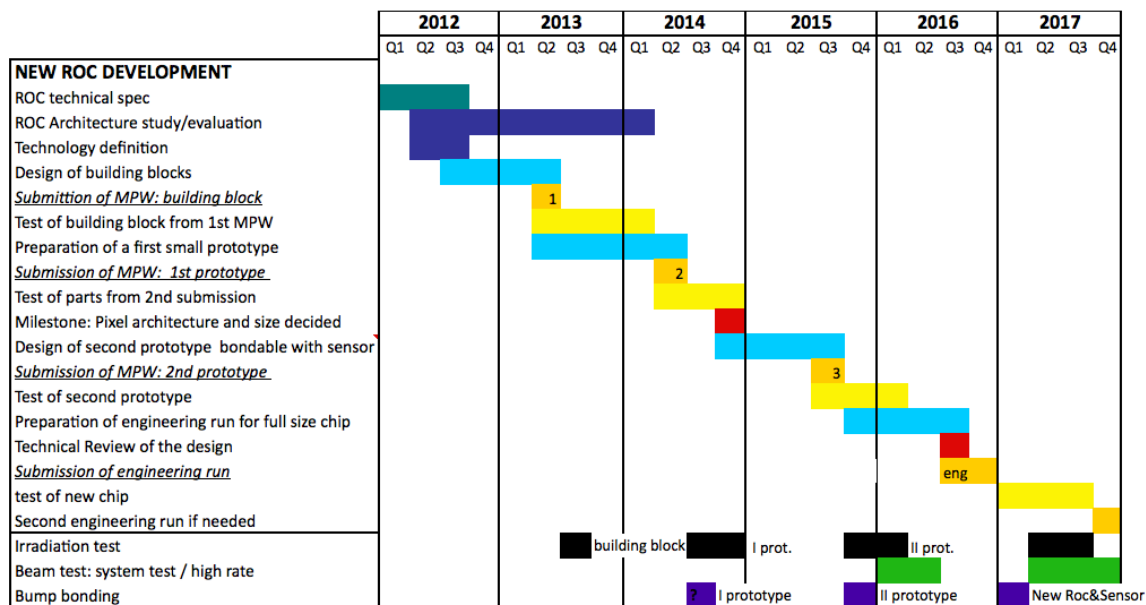


Figure A.8: Working 5-year plan for new ROC development.

Item	Approximate Cost	Comments
3 MPW with small prototypes in 65 nm CMOS technology	250 KCHF	Third submission more expensive than first and second
1 Engineering run	1 MCHF	Investigating cheaper options, like Multi Layer Masking, shared reticule

Table A.2: Cost for a new ROC development 5-year plan.

An engineering run will be needed to realise the first full scale chip and understand system aspects. This chip will be fully characterized and tested in test beams, before and after irradiation. The cost of the development of the new ROC, is shown in Table A.2, where costs are approximate since a contract with the vendor still needs to be finalized. Experience shows that there would possibly be a need for a second engineering run after this. Eventual production costs are not included here, but correspond to about 250 kCHF per square meter.

A.5.2 Sensor Development

For sensors, R&D work is ongoing on different technologies: on 3D pixel sensors, groups from USA (FNAL, Purdue, SUNY, TAMU, UMiss), INFN (Bari and Torino) and PSI are involved; on diamond detector USA (Colorado, FNAL, Rutgers, Tennessee) and Europe (Milano, Perugia, Strasbourg, ETH); testing thin planar, silicon pixel sensors in performed in several USA groups (JHU, FNAL, Purdue, TAMU).

The development plan for sensor is shown in Figure A.9. In the first year the irradiation studies from various vendors (3D: FBK, CMN, SINTEF; Diamond: DDL, II-IV; planar: HPK) will be finished. New submissions for 3D pixel, and diamond detectors will be done. For silicon planar sensors studies of different combination of materials, thicknesses and production technologies are under way. In particular, Float Zone, magnetic-Czochralski and epitaxial for 100, 200, 300 μm thickness: first conclusions are expected already at the end of this year. Thin pla-

Item	Approximate Cost	Comments
Planar silicon	part of silicon strips R&D	Using sensors from HPK
3D pixel	150 kCHF	One run per FBK and CNM
Diamond	50 kCHF	
Engineering run	150 kCHF	Sensor type to be decided

Table A.3: Cost for the sensor development 5-year plan.

nar sensors from Hamamatsu will be bump bonded and tested with the new PSIdig chip that has a lower threshold than the present one, to understand more in depth the signal collection after irradiation and in general the performance.

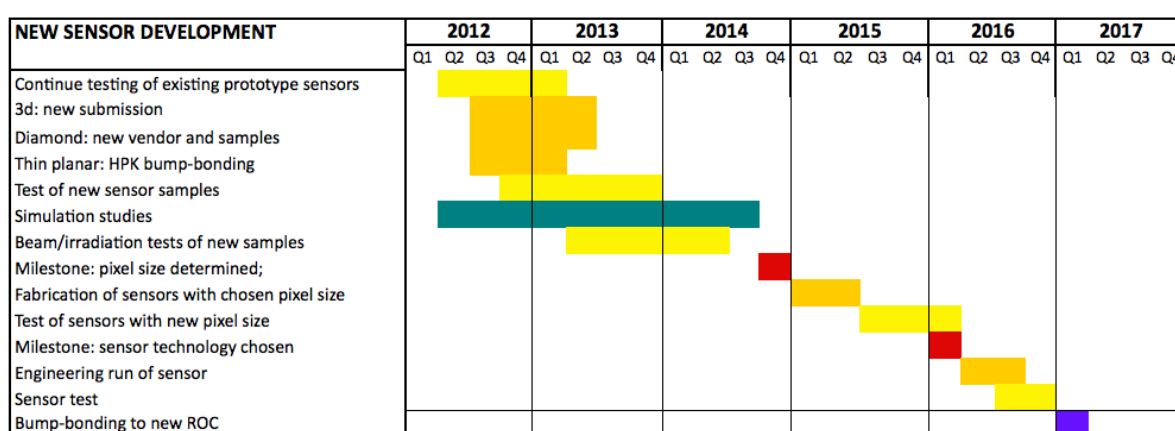


Figure A.9: Development 5-year plan for new sensors.

Simulation studies will be done to optimise the sensor design. After the pixel cell size will be chosen, the sensor will be produced with the required geometry and about one year later the sensor technology will be chosen. For 3D pixel sensors, additional valuable information will come from ATLAS IBL detector, which implements sensors from two different vendors (FBK and CNM). The cost of the sensor development program is shown in Table A.3.

A.5.3 System Development

It is important to understand and study system aspects. A module concept will be studied in more detail, in particular the powering scheme, the readout of the module and the inter-

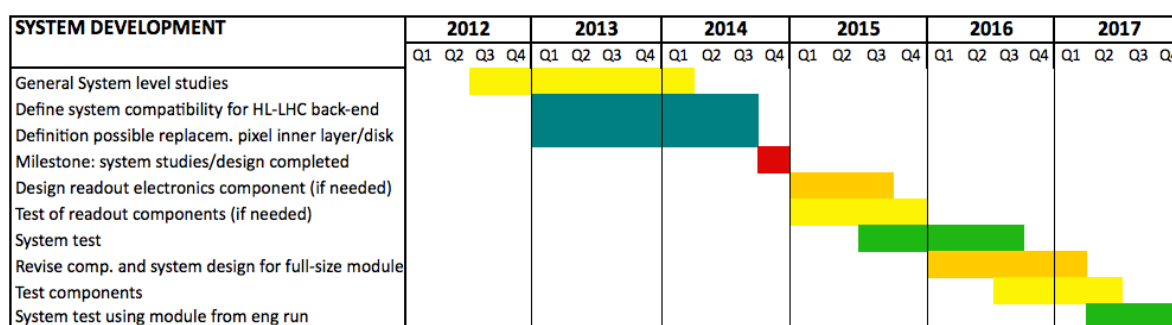


Figure A.10: Planning for system aspects.

Item	Approximate Cost	Groups involved
Development of New Pixel ROC in 65 nm CMOS	1.25 MCHF	INFN (Torino, Perugia, Pisa) and FNAL committed; (CERN and other institutes interested)
Development of New sensors	350 kCHF	USA (FNAL, Purdue, SUNY, TAMU, UMiss, Colorado, Rutgers, Tennessee, JHU) INFN (Milano, Bari, Torino, Perugia) PSI, ETH, Strasbourg

Table A.4: Cost for New Pixel detector 5-year development plan.

connections with the trigger for a HL-LHC detector. The option for the replacement of the inner barrel layer will be studied, to understand the compatibility with available services and backend electronics. A general plan for the system development is shown in Figure A.10.

The total costs for the 5 year development plan is shown in a summary Table A.4 together with the currently interested countries.

Appendix B

Glossary

List of acronyms used in this document:

1E: 1 n-type Electrode

2D: 2-Dimentional

2E: 2 n-type Electrodes

2PACL: 2-Phase Accumulator Controlled Loop

3D: 3-Dimentional

4E: 4 n-type Electrodes

AC: Alternate Current

ADC: Analog-to-Digital Converter

ALARA: As Low As Reasonably Achievable

ALT: Analogue Level Translator

AMC: Advanced Mezzanine Card

AMS: Alpha Magnetic Spectrometer

AOH: Analog Opto-Hybrid

API: Application Programming Interface

ASIC: Application-Specific Integrated Circuit

AWG: American Wire Gauge

BBM: Bump-Bonded Module

BCM: Beam Condition Monitor

BER: Bit Error Rate

BP: Beam Pipe

BPIX: Barrel Pixel Detector

BRM: Beam Radiation Monitor

CAD: Computer-Aided Design

CADI: CMS Analysis Database Interface

C-C: Carbon-fiber reinforced Carbon

CCD: Charge Collection Distance

CCU: Communication and Control Unit

CDC: Column Drain Cluster

CF: Carbon Fiber

CFK: Carbon-Carbon Filling K1100

CFRP: Carbon-Fiber Reinforced Plastic

CHF: Swiss Franc

CM: Center of Mass

CMM: Coordinate Measuring Machine

CMOS: Complementary Metal Oxide Semiconductor

CMS: Compact Muon Solenoid

CMSSW: Compact Muon Solenoid SoftWare

CNC: Computerized Numerical Control

CORA: CO₂ Research Apparatus

CORE: (LHCC) CO₂ REVIEW committee

CPLD: Complex Programmable Logic Device

CSI: Common Systems and Integration

CSV: Comma Separated Values

CT2: CASTOR-T2 (beam pipe)

CTE: Coefficient of Thermal Expansion

CVD: Chemical Vapor Deposition

DAC: Digital-to-Analog Converter	FPGA: Field Programmable Gate Array
DAQ: Data AcQuisition	FPIX: Forward Pixel Detector
DB: Database	FRL: Frontend Readout Link
DC: Direct Current	FTE: Full Time Equivalent
DCS: Detector Control System	FZ: Float Zone
DDR: Double Data Rate (RAM)	GbE: Gigabit Ethernet
DDTC: Double side Double Type Column	HAL: Hardware Access Library
DLT: Digital Linear Tape	HC: Half Cylinder
DOFZ: Diffusion Oxygenated Float Zone	HD: Half Disk
DOH: Digital Opto-Hybrid	HDI: High-Density Interconnect
DQM: Data Quality Monitoring	HF: Hadron Forward (Calorimeter)
DR: Digital Receiver	HL: High Luminosity
DSS: Detector Safety System	HL-LHC: High-Luminosity LHC
DTR: Digital Trasmitter/Receiver	HLT: High Level Trigger
ECAL: Electromagnetic Calorimeter	HMX: Heat and Mass eXchanger
EDR: Engineering Design Review	HPC: High Pin Count
EE: ECAL Endcap	I2C: Inter-Integrated Circuit
EMC: ElectroMagnetic Cmpatibility	IBL: Insertable Barrel layer
EOC: End Of Column	IC: Integrated Circuit
ES : ECAL preShower detector	ID: Identification
EUR: Euro	ID: Inner Diameter
FA: Funding Agency	IP: Interaction Point
FB: Finance Board	IP: Internet Protocol
FE: Front End	IPMI: Intelligent Platform Management In- terface
FE: Finite-Element (simulation)	ISS: International Space Station
FEA: Finite Element Analysis	IV: Current vs. Voltage (curve)
FEC: Front End Controller	JTAG: Joint Test Action Group
FED: Front End Driver	L0: Level 0
FIFO: Fan-In/Fan-Out	L1: Layer 1 (referred to BPIX)
FMC: FPGA Mezzanine Card	L1: Level 1 (referred to Trigger)

L1A: Level-1 (Trigger) Accept	MPW: Multi Project Wafer
L2: Layer 2	MS: Multi-Service (cable)
L3: Layer 3	μ TCA: Micro Telecommunications Computing Architecture
L4: Layer 4	μ TP: Micro Transfer Protocol
LC: Lucent Connector	Mx: Metric size x (referred to screws, threads, nuts)
LDMOS: Laterally Diffused Metal Oxide Semiconductor	NIEL: Non Ionizing Energy Loss
LED: Light-Emitting Diode	NRZI: Non-Return-to-Zero, Inverted
LHC: Large Hadron Collider	NRZI: Non-Return-to-Zero
LHCb: Large Hadron Collider beauty	OG: Orbit Gap
LHCC: Large Hadron Collider Committee	OMA: Optical Modulation Amplitude
LLD: Linear Laser Driver	P5: LHC Access Point n. 5
LPGBT: Low Power GigaBit Transceiver	PACL: Phase Accumulator Controlled Loop
LS1: Long Shutdown 1	PBS: Project Breakdown Structure
LS2: Long Shutdown 2	PC: Personal Computer
LS3: Long Shutdown 3	PCB: Printed Circuit Board
LSS: Long Straight Section (referred to LHC)	PCIe: Peripheral Component Interconnect express
LT: Laser Transmitter	PEEK: Poly-Ether Ether Ketone
LVDS: Low Voltage Differential Signal	PFN: Physical File Name
M&S: Materials and Services	PIO: Programmed Input/Output
MARCO: Multipurpose Apparatus for Research on CO ₂	PLC: Programmable Logic Controller
MB: Management Board	PLL: Phase-Locked Loop
MCH: MicroTCA Carrier Hub	PLT: Pixel Luminosity Telescope
MCZ: Magnetic CZochralski	PM: Project Manager
MIB: Machine Induced Background	POD: Plain Old Data
MIP: Minimum Ionizing Particle	POH: Pixel Opto-Hybrids
MMC: Memory Management Controller	PP0: Patch Panel 0
MOS: Metal Oxide Semiconductor	PP1: Patch Panel 1
MoU: Memorandum of Understanding	PRBS: Pseudo-Random Bit Stream
MP7: Master Processor board, Virtex-7	

PROM: Programmable Read-Only Memory	SDHC: Secure Digital High capacity (referred to Memory Cards)
PRR: Procurement Readiness Review	SEU: Single Event Upset
PS: Power Supply	SFP: Small Form-factor Pluggable (transceiver)
PSU: Poer Supply Unit	SFP+: Small Form-factor Pluggable plus (transceiver)
PT: Pressure Transmitter	SQL: Structured Query Language
PU: Pile-up	SRAM: Static Random-Access Memory
PUC: Pixel Unit Cell	SS: Stainless Steel
PVSS: ProzessVisualisierungs und SteuerungsSystem (Process Visualization and Control System)	sTTS: synchronous Trigger Throttling System
QA: Quality Assurance	TAS: Front Quadrupole Absorber (sic!)
QC: Quality Control	TBD: To Be Determined
QDR: Quad Data Rate (RAM)	TBM: Token Bit Manager
QFN: Quad Flat No-leads (package)	TCAD: Technology Computer-Aided Design
R&D: Research and Development	TDR: Technical Design Report
RAM: Random-Access Memory	TE: Technology (Department at CERN)
RJ: Registered Jack	TE: TEMperature sensor
RMS: Root Mean Square	TEC: Tracker End Cap
ROC: Read-Out Chip	TIB: Tracker Inner Barrel
ROI: Regions Of Interest	TIB: Tracker Institution Board
ROSE: Research and development On Silicon for future Experiments	TID: Tracker Inner Disks
RRB: Resource Review Board	TID: Total Ionizing Dose
RTD: Resistance Temperature Detector	TIF: Tracker Integration Facility
S/N: Signal-to-Noise (ratio)	TIM: Thermal Interface Materials
S1: A group of racks in USC	TMR: Triple Modular Redundancy
S1G01-4: A rack belonging to the S1 group	TOB: Tracker Outer Barrel
S1G02: A rack belonging to the S1 group	TOSA: Transmitter Optical Sub-Assembly
SAR: Successive Approximation Register	TOT: Time Over Threshold
SATA: Serial Advanced Technology Attachment	TPG: Thermal Pyrolytic Graphite
SC: Service Cavern	TS: Thermal Screen
	TTC: Trigger Timing and Control

TTs: Trigger Throttling system

UBM: Under Bump Metal

UDP: User Datagram Protocol

uHAL: (see HAL)

UNICOS: UNIX Cray Operating System

URL: Uniform Resource Locator

USB: Universal Serial Bus

USC: Underground Service Cavern

USD: United States of America Dollar

UXC: Underground eXperimental Cavern

VBF: Vector Boson Fusion

VCR: Vacuum Coupling Radiation (fitting)

VELO: VERtex LOcator

VHDI: Very High-Density Interconnect

VME: VERSA Module Eurocard (a data bus standard)

WG: Working Group

X2: A group of racks in UXC

XML: eXtensible Markup Language

YB0: Yoke Barrel 0

YE1: Yoke Endcap 1

YETS: Year-End Technical Stop

References

- [1] CMS Collaboration, “Observation of a new boson at a mass of 125 GeV with the CMS experiment at the LHC”, *Phys.Lett.B* (2012). CMS-HIG-12-028, CERN-PH-EP-2012-220.
- [2] CMS Collaboration, “The CMS tracker system project : Technical Design Report”, Technical Report CERN-LHCC-98-006, CERN, (1998).
- [3] CMS Collaboration, “The CMS tracker : addendum to the Technical Design Report”, Technical Report CERN-LHCC-2000-016, CERN, (2000).
- [4] CMS Collaboration, “Description and Performance of the CMS Track and Primary Vertex Reconstruction”, Paper to be submitted to JINST CMS-PAPER-TRK-11-001, CERN, (2012).
- [5] CMS Collaboration, “Tracking and Primary Vertex Results in the First 7 TeV Collisions”, Technical Report CMS-PAS-TRK-10-005, CERN, (2010).
- [6] A. Dominguez, “The CMS pixel detector”, *NIM A* **581** (2007) 343.
- [7] C. Roland, “Track reconstruction in heavy ion events using the CMS tracker”, *Nuclear Instruments and Methods in Physics Research Section A* **566** (2006), no. 1, 123–126.
- [8] S. Agostinelli et al., “Geant4—a simulation toolkit”, *Nuclear Instruments and Methods in Physics Research Section A* **506** (2003), no. 1, 250–303.
- [9] J. Allison et al., “Geant4 developments and applications”, *IEEE Transactions on Nuclear Science* **53** (2006), no. 1, 270–278.
- [10] V. Khachatryan et al., “CMS Tracking Performance Results from early LHC Operation”, *European Physical Journal C* **70** (2010) 1165–1192.
- [11] CMS Collaboration, “Algorithms for b Jet Identification in CMS”, Physics Analysis Summary CMS-PAS-BTV-09-001, CERN, (2009).
- [12] C. Weiser, “A Combined Secondary Vertex Based B-Tagging Algorithm in CMS”, CMS Note CERN-CMS-NOTE-2006-014, CERN, (2010).
- [13] CMS Collaboration, “Commissioning of the Particle-Flow Reconstruction in Minimum-Bias and Jet Events from pp Collisions at $\sqrt{s} = 7$ TeV”, Physics Analysis Summary CMS-PAS-PFT-10-002, CERN, (2010).
- [14] M. Cacciari, G. P. Salam, and G. Soyez, “The anti-kt jet clustering algorithm”, *JHEP* **04** (2008) 063.
- [15] M. Cacciari and G. P. Salam, “Dispelling the N³ myth for the k(t) jet-finder”, *Phys. Lett. B* **641** (2006) 57.

- [16] M. Cacciari, G. P. Salam, and G. Soyez, “FastJet User Manual”, *Eur. Phys. J.* **C72** (2012) 1896.
- [17] CMS Collaboration, “Determination of the Jet Energy Scale in CMS with pp Collisions at $\sqrt{s} = 7$ TeV”, Physics Analysis Summary CMS-PAS-JME-10-010, CERN, (2010).
- [18] T. Sjöstrand, S. Mrenna, and P. Skands, “PYTHIA 6.4 Physics and Manual”, Preprint LU TP 06-13, Lund, (2006).
- [19] CMS Collaboration, “Search for the Higgs Boson in VH Production with H to bb”, Physics Analysis Summary CMS-PAS-HIG-11-031, CERN, (2011).
- [20] CMS Collaboration, “Search for the standard model Higgs boson produced in association with W or Z bosons, and decaying to bottom quarks for ICHEP 2012”, Physics Analysis Summary CMS PAS HIG-12-019, CERN, (2012).
- [21] W. Adam, V. Adler, B. Hegner et al., “PAT: the CMS Physics Analysis Toolkit. oai:cds.cern.ch:1196152”, Technical Report CMS-CR-2009-083, CERN, Geneva, (May, 2009).
- [22] The HZZ4l Team, “Search for the standard model Higgs boson in the decay channel H to ZZ to 4l in pp collisions”, CMS Note CMS NOTE AN-12-141, CERN, (2012).
- [23] CMS Collaboration, “Evidence for a new state in the search for the standard model Higgs boson in the $H \rightarrow ZZ \rightarrow 4l$ channel in pp collisions at $\sqrt{s} = 7$ TeV and 8 TeV”, Physics Analysis Summary CMS PAS HIG-12-016, CERN, (2012).
- [24] S. Martin, “A supersymmetry primer”. hep-ph/9709356v5, 1997.
- [25] C. Lester and J. Summers, “Measuring masses of semi-invisibly decaying particles pair produced at colliders”, *Phys. Lett.* **B463** (1999) 99.
- [26] A. Barr, C. Lester, and P. Stephens, “ M_{T2} : the truth behind the glamour”, *J. Phys.* **G29** (2003) 2343.
- [27] A. Barr and C. Gwenlan, “The race for supersymmetry: using M_{T2} for discovery”. arXiv:0907.2713, 2009.
- [28] U. Langenfeld, S. Moch, and P. Uwer, “Measuring the running top-quark mass”, *Phys. Rev.* **D80** (2009) 054009.
- [29] CMS Collaboration, “CMS Technical Design Report, Volume 2: Physics performance”, *J. Phys.* **G34** (2007) 995.
- [30] CMS Collaboration, “Search for supersymmetry in hadronic final states using MT2 in pp collisions at $\sqrt{s} = 7$ TeV”. arXiv:1207.1798, Submitted to JHEP, 2012.
- [31] CMS Collaboration, “Particle Flow Event Reconstruction in CMS and Performance for Jets, Taus and MET”. CMS-PAS-PFT-09-001, 2009.
- [32] M. Cacciari, G. Salam, and G. Soyez, “The anti-kt clustering algorithm”, *JHEP* **0804** (2008) 63.
- [33] CMS Collaboration, “Jet Performance in pp Collisions at $\sqrt{s} = 7$ TeV”, Physics Analysis Summary CMS-PAS-JME-10-003, CERN, (2010).

- [34] L. Caminada and A. Starodumov, "Building and commissioning of the CMS pixel barrel detector", *JINST* **4** (2009) P03017.
- [35] L. Amaral, S. Dris, A. Gerardin et al., "The Versatile Link, a common project for super-LHC", *Journal of Instrumentation* **4** (2009), no. 12, P12003.
- [36] J. Troska and others., "Versatile Transceiver developments", *Journal of Instrumentation* **6** (2011) C01089.
- [37] J. Troska, "Optical Link Power Budget Calculation, CMS Pixel Detector Phase I Upgrade Optical Links", EDMS Document CMS-TK-ER-0030, CERN, (2011).
- [38] S. Haas and E. van de Bij, "S-LINK Specification", preprint, CERN, (2003).
- [39] G. Iles, J. Jones, and A. Rose, "MP7", preprint, Imperial College London, Iceberg Technologies, (2012).
- [40] R. Frazier, M. Magrans, and A. Rose, "Code Archive for CERN Trigger Upgrades", preprint, CERN, (2012).
- [41] E. Hazen, "AMC13", preprint, Boston University, (2012).
- [42] J. Varela, "CMS L1 Trigger Control System", CMS Note CERN-CMS-NOTE-2002-033, CERN, (2002).
- [43] CMS Collaboration, "The CMS experiment at the CERN LHC", *JINST* **3** (2008), no. S08004.
- [44] T. Rohe, A. Bean, V. Radicci et al., "Planar sensors for the upgrade of the CMS pixel detector", *Nucl.Instrum.Meth.* **A650** (2011) 136–139.
- [45] G. Cerati, M. Dinardo, A. Florez et al., "Radiation tolerance of the CMS forward pixel detector", *Nucl.Instrum.Meth.* **A600** (2009) 408–416.
- [46] F. Lemeilleur, G. Lindström, and S. Watts, "Third RD48 status report", technical report, CERN, (2000). LHCC-2000-009.
- [47] S. König, C. Hormann, R. Horisberger et al., "Building CMS pixel barrel detector modules", *Nucl.Instrum.Meth.* **A582** (2007) 776–780, doi:10.1016/j.nima.2007.07.090, arXiv:physics/0702181.
- [48] C. Broennimann, F. Glaus, J. Gobrecht et al., "Development of an indium bump bond process for silicon pixel detectors at PSI", *Nucl.Instrum.Meth.* **A565** (2006) 303–308, doi:10.1016/j.nima.2006.05.011, arXiv:physics/0510021.
- [49] L. Caminada and A. Starodumov, "Building and commissioning of the CMS pixel barrel detector", *JINST* **4** (2009) P03017.
- [50] F. Faccio, B. Allongue, G. Blanchot et al., "TID and displacement damage effects in vertical and lateral power MOSFETs for integrated DC-DC converters", in *Radiation and Its Effects on Components and Systems (RADECS), 2009 European Conference on*, pp. 46–53, IEEE. 2009. doi:10.1109/RADECS.2009.5994551.
- [51] S. Michelis et al., "DC/DC ASIC converters in 0.35 μ m CMOS technology", in *TWEPP-2011*. 2011. To be published in *JINST*.

- [52] S. Müller (2012). Private communication.
- [53] F. Faccio, S. Michelis, et al., “Development of custom radiation-tolerant DC/DC converter ASICs”, *JINST* 5 (2010) C11016.
- [54] L. Feld, R. Jussen, W. Karpinski et al., “DC-DC conversion powering for the CMS tracker at SLHC”, *NIM A* 628 (2011), no. 1, 453–456.
- [55] L. Feld, R. Jussen, W. Karpinski et al., “DC-DC buck converters for the CMS tracker upgrade at SLHC”, *JINST* 6 (2011) C01020.
- [56] G. Blanchot, C. Fuentes, et al., “Low noise DC to DC converters for the SLHC experiments”, *JINST* 5 (2010) C11011.
- [57] K. Klein et al., “Powering for future detectors: DC-DC converters for the CMS tracker upgrade”, *PoS* (2011) 041. Vertex 2011.
- [58] J. Sammet et al., “Radiated electromagnetic emissions of DC-DC converters”, *JINST* 5 (2010) C12055.
- [59] C. Ljuslin, M. Marchioro, and C. Paillard, “The CCU25: a network oriented communication and control unit integrated circuit in a 0.25 μm CMOS technology”, in *Proceedings of the Eighth Workshop on Electronics for LHC Experiments*, C. Isabella, ed., CERN. 2002. CERN 2002-003.
- [60] M. Huhtinen, A. Rubbia, and P. Aarnio, “Calculation of neutron background generated by various beam pipe geometries at LHC”, *NIM A* 351 (1994) 236–239.
- [61] P. Aarnio and M. Huhtinen, “Beam Pipe Related Background Revisited”, CMS Internal Note CMS-IN-1997/025, CERN, (1997).
- [62] M. Huhtinen, “Impact of beam-pipe geometry on radiation background in CMS”, Technical Report CMS-IN-2000/069, CERN, (2000).
- [63] “AlBeMet® is the trade name of the Materion Brush Beryllium & Composites (formerly known as Brush Wellman) company for a beryllium and aluminum composite material derived by a powder metallurgy process. This powder metallurgical product is produced by gas atomization available as rod, bar, tube and sheet. These shapes are derived by consolidating the Al/Be powder by hot isostatic pressing (HIP) and cold isostatic pressing (CIP) followed by extrusion. The extruded bar is fabricated by CIP’ing the isotropic spherical Al/Be powder into semi-dense billets and then canning the billet for subsequent extrusion with a minimum of 4:1 reduction ratio”.
- [64] G. Sguazzoni and C. Cerrati, “Tracker Material Budget Estimation with Photon Conversions in Minbias Data”, CMS Analysis Note CMS-AN-2010/040, CERN, (2010).
- [65] B. Jeanneret, “Geometrical acceptance in LHC v5.0”, Technical Report LHC-PROJECT-NOTE 111, CERN, (1997).
- [66] P. Bhat, N. Mokhov, A. Singh et al., “Simulation Studies of the Radiation Environment in the CMS Detector for pp Collisions at the LHC”, CMS Note CMS-CR-2009/262, CERN, (2009).

- [67] G. Battistoni, F. Cerutti, A. Fasso et al., "The FLUKA code: Description and benchmarking", in *Hadronic Shower Simulation Workshop(AIP Conference Proceedings Volume 896)*, volume 896, p. 31, American Institute of Physics, 2 Huntington Quadrangle, Suite 1 NO 1, Melville, NY, 11747-4502, USA. 2007.
- [68] S. Agostinelli, J. Allison, K. Amako et al., "GEANT4a simulation toolkit", *Nuclear Instruments and Methods in Physics Research Section A: Accelerators, Spectrometers, Detectors and Associated Equipment* **506** (2003), no. 3, 250–303.
- [69] J. Allison, K. Amako, J. Apostolakis et al., "Geant4 developments and applications", *Nuclear Science, IEEE Transactions on* **53** (2006), no. 1, 270–278.
- [70] B. Verlaet and A.-P. Colijn, "CO₂ Cooling Developments for HEP Detectors", in *VERTEX2009*, p. 031. PoS, 2009.
- [71] J. Alcaraz et al., "The alpha magnetic spectrometer (AMS)", *NIM* **A478** (2002) 119.
- [72] J. Augusto Alves, A. et al., "The LHCb detector at the LHC", *JINST* **3** (2008) S08005.
- [73] P. Tropea and S. Moccia, "Tracker and Pixel cooling pipework", EDMS Document CMS-IW-ER-0001, CERN, (2011).
- [74] J. Daguin and P. Tropea, "CMS Pixel cooling pipes safety file", EDMS Document CMS-IW-YR-0001, CERN, (2012).
- [75] M. Huhtinen (2002). Private communication.
- [76] C. Da Via, J. Hasi, C. Kerney et al., "Radiation hardness properties of full-3D active edge silicon sensors", *Nuclear Instruments and Methods in Physics Research Section A: Accelerators, Spectrometers, Detectors and Associated Equipment* **587** (2008), no. 2, 243–249.
- [77] A. Zoboli, M. Boscardin, L. Bosisio et al., "Double-sided, double-type-column 3-D detectors: Design, fabrication, and technology evaluation", *Nuclear Science, IEEE Transactions on* **55** (2008), no. 5, 2775–2784.
- [78] M. Swartz, "CMS pixel simulations", *NIM* **A511** (2003) 88.
- [79] G. Pellegrini, M. Lozano, M. Ullan et al., "First double-sided 3-D detectors fabricated at CNM-IMB", *Nuclear Instruments and Methods in Physics Research Section A: Accelerators, Spectrometers, Detectors and Associated Equipment* **592** (2008), no. 1, 38–43.
- [80] T. Hansen, A. Kok, T. Hansen et al., "First fabrication of full 3D-detectors at SINTEF", *Journal of Instrumentation* **4** (2009) P03010.
- [81] M. Garcia-Sciveres, D. Arutinov, M. Barbero et al., "The FE-I4 pixel readout integrated circuit", *Nuclear Instruments and Methods in Physics Research Section A: Accelerators, Spectrometers, Detectors and Associated Equipment* **636** (2011), no. 1, S155–S159.
- [82] S. Bonacini, P. Valerio, R. Avramidou et al., "Characterization of a commercial 65 nm CMOS technology for SLHC applications", *Journal of Instrumentation* **7** (2012) P01015.
- [83] P. Valerio (2011). Private communication.
- [84] P. Valerio and S. Bonacini, "Designing HEP circuits in 65nm".
<https://indico.cern.ch/conferenceDisplay.py?confId=173640/>, 2012.
- [85] "GBT link chip specifications".
<https://espace.cern.ch/GBT-Project/GBTX/Specifications/>.